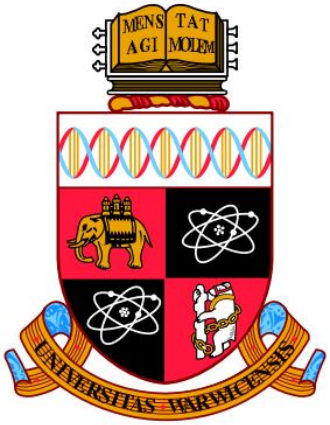

Search for the decays $\Xi_b^-(\Omega_b^-) \to \Lambda_c^+ h^- h'^-$ where h, h' are K or π at LHCb

by

Bhagyashree Pagare

Thesis

Submitted to the University of Warwick

for the degree of

Doctor of Philosophy

Department of Physics

September 2023

THE UNIVERSITY OF WARWICK

Contents

List of Figures

List of Tables

Acknowledgments

First and foremost, I would like to thank my parents Mr. Devidas Pagare and Mrs. Surekha Pagare, for bringing to my attention the Rajarshi Shahu Maharaj Foreign Scholarship Scheme for pursuing my PhD. I am indebted for every possible support they were able to provide during the process of application. I am grateful to the Commissionerate of the social welfare and their entire team for offering me the scholarship to fund my doctoral studies, particularly during the pandemic times.

Secondly, I would like to thank Prof. Timothy Gershon, Prof. Bill Murray and Dr. Thomas Blake for giving me an opportunity to work with the world's most powerful particle accelerator to dive into my quests about the fundamental understanding of the Universe through my doctoral studies. Thanks also to Dr. Umesh Kadhane, Dr. Aveek Sarkar and Dr. Anand Narayanan for being my referee for the PhD application.

Thirdly, I would like to thank my supervisor Prof. Timothy Gershon for their invaluable time, infinite patience and responsible guidance that helped me to grow professionally in the field. Their methods of providing the right direction left no stones unturned for successfully leading me towards my dissertation. Thanks to Dr. Tom Latham and Dr.Mark Whitehead for their prompt answers to any coding related question that I had. Thanks also to Arnau for introducing me to various aspects of the graduate studies at the start of my PhD.

I am also grateful to all the team members of the VELO group. Thanks to Dr. Victor Coco for all his help while navigating at CERN and for his efforts in providing infinite platforms to explore my skills. I am very grateful to Dr. Paula Collins for bringing out the best in me while at CERN by maintaining a right balance between her leadership and mentorship. Thanks also to my dance teacher Mrs. Sujatha Venkatesh for her wisdom. I could not have imagined my time at CERN if I wouldn't have met you.

Without forgetting, I am grateful to Dr. Fernando Abudinen. His precise comprehension and fruitful thoughts has helped me to come a long way during my PhD. I would also like to express my sincere gratitude towards Dr. Daniel Johnson for showing me the mirror, possibly without his knowledge. I must say, I was lucky to have met you. It's a bit unfortunate that I did not manage to work with you for my Post-Doc, inspite of your encouragement to apply. Nonetheless, I look forward to collaborate with such a great personality in future! As I have promised, I would also like to thank Alex and Luke for taking over the teaching contract and reducing my workload in the final year. Thanks also to Lee, my landlord, for all the adjustments during the times of pandemic.

Returning back, I am thankful to my family, my parents, my cute little brother Abhijeet, who has been a constant motivator, for being there for me at every moment and every ups and downs of my life by being my lifeline. Thanks to my dear friend Arunita for keeping me sane throughout my PhD through all our thoughtful discussions.

With no doubt, I am thankful to all my wise and beautiful friends and flatmates, for providing a great environment and a pleasant experience during the final year of my PhD. Flat 16 has been the most memorable thing that has happened during the entire duration of my PhD. Abhishek, Aishwarya, Andy, Bhushan, Dev, Goncalo, Hazique, Levi, Niketa, Ply, Rowan, Sanugi and Sarthak, each of you guys made the flat 16 a heaven on the earth...!!! Will miss you guys, the party's and all the thoughtful discussions, as well as the late night walks with Aishwarya, Bhushan and Hazique.

Declarations

The work presented in this thesis is all of my own work, unless it is specifically referenced to the contrary. This thesis has not been submitted, in any form, to this or any other university for another qualification. My analysis work has also been documented in an LHCb conference note [1], which therefore has some overlap with the content of this thesis.

Abstract

This thesis presents studies of three body decays of b baryons, in particular the Ξ_b^- and Ω_b^- baryons decaying to $\Lambda_c^+ h^- h'^-$ final states, where $h^{(\prime)}$ is a kaon or pion. Additionally, studies of the mode $B^- \to \Lambda_c^+ \overline{p} K^-$ are also presented. The analysis makes use of the data collected by the LHCb experiment at pp collision centre-of-mass energies of 7, 8 and 13 TeV from Run I and Run II, corresponding to an integrated luminosity of $8.7\,\text{fb}^{-1}$. We observe significant yields in four decays: $B^- \to \Lambda_c^+ \overline{p} K^-$, $\Xi_b^- \to \Lambda_c^+ K^- K^-$, $\Xi_b^- \to \Lambda_c^+ K^- \pi^-$ and $\Omega_b^- \to \Lambda_c^+ K^- K^-$ which have never been observed before at any experiment. The branching fractions and production rates of all the studied decays are measured with respect to that of the $B^- \to \Lambda_c^+ \overline{p} \pi^-$ decay. Additionally, branching fractions of the Ξ_b decays are measured with respect to $\Xi_b^- \to \Lambda_c^+ K^- \pi^-$, while branching fractions of Ω_b^- decays are measured with respect to $\Omega_b^- \to \Lambda_c^+ K^- K^-$. Limits are determined on the branching fractions and production rates of channels for which there is no significant yield. Studies of the differential production rate of $\Xi_b^- \to \Lambda_c^+ K^- \pi^-$ relative to $B^- \to \Lambda_c^+ \overline{p} \pi^-$ are also performed. The production asymmetry of the b baryons and its kinematic dependence is also studied. A first look at the Dalitz plot distributions and the intermediate resonances of the modes is also documented.

Chapter 1

Introduction

"The value of an idea lies in the using of it."
– Thomas Edison

The standard theories about the start of our Universe, and its early evolution, suggest that matter and antimatter must have been produced in equal amounts. However experimental observations show a matter dominated Universe. Theories of baryogenesis aim to provide an explanation of this effect. In 1967, Sakharov proposed a set of conditions that would support the condition of baryogenesis [2] : 1) baryon number violation, 2) C violation and CP violation, 3) interactions out of thermal equilibrium.

Turning to studies of fundamental particles and their interactions, in 1963, Cabibbo introduced a mixing angle so as to preserve the universality of weak interactions [3]. Later in 1964, Gell-Mann postulated the existence of quarks [4]. Further to which, the Glashow-Iliopoulos-Maiani proposed a mechanism called GIM mechanism which brought in the fourth charm quark in 1964 [5, 6]. This led to a Cabibbo matrix with a four-quark model. At the same time, the phenomenon of CP violation was discovered in 1964 in the kaon decays [7]. This motivated further searches for CP violation in the quark sector. However, the four-quark model did not provide any explanation for the observed CP violation. Later in 1973, Kobayashi and Maskawa generalised the Cabibbo matrix to three generation of quarks in order to explain the observed CP violation, giving rise to the CKM matrix [8]. This was followed by the discovery of the bottom quark at Fermilab in 1977 [9], which was followed by searches for and the eventual discovery of the missing third generation quark, the top quark, in 1995 by the CDF [10] and the D0 [11] experiments at Fermilab. In 1980 Sanda, Carter and Bigi predicted the existence of sizeable CP violation in the B^0 meson system [12–14]. This motivated the development of dedicated experiments to search for CP violation in the B system. The CKM mechanism was then confirmed by Belle [15] and BaBar [16], leading Kobayashi and Masawaka to win the Nobel prize in 2008. LHCb is today's

leading B physics experiment that detects unprecedented quantities of b hadrons produced by the pp collisions at LHC. One of its primary aims is to perform CP violation studies in b hadrons. As CP violation has been observed in B mesons but not in b baryons, this naturally makes it interesting to look for signatures of CP violation in b baryon decays.

Not many b baryon decays have been discovered as of yet especially for the Ξ_b^- and Ω_b^- baryons [17–24]. New measurements of the production and decay properties of b baryons will improve our knowledge. In particular, knowledge of production asymmetries is essential in order to be able to study CP violation in b baryon decays. [20]. Current measurements of Ξ_b^- production asymmetries using $\Xi_b^- \to J/\psi\,\Xi^-$ have large uncertainties [25]. This motivates more precise measurements of the production asymmetries, which could potentially be made by Cabibbo-favoured decays of the Ξ_b^- and Ω_b^- baryons to $\Lambda_c^+ h^- h'-$ final states, where h is a pion or kaon. These measurements are the ultimate aim of the work presented in this thesis. Furthermore, investigations of the phase-space distributions of three-body b baryon decays can be used to perform spectroscopic studies, in particular of the charm baryons and potentially exotic hadrons. No observations have been made previously for the decay channels that are studied in this thesis. This work presents first observations of several decay channels. The first-order tree level Feynman diagrams for the decays can be seen in Figure 1.1. No such diagrams exist for the $\Xi_b^- \to \Lambda_c^+ \pi^- \pi^-$, $\Omega_b^- \to \Lambda_c^+ K^- \pi^-$ and $\Omega_b^- \to \Lambda_c^+ \pi^- \pi^-$ decays and therefore these are expected to be significantly suppressed.

The thesis is organised as follows :

- Chapter 2 : This chapter starts with the introduction of the Standard Model of particle physics and gives some insights into the theoretical aspects of the types of CP violation in quarks and their relation with the CKM matrix. It also includes a discussion of recent results and theoretical developments on the production of b quarks and baryons.

- Chapter 3 : A description of the LHCb detector and its subdetectors is given in this chapter, along with a discussion about the detector performance.

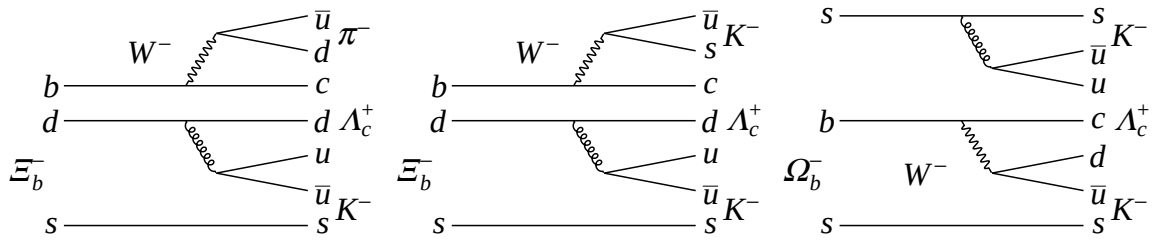

Figure 1.1: Example decay diagrams for the (left) $\Xi_b^- \to \Lambda_c^+ K^- \pi^-$, (centre) $\Xi_b^- \to \Lambda_c^+ K^- K^-$ and (right) $\Omega_b^- \to \Lambda_c^+ K^- K^-$ channels.

- Chapter 4 : The data samples that are used in this analysis are described in this chapter. It also presents details about the event selection to reduce various backgrounds.

- Chapter 5 : In this chapter, the fitting strategy and the modelling of the signal and background contributions are described. Using this, the signal yields for each of the decay channels can be computed. Once the fit is established, the `sPlot` technique is used to perform background subtraction by assigning weights for every event.

- Chapter 6 : This chapter presents the techniques with which the efficiencies are computed. Efficiency maps are obtained as a function of phase space distribution. Using such maps, the efficiency for every event can be determined depending upon the position in phase space.

- Chapter 7 : The chapter describes the various sources of systematic uncertainties that are considered in the measurements.

- Chapter 8 : This chapter documents all the results of branching fractions and production properties produced from this analysis. Every measurement in this analysis relies on two components: the signal weight for every selected candidate, which is obtained from the fit to the b-hadron candidate mass distribution of the selected candidates and the efficiency for that candidate. These are used to compute the background-subtracted and efficiency-corrected yields for each decay as $N^{\rm corr} = \sum_{i=1}^{N} w_i/\epsilon_i$, where the index i runs over the N selected events, and w_i and ϵ_i are the signal weight and efficiency, respectively. The final combination of these ingredients to compute branching fractions and production asymmetries is described in this chapter.

- Chapter 9 : This chapter summarises the work of this thesis and presents the future prospects for enhancing these studies.

Chapter 2

Theory

This chapter gives an insight into the theoretical background that is relevant for the analysis which is presented in this thesis. A large fraction of the content of this section has been gathered from books [26–28] and reviews [29]. It starts with an introduction of the framework and formulation of the Standard Model including by the spontaneous symmetry breaking that explains the origins of the mass terms and mixings of the fermions which give rise to *CP* violation. Production of b baryons in high energy proton-proton collisions is also discussed.

2.1 Introduction to the Standard Model

2.1.1 Framework

The Standard Model (SM) is a relativistic quantum field theory that describes the dynamics of the fundamental forces of the Universe and classifies all the known elementary particles by their quantum numbers, as shown in Figure 2.1. The particles are understood as the excited quanta of the fundamental fields which permeate the Universe. These particles can be classified into two types: bosons and fermions. Particles having spins that are multiples of an integer are called bosons whereas those with spins that are half-integer multiples are called fermions. Fermions are further divided depending on whether or not they couple to the strong interaction (i.e. if they are charged under $SU(3)_C$) and are arranged into three generations with increasing mass. The higher generation particles typically decay into lower generation particles. Every fermion has an antimatter equivalent having the same mass but oppositely-signed charge quantum numbers and the interaction of both results in their annihilation. These fermions interact with the fundamental forces of nature via the bosons. The strong nuclear, electromagnetic and the weak nuclear nuclear forces are mediated by the gluons, photons and W and Z bosons as described by Quantum Chromodynamics (QCD) and electroweak theory respectively. The SM also includes a single scalar boson called the Higgs boson which is an excitation of the Higgs field, as discussed in

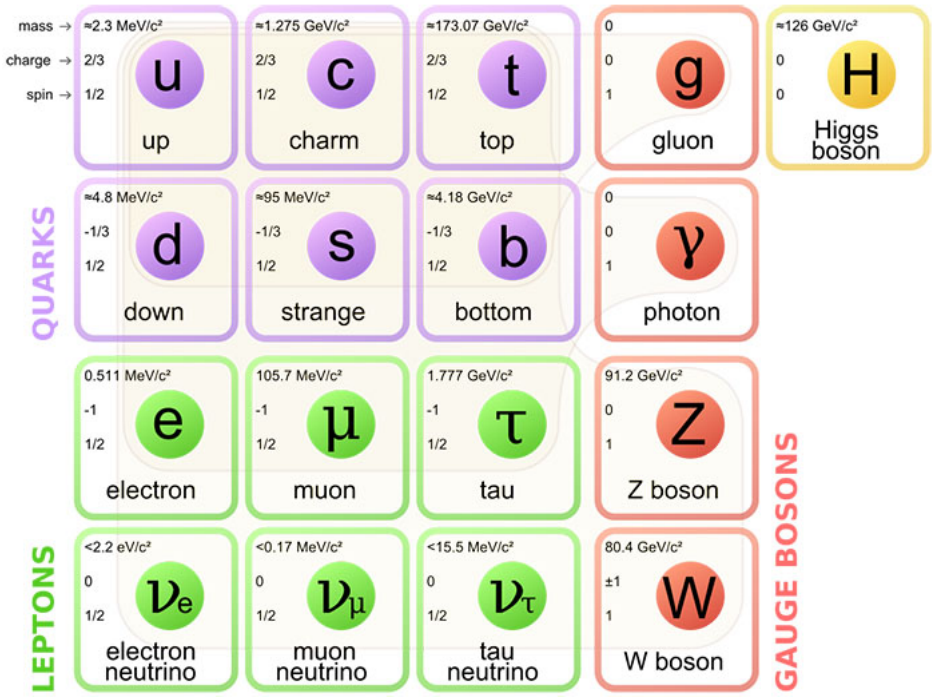

Figure 2.1: The Standard Model classification of elementary particles. [30]

later sections. However, the SM does not have any place for the hypothesised mediators of the force of gravity called gravitons, despite many attempts to combine Einstein's theory of general relativity with quantum mechanics.

2.1.2 Formulation of the Standard Model

The Standard Model is based on the symmetries of the gauge group $G = SU(3)_C \times SU(2)_L \times U(1)_Y$. The subscripts C, L, Y stand for color, weak isospin and weak hypercharge, respectively. L indicates that the weak isospin is only on the left-handed (chiral) components of the fermion fields. The symmetry associated with the strong force is $SU(3)_C$ described by QCD in which the gluons are mediators of the strong interaction and, since QCD is a non-Abelian gauge theory, also carry color charge. The electroweak theory is related to the $SU(2)_L \times U(1)_Y$ symmetry; the connection to the physical $W^{\pm}$, Z and γ gauge bosons is described later after discussion of spontaneous symmetry breaking.

The Lagrangian of the Standard Model can be formulated according to Equation (2.1).

$$\mathcal{L}_{\text{SM}} = \mathcal{L}_{\text{gauge}} + \mathcal{L}_{\text{fermion}} + \mathcal{L}_{\text{Higgs}} + \mathcal{L}_{\text{Yukawa}}. \tag{2.1}$$

The terms $\mathcal{L}_{\text{gauge}}$, $\mathcal{L}_{\text{fermion}}$ and $\mathcal{L}_{\text{Higgs}}$ describe kinetic terms for the gauge, fermion and Higgs fields. The term $\mathcal{L}_{\text{Higgs}}$ is also responsible for generating the mass terms and mixing of EW

gauge bosons, whereas the Yukawa term is responsible for the mass terms for fermions (except neutrinos) and is the source of *CP* violating effects. The SM Lagrangian also exhibits global continuous symmetries. The gauge boson term is

$$\mathcal{L}_{\text{gauge}} = -\frac{1}{4}\left[G^i_{\mu\nu}G^{\mu\nu i} + W^i_{\mu\nu}W^{\mu\nu i} + B_{\mu\nu}B^{\mu\nu}\right] \tag{2.2}$$

where G, W, B are the field strength tensors for $SU(3)$, $SU(2)$ and $U(1)$, respectively and are given as

$$\begin{aligned} G^i_{\mu\nu} &= \partial_\mu G^i_\nu + \partial_\nu G^i_\mu - g_s f_{ijk} G^j_\mu G^k_\nu, \qquad i,j,k = 1...8 \\ W^i_{\mu\nu} &= \partial_\mu W^i_\nu + \partial_\nu W^i_\mu - g_w \epsilon_{ijk} W^j_\mu W^k_\nu, \quad i,j,k = 1...3 \\ B_{\mu\nu} &= \partial_\mu B_\nu + \partial_\nu B_\mu \end{aligned} \tag{2.3}$$

where g_s and g_w are the strong and weak coupling strengths respectively. The factors f_{ijk}, ϵ_{ijk} are the structure constants for $SU(3)$ and $SU(2)$, respectively. The terms involving the structure constant describe how the gauge bosons interact with each other. The fermion term describes the interactions of the fermions with the gauge bosons and is

$$\mathcal{L}_{\text{fermion}} = \bar{Q}_i D_\mu Q + \bar{U}_i D_\mu U + \bar{D}_i D_\mu D + \bar{L}_i D_\mu L + \bar{E}_i D_\mu E \tag{2.4}$$

where Q, U, D, L, E represent the different fermion fields, the properties of which are listed in Table 2.1. D_μ is the covariant derivative which preserves gauge invariance under the symmetry group of the Standard Model. It is given by

$$D_\mu \psi = \left(\partial_\mu - i\frac{g_s}{2}\lambda_a G^a_\mu - i\frac{g_w}{2}\sigma_i W^i_\mu + i\frac{g}{2}Y_q B_\mu\right)\psi. \tag{2.5}$$

Table 2.1: Fermionic fields. For $SU(3)_C$ and $SU(2)_L$, $\{3, 2, 1\}$ indicates $\{\text{triplet}, \text{doublet}, \text{singlet}\}$. For $U(1)_Y$ and Q_e, the value quoted is the charge.

Fermionic fields	Generations	$SU(3)_C$	$SU(2)_L$	$U(1)_Y$	Q_e
Q	$\begin{bmatrix}u_l\\d_l\end{bmatrix}, \begin{bmatrix}c_l\\s_l\end{bmatrix}, \begin{bmatrix}t_l\\b_l\end{bmatrix}$	3	2	+1/3	+2/3,−1/3
U	u_r, c_r, t_r	3	1	+4/3	+2/3
D	d_r, s_r, b_r	3	1	+2/3	−1/3
L	$\begin{bmatrix}e_l\\\nu_l^e\end{bmatrix}, \begin{bmatrix}\mu_l\\\nu_l^\mu\end{bmatrix}, \begin{bmatrix}\tau_l\\\nu_l^\tau\end{bmatrix}$	1	2	−1	−1,0
E	e_r, μ_r, τ_r	1	1	+4/3	−1

Combining both the terms the combined Lagrangian can be written as below and is invariant under the Standard Model symmetry group. However, this requires that the bosons and fermions are massless. Any fermion mass term would couple the left and right-handed chiral

components and since only the left handed component couples to $SU(2)_L$, such terms would violate the gauge invariance.

$$\begin{aligned}\mathcal{L}_{\text{SM}} = -\frac{1}{4}\left[G^i_{\mu\nu}G^{\mu\nu i} + W^i_{\mu\nu}W^{\mu\nu i} + B_{\mu\nu}B^{\mu\nu}\right] + \\ +\bar{Q}\gamma^\mu\left(\partial_\mu - i\frac{g_s}{2}\lambda_a G^a_\mu - i\frac{g_w}{2}\sigma_i W^i_\mu - i\frac{g}{2}Y_q B_\mu\right)Q + \\ +\bar{U}\gamma^\mu\left(\partial_\mu - i\frac{g_s}{2}\lambda_a G^a_\mu - i\frac{g}{2}Y_u B_\mu\right)U + \\ +\bar{D}\gamma^\mu\left(\partial_\mu - i\frac{g_s}{2}\lambda_a G^a_\mu - i\frac{g}{2}Y_d B_\mu\right)D + \\ +\bar{L}\gamma^\mu\left(\partial_\mu - i\frac{g_w}{2}\sigma^i w^i_\mu - i\frac{g}{2}Y_L B_\mu\right)L + \\ +\bar{E}\gamma^\mu\left(\partial_\mu - i\frac{g}{2}Y_e B_\mu\right)E.\end{aligned} \tag{2.6}$$

The chiral nature of the Standard Model fundamentally forbids mass terms. Since, in reality the fermions possess mass, this needs to be included in the Lagrangian in a way that preserves gauge invariance the gauge invariance is preserved. This is done using the Higgs mechanism which is responsible for the spontaneous electroweak symmetry breaking as discussed in the next section.

2.2 Spontaneous symmetry breaking

The Higgs mechanism [31–33] introduces a new scalar field into the theory. This new scalar field has a non-vanishing expectation value, which means the resulting Lagrangian maintains the symmetry of the group, but has a vacuum state which breaks the symmetry transformations. Consider the terms for the Lagragian that include only the $SU(2)_L$ and $U(1)_Y$ terms, together with the new scalar doublet,

$$\mathcal{L} = -\frac{1}{4}W^i_{\mu\nu}W^{\mu\nu i} - \frac{1}{4}B_{\mu\nu}B^{\mu\nu} + (D_\mu\phi)^\dagger D_\mu\phi - V(\phi), \tag{2.7}$$

where $\phi = \begin{bmatrix}\phi_1 \\ \phi_2\end{bmatrix}$ is a $SU(2)_L$ doublet. As per the ϕ^4 theory, the scalar field potential can be written as

$$V(\phi) = -\mu^2(\phi^\dagger\phi) + \lambda(\phi^\dagger\phi)^2, \tag{2.8}$$

giving a minimum of the potential of $|\phi|$ as $v/\sqrt{2}$, where $v^2 = \frac{\mu^2}{\lambda}$ is called the expectation value. If $\mu^2 > 0$, the number of minima is infinite, corresponding to a circle in the complex plane as shown in Figure 2.2. A form of ϕ which is a neutral field chosen with the expectation value as $< \phi >= \frac{1}{\sqrt{2}}\begin{bmatrix}0 \\ v\end{bmatrix}$ breaks the $SU(2)_L \times U(1)_Y$ electroweak gauge symmetry, leaving a new unbroken $U(1)_Q$ electromagnetic gauge symmetry. This non-zero expectation value gives rise to new terms in the covariant derivative of ϕ, which are interpreted as gauge boson masses.

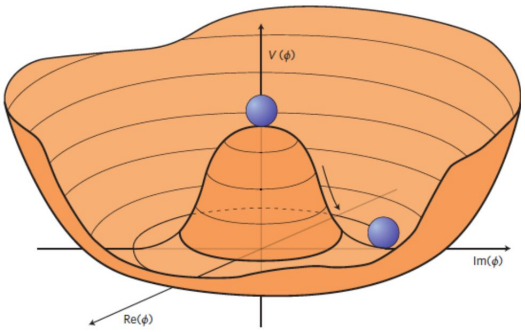

Figure 2.2: "Mexican-hat" potential of vacuum [34]

The same Higgs field also generates fermion mass terms. These occur through the gauge invariant interaction terms of the fermions with the Higgs field, encoded in the Yukawa term in the Lagrangian,

$$\mathcal{L}_{\text{Yukawa}} = -\lambda_i \bar{\psi}^i{}_L \Phi \psi^i_R \tag{2.9}$$

where λ_i represents the interaction strength which is different for each different fermion field. Using the parametrisation of the field obtained from the bosonic interaction terms, we get the mass terms for the fermions,

$$m_f = \frac{\lambda_f v}{\sqrt{2}} \tag{2.10}$$

This tells that the mass is proportional to the strength of the interaction between the Higgs fields and the fermions.

2.3 The CKM matrix

The Yukawa term for the quarks can be written as

$$\mathcal{L}_Y = -Y^d_{ij} \bar{Q}_{Li} \Phi d_{Rj} - Y^u_{ij} \bar{Q}_{Li} \epsilon \Phi^* u_{Rj} \tag{2.11}$$

where Y represent the 3×3 Yukawa matrices in the flavour basis separately for up-type (u,c,t) and down-type (d,s,b) quarks. This makes the mass term from Equation (2.10) become $\frac{v}{\sqrt{2}} Y^d_{ij} \bar{q_L} q_R$. To convert it into the mass basis, the Yukawa matrices need to be diagonalised. This results in couplings of the charged-current $W^\pm$ interactions to the physical up-type and down-type quark states d_{Rj} and u_{Rj}, which can be given by the expression

$$\frac{-g}{\sqrt{2}} (\bar{u}_L, \bar{c}_L, \bar{t}_L) \gamma^\mu W^+_\mu V_{\text{CKM}} \begin{bmatrix} d_L \\ s_L \\ b_L \end{bmatrix} + h.c. \tag{2.12}$$

where, $V_{\rm CKM} \equiv V_L^u V_L^{d\dagger}$ is a 3×3 matrix and $\mathrm{V_L(u,d)}$ are the similarity matrices obtained in the process of diagonalising $\mathrm{Y(u,d)}$. The $V_{\rm CKM}$ matrix, also called the Cabibbo-Kobayashi-Maskawa (CKM) matrix [3, 8], is a unitary matrix. The elements of the matrix give information about the strength of mixing between different quarks. The mixing between the down-type quarks' mass and weak eigenstates can be formulated as

$$\begin{bmatrix} d' \end{bmatrix} = V_{\rm CKM} \begin{bmatrix} d \end{bmatrix} = \begin{bmatrix} d' \\ s' \\ b' \end{bmatrix} = \begin{bmatrix} V_{ud} & V_{us} & V_{ub} \\ V_{cd} & V_{cs} & V_{cb} \\ V_{td} & V_{ts} & V_{tb} \end{bmatrix}_{\rm CKM} \begin{bmatrix} d \\ s \\ b \end{bmatrix}. \tag{2.13}$$

The CKM matrix can be parameterised with three mixing angles and the CP-violating KM phase as

$$V_{\rm CKM} = \begin{bmatrix} c_{12}c_{13} & s_{12}c_{13} & s_{13}e^{-i\delta} \\ -s_{12}c_{23} - c_{12}s_{23}s_{13}e^{i\delta} & -c_{12}c_{23} - s_{12}s_{23}s_{13}e^{i\delta} & s_{23}c_{13} \\ s_{12}s_{23} - c_{12}c_{23}s_{13}e^{i\delta} & -c_{12}s_{23} - s_{12}c_{23}s_{13}e^{i\delta} & c_{23}c_{13} \end{bmatrix}, \tag{2.14}$$

where $c_{ij} = \cos\theta_{ij}, s_{ij} = \sin\theta_{ij}$ and δ is the KM phase responsible for the CP violating phenomenon in flavour-changing processes. It is seen experimentally that $s_{13} \ll s_{23} \ll s_{12} < 1$. Exploiting this fact, Wolfenstein came up with an alternative parametrisation in terms of free parameters λ, A, ρ and η [35], defined as

$$s_{12} = \lambda \approx 0.23, \quad s_{23} = A\lambda^2, \quad s_{13}e^{i\delta} = A\lambda^3(\rho - i\eta), \tag{2.15}$$

which ensures that this parametrisation remains unitary to all orders in λ. Therefore, the CKM matrix now becomes

$$V_{\rm CKM} = \begin{bmatrix} 1 - \frac{1}{2}\lambda^2 & \lambda & A\lambda^3(\rho - i\eta) \\ -\lambda & 1 - \frac{1}{2}\lambda^2 & A\lambda^2 \\ A\lambda^3(1 - \rho - i\eta) & -A\lambda^2 & 1 \end{bmatrix} + \mathcal{O}(\lambda^4) \tag{2.16}$$

Since the matrix is unitary, $VV^\dagger = 1$. This gives rise to the following equations,

$$\sum_{i=1}^{3} V_{ki}^* V_{kj} = \delta_{ij}, \tag{2.17}$$

where δ_{ij} is the Dirac delta. One of these equations can be written as below and can be represented as a triangle in the complex plane as shown in Figure 2.3.

$$V_{ud}V_{ub}^* + V_{cd}V_{cb}^* + V_{td}V_{tb}^* = 0. \tag{2.18}$$

In Figure 2.3, the triangle has been scaled by $1/V_{cd}V_{cb}^*$ so that the length of the sides are

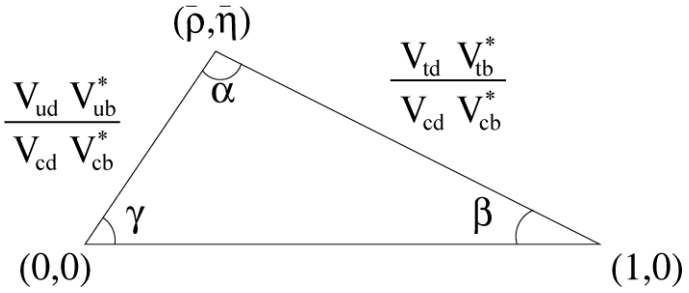

Figure 2.3: The unitarity triangle. [36]

given by 1, $|\frac{V_{ud}V_{ub}^*}{V_{cd}V_{cb}^*}|$,$|\frac{V_{td}V_{tb}^*}{V_{cd}V_{cb}^*}|$. The angles of the triangle can be written as

$$\begin{aligned}\alpha &\equiv \arg(-\frac{V_{td}V_{tb}^*}{V_{cd}V_{cb}^*}).\\ \beta &\equiv \arg(-\frac{V_{cd}V_{cb}^*}{V_{td}V_{tb}^*}).\\ \gamma &\equiv \arg(-\frac{V_{ud}V_{ub}^*}{V_{cd}V_{cb}^*}).\end{aligned} \tag{2.19}$$

From the above it can be seen that for *CP* violation in the quark sector, we require i) non-degeneracy among the masses of the up-type and down type quarks, ii) none of the mixing angles must be zero or $\pi/2$, iii) the *CP*-violating phase should be neither 0 or π. The area of the unitarity triangle of Equation (2.18) then gives the amount of *CP* violation in the Standard Model.

From the matrix, it can be seen that the intra-generational couplings are stronger compared to inter-generational couplings. It is also possible to define a Jarlskog parameter [37] that can be written as

$$J = c_{12}c_{23}c_{13}^2 s_{12}s_{23}s_{13}\sin\delta \tag{2.20}$$

or, in terms of Wolfenstein parameters,

$$J = A^2\lambda^6\eta(1-\lambda^2/2) + \mathcal{O}(\lambda^{10}). \tag{2.21}$$

The area of the unitarity triangle can also be given by the Jarlskog parameter as $|J|/2$. In fact, the area of all the possible triangles that can be formed using Equation (2.17) is the same. Furthermore, the complex phase δ can be directly represented in terms of the UT angles as

$$\gamma = \delta + \mathcal{O}(\lambda^4). \tag{2.22}$$

The magnitudes of the elements of the CKM matrix have been measured experimen-

tally [38], and are

$$|V_{\rm CKM}| = \begin{bmatrix} 0.97425^{+0.00007}_{-0.00009} & 0.22542^{+0.00042}_{-0.00031} & 0.00371^{+0.00007}_{-0.00006} \\ 0.22529^{+0.00041}_{-0.00032} & 0.97339^{+0.00007}_{-0.00009} & 0.04180^{+0.00033}_{-0.00068} \\ 0.00867^{+0.00008}_{-0.00015} & 0.04107^{+0.00031}_{-0.00067} & 0.99911^{+0.00002}_{-0.00001} \end{bmatrix}. \tag{2.23}$$

Tree-level measurements of Unitarity angle γ provides info about the *CP* violation in the Standard Model. These measurements are performed using various B and D meson decays. Combining the results of the measurements from different channels, LHCb has found the value of γ to be

$$\gamma = (66.2^{+3.4}_{-3.6})^0, \tag{2.24}$$

with statistical and systematic uncertainties combined [39]. This is the most precise value of γ to date.

2.4 *CP* violation in quarks

The Charge-Parity phenomenon is the combination of the charge conjugation (C) and parity (P) transformations. Under C, particles and anti-particles are interchanged. This corresponds to conjugating the internal quantum numbers for e.g. charge Q getting inverted as $Q \to -Q$. Under P, spatial co-ordinates are inverted i.e. $\vec{x} \to -\vec{x}$. This corresponds to changing the handedness i.e. a left-handed co-ordinate set becomes right-handed and vice-versa. Violation of symmetry under the combination of charge (C) and parity (P) together is a necessary condition for baryogenesis. Hadron decays occuring via the weak interaction provide probes of flavour-changing *CP* violation. In this section, *CP* violation due to flavour-changing processes is described.

The source of *CP* violation in the quark sector is the complex phase that appears in the CKM matrix. *CP*-violating effects in hadrons can be distinguished into three types :

- ***CP* violation in decay:** Possible if a decay occurs via multiple interaction mechanisms having different amplitudes. This can potentially occur in the decays of both mesons and baryons, whether charged or neutral decays. The *CP* asymmetries are then defined as

$$\mathcal{A}_{f\bar{f}} \equiv \frac{\Gamma(|\psi\rangle_{\bar{B}} \to \bar{f}) - \Gamma(|\psi\rangle_B \to f)}{\Gamma(|\psi\rangle_{\bar{B}} \to \bar{f}) + \Gamma(|\psi\rangle_B \to f)} = \frac{|\bar{A}_{\bar{f}}/A_f|^2 - 1}{|\bar{A}_{\bar{f}}/A_f|^2 + 1} \tag{2.25}$$

  where A_f is the amplitude of the state $|\psi\rangle_B$ decaying to final state f and the bar over the amplitudes represents the conjugate process. Γ represents the corresponding decay rate. This expression shows that a non–zero *CP* asymmetry occurs when $|\bar{A}_{\bar{f}}/A_f| \neq 1$. The

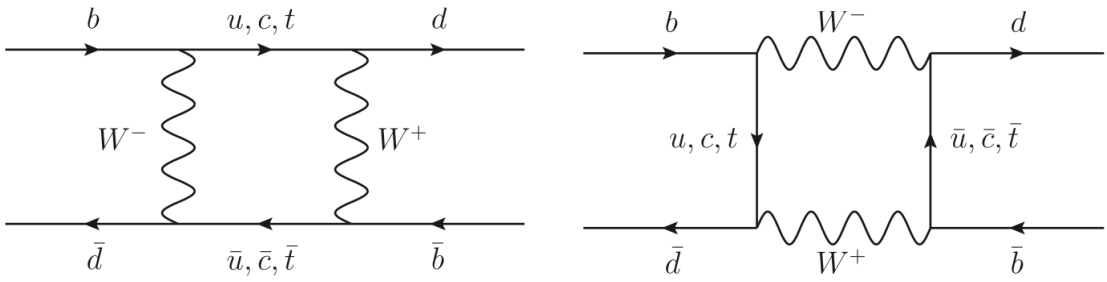

Figure 2.4: Flavour Changing Neutral Current (FCNC) transitions leading to $B^0 - \bar{B^0}$ oscillations [36].

amplitudes can written in terms of two components.

$$\begin{aligned} A_f &= |a_1|e^{i(\delta_1+\phi_1)} + |a_2|e^{i(\delta_2+\phi_2)} \\ \bar{A}_{\bar{f}} &= |a_1|e^{i(\delta_1-\phi_1)} + |a_2|e^{i(\delta_2-\phi_2)} \end{aligned} \tag{2.26}$$

where ϕ_i, δ_i and $|a_i|$ are the weak phase, strong phase and the magnitude of the component i. The *CP* asymmetry can now be re-written as

$$\mathcal{A}_{f\bar{f}} = -\frac{2|a_1 a_2|\sin(\delta_2-\delta_1)\sin(\phi_2-\phi_1)}{|a_1|^2+|a_2|^2+2|a_1 a_2|\cos(\delta_2-\delta_1)\cos(\phi_2-\phi_1)}. \tag{2.27}$$

This further implies that for a non-zero *CP* asymmetry, neither the strong phases nor the weak phases can be the same between the two components. Additionally, both $|a_1|$, $|a_2|$ must be non-zero.

- *CP* **violation in mixing:** This occurs only for neutral mesons since only these exhibit flavour oscillations, for example the $B^0 - \bar{B^0}$ mixing shown in Figure 2.4 . This can be measured using semi-leptonic decays of the neutral meson. Since these decays are flavour specific (the charge of the lepton unambiguously corresponds to the flavour of the decaying B meson) and have no CP violation in decay, the asymmetries in such case are given by

$$\begin{aligned} \mathcal{A}_{fs} \equiv \frac{d\Gamma/dt[|\psi(t)\rangle_{\bar{B}} \to l^+X] - d\Gamma/dt[|\psi(t)\rangle_B \to l^-X]}{d\Gamma/dt[|\psi(t)\rangle_{\bar{B}} \to l^+X] + d\Gamma/dt[|\psi(t)\rangle_B \to l^-X]} \\ = \frac{1-|q/p|^4}{1+|q/p|^4} \end{aligned} \tag{2.28}$$

where $d\Gamma/dt$ is the time-dependent decay rate and p and q are complex parameter that represent the components of a meson (M^0) and anti-meson ($\bar{M^0}$) in the heavy (M_H) and light (M_L) mass eigenstates of the $M^0 - \bar{M^0}$ meson system as formulated as

$$\begin{aligned} |M_H\rangle &= p|M^0\rangle + q|\bar{M^0}\rangle, \\ |M_L\rangle &= p|M^0\rangle - q|\bar{M^0}\rangle. \end{aligned} \tag{2.29}$$

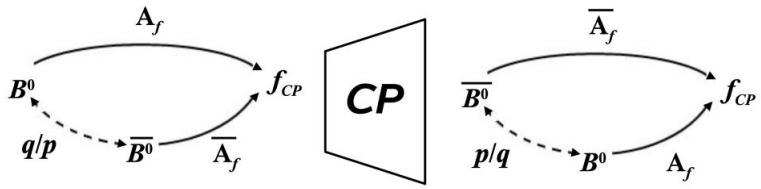

Figure 2.5: Schematic of the amplitudes giving rise to *CP* violation due to interference in decay with and without mixing [40].

A non-zero *CP* asymmetry arises when $|q/p| \neq 1$.

- ***CP* violation in interference between decays with and without mixing:** This occurs when B^0 and $\bar{B^0}$ can decay to same final state. The interference of a decay without mixing $M^0 \to f$ and with mixing $M^0 \to \bar{M^0} \to f$ can give rise to this type of *CP* violation as illustrated in Figure 2.5. Assuming that the final state is a *CP* eigenstate, the asymmetry can be formulated as

$$\mathcal{A}_f \equiv \frac{d\Gamma/dt[|\psi(t)\rangle_{\bar{B}} \to f] - d\Gamma/dt[|\psi(t)\rangle_B \to f]}{d\Gamma/dt[|\psi(t)\rangle_{\bar{B}} \to f] + d\Gamma/dt[|\psi(t)\rangle_B \to f]} \tag{2.30}$$

This can occur when $\lambda_f \equiv \frac{q}{p}\frac{\bar{A}_f}{A_f}$ follows the condition $arg(\lambda_f) + arg(\lambda_{\bar{f}}) \neq 0$. For final *CP* eigenstate, where there is no distinction between f and $\bar{f}$ this condition simplifies to $\mathcal{I}m(\lambda_f) \neq 0$

The first discovery of *CP* violation was made in neutral K decays [7] in 1964. This corresponds to *CP* violation in mixing. Later it was also discovered in the B system in 2001 by Belle [41] and Babar [42], which corresponds to *CP* violation due to interference between mixing and decay. Further it was also observed in D system in 2019 [43] by the LHCb collaboration which corresponds to *CP* violation in decay. All the 3 categories of *CP* violation are now observed in kaons. *CP* violation in decays is also seen in B meson decays. However, for D meson decays no *CP* violation in mixing or interference is observed yet.

CP violation in baryon decays is expected. However, no such effects have been observed as of yet. Furthermore, other forms of *CP* violation cannot occur since baryons do not mix due to baryon number conservation.

2.5 b baryon production

The production of b quarks in hadron collisions is predominantly as $b\bar{b}$ pairs. This occurs either through gluon-splitting or flavour excitation [44][45]. The hard process for $b\bar{b}$ production is followed by soft processes leading to hadronisation [46]. Even though the b and $\bar{b}$ quarks occur in pairs, the production rate of b and $\bar{b}$ baryons are not expected to be identical. This is because during the production process the b and $\bar{b}$ quarks might have different probabilities of coalescing

with u or d valence quarks. This implies that production rate of b baryons may exceed those of $\bar{b}$ baryons in certain regions of kinematic phase-space and vice versa [47]. The measurement of such asymmetries thus helps to investigate the b hadron production mechanisms. Moreover, knowledge of production asymmetries is essential for CP violation measurements at the LHC. The production asymmetries can be formulated as

$$A_P(X_b) = \frac{\sigma(\bar{X}_b) - \sigma(X_b)}{\sigma(\bar{X}_b) + \sigma(X_b)} \tag{2.31}$$

where X_b is any b hadron and σ is the associated production cross-section for $pp \to X_b +$ other particles, and can be defined in a certain kinematic (fiducial) region, and for specific pp centre-of-mass energy. Since each b and $\bar{b}$ quark must hadronise into something, the production asymmetries for different b hadrons are related,

$$\sum f_{X_b} A_P(X_b) = 0 \tag{2.32}$$

where f_{X_b} is the fragmentation fraction of the X_b hadron and the sum is over all relevant b hadron species. The only baryons for which production asymmetry measurements currently exist are the Λ_b^0 and Ξ_b^- baryons [48, 49]. For the former, measurements have been made at 7 and 8 TeV

$$\begin{aligned} A_P(\Lambda_b^0)_{\sqrt{s}=7\text{TeV}} &= (1.92 \pm 0.35)\%, \\ A_P(\Lambda_b^0)_{\sqrt{s}=8\text{TeV}} &= (1.09 \pm 0.29)\%. \end{aligned} \tag{2.33}$$

The first measurement of the production asymmetry of the Ξ_b^- baryon [49] was made using $\Xi_b^- \to J/\psi \Xi^-$ decays,

$$\begin{aligned} A_P(\Xi_b^-)_{\sqrt{s}=7,8\text{TeV}} &= (1.1 \pm 5.6 \pm 1.9)\%, \\ A_P(\Xi_b^-)_{\sqrt{s}=13\text{TeV}} &= (-3.9 \pm 4.9 \pm 2.5)\%, \end{aligned} \tag{2.34}$$

The results are compatible with zero due to large statistical and systematic uncertainties. Thus this analysis also aim to improve the precision of the Ξ_b^- production asymmetry.

At e^+e^- colliders, where b quarks are produced from $Z^0 \to b\bar{b}$ decays we expect the b quarks to have non-zero longitudinal polarisation around -0.94 [50]. Whereas, the OPAL [45], ALEPH [51] and DELPHI [52] collaborations measured the Λ_b^0 polarisation to be $-0.56^{+0.20}_{-0.13} \pm 0.09$, $-0.23^{+0.24+0.08}_{-0.20-0.07}$ and $-0.49^{+0.32}_{-0.30} \pm 0.17$. Since this was the first b baryon discovered it has relatively large samples compared to others like Ξ_b and Ω_b. The sign of the measured polarization tells us about the chirality of the b quark coupling to the weak charged current. If the b quarks form B mesons the polarisation is lost, but if they form b baryons,

it is preserved provided the baryon is produced directly from the collisions and not via any intermediate state. If it is produced via an intermediate resonance, the b quark polarisation is not directly transferred to the final b baryon and can depend upon the spin of the diquark combination in the resonance, degrading the polarisation [44][45][53]. This implies that the polarisation of all the b baryons produced directly from the collisions should be the same, at least to a reasonable approximation. However, there are as of yet no measurements with any b baryon other than the Λ_b to test this prediction. Similarly to the lepton collider, experiments at hadron colliders also measured the polarisation of the Λ_b^0 baryons. CMS measured the polarisation from the Λ_b^0 decays as $0.00 \pm 0.06(\text{stat}) \pm 0.06(\text{syst})$ and LHCb [54] measured a transverse production polarisation of $0.06 \pm 0.07 \pm 0.02$ which is consistent with the theoretical predictions of 0.10 [55] and 0.20 [56]. As per the heavy quark effective theory, a large fraction of the b-quark polarisation is transferred to the Λ_b^0 baryon unlike the longitudinal polarisation which would vanish due to parity conservation in strong interactions. This thesis therefore assumes a zero polarisation of the baryons while handling the modelling of the efficiency variation as a part of systematics.

From the Tevatron and LHC data, it is known that the fragmentation fractions of different b hadrons depend on the production kinematics [29]. This, however, has not yet been measured for Ξ_b^- and Ω_b^- baryons. This thesis aims to study the variation of the production rate which is the product of the fragmentation fraction and the branching fraction with respect to production kinematics. Since the branching fraction is constant, independent of the production kinematics, this study would help to understand the variation of the fragmentation fractions.

Chapter 3

The LHC and the LHCb Detector

3.1 The Large Hadron Collider

The Large Hadron Collider [57] is the most powerful accelerator in the world to date, that is able to achieve the highest energy particle collisions of up to 13.6 TeV so far. It is a circular ring of circumference 27 km where the proton beams are accelerated in a 3 m wide tunnel. These proton beams are counter-circulating and are guided by superconducting dipole magnets of strength 8.7 T which bend the beam in two different beam pipes. These pipes are maintained at a very low pressure of 10^{-7} Pa to minimise the interactions of the proton beams with the gas inside the beam pipe.

The generation of protons is achieved by ionising hydrogen gas. These protons are then accelerated through the CERN accelerator complex as shown in Figure 3.1. Protons are first injected into Linac2 followed by the Proton Synchrotron Booster (PSB), the Proton Synchrotron (PS) and the Super Proton Synchrotron (SPS) accelerators. This helps to increase the energy of the beam in steps from 50 MeV, 1.4 GeV, 25 GeV and 450 GeV respectively. The beam is then finally transferred to the LHC which accelerates it up to multi-TeV energies. These counter-circulating beams are focussed to collide at four crossing points. The crossing points have 4 different experiments LHCb [58], ATLAS [59], CMS [60], ALICE [61] to study the physics of the collision. ATLAS and CMS are designed in a fashion so as to study particles produced at high transverse momentum. However, the aim of LHCb is to study the physics of hadrons containing the b quark. Since such b-hadrons are particles containing b quarks are predominantly produced in a smaller acceptance region from pseudorapidity 1.5 to 6, it is designed as a single-arm forward spectrometer.

The circulating beams in LHC are however discretised into bunches of protons rather than being a continuous beam of particles. This is due to the use of electromagnetic radiofrequency cavities during acceleration. The bunches are spaced in intervals of 25 ns, corresponding to a

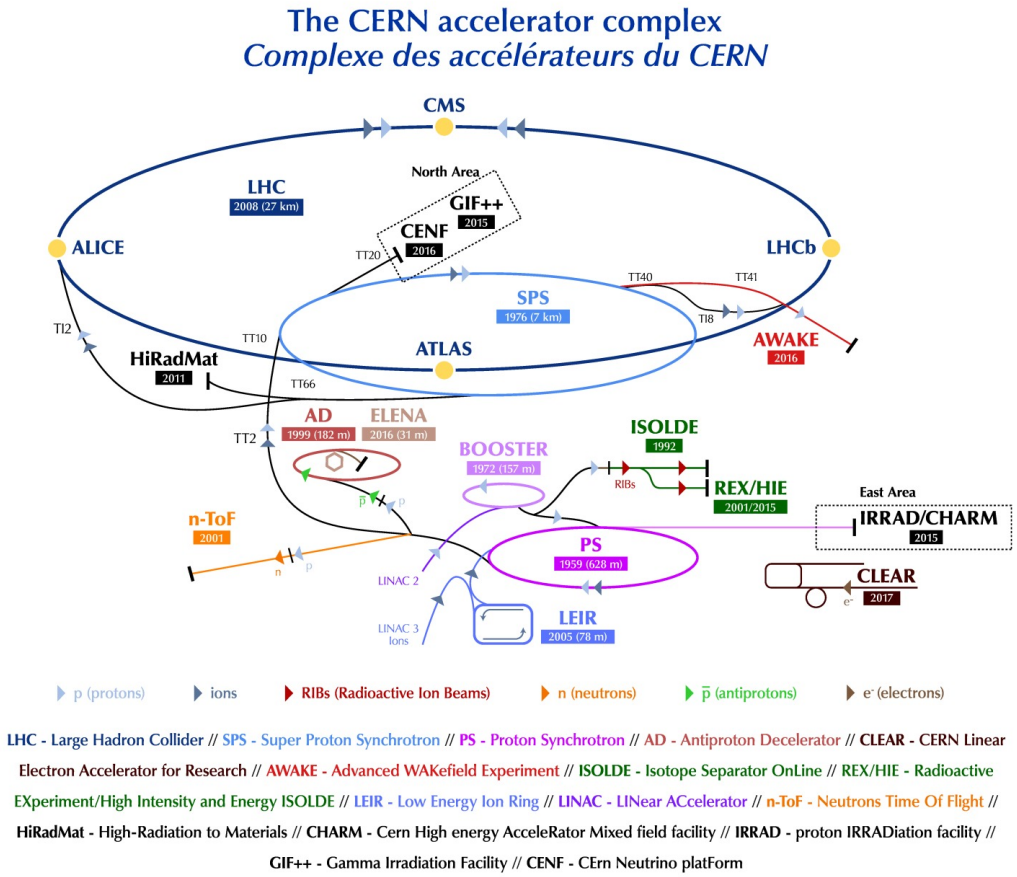

Figure 3.1: Schematic of the CERN accelerator complex [62].

bunch crossing frequency of 40 MHz. The LHC vacuum system has two components: primary vacuum also called beam vacuum, and secondary vacuum, also called cryogenic insulation vacuum. They are entirely separate from each other. The pressure of the secondary vacuum is of the order of 10^{-6}mbar, whereas the beam vacuum is three orders of magnitude better, in order to have a good beam lifetime.

3.2 The LHCb detector and its subdetectors

As mentioned in section 3.1, LHCb is a forward arm spectrometer designed to study b physics, since $b\bar{b}$ pairs are typically boosted in the direction of the beam. The same is true for $c\bar{c}$ pairs, so LHCb is also well-suited for charm physics. It provides coverage of 10 mrad to 300(250) mrad in the horizontal (vertical) direction. A pictorial representation of the experiment and its sub-detectors is shown in Figure 3.2. LHCb operates at a 50 times lower luminosity than the maximum LHC luminosity in contrast to ATLAS and CMS. experiments. This reduces the

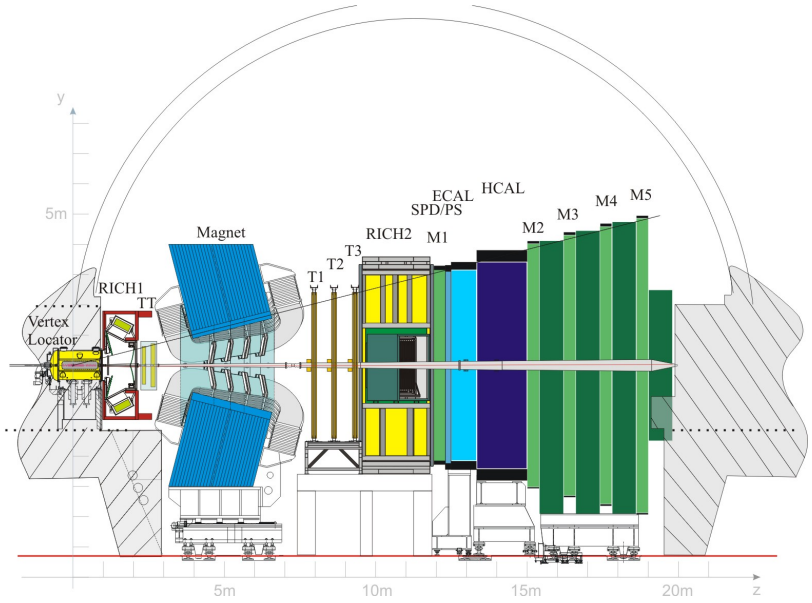

Figure 3.2: Layout of the LHCb detector and sub-detectors [58]. It makes use of Cartesian reference frame coordinate system. The z axis is defined as the direction of the beam and the y axis is defined in the vertical direction normal to the z axis.

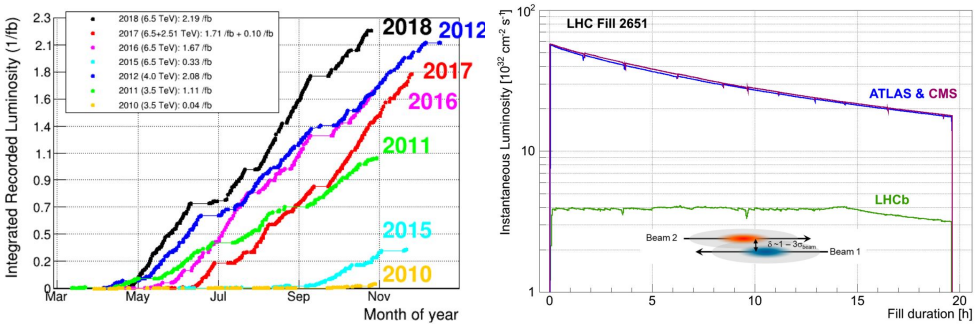

Figure 3.3: (Left) LHCb integrated luminosity for different data taking years. (Right) Instantaneous luminosity profile during an entire LHC fill duration for LHCb, ATLAS and CMS [63].

number of pp interactions per bunch crossing to $\mathcal{O}(1)$, which helps to correctly associate the secondary vertices to their corresponding primary vertices from the collisions. The detector has been designed to operate at a luminosity of $2 \times 10^{32}\text{cm}^{-2}\text{s}^{-1}$. However, the detector routinely operated with twice the designed luminosity during Run I and Run II. It has managed to record more than 9fb^{-1} in total since 2011. LHCb operates with constant instantaneous luminosity through the use of luminosity levelling achieved by adjusting the overlap of the beams Figure 3.3. At the beginning of every fill the overlap between the beams at the interaction point is minimal, which is just sufficient enough to reach the target luminosity. As the numbers of protons in the bunches decrease, the beam overlap is increased to compensate.

LHCb is divided into subdetectors. The very first subdetector that surrounds the interaction point is the VErtex LOcator(VELO). The beams, on collision, generate a shower of particles which then traverses through the other detectors. LHCb uses the VELO, tracking stations (TT, T1-T3) together with a dipole magnet to reconstruct the trajectory of charged particles and provide momentum estimates. LHCb additionally has RICH detectors, calorimeters and 4 muon chambers that help to identify the particle species. Details of each of the sub-detectors are presented in the following sub-sections.

3.2.1 Vertex Locator

The VErtex LOcator (VELO) [64], is the very first sub-detector that particles cross after emerging from the pp collisions. It surrounds the interaction point spanning from $-0.2 < z < 0.8$m and provides precise measurements of track positions close to the interaction region giving rise to accurate reconstruction of the primary and secondary vertices. A layout of the detector can be seen in Figure 3.4.

The VELO is composed of two halves, each side has 21 modules, giving rise to a total of 42 modules, which are oriented perpendicular to the beam line. These modules are more densely spaced near and more sparsely spaced further from the interaction region, to help reduce the extrapolation distance from the first measured hit to the actual vertex and thereby give precise vertex measurements. The spacing is chosen in a fashion such that a combination of hits from at least four modules can be used to reconstruct a track. Each module consists of two semi-circular silicon strips sensors, namely R and ϕ sensors. The two halves overlap by around 1.5mm so as to provide a full coverage of the azimuthal acceptance. This also helps with the alignment of the different modules in the detector. Each R sensor is divided into 4 equal sectors, each of which consists of 512 annular silicon strips. A layout of the VELO module can be seen in Figure 3.5. Higher occupancy in the sensor could lead to poor resolution of the hits in the sensor and lower efficiency. Hence, the division of the sensor is done to reduce the occupancy of a single sensor. The inner-strip distance, also called the strip pitch, increases with radius from 38 to 102μm. This is done to equalise the occupancy across the different strips. Similarly, the ϕ sensor is divided into 2 regions: an inner region with 683 strips and an outer region with 1365 strips. Here again the pitch increases linearly from innermost edge of a region to outermost edge varying from 38-78μm for the inner region and 39-97μm for the outer region. A pictorial representation of the sensors is shown in Figure 3.5. Additionally, there are 4 modules consisting of R sensors only upstream of the detector, called the pile-up system. They were initially intended to be used as a trigger in order to help reject events with large number of primary vertices. However, since it was realised that LHCb could operate with multiple primary vertices, they are not really used in the detector. The VELO has been measured to have an impact parameter resolution of around $(15 + 29/p_{\mathrm{T}})\mu$m for a charged particle.

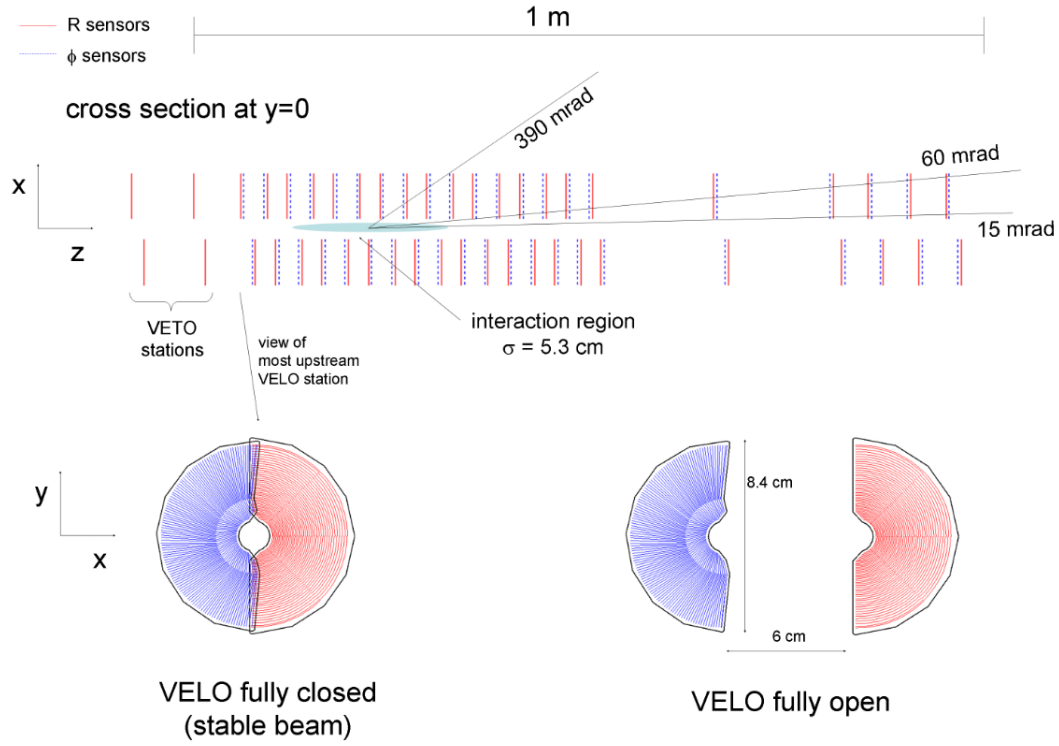

Figure 3.4: Layout of the VELO sub-detector. (top) Module positions across the beam line. (bottom) Layout of a pair of modules in VELO open and VELO closed position [64]

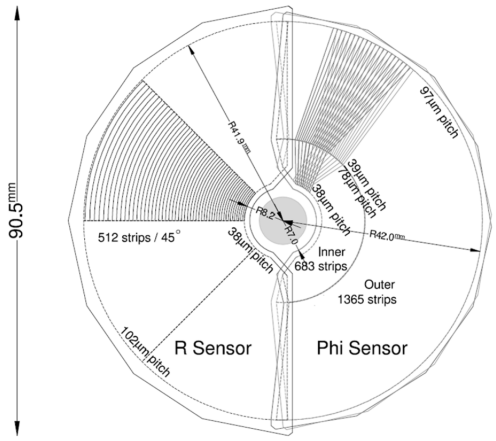

Figure 3.5: Strip geometry of the R and ϕ sensor of a module [58]

The VELO modules and the electronics associated to them are placed inside the secondary vacuum. They are separated from the primary vacuum by the RF foil made from aluminium. This helps to prevent any RF pickups and interference from the beam affecting the readouts of the modules. The thickness of the foil is 300μm minimised to reduce the material budget.

The VELO can operate in both open and closed position. When the VELO is fully open, the halves are at a distance of 30 mm from the beam. When it is fully closed, they are at a distance of 8.2 mm from the beam. During the injection phase and the ramping phase the beam profile is sufficiently large that the VELO must be kept open to avoid the risk of radiation damage and to avoid interfering with the beam. Once the stable beam state has been reached, the VELO is gradually closed. For every fill the position of the beam varies slightly. This means the VELO needs to be centered around the current position for every fill.

3.2.2 Tracking stations: TT, T1, T2, T3

Tracker Turicensis

The next tracking device after the VELO, but before the magnet is the Tracker Turicensis (TT). It covers the entire LHCb acceptance and is a silicon strip detector with dimensions 150×130cm. It provides tracking measurements just upstream of the magnet and is also useful to reconstruct decays of long lived particles like K^0_S mesons or Λ baryons. Such particles typically do not decay inside the VELO, which would cause them to have a low reconstruction efficiency. Furthermore, they also provide reconstruction of soft particles having low momentum, that never reach T1-T3 trackers, but they are rarely used in LHCb analyses. Of the K^0_S's that are reconstructed, a bit less than 1/3rd are from pairs of long tracks which are defined to have hits in VELO and the tracking stations as also described in Section 3.3.1.

The layout of the TT is shown in Figure 3.6, consisting of 4 layers. The first and last layers are aligned with the x and y axes of the detector, while the second and third layers are tilted by angles of -5^0 and 5^0. Each half-layer consists of columns of 7 silicon sensors with 512 readout strips with pitch of 183μm. Each column is divided into 3 sectors K, L and M, having different numbers of sensors and separate readout channels. The L sector is the farthest one from the beam, consisting of 4 sensors. The K sector is the closest to the beam and has only one sensor. The remaining M sector is the middle one with 2 sensors.

Inner Tracker

In addition to TT, there are 3 tracking stations after the magnet, T1-T3. Every station is divided into two sections: inner and outer trackers IT [66] and OT [67]. The inner region which is close to the beam line has the highest multiplicity, thus the IT is a silicon strip detector. Similar to TT, the IT has 4 layers of silicon microstrip sensors in each station of which the middle two are rotated by 5^0. The layout of the inner tracker can be seen in Figure 3.7. Every layer has 4 separate sections surrounding the beam pipe. They are roughly 130 cm wide and 45 cm high. The sections that are above and below the beam have one row of seven silicon sensors, whereas, those that are on the sides have 2 rows of 7 sensors. Every sensor has 384 silicon strips with a

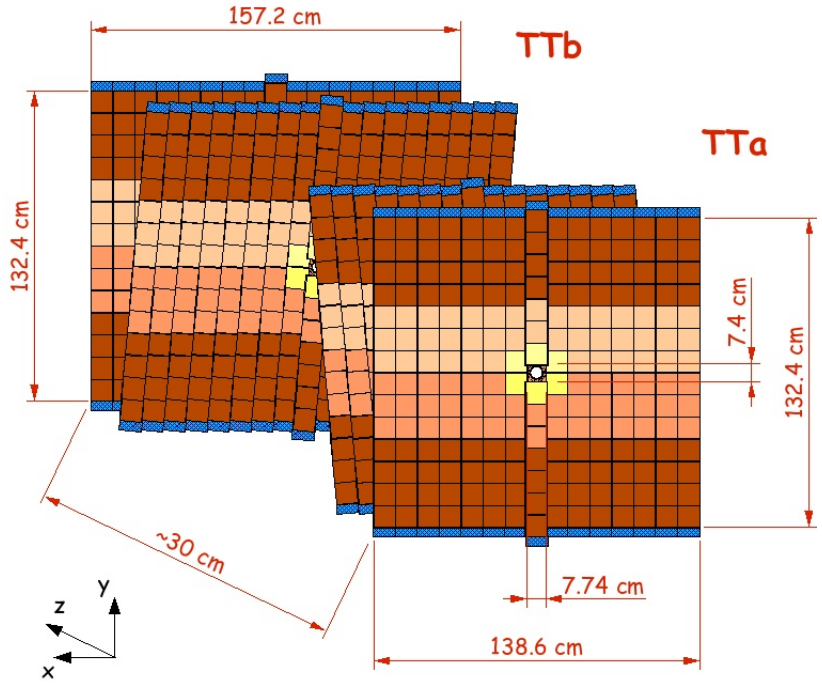

Figure 3.6: Layout of the 4 layers TT [65].

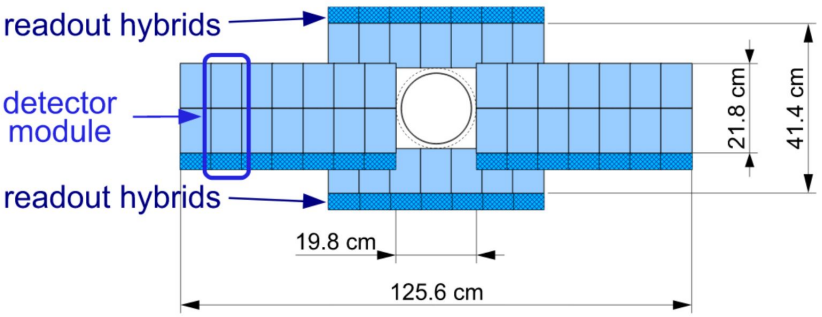

Figure 3.7: Layout of the IT around the beam pipe [58]

strip pitch of 196μm. Despite covering only 1.3% of the total area of the tracking station, almost 20% of the charged particles in the LHCb acceptance pass through IT.

Outer Tracker

The outer part of the tracking stations consists of the outer tracker (OT) [67], which is a drift time detector. It has a horizontal angular coverage of 300 mrad and vertical angular coverage of 250 mrad. It has 4 modules of straw drift tubes, where the middle two are tilted by $\pm 5^0$, similarly to the TT and IT. Every module has 2 layers of 64 drift tubes, where each tube has a

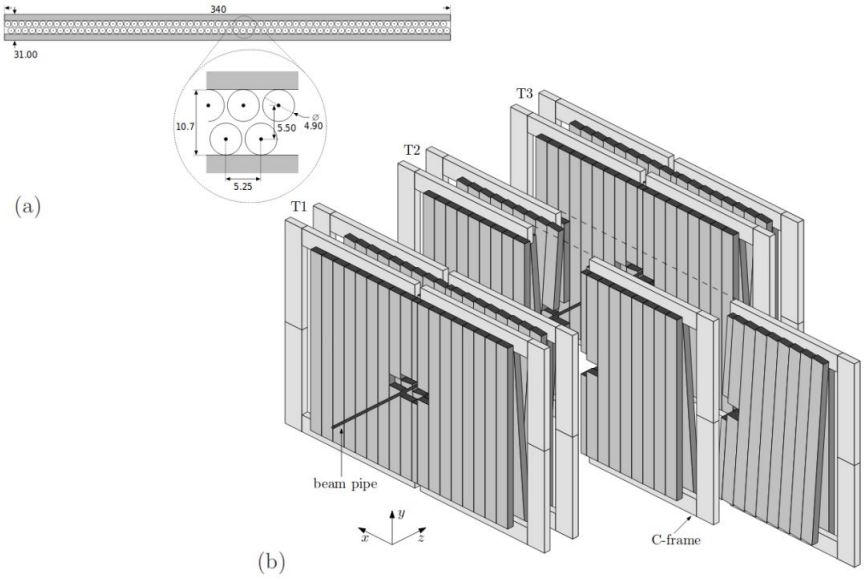

Figure 3.8: (a) Top view of an OT straw tube module. (b) Layout of the OT stations where a part of T2 is retracted [68].

length of 2.4 m and a diameter of 4.9 mm. A layout can be seen in Figure 3.8. The tubes consist of 2 layers of thin foil. The inner layer is a carbon-doped polyamide acting as cathode along with a gold-plated tungsten wire acting as anode through the middle of each tube. The outer layer provides shielding and helps to avoid any gas leakage, and is a laminate of polyamide and aluminium. The gas inside the tube consists of 70% Argon, 28.5% CO_2 and 1.5% of O_2. When a charged particle travels through the OT, it ionises the gas inside the tubes. The ions travel towards the anode at the centre of the tube. The travel times of the ions from the interaction point to the anode which are at the extreme ends of the layers, give information about the position of the hit mainly in the vertical direction.

3.2.3 Magnet

LHCb's warm dipole magnet is positioned between the TT and the T1-T3 trackers. Deflection of charged particles in the magnetic field allows precise measurement of the momentum and charge of the particles [69].

The magnet has 4 Tm of bending power. The magnetic field is parallel to the y-axis of the co-ordinate system shown in Figure 3.2. It covers an acceptance range of ±250mrad in vertical direction and ±300mrad in horizontal direction. A warm dipole magnet was chosen over a super-conducting magnet due to economic, power supply and time constraints.

The magnet has two separate aluminimum coils placed symmetrically about the z-axis consisting of 15 layers of hollow Al conductors. They all have a central water cooling channel.

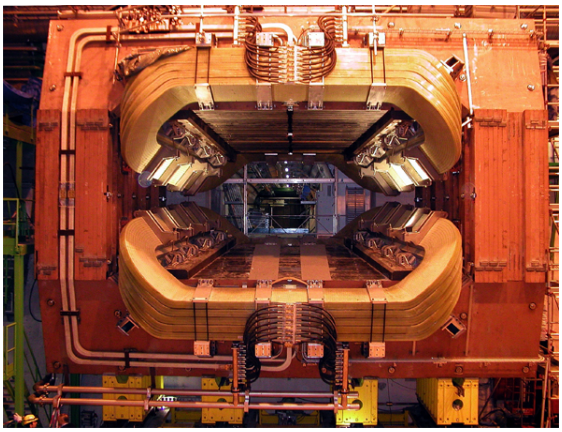

Figure 3.9: Picture of the LHCb magnet [69].

These coils are attached to a slanted rectangular yoke with a wedge-shaped window. The yoke consists of 27 layers of laminated low carbon steel. Each layer is 100 mm thick and the total mass is about 25 tonnes. The nominal current passing through the coil is 5.85 kA. A layout of the magnet is shown in Figure 3.9.

The momentum resolution obtained with this design of the magnet, is around $\delta|\bar{p}|/|\bar{p}| = 4 \times 10^{-3}$ for particles having p_{T} of 10 GeV/c. To achieve this, the magnetic field is measured to a relative precision $\mathcal{O}(10^{-4})$ using arrays of Hall probes before collecting the data. This implies that we can estimate the peak position of the magnetic field within a few mm. The profile of the magnetic field along the z-axis is shown in Figure 3.10. Since the magnetic field profile is small in the VELO region, the tracks are straight. However, since the magnetic field is larger in the RICH region, there is a possibility for the detectors to be affected. This is prevented by enclosing the RICH photon detectors with iron shielding.

3.2.4 Ring Imaging Cherenkov Detectors

RICH[71] is one of the detectors which is commonly used in the identification of the different species of particles, particularly between kaons and pions, over a wide range of momentum. It is based on the Cherenkov effect, where a charged particle when traversing through a medium with a speed greater than the speed of light in that medium, emits electromagnetic radiation, in the form of conical wavefronts as shown in Figure 3.11. The angle between the wavefronts and the momentum of the charged particle can be given as $\cos\theta = \frac{1}{n\beta} = \frac{E}{n|\bar{p}|} = \frac{\sqrt{|\bar{p}|^2+m^2}}{n|\bar{p}|}$, where n is the refractive index of the medium which the charged particle is traversing and β is the speed of the particle relative to the speed of light, p is the momentum, and m is the mass of the particle. The idea behind the RICH detectors is to obtain the Cherenkov angle in order to compute the mass of the particle, once the momentum is known from the tracking system. LHCb has two RICH detectors, that provide particle identification in different momentum ranges.

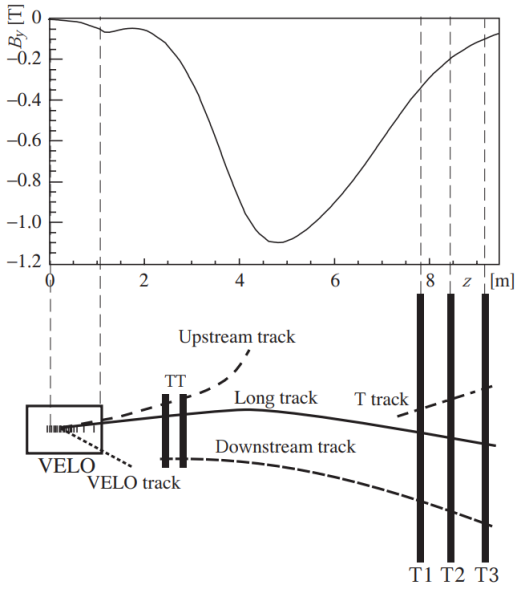

Figure 3.10: Profile of the magnetic field in the direction of beam and definition of the different LHCb track types [70].

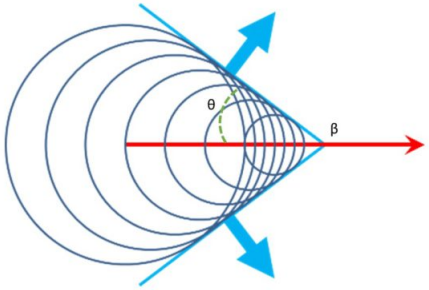

Figure 3.11: Cherenkov wavefront

RICH1

RICH1 is located between the VELO and the TT tracker. A layout of the detector can be seen in Figure 3.12. It covers a full angular acceptance of $25 - 300$ mrad and provides PID information for particles that have momentum in the range of $2 - 40\,\mathrm{GeV}/c$. It uses aerogel and C_4F10 radiators that have refractive index of 1.03 and 1.0014 respectively for light of wavelength 400 nm. The radiator has $3.5\,\mathrm{m}^2$ volume of C_4F_{10} gas and the silicon aerogel. It also has 4 spherical mirrors which are placed symmetrically around the beam pipe within the acceptance region, along with 2 flat mirrors that are located outside the acceptance region, that reflect the photons to the hybrid photodetectors (HPDs). The use of spherical mirrors, made from light-weight carbon-fibre reinforced polymer helps to maintain the material budget under 2% of radiation

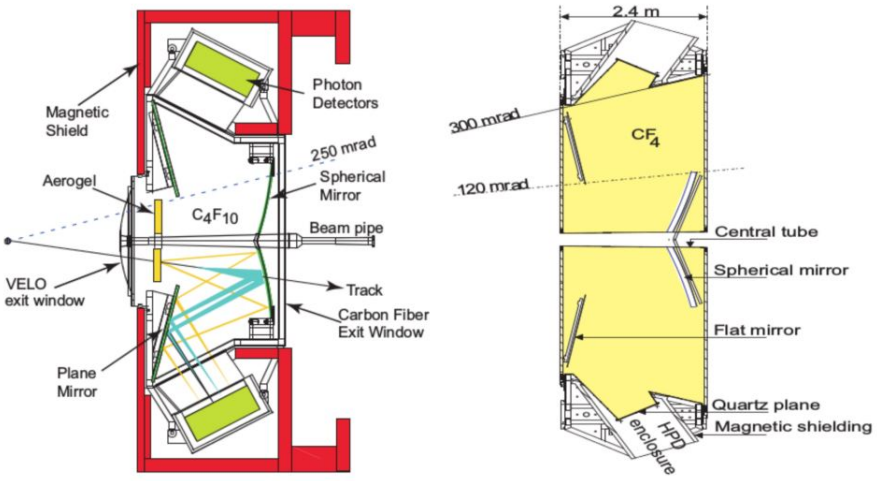

Figure 3.12: RICH1 (left) and RICH2(right) layout [63]

length.

The radiators, mirrors and the photon detectors are sealed inside an aluminimum box. The Cherenkov photons emitted by the track are focused using the optical system on a plane of hybrid of photodetectors(HPDs). These photodetectors are placed outside the LHCb acceptance. They are designed to detect photons in the wavelength range of $200 - 600\,\text{nm}$. They are surrounded by iron shields to prevent interference due to magnetic fields from the LHCb magnet. Given the radius r of the ring formed on the photodetectors due to the photons, we can compute the Cherenkov angle as $\tan\theta = r/f$, where f is the focal length of the spherical mirror. This helps us to get the mass hypothesis of the particle in order to identify it as a particular species of particle. The Cherenkov angle as a function of momentum for different species can be seen in Figure 3.13. From the profile of the angle it can be seen that at high momentum there is a saturation of the Cherenkov angle and at low momentum there is a requirement of a threshold for the emission of Cherenkov photons. The aerogel was used with an intention to get an improved PID performance since it provides good discriminating power at low energies. However, since the detector operated at a luminosity which was higher than the designed value, that was not the case and it was decided to remove the aerogel for Run II which led to an improved PID performance [72] in addition to the improvements due to increased boost from the higher centre-of-mass energy.

RICH2

RICH2 is located after the T1-T3 tracking stations. It uses CF_4 gas of volume $95m^3$ as radiator. It provides particle identification of the species having momentum in the range $15 - 100\,\text{GeV}/c$. Hence, the coverage of the RICH2 is less than RICH1 with the angular acceptance of 15-120mrad, as the tracks with high momentum range are generally closer to the beam line. The layout

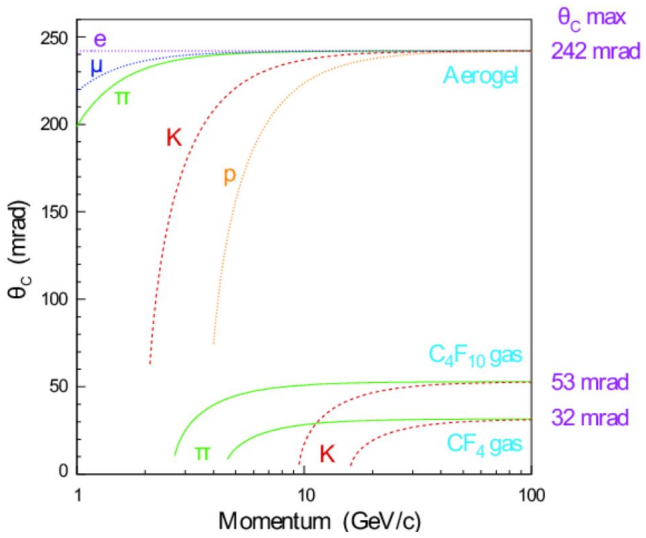

Figure 3.13: Cherenkov angle with respect to particle momentum [63]

of RICH2 can also be seen in Figure 3.12. It makes use of 52 spherical mirrors which focus Cherenkov light onto 2 planes of flat mirrors placed to the left and right of the beam line.

3.2.5 Calorimeters

The next detectors that the particles encounter are the calorimeters. They are principally used to stop the particles and infer the energy deposited. As the particle traverses, it produces a cascade shower of particles producing scintillating light and thus losing its energy [73]. Thus they have high material budgets compared to other detectors. The scintillation light is collected by the multianode photomultiplier tubes (PMTs) using wavelength-shifting fibres. The light is then converted into an electrical signal. The calorimetric system consists of 4-subdetectors: Scintillator Pad Detector (SPD), Pre-Shower detector (PS), Electromagnetic calorimeter (ECAL) and Hadronic calorimeter (HCAL). This system of sub-detectors is located between the first and second muon stations as shown in Figure 3.15. The information obtained from the system is used for identifying the species of particle as either electrons, photons or hadrons. All the sub-detectors make use of scintillator material (doped polystyrene) and absorber material with large radiation length to contain all the showering particles.

SPD and PS

The SPD and PS detectors are placed before ECAL. They are separated by 15mm thickness of lead. The SPD is about 0.45% smaller than the PS. This helps to maintain a same angular acceptance for both. The SPD provides measurement of event occupancy. When a charged particle travels through SPD, it generates signal unlike neutral particles, this helps SPD to

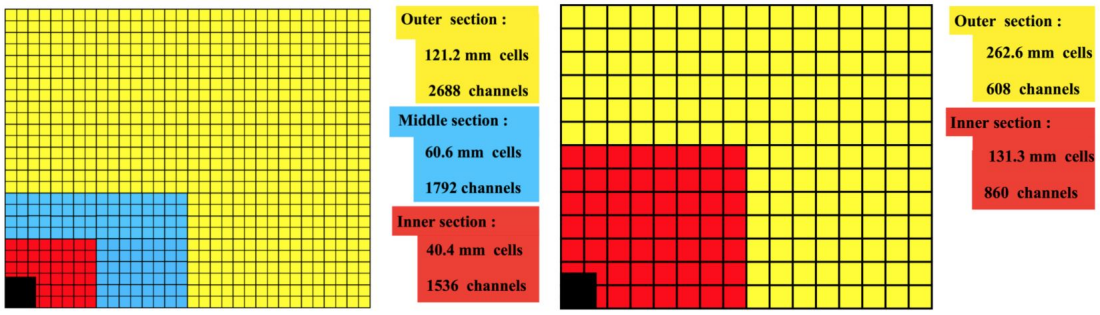

Figure 3.14: Design of the calorimeters SPD,PS,ECAL(left) and HCAL(right). Beam pipe is shown in black [73].

determine whether the particle is charged or neutral before it showers. This information is useful along with the information obtained from ECAL to discrimate between photons, electrons and pions. Photons however, initiate a shower in the lead absorber layer between SPD and PS and generate signal in PS. This helps to easily identify a photon, as it will show a signal in PS but none in SPD. Similarly electrons are more likely to shower in the lead absorber compared to charged hadrons. This makes it easier for PS to distinguish them from charged hadrons. Thus, we get the pion-rejection rate of 92% and electron acceptance rate of 95% from PS alone. However, if the information from ECAL and tracking is included the pion-rejection rate increases to 99%. These detectors are separated into 3 regions inner, middle and outer region with cell areas in each as $4 \times 4\text{cm}^2$, $6 \times 6\text{cm}^2$, $12 \times 12\text{cm}^2$. Since we expect large particle flux near the beam line, the cell size is finer in the innermost region and it increases as you go from inner region to outer region as shown in Figure 3.14. Moreover, we also expect the hit occupancy to vary by two orders of magnitude due to differences in shower size in each region.

ECAL

The Electromagnetic calorimeter [74] has 66 layers of lead absorber and polysterene scintillator with thickness 2 and 4 mm respectively. These layers are arranged alternatively and are perpendicular to the beam line with total thickness of 42cm and 25 radiation lengths. This is sufficient to contain all the electromagnetic showers produced by high-energy photons and electrons and provide an energy resolution of $\sigma_E/E = \frac{10\%}{\sqrt{E/GeV}} \oplus 1\%$ and a π^0 mass resolution of around $8MeV/c^2$. The layout of the layers is similar to that of SPD and PS with the layer being divided into 3 regions with finer cell size near the beam line.

HCAL

The Hadronic calorimeter make use of the iron as the absorber and scintillating tiles. It has a depth of 1.65m. The scintillating tiles are kept parallel to the beam axis unlike ECAL. This

is because the primary goal of the HCAL is to be used in the hardware trigger and it is less important for the HCAL to fully contain the hadronic shower. Unlike ECAL these layers are separated into 2 regions inner and outer as shown in Figure 3.14. Moreover, the readout cells in HCAL are larger than ECAL since the structures of hadronic and electromagnetic shower are quite different. Hadrons react via long-range nuclear interactions while electrons or photons interact via electromagnetic interaction. Thus hadrons create a wider shower structure compared to electrons or photons. Due to this the energy resolution of HCAL is far worse than ECAL with $\sigma_E/E = \frac{69\%}{\sqrt{E/GeV}} \oplus 9\%$.

3.2.6 Muon System

Muons are present in the final state of many decays, particularly decays like leptonic and semi-leptonic b and c-hadron decays. They have long lifetimes of around $2.2\mu s$. Their interaction probablity is quite low. Hence, they pass through the whole calorimeter system. This makes it important to detect them additionally, through the use of muon chambers. The muon stations [75][76] are also useful to get the information for flavour tagging and trigger decision.

The muon system consists of 5 stations (M1-M5) which are perpendicular to the beam line. All of them have an horizontal acceptance of $20 - 306\,\text{mrad}$ and a vertical acceptance of $16 - 258\,\text{mrad}$, the layout of the system can be seen in Figure 3.15. The first muon station, unlike others, is located upstream of the calorimeter. This helps to obtain a better estimate for the transverse momentum of the muons before they traverse through the calorimeter. The M2-M4 stations are separated by 80 cm thick iron blocks. The iron blocks absorb any hadronic backgrounds. Muons that have momentum greater than $6\,\text{GeV}/c$ pass through all the muon stations. M1-M5 offer a p_T resolution of around 20% in horizontal direction. The job of M4 and M5 is to confirm that the muonic particle has penetrated through the iron absorbers. This tells us that for a particle to classify as muon, it should have hits in all of the stations. Every station has multi-wire gas layers to detect the particles. These layers are divided into 4 sections R1, R2, R3, R4 and can be seen in Figure 3.15. Similar to all the other detectors, the granularity of these sections vary as you go away from the beam line to maintain same occupancy and particle flux.

3.3 Detector performance

3.3.1 Tracking and vertexing performance

The hits from different tracking stations are combined to reconstruct the trajectory of the particles, of which the charge and momentum can be estimated from the magnetic field. The reconstructed tracks can be classified as below as can also be pictured in Figure 3.10:

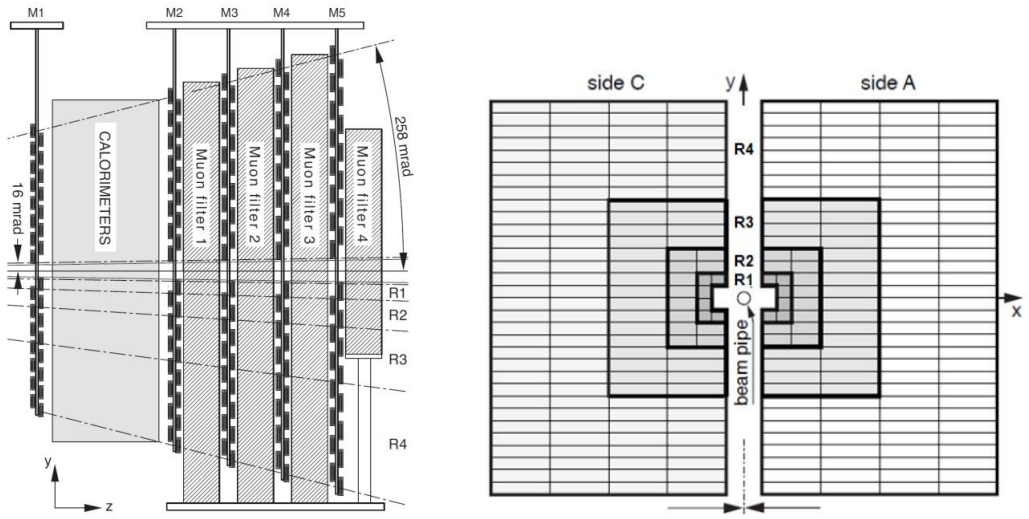

Figure 3.15: (Left) Layout of the muon system. (Right) Layout of each muon station [58]

- **VELO tracks** - These tracks have hits only in the VELO. They are normally outside the LHCb acceptance. They are only used for primary vertex reconstruction.
- **Upstream tracks** - These are low momentum tracks which are typically bent by the magnet outside the LHCb acceptance. They have hits only in VELO and TT.
- **Downstream tracks** - These are tracks often resulting due to long lived particles that decay outside VELO and they have hits in the TT,T1,T2,T3 stations.
- **Long tracks** - These are higher momentum tracks originating inside the VELO within the LHCb acceptance and travel upto the final tracking stations. They have hits in the VELO, TT, T1,T2,T3 stations. They have the best resolution. In this analysis we focus mainly on the Long tracks.
- **T tracks** - These are produced from secondary interaction away from VELO. They have hits in T1, T2, T3 stations.

These reconstructed tracks are used to determine the primary vertices (PV). An important metric that describes the performance of the VELO is the PV resolution. It depends upon the number of tracks used in the reconstruction and is measured by taking into the account the vertices that have a large number of tracks. The tracks are randomly split into two groups and the PV's are reconstructed for both the groups. It is then used to obtain a distribution of the difference in vertex positions from both the groups. The width of this distribution divided by $\sqrt{2}$ gives an estimate of the PV resolution. A plot of PV resolution as a function of number of tracks can be seen in Figure 3.16. It can be seen from the plot that as the number of tracks increases the resolution becomes better.

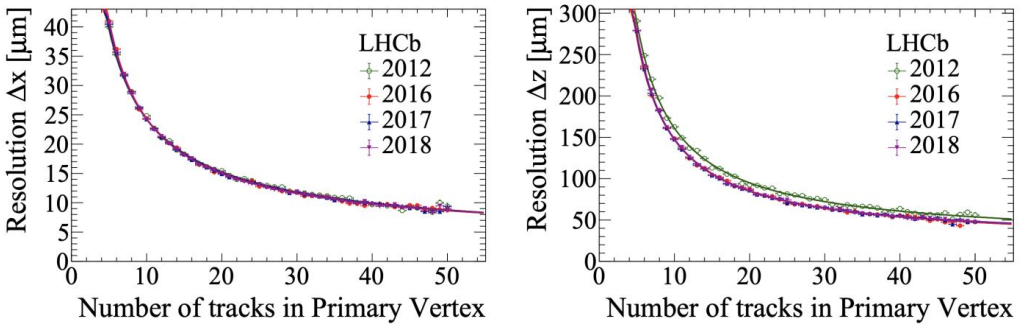

Figure 3.16: Resolution of PV in x direction (left) and z direction(right) as a function of number of tracks for different years of data taking. [77]

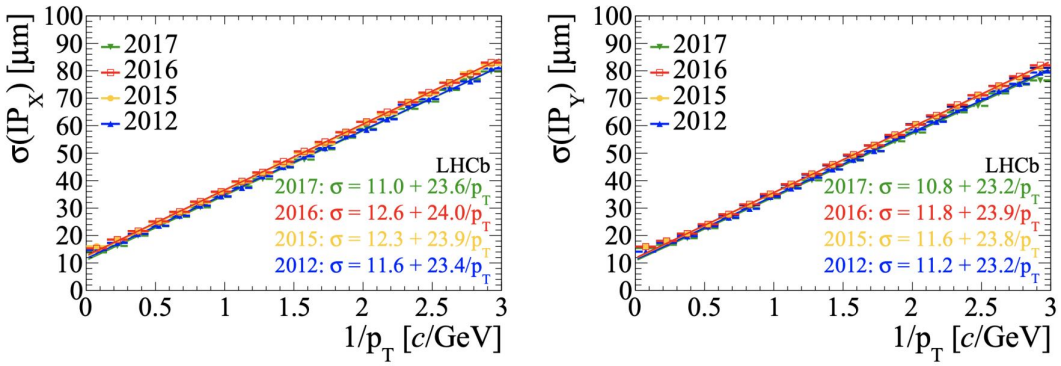

Figure 3.17: IP resolution in x direction (left) and z direction(right) as a function of p_T for different years of data taking [77]

Another metric determining the detector performance is the impact parameter (IP). It is the distance of the closest approach of a track with the designated PV [78]. This is a useful parameter in the selection of heavy flavour decays. This is because the tracks from secondary vertices of such decays will have larger IP as they are significantly displaced from the PV. The measurement of the IP resolution is done similarly to that of PV resolution. The reconstruction of a PV requires to have at least 25 long tracks. The IP resolution is given by the width of the IP distributions obtained by excluding a track randomly and re-fitting the PV again. A plot showing the x and y components of the IP resolution as function of p_T can be seen in Figure 3.17. It can be seen that IP resolution is best for high momentum tracks and is around $13\mu m$. The VELO thus helps to reconstruct the primary and secondary vertices, giving a precise determination of the decay time and impact parameter.

A metric that can be used to study the performance of the TT and IT is the tracking resolution. The resolution is obtained from the distribution of the difference between the position of a hit in the detector and the position estimated based on the other hits of the track. The track resolution is found to be around $50\mu m$. A plot showing the resolution of particle hits across TT

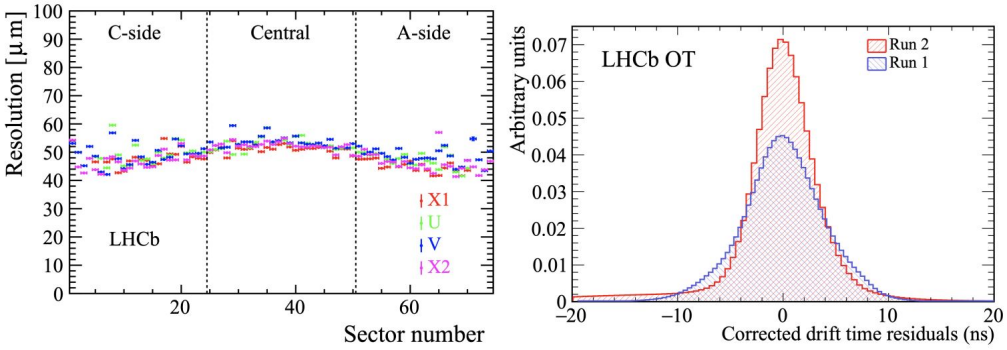

Figure 3.18: (left) Resolution of particle hits for TT for different x-u-v-x layers [63]. (Right) Distribution of drift time residuals for OT [79]

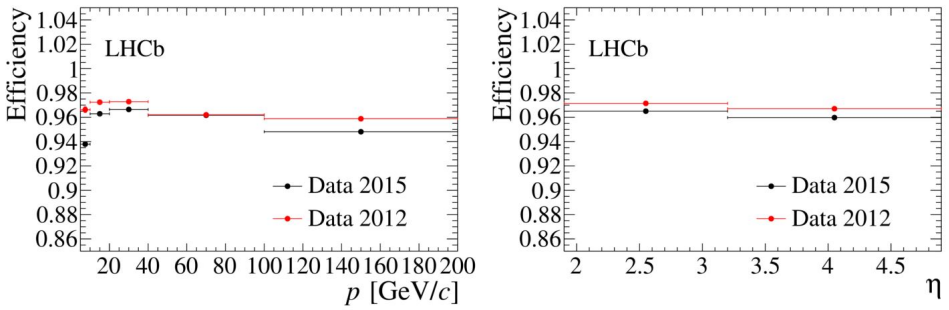

Figure 3.19: Tracking efficiency as a function of momentum (left) and pseudorapidity (right) [63]

can be seen in Figure 3.18. On the other hand, the performance of the OT can be studied using drift time resolution and can also be seen in Figure 3.18.

The tracking efficiency of the tracks is measured using 'tag and probe' method. It makes use of the decay $J/\psi \to \mu^+\mu^-$ from which one muon is fully reconstructed whereas the other is partially reconstructed using only the information from the muon system. The tracking efficiency is thus computed as the proportion of probe muons which can be matched successfully to fully reconstructed long tracks. This gives rise to an average efficiency above 96% in the momentum range $5 < p < 200\,\text{GeV}/c$. However, there is a small dependence upon track momentum, pseudorapidity, track multiplicity and number of primary vertices [72]. A variation of the efficiency with respect to momentum and pseudorapidity can be seen in Figure 3.19.

3.3.2 PID performance

To associate a mass hypothesis to a particle, we need information from RICH, calorimeters and muon system [80]. This can be done in two ways. In the first approach, the relative likelihood of a particle being a desired species is computed with respect to the likelihood of being pions and is given by DLL_a, where a is the desired species. The reconstruction algorithm of each sub

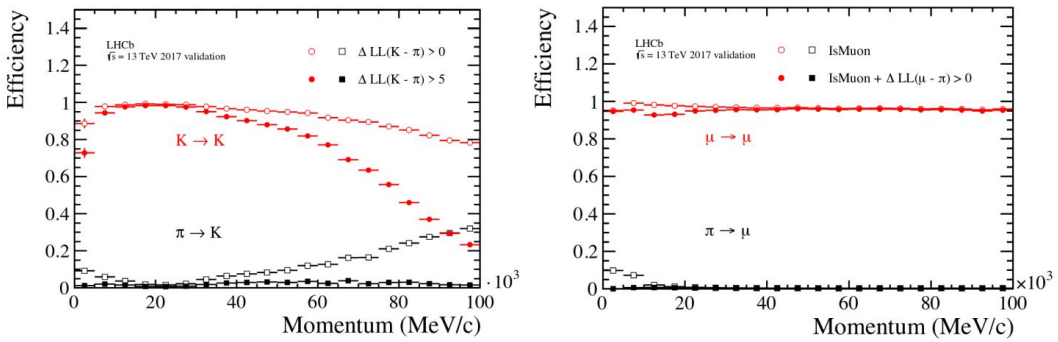

Figure 3.20: PID efficiencies for different mass hypothesis as a function of momentum. (Left) Efficiencies for correctly identified kaon and incorrectly identified pion as a kaon. (Right) Efficiencies for correctly identified muon and incorrectly identified pion as a muon for year 2017. [72]

detector is used to get an overall likelihood of a track being a particular species. It is compared with respect to the likelihoods of pions because pions are the most common particle species.

$$\mathrm{DLL}_a = ln\mathcal{L}_a - ln\mathcal{L}_\pi = ln[\frac{\mathcal{L}_a}{\mathcal{L}_\pi}] \tag{3.1}$$

However this technique does not take into account any effects due to correlations between the likelihood of different subdetectors.

The second approach tries to cover the limitations of the first approach. It is based on multivariate analysis. It uses likelihoods and some variables like event multiplicity that describe the whole event as an input to the neural networks. This ensures that the correlations between different inputs are taken into account. It also ensures that the information from the calorimeters is used. This gives rise to PID variables like probNN_a, which give some measure of the probability of a given particle to be species a.

The performance of the PID techniques and the detectors in terms of PID efficiencies are obtained from data-driven calibration samples. For pions and kaons, the decay channel $D^{*+} \to (D^0 \to K^-\pi^+)\pi^+$ is used. For protons the samples used are $\Lambda \to p\pi^-$ and $\Lambda_c^+ \to pK^-\pi^+$. Whereas, for muon PID efficiencies, the samples are $J/\psi \to \mu^+\mu^-$. The PID performance plots for 2017 data samples are shown in Figure 3.20. A comparison of PID efficiencies for Run 1 and Run 2 from Figure 3.21 concludes that the PID efficiencies are better in Run 2 compared to Run 1. In addition to the larger boost from the higher centre-of-mass energy in Run II, the probNN variables are trained on large data samples giving better separation between the PID hypothesis. These figures also point out the fact that the efficiencies decreases for both high and low momentum tracks. The decrease at low momentum is due to a minimum requirement of threshold momentum for the Cherenkov radiation to occur. Whereas, for high momentum particles it is due to saturation of the Cherenkov angle.

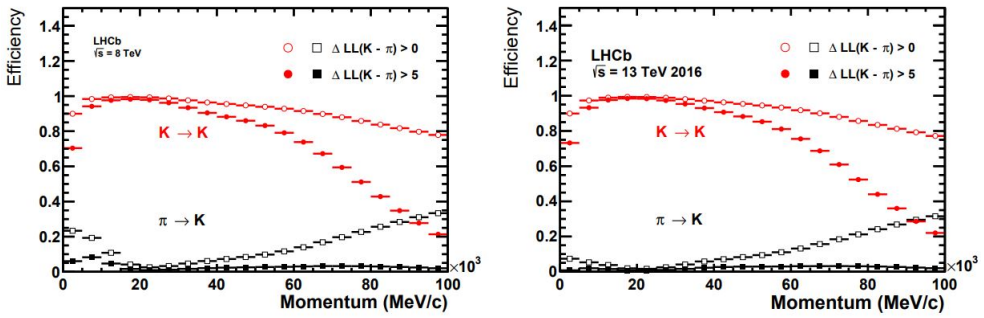

Figure 3.21: Comparison of the PID efficiencies for Run1 and Run2 [72]

3.4 Trigger system at the LHCb

The primary aim of the trigger system is to retain the events of interest. There are abort gaps in the proton beams. This leads to an average crossing frequency of 30 MHz instead of the 40 MHz which is the bunch frequency. Given, the inelastic p-p collision cross-section as 60mb at $\sqrt{s} = 14$ TeV and the luminosity as $\mathcal{L} = 2 \times 10^{32}\text{cm}^{-2}\text{s}^{-1}$, the frequency of p-p interactions is around 12 MHz. Moreover, large quantities of events do not have $b\bar{b}$ pairs and some events have decays that are outside the interest of LHCb. Given the limited storage capacity, it is not possible to write out data from every single bunch crossing. Additionally, there is a hard limit for reading out the detector electronics of 1 MHz, for which we need a hardware trigger in Run I and Run II, Therefore, we need a trigger system to reduce this rate and retain the events of interest. The triggering is done at 2 levels as also shown in Figure 3.22 : i) Level Zero (L0) trigger which is a hardware trigger and ii) High Level Trigger which is a software trigger. All of that reduces the rate to 3.5-12.5kHz [81, 82]. The trigger decisions about the offline reconstructed signal candidates are classified into 3 categories : i) Trigger On Signal (TOS), ii) Trigger Independent of Signal (TIS) and iii) Trigger on Both (TOB). If a trigger decision is solely due to the final state of particles of the signal then it would be classified as TOS. Whereas, if a decision is solely due to other particles in the same event, it would be classified as TIS. TOB decisions are those that would require both signal and rest of the event to trigger. In a given event there can be both TOS and TIS trigger decisions with respect to a given signal candidate. Details about the different trigger system as mentioned below.

3.4.1 Hardware trigger - L0

The hardware trigger is synchronised with the LHC clock through the use of custom electronics. The hardware trigger is required in order to reduce the rate to, at most, the maximum possible readout rate of the subdetectors, which is 1 MHz. The L0 trigger is based on the information from the calorimeters and the muon stations in order to decide if the full event should pass to

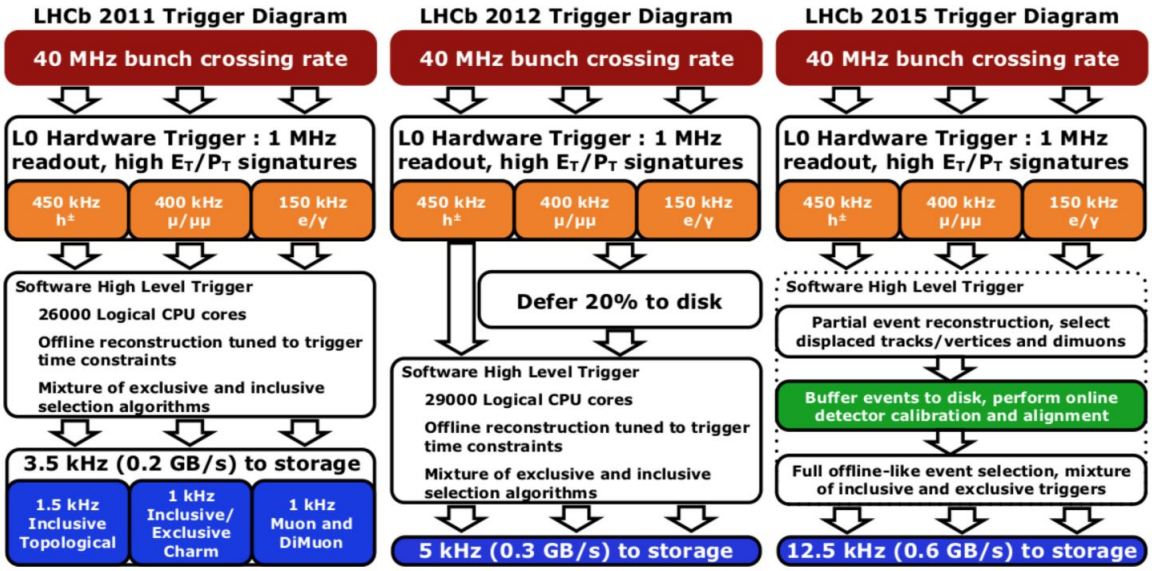

Figure 3.22: Data flow through the trigger system [83]

the HLT or not. After taking into account the cable length, time of flight of the particle and electronics latency, it has a time limit of $2\mu s$ to make a decision.

The calorimeter trigger aims to identify high E_T clusters that are caused by electrons, photons or hadrons. The three different cases are distinguished by the response of the SPD and PS, as well as the relative size of the ECAL and HCAL clusters. Clusters consistent with being an electron, photon or hadron are, respectively, classified as `L0_electron`, `L0_photon`, or `L0_hadron`, if they also satisfy the corresponding E_T thresholds. It is possible for several clusters in an event to cause positive trigger decisions but only one is required for the event to be triggered. The muon system similarly applies p_T thresholds to either single muons (`L0_muon`) or pairs of muons (`L0_dimuon`).The energy thresholds of the decisions are different for each year depending upon the data rate requirements and are quoted in Table 3.1.

Table 3.1: Thresholds of the transverse energy in GeV/c^2 for different L0 decision [84].

L0 decision	2011	2012	2015	2016	2017	2018
`L0_photon`	2.5	3.0	2.7	2.8	2.5	2.5
`L0_electron`	2.5	3.0	2.7	2.4	2.1	2.1
`L0_hadron`	3.5	3.7	3.6	3.7	3.5	3.5
`L0_muon`	1.5	1.8	2.8	1.8	1.4	1.4
`L0_dimuon`	1.3^2	1.6^2	1.3^2	1.5^2	1.3^2	1.3^2

3.4.2 Software trigger - HLT1, HLT2

The software trigger is asynchronous with the LHC clock unlike the hardware trigger. The high level trigger (HLT) makes use of the complete event information and reduces the data rate from 1 MHz to 5(12)kHz for Run I(II). The events are then later stored for further analysis offline. The software triggering occurs in two steps : HLT1, HLT2. In the first step, the events are partially reconstructed and selections applied to reduce to 40kHz before being passed to HLT2 to perform full event reconstruction.

The partial reconstruction occurs when minimum of 5 VELO tracks are reconstructed and the primary vertices are identified by considering vertices that are within 300μm from the bunch crossing centre. These tracks are used along with the information from the trackers and a Kalman fit [85] is performed to form upstream and long tracks. The HLT1 trigger makes use of the transverse momentum of these tracks to make the decision by selecting at least one track displaced from the primary vertex with high transverse momentum (e.g. a threshold of $p_{\mathrm{T}} > 1.6\,\mathrm{GeV}/c$ was used in 2012). Further, a full event reconstruction is performed at the HLT2 stage. There are two types of HLT2 lines, which can cause events to be triggered: inclusive and exclusive lines. Exclusive lines reconstruct and select specific final states, while inclusive lines perform partial reconstruction of 2-, 3- or 4-body candidates that have a displaced vertex using a number of topological variables to discriminate against prompt backgrounds. It is possible for both inclusive and exclusive lines to fire on a given event. The inclusive topological lines are used in this analysis. The events are saved to the disk if at least one of the HLT2 lines is fired. As discussed previously for the L0 trigger decisions, it is also possible to classify the HLT decisions with respect to an offline reconstructed signal candidate as being TOS, TIS or TOB. The next section describes the the offline selections of the triggered candidates.

Chapter 4

Dataset and candidate selection

4.1 Dataset

The analysis presented in this thesis is based on the data collected by the LHCb experiment from proton-proton collisions during both Run I and Run II periods, having centre of mass energies of 7-8 TeV and 13 TeV respectively. This corresponds to an integrated luminosity of approximately $8.7\,\text{fb}^{-1}$ as shown in Table 4.1. The focus of this analysis is to select the data corresponding to the channels $\Xi_b^-(\Omega_b^-) \to \Lambda_c^+ K^- K^-$, $\Xi_b^-(\Omega_b^-) \to \Lambda_c^+ K^- \pi^-$, $\Xi_b^-(\Omega_b^-) \to \Lambda_c^+ \pi^- \pi^-$ and $B^- \to \Lambda_c^+ \overline{p} K^-$ along with the control channel $B^- \to \Lambda_c^+ \overline{p} \pi^-$. This decay is used as a control mode in the analysis to reduce the systematic uncertainties in the final measurements. The motivation behind choosing $B^- \to \Lambda_c^+ \overline{p} \pi^-$ as the control mode is that it has the same topology, and has similar kinematics as the signal channels. In every channel the Λ_c^+ decays to $pK^-\pi^+$.

Table 4.1: Data samples used in the analysis, with year of data taking and integrated luminosity.

	Year	$\int \mathcal{L} dt$
Run I	2011	$1.0\,\text{fb}^{-1}$
	2012	$2.0\,\text{fb}^{-1}$
Run II	2015	$0.3\,\text{fb}^{-1}$
	2016	$1.6\,\text{fb}^{-1}$
	2017	$1.7\,\text{fb}^{-1}$
	2018	$2.1\,\text{fb}^{-1}$

4.1.1 Trigger, stripping and reconstruction

Charged particles such as kaons, pions and protons are relatively stable compared to other heavy particles containing b or $\bar{b}$ quarks. They are able to traverse through the whole detector before

decaying. Hence they fall under the category of final state particles. The properties of the particles produced in the collision are inferred through the readout of the detector.

As mentioned in Section 3.4, only a small fraction of the data from the collision is retained. It is filtered using the trigger system that decides which events to retain. The triggered data is reconstructed to form tracks with the help of pattern recognition algorithms. Later the tracks are fitted using a Kalman filter. Further selection is applied on the properties of tracks and the resultant subset of data corresponding to a specific decay channels are stored separately. This process is called stripping and the subset of data is called the stripping line. The stripping lines store the information of the decay tree of the candidate. Hence, full information of an event is needed in order to run the stripping. Since the different data-taking years might have different centre of mass energies and detector configurations, the stripping configurations for different years can require different tuning and are run independently. However, for the purpose of this analysis the configurations of the stripping lines from the different years are the same.

4.1.2 Monte Carlo

The analysis also makes use of Monte Carlo simulation. This is done to get confidence on some aspects of the analysis where a data-driven approach is not viable. This includes multivariate training for selecting signal-like events, modelling the shapes of the signal and getting the detection efficiency. These MC samples have been generated using `PYTHIA` [86][87], which is a tool that aims to mimic the high-energy collisions comprising modelling the evolution of the partonic showers from the initial state to the final states. The decays generated in the process are handled by `EvtGen` [88], which provides a framework to implement the physics processes of hadron decays. This helps to get a phase space distribution of the generated decay. This is then passed through the `GEANT4`[89][90] package that simulates the passage of the particles through the detector material.

In this analysis we generate MC samples that mimic the LHCb detector configuration for each year to match the data samples. The MC samples for different years are generated in proportion to the luminosity for different years. All the MC samples for this analysis are generated with a `SQDALITZ` [91] model for the b hadrons. This model generates events uniformly across the square Dalitz plot (SDP) of the three-body decay. A SDP is a 2D plot of variables m' and θ' that represents the phase-space of a 3-body decay. The variables are defined as [91]

$$m' = \frac{1}{\pi}\cos^{-1}\left(2\frac{m_{12} - m_{12}^{\min}}{m_{12}^{\max} - m_{12}^{\min}} - 1\right) \quad \text{and} \quad \theta' = \frac{1}{\pi}\theta_{12} \tag{4.1}$$

where m_{12} is the invariant mass of the particles labelled 1 and 2 that has kinematic limits $m_{12}^{\max} = m_{X_b} - m_3$ and $m_{12}^{\min} = m_1 + m_2$. m_{X_b} is the mass of the b hadron, m_i is the mass of the particle labelled i and θ_{12} is the helicity angle between the particles numbered 1 and 3 in the

rest frame of the "12" system. It is preferable to use a SDP to generate uniform distribution of phase space. This is because such decays generally proceed via intermediate resonances. Thus they tend to populate the regions around the edges of the conventional Dalitz plot. The SDP transform tends to enhance these regions with respect to the Dalitz plot centre so we get more simulated events in the regions where we have more data events. Additionally we use the MC samples later for making binned efficiency maps, for which having square boundaries is helpful.

We also generate samples for the partially reconstructed background as described in Chapter 5. These are generated using `RapidSim` [92], which provides fast simulation of the beauty and charm hadron decays in order to study the signals and also perform background characterisation. It generates the events uniformly across the phase space with the final state particles lying within the LHCb geometrical acceptance. Details of all the simulation samples are shown in Table 4.2 and Table 4.3. These MC samples are generated with the information of the particle properties available at that time which are described in Table 4.4. These can differ from the latest world averages from PDG [93], which adds corrections to the simulation as described in Chapter 6.

Table 4.2: `RapidSim` samples of $\Xi_b^- \to \Sigma_c^+ hh'$, where $\Sigma_c^+ \to \Lambda_c^+ \pi^0$.

Decay	Events	Options
$\Xi_b^- \to \Sigma_c^+ K^- K^-$	10000	$2 < \eta < 5$, 8 TeV, 13 TeV
$\Xi_b^- \to \Sigma_c^+ K^- \pi^-$	10000	$2 < \eta < 5$, 8 TeV, 13 TeV
$\Xi_b^- \to \Sigma_c^+ \pi^- \pi^-$	10000	$2 < \eta < 5$, 8 TeV, 13 TeV

Table 4.3: Monte Carlo simulation samples for Run I and Run II at generator level.

Decay	2011	2012	2015	2016	2017	2018
$\Xi_b^- \to \Lambda_c^+ \pi^- \pi^-$	60 M	147 M	38 M	101 M	104 M	94 M
$\Xi_b^- \to \Lambda_c^+ K^- \pi^-$	56 M	134 M	38 M	98 M	99 M	94 M
$\Xi_b^- \to \Lambda_c^+ K^- K^-$	56 M	137 M	37 M	94 M	95 M	96 M
$\Omega_b^- \to \Lambda_c^+ \pi^- \pi^-$	59 M	141 M	39 M	101 M	97 M	98 M
$\Omega_b^- \to \Lambda_c^+ K^- \pi^-$	59 M	143 M	38 M	100 M	98 M	92 M
$\Omega_b^- \to \Lambda_c^+ K^- K^-$	60 M	134 M	37 M	92 M	92 M	90 M
$B^- \to \Lambda_c^+ \overline{p} \pi^-$	70 M	148 M	41 M	93 M	93 M	95 M
$B^- \to \Lambda_c^+ \overline{p} K^-$	73 M	151 M	42 M	101 M	89 M	109 M

Truth matching

The Monte Carlo involves the full pp collision simulation, which is further triggered, reconstructed and passed through the selections of stripping lines in order to generate samples of a desired decay similarly to data. This gives rise to a possibility that the candidate built by a stripping line could be a part of a combinatorial background where tracks that are not a part of a decay are identified

Table 4.4: Particle properties in simulation and their latest world averages.

Particle	Lifetimes		Masses	
	Simulated (ps)	PDG (ps)	Simulated (GeV/c^2)	PDG (GeV/c^2)
Ξ_b^-	1.56	1.572	5.7949	5.797
Ω_b^-	1.1	1.64	6.0488	6.0461
B^-	1.638	1.638	5.27926	5.27934

incorrectly as originating from the decay. Thus we need to ensure that such backgrounds are excluded while trying to describe a generated decay. This is done through the use of truth matching. This would ensure that all reconstructed final-state particles are required to match with the corresponding MC particle in the generated decay. The matching looks at the number of detector hits that are in common between the MC particle and reconstructed track. If $> 70\%$ of the hits are in common then they are considered to be matched. In this analysis we apply the truth matching based on the particle ID, which is a ID number used to assign to a species, of the final state candidates that are reconstructed in MC compared with the ID of the generated decay.

PID variable correction

As mentioned in Section 3.3.2, information from the RICH, calorimeters, muon and tracking system is combined into `probNN` PID variables for both data and MC. However, the response of the simulation for these variables, does not match very well with the data. Hence, we cannot rely on MC samples to compute the efficiencies for our PID selections, which is needed for our measurement as discussed in Chapter 6. This motivates us to correct these variables, which is done using the `PIDcorr` package [77]. This package makes use of the clean and high statistics samples of $D^0 \to K^-\pi^+$ for kaons and pions, whereas for protons, it uses $\Lambda_c^+ \to pK^-\pi^-$ for Run I and $\Lambda_b \to p\pi^-$ for Run II. The package resamples the `probNN` values from the control samples in bins of the track kinematics and event multiplicity. `PIDcorr` uses MC samples of the control channels so that it can match the points on the cumulative distribution functions of the MC and data for each variable - this is how the correlations between the different `probNNs` for a given track are preserved. The agreement between our selected data and MC for these variables is discussed in later Section 7.2.3 . The good agreement confirms that we can evaluate the PID efficiencies from MC using the corrected PID variables.

4.2 Offline candidate selection

4.2.1 Multivariate analysis

Once the reconstructed data is obtained from the stripping lines, we perform further offline selections to separate the signal-like events from the backgrounds-like events arising due to random combinations of tracks, referred to as combinatorial background, by performing multivariate analysis. A Boosted Decision Tree (BDT) algorithm provided by `XGBoost` [94] is used. This is done twice in the study: first to reject fake $\Lambda_c^+ \to pK^-\pi^+$ candidates and second to reject fake $X_b \to \Lambda_c^+ hh$. We perform the procedure separately for Run I and Run II, since the trigger requirements are different for different runs as well as the centre-of-mass energy. A larger centre of mass energy in Run II leads to larger boosts of the particles and so the flight distances tend to be larger. Additionally, the PID variables have different tunings in the two Runs and the PID performance in Run II is better as discussed before.

BDT1

The first BDT aims to distinguish true $\Lambda_c^+ \to pK^-\pi^+$ decays from the combinatorial background. It is trained using the truth-matched samples from the MC as a reference for signal-like events and the sidebands of the Λ_c^+ candidate invariant mass distribution from data as a reference for background-like events. The Λ_c^+ candidate invariant mass distribution can be seen in Figure 4.1 (left). The sideband region is chosen as $2190 < m(pK^-\pi^+) < 2241\,\text{MeV}/c^2$ and $2331 < m(pK^-\pi^+) < 2380\,\text{MeV}/c^2$ and the input variables summarised in Table 4.5 are used for the training. Since the MC samples are resampled using `PIDcorr`, it is trivial to include those variables in the training. The samples of the three signal modes $\Xi_b^- \to \Lambda_c^+ K^- K^-$, $\Xi_b^- \to \Lambda_c^+ K^-\pi^-$ and $\Xi_b^- \to \Lambda_c^+ \pi^-\pi^-$ from the simulation are combined.

BDT2

The second BDT aims to distinguish true $X_b \to \Lambda_c^+ hh$ decays, where X_b is either the B meson, Ξ_b^- or Ω_b^-, from their fake counterparts. The output of the first BDT1 is now used as an input to the second BDT. A loose cut is applied on the first BDT so that a significant background from the fake Λ_c^+ hadrons is reduced. The second BDT is trained in a similar fashion as done for BDT1. Similar to BDT1, the samples of the three signal modes $\Xi_b^- \to \Lambda_c^+ K^- K^-$, $\Xi_b^- \to \Lambda_c^+ K^-\pi^-$ and $\Xi_b^- \to \Lambda_c^+ \pi^-\pi^-$ are combined from simulation as a reference for signal-like events and the sideband of the X_b candidate invariant mass distribution in data, defined as $5400 < m(X_b) < 5742\,\text{MeV}/c^2$ and $5852 < m(X_b) < 7500\,\text{MeV}/c^2$ is considered as a reference for the background-like events. The distribution of the X_b candidates invariant mass from the simulation can be seen in Figure 4.1. The input variables used to train the second BDT are

Table 4.5: Input variables used to train the `XGBoost` classifier to identify true Λ_c^+ hadrons, together with their ranking as obtained from the training. Note that "Children" refers to the Λ_c^+ decay products, *i.e.* p, K and π (in that order, where appropriate).

Particle	Variable	Ranking (Run I)	Ranking (Run II)
Λ_c^+	$\min_{\text{PVs}} \chi^2_{\text{IP}}$	9	12
	Directional Angle	6	13
	$\chi^2_{\text{vertex distance w.r.t. own PV}}$	2	5
	$\chi^2_{\text{vertex distance w.r.t Xb vertex}}$	4	6
	$\chi^2_{\text{end vertex}}$	13	16
Children	$\chi^2_{\text{track, NDOF}}$	15, 10, 8	7, 8, 10
	Highest p_{T}	5	3
	`ProbNNp`	1, 17, 11	2, 15, 11
	`ProbNNpi`	14, 16, 7	14, 17, 4
	`ProbNNK`	12, 3, 18	9, 1, 18

shown in Table 4.6. The variable $A_{p_{\text{T}}}$ describes the p_{T} asymmetry in a cone with half-angle of 1.5 units in the plane of pseudorapidity and azimuthal angle around the B candidate flight direction. Mathematically it is defined as $A_{p_{\text{T}}} = \frac{p_{\text{T}}(B) - \sum_n p_{\text{T}}(n)}{p_{\text{T}}(B) + \sum_n p_{\text{T}}(n)}$, where the summation is over the tracks within the cone excluding those that are associated with the B candidate. This variable proves to be quite helpful to reject the isolated events that have no tracks within a cone of 1.5 rad around the B candidate momentum direction. The same BDT's are applied to the control mode as well as both Ξ_b^- and Ω_b^- decays.

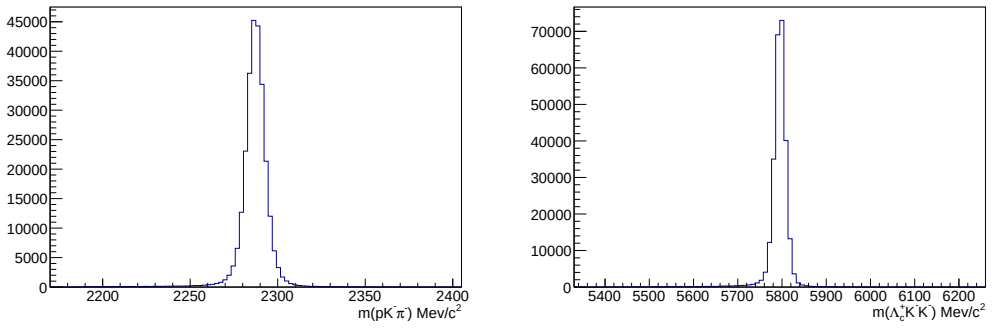

Figure 4.1: Distribution of reconstructed $\Lambda_c^+ \to pK^-\pi$ and $\Xi_b^- \to \Lambda_c^+ K^- K^-$.

The outcomes of the training can be seen in Figure 4.2 and Figure 4.3 for the first and second BDTs, respectively. It can be seen that there is good consistency between the training and the testing samples and there is no overtraining. This is also confirmed by studying the Kolmogorov-Smirnov test. The p-values for both the signal and background distributions is greater than 0.05, indicating that we can accept the null-hypothesis that the training and testing samples have been drawn from the same distribution and there is no over-training within the classifier.

Table 4.6: Input variables used to train the `XGBoost` classifier to separate X_b candidates from combinatorial backgrounds, together with their ranking as obtained from the training.

Particle	Variable	Ranking (Run I)	Ranking (Run II)
X_b	p_{T}	2	2
	$\min_{\mathrm{PVs}} \chi^2_{\mathrm{IP}}$	1	1
	$\chi^2_{\text{flight w.r.t. own PV}}$	8	8
	$A_{p_{\mathrm{T}}}$ in 1.5 rad cone	7	7
	$\chi^2_{\text{end vertex}}$	6	5
Λ_c^+	BDT1(Λ_c^+)	3	3
Children	Highest p_{T}	4	4
	$\Sigma(\min_{\mathrm{PVs}} \chi^2_{\mathrm{IP}})$	5	6

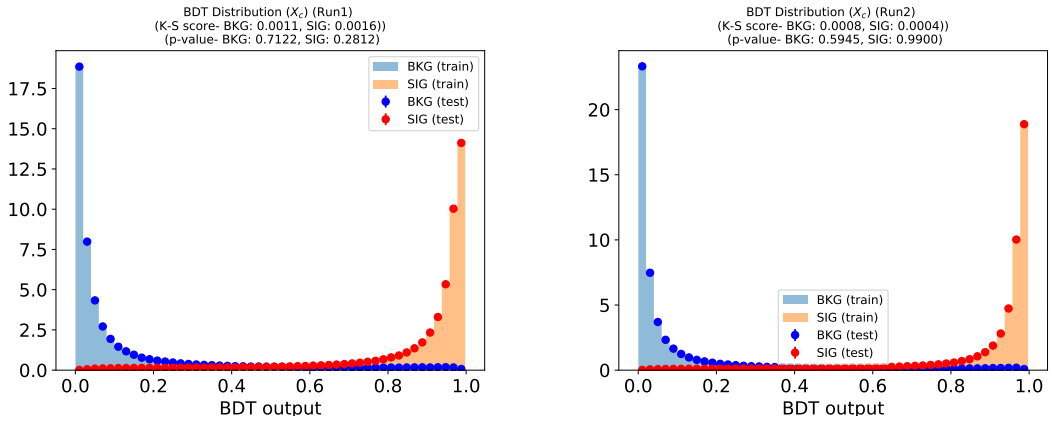

Figure 4.2: Output of training the BDT1 classifier that differentiates background and signal for Λ_c^+ candidates in Run I (left) and Run II (right).

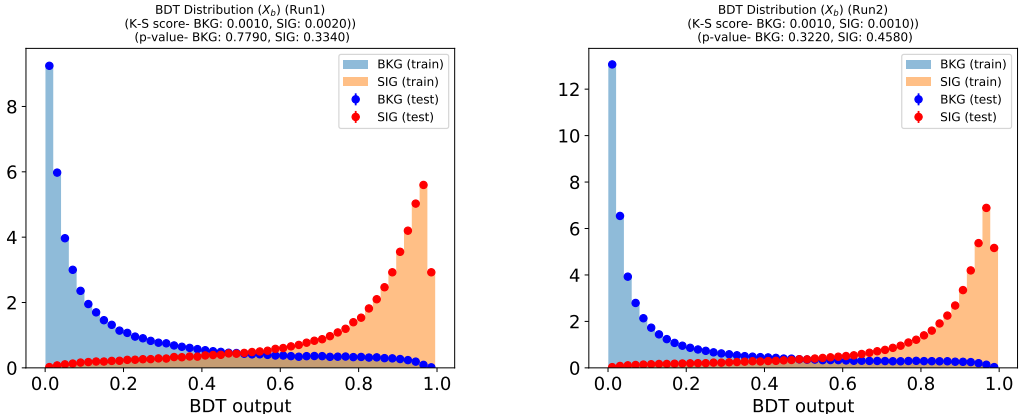

Figure 4.3: Output of training the BDT2 classifier that differentiates background and signal for X_b candidates in Run I (left) and Run II (right).

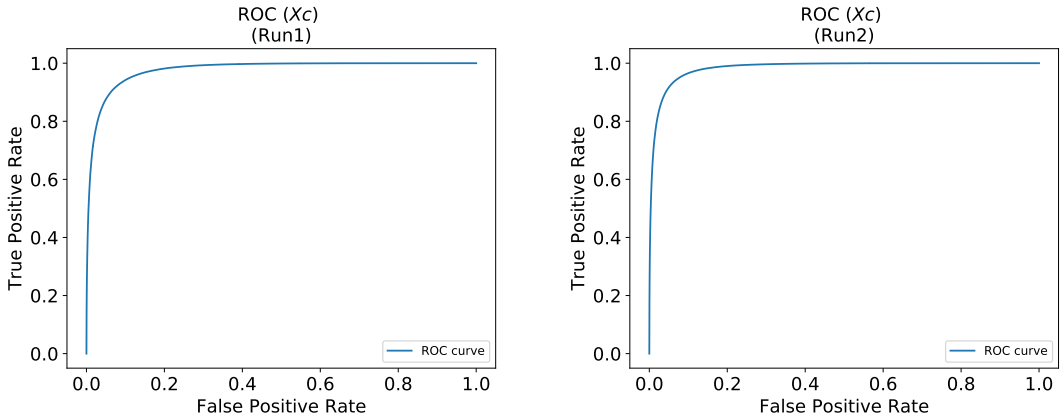

Figure 4.4: ROC curves for the BDT1 classifier trained to identify true Λ_c^+ candidates, for Run I (left) and Run II (right).

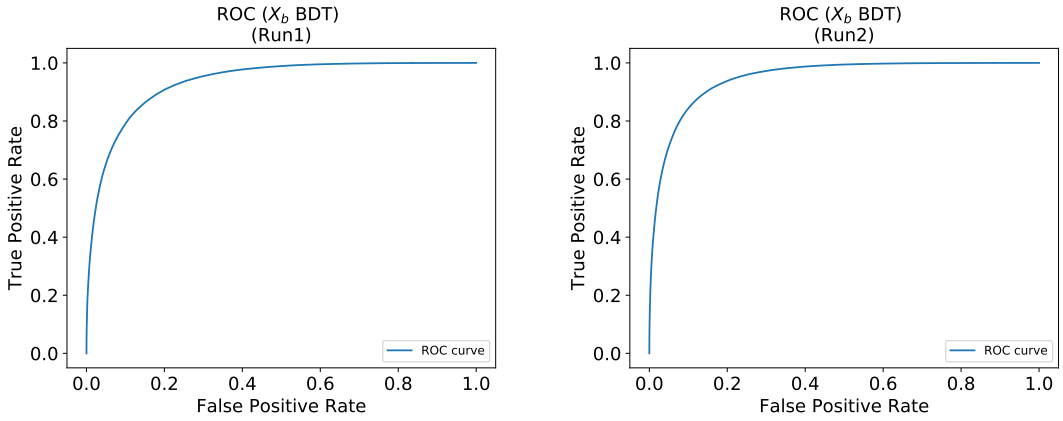

Figure 4.5: ROC curves for the BDT2 classifier trained to identify true X_b candidates, for Run I (left) and Run II (right).

We also study the performance of the classifiers through receiver operating characteristic (ROC) curves, which shows the plot of true positive rate vs false positive rate. It can be seen from Figure 4.4 and Figure 4.5 that the two classifiers perform well.

A requirement on the BDT2 output is then defined through an optimisation procedure aimed to maintain maximum signal efficiency and minimum background. We perform this using the Punzi figure of merit [95] defined as

$$\text{FOM} = \frac{\epsilon}{(\frac{\sigma}{2} + \sqrt{B})}, \tag{4.2}$$

where ϵ is the signal efficiency obtained from the MC simulation, σ is set to 5 and B is the expected number of background events in the signal region. The signal region is defined to be the Ξ_b^- candidate invariant mass of range 5770–5830 MeV/c^2. We perform an exponential fit to

the upper mass sideband of the data distribution defined as (5830–6800 MeV/c^2). This, when extrapolated into the signal region gives the expected number of background events in the signal region for a given BDT2 requirement. The scans for the FOM are shown in Figure 4.6. It can be seen that the maximum value of the FOM occurs when BDT2 is chosen as 0.94 (0.90) for the Run I (Run II) samples. This is done for all three Ξ_b^- decays, but the final requirement is that optimised for $\Xi_b^- \to \Lambda_c^+ K^- \pi^-$

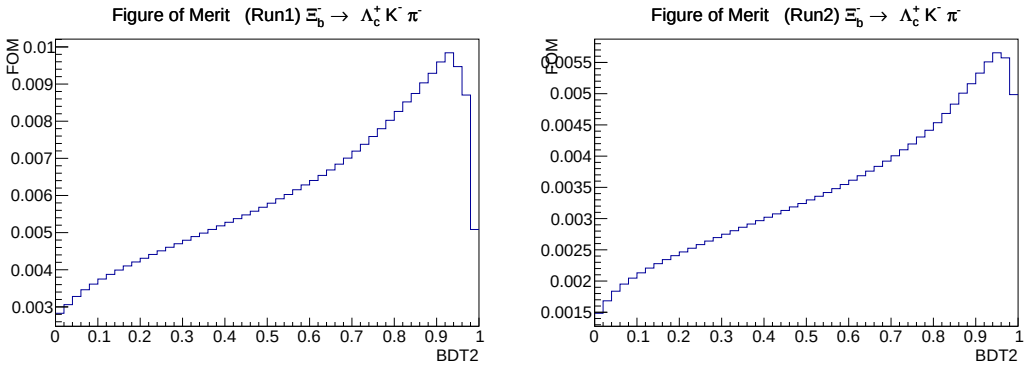

Figure 4.6: Figure of merit as a function of requirement on BDT2 output for $\Xi_b^- \to \Lambda_c^+ K^- \pi^-$, and for Run I (left) and Run II (right).

4.2.2 Particle identification (PID) requirements

In addition to the requirements on the BDT output, we also need to apply requirements on the PID variables in order to distinguish the different $\Lambda_c^+ hh$ final states. To ensure that we have reasonable PID information, we put requirements on the momenta of the final state tracks: 2.5 GeV/$c < p_{K,\pi} <$ 100 GeV/c and 9.5 GeV/$c < p_p <$ 100 GeV/c. Furthermore, to remove backgrounds coming from the semileptonic decays, we additionally require each final-state particle that passes through the acceptance of the muon counters is not identified as a muon. This is done by adding the requirement of `isMuon==0` on all the final states.

In our signal channels, it is possible for a kaon to be misidentified as a pion and vice versa. Thus, PID requirements reduce the misidentified backgrounds from the reconstructed signal channels. This is done following the strategy in Ref. [96], illustrated through a 2-D scatter plot of the variables `ProbNNK` *vs.* `ProbNNpi` as shown in Figure 4.7 for one of the tracks of the signal channel $\Xi_b^- \to \Lambda_c^+ K^- \pi^-$ from Run II. Particles that are clustered around the upper-left corner have a higher probability of being a kaon, while those that are clustered around lower-right corner have a greater probability of being a pion. This helps to separate the two cases using arcs of a circle that are centered on the bottom right corner of the plot. Particles lying inside the arc of radius r_π are classified as pions and those lying outside the arc of radius (r_K) are classified as kaons.

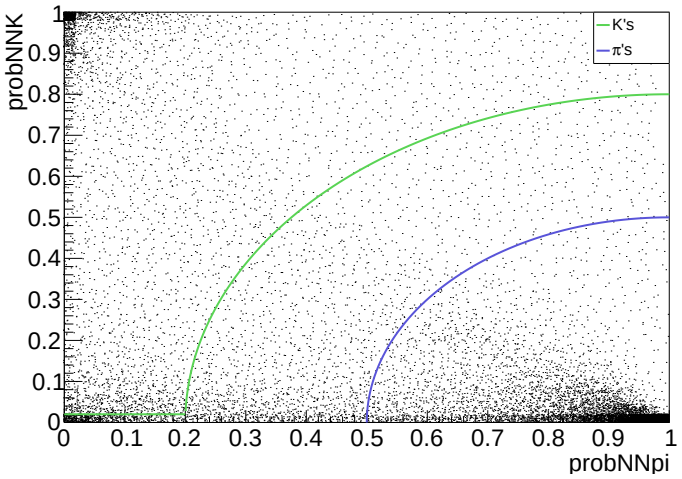

Figure 4.7: Scatter plot of `ProbNNK` *vs.* `ProbNNpi` for $\Xi_b^- \to \Lambda_c^+ K^- \pi^-$ candidates selected in Run II data.

For the tracks that originate directly from the b-baryon, the PID requirements imposed are

$$(\mathrm{pNN}_\pi - 1)^2 + (\mathrm{pNN}_K)^2 > r_K^2, \;\; (\mathrm{pNN}_\pi - 1)^2 + (\mathrm{pNN}_K)^2 < r_\pi^2 \tag{4.3}$$

We optimise the radii of the two arcs by minimising the misidentified events. Since we expect the largest yield in the channel $\Xi_b^- \to \Lambda_c^+ K^- \pi^-$, we consider misidentified backgrounds from this source to each of the $\Lambda_c^+ K^- K^-$ and $\Lambda_c^+ \pi^- \pi^-$ final states. We obtain figures of merit for the two cases defined as

$$\mathrm{FOM} = \frac{\epsilon_{\mathrm{sig}}}{\epsilon_{\mathrm{sig}} + \Sigma r_{\mathcal{B}} \epsilon_{\mathrm{misID}}}, \tag{4.4}$$

where ϵ_{sig} is the signal efficiency for a given PID cut, $\epsilon_{\mathrm{misID}}$ is misidentification rate and $r_{\mathcal{B}} = \mathcal{B}(\mathrm{misID})/\mathcal{B}(\mathrm{sig})$ is the ratio of branching fractions of the signal mode and the misID background. We define the ratio $r_{\mathcal{B}}$ from the Cabibbo suppression factor $|V_{us}/V_{ud}|^2$, *i.e.* $r_{\mathcal{B}} = 1/5\% = 20$ when $\Xi_b^- \to \Lambda_c^+ K^- \pi^-$ is mis-identified as $\Xi_b^- \to \Lambda_c^+ K^- K^-$. However, in the case where $\Xi_b^- \to \Lambda_c^+ K^- \pi^-$ is mis-identified as $\Xi_b^- \to \Lambda_c^+ \pi^- \pi^-$ we define $r_{\mathcal{B}} = 1000$ as we expect $\Xi_b^- \to \Lambda_c^+ \pi^- \pi^-$ to be highly suppressed since there is no tree-level diagram and neither loop-level diagram.

The scans for the FOM are shown in Figure 4.8 for different value of the radii of the arcs. The figures show that the FOM would be maximum at an optimum value of 1.32 (1.44) for r_K^2 in the Run I (Run II) samples. However, it prefers a very tight value for r_π^2 which would introduce large systematics in the later part of the analysis. Hence, we prefer to choose a loose pion ID requirement ($r_\pi^2 < 0.2$). This ensures that we do not make the selection efficiency sensitive to small perturbations. The B meson decay modes also have protons coming from the b meson. We apply a requirement of `ProbNNp` > 0.5 for the proton tracks. Since, we expect quite large yields of such channels, we do not perform any optimisation for the proton PID cut. However, we do

ensure a good background rejection while maintaining high signal efficiency.

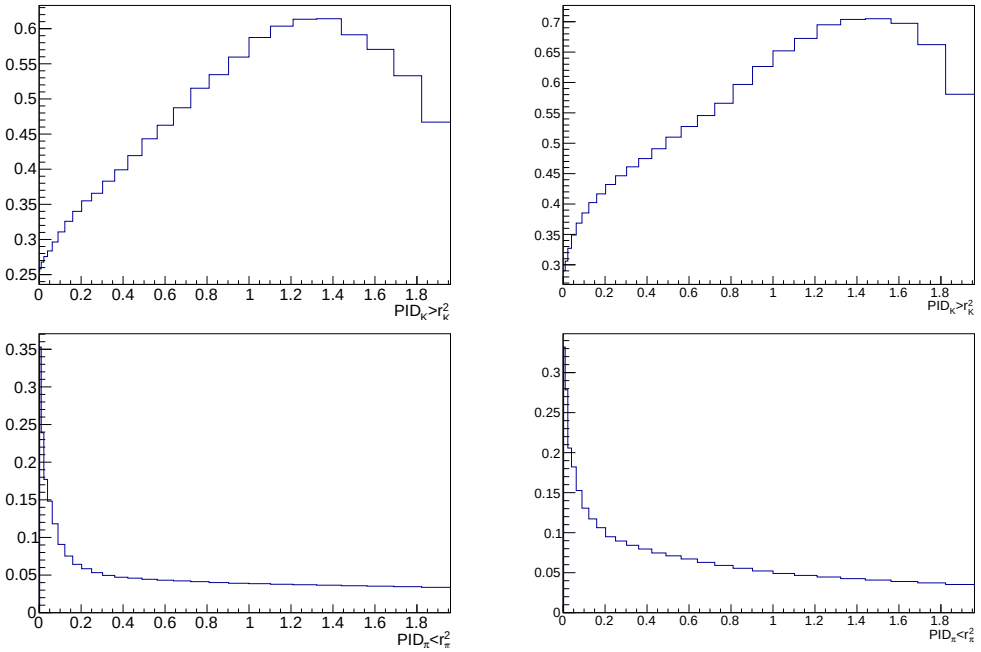

Figure 4.8: Figure of merit as a function of PID requirement, aiming to optimise the rejection of misidentified background from $\Xi_b^- \to \Lambda_c^+ K^- \pi^-$ decays to $\Xi_b^- \to \Lambda_c^+ K^- K^-$ (top) and $\Xi_b^- \to \Lambda_c^+ \pi^- \pi^-$ (bottom) for Run I (left) and Run II (right).

After the PID selection is finalised, we revisit the BDT2 optimisation. This is because there is a possibility for correlations between the PID and BDT variables to result in the change of the optimal point. The new optimal requirements are 0.85 and 0.90 for Run I and Run II, respectively.

4.2.3 Clone removal

The two final state tracks originating from the b hadron possess the same charge. This gives rise to a possibility that they could be clones. This is confirmed by studying the opening angle between the two tracks in the lab frame of b hadron. Figure 4.9 shows the distribution of opening angles both data and MC. It can be seen that there is a small contribution from clones in the $\Xi_b^- \to \Lambda_c^+ \pi^- \pi^-$ mode. We chose a cut of $\log(1 - \cos(\theta_{hh})) > -10$ to remove the clones from the samples. The cut is added on all the final states where the two tracks coming from the b hadron share the same PID requirements.

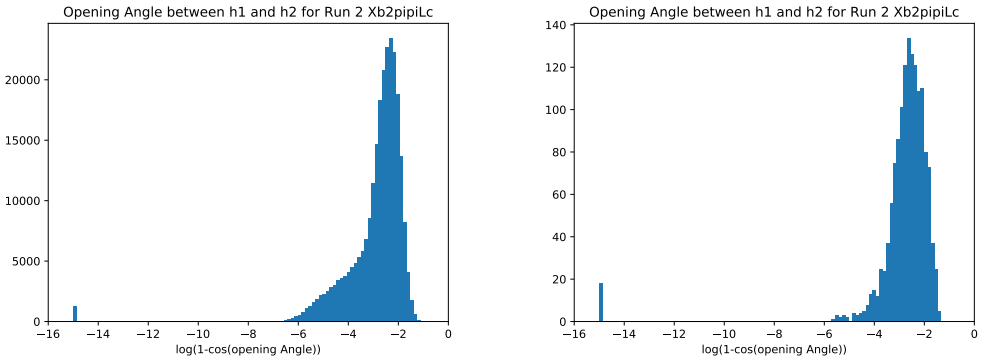

Figure 4.9: Opening angle between the two tracks directly originating from the b-hadron decay for $\Xi_b^- \to \Lambda_c^+\pi^-\pi^-$ candidates for (left) data and (right) MC. The peak at $\log(1-\cos(\theta_{hh})) = -15$ is due to cloned tracks. The shape of the core peak depends on the Dalitz plot distribution and can therefore differ between data and MC.

4.2.4 Veto of misreconstructed decays

Mis-reconstructed decays occur when the final state tracks originating from the $b-$hadron and Λ_c^+ decay vertex are swapped during the reconstruction. This can occur if when they are the same charged particle species. In this analysis, such backgrounds arise in $\Xi_b^- \to \Lambda_c^+ K^-\pi^-$ and $B^- \to \Lambda_c^+ \bar{p} K^-$ decays, since the b hadron and the Λ_c^+ hadron decay products both include a negatively charged kaon. Such decays are studied through the 3-body invariant masses calculated from the final state tracks of all the decay modes. Figure 4.10 and Figure 4.11 show the invariant masses for the $\Xi_b^- \to \Lambda_c^+ K^-\pi^-$ and $B^- \to \Lambda_c^+ \bar{p} K^-$ when the two kaons are swapped. A peak can be seen at $2285\,\mathrm{MeV}/c^2$ corresponding to misreconstructed decays. Such backgrounds are vetoed by removing candidates with $2260 < m(p_{\Lambda_c^+} K^- \pi^+_{\Lambda_c^+}) < 2310\,\mathrm{MeV}/c^2$. There is also a possibility of such backgrounds in the decay $\Xi_b^- \to \Lambda_c^+ K^- K^-$. But since there are limited statistics in this channel no such misreconstructed background peaks are seen in the invariant mass combination and hence no corresponding veto is applied.

4.2.5 Veto of partially combinatorial background

Partially combinatorial background occurs when a b hadron decay is combined with an extra random track giving rise to the reconstruction of a signal candidate. In this analysis, such backgrounds mainly occur from $\Lambda_b^0 \to \Lambda_c^+\pi^-$ or $\Lambda_b^0 \to \Lambda_c^+ K^-$ decays combined with either a kaon or pion. Such backgrounds are evident from the data seen in Figure 4.12 that shows the $\Lambda_c^+\pi^-$ and $\Lambda_c^+ K^-$ invariant mass distributions. Peaks around the known Λ_b^0 mass shows the evidence of such decays. It can also be seen that the peaks for $\Lambda_b^0 \to \Lambda_c^+ K^-$ are smaller than those for $\Lambda_b^0 \to \Lambda_c^+\pi^-$ due to the relative branching fractions [97].

The background coming from $\Lambda_b^0 \to \Lambda_c^+\pi^-$ with an additional π^- track is a large source

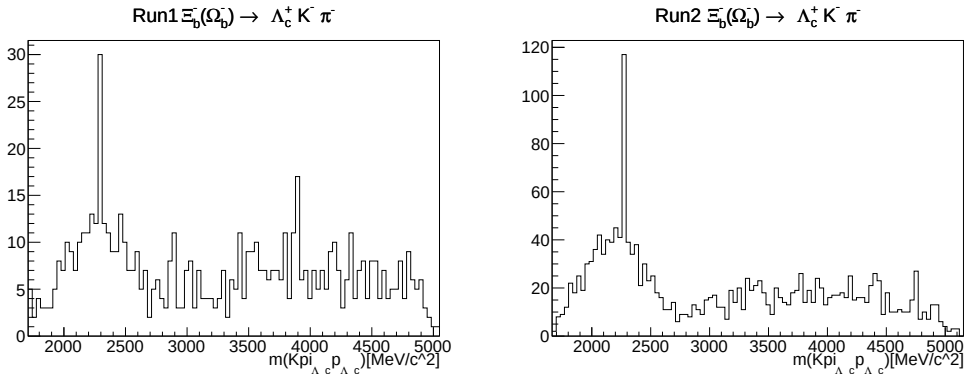

Figure 4.10: Three-body invariant mass combinations for the decay mode $\Xi_b^- \to \Lambda_c^+ K^- \pi^-$. Tracks originating from the Λ_c^+ decay are denoted with a subscript.

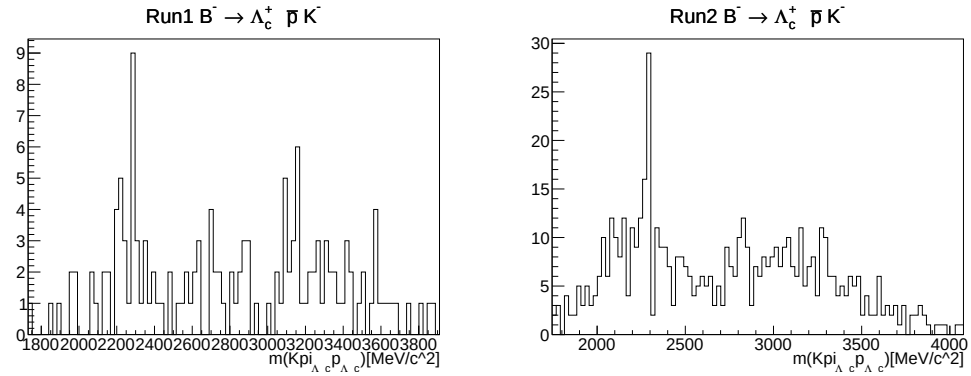

Figure 4.11: Three-body invariant mass combinations for the decay mode $B^- \to \Lambda_c^+ \bar{p} K^-$. Tracks originating from the Λ_c^+ decay are denoted with a subscript.

of background in the $\Lambda_c^+ \pi^- \pi^-$ final state. Furthermore, this background peaks close to the Ξ_b^- signal region. As no signal is expected in the $\Xi_b^- \to \Lambda_c^+ \pi^- \pi^-$ channel, the background is likely to inflate the invariant mass peak in the Ξ_b^- region and hence limit the sensitivity. Thus, such backgrounds are removed by vetoing around the Λ_b^0 peak, $5500 < m(\Lambda_c^+ \pi^-) < 5700\,\mathrm{MeV}/c^2$.

The same veto is applied for the other backgrounds in the invariant mass $m(\Lambda_c^+ \pi^-)$ and $m(\Lambda_c^+ K^-)$ for $\Xi_b^- \to \Lambda_c^+ K^- \pi^-$ candidates. Even though in this case the background is much smaller, it can still limit the sensitivity due to having similar shape as that of signal. This veto however causes a loss in the signal, which is then treated as a source of systematic uncertainty.

4.2.6 Selection summary

All the selection cuts discussed above are summarised in Table 4.7. Furthermore, since this is a first search for these Ξ_b^- and Ω_b^- decays, we blind the signal regions throughout the selection process. The number of retained candidates after all of the selection requirements are shown in Table 4.8 This does not include the candidates in the blinded regions.

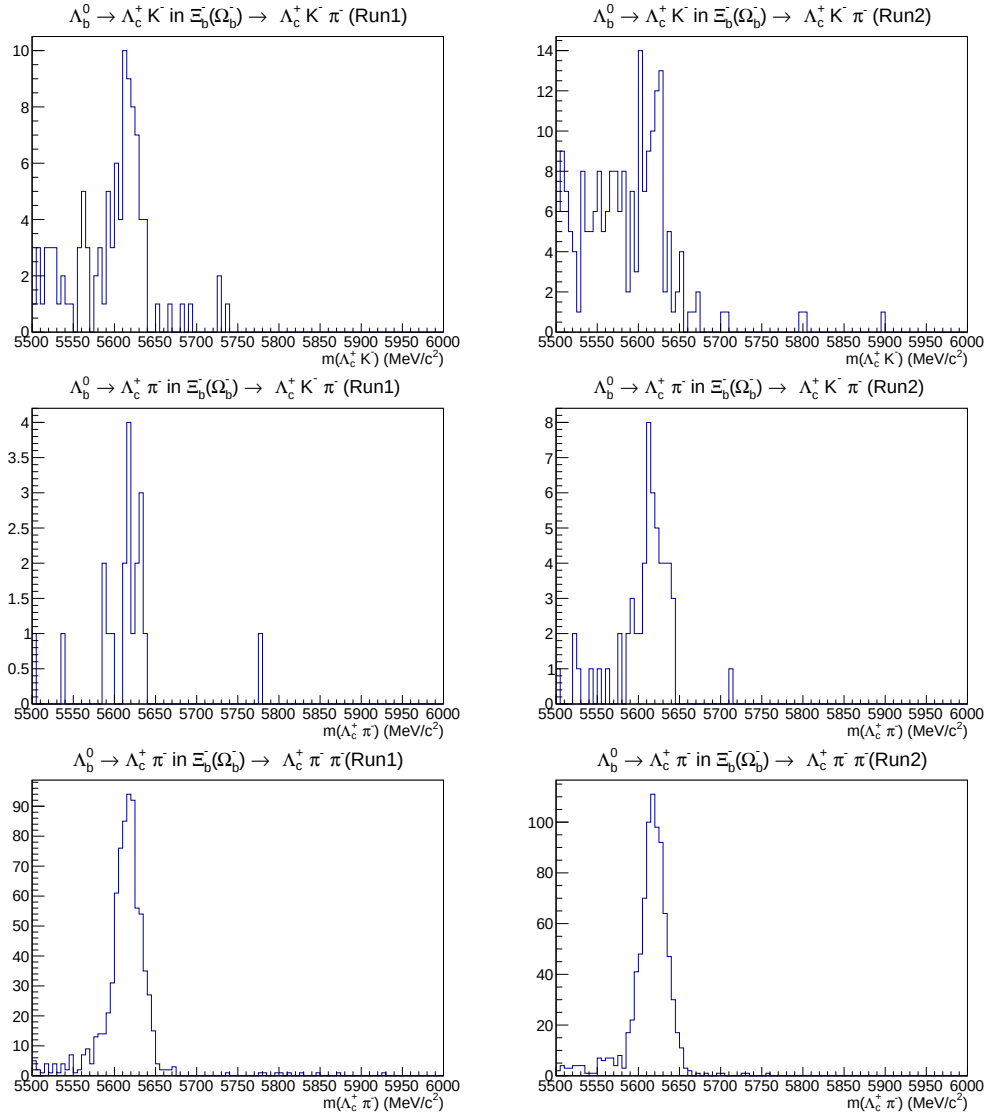

Figure 4.12: Two-body $\Lambda_c^+ K^-$ and $\Lambda_c^+ \pi^-$ mass combinations in the high X_b mass sideband region of the signal modes. Top: $m(\Lambda_c^+ K^-)$ from the $\Lambda_c^+ K^- \pi^-$ sample; middle: $m(\Lambda_c^+ \pi^-)$ from the $\Lambda_c^+ K^- \pi^-$ sample; bottom: $m(\Lambda_c^+ \pi^-)$ from the $\Lambda_c^+ \pi^- \pi^-$ sample; all for (left) Run I and (right) Run II.

Table 4.7: Summary of offline selections. The requirement labelled † is applied in the $\Lambda_c^+ K^- \pi^-$ and $\Lambda_c^+ \bar{p} K^-$ final states only; that labelled ‡ is applied in the $\Lambda_c^+ \pi^- \pi^-$ and $\Lambda_c^+ K^- \pi^-$ final states only; that labelled $*$ is applied in the $\Lambda_c^+ K^- \pi^-$ final state only.

	Run I	Run II
X_c	BDT1 > 0.2	BDT1 > 0.2
X_b	BDT2 > 0.85	BDT2 > 0.9
kaons	$r_K^2 > 1.3225$	$r_K^2 > 1.44$
pions	$r_\pi^2 < 0.2$	$r_\pi^2 < 0.2$
protons	`ProbNNp` > 0.5	`ProbNNp` > 0.5
`isMuon` $== 0$ for all final state tracks		
$2 < \eta < 5$ for all final state tracks		
$2.5 < P_{K,\pi} < 100\,\text{GeV}/c$		
$9.5 < P_p < 100\,\text{GeV}/c$		
Veto $2240 < m(p_{\Lambda_c^+} K^- \pi^+_{\Lambda_c^+}) < 2320\,\text{MeV}/c^2$ †		
Veto $5500 < m(\Lambda_c^+ \pi^-) < 5700\,\text{MeV}/c^2$ ‡		
Veto $5500 < m(\Lambda_c^+ K^-) < 5700\,\text{MeV}/c^2$ $*$		
$\log(1 - \cos(\theta_{hh})) > -10$		

Table 4.8: Number of candidates retained after the above selection criteria, excluding signal mode candidates in the blinded regions.

Decay	Yields	
	Run I	Run II
$B^- \to \Lambda_c^+ \bar{p} \pi^-$	2299	9707
$B^- \to \Lambda_c^+ \bar{p} K^-$	128	512
$\Xi_b^- (\Omega_b^-) \to \Lambda_c^+ K^- K^-$	40	123
$\Xi_b^- (\Omega_b^-) \to \Lambda_c^+ K^- \pi^-$	529	1474
$\Xi_b^- (\Omega_b^-) \to \Lambda_c^+ \pi^- \pi^-$	850	720

Chapter 5

Invariant mass modelling and backgrounds

Once the candidates are selected, the aim is to determine, statistically, the number of signal decays in the selected samples. This is achieved by performing the fits that are described in this chapter. The fits are performed simultaneously so as to be able to share some common parameters as discussed in Section 5.2. They are performed separately for signal and control channels and independently for Run I and Run II. The distributions will contain signal and background components, the shapes of which are modelled using Monte Carlo simulation. The different components and their characterisation are discussed in the sections below.

5.1 MC models for the signal and background components

5.1.1 Signal mass shapes

The signal components are modelled from the truth-matched MC. In high-energy physics, it is common to use the Crystal Ball function [98] to model the invariant mass distribution of processes that may be affected by final state radiation. This function consists of a Gaussian combined with a power-law tail as formulated in Equation (5.1).

$$
\begin{aligned}
f(a,n,\bar{x},\sigma) &= N \begin{cases} e^{-\frac{(x-\bar{x})^2}{2\sigma^2}}, & \text{if } \frac{x-\bar{x}}{\sigma} > -a \\ A(B-\frac{x-\bar{x}}{\sigma})^{-n}, & \text{otherwise} \end{cases} \\
A &= (\frac{n}{|a|})^n \\
B &= \frac{n}{|a|} - |a| \\
N &= \frac{1}{\sigma(C+D)} \\
C &= \frac{n}{|a|}\frac{1}{n-1}e^{-\frac{|a|^2}{2}} \\
D &= \sqrt{\frac{\pi}{2}}(1+\text{erf}(\frac{|\text{a}|}{\sqrt{2}}))
\end{aligned}
\tag{5.1}
$$

We use the sum of two Crystal-Ball functions which have a common peak position and width, but independent power-law tails on each side of the peak. The PDF for the combined function can be defined as

$$
\mathcal{P}_{(\text{sig})}(m) = (1.0 - \text{Frac}) \times \text{ CB}(\text{m}; \text{m}_\text{B}, \sigma, \text{a1}, \text{n1}) + \text{Frac} \times \text{ CB}(\text{m}; \text{m}_\text{B}, \sigma, \text{a2}, \text{n2}). \tag{5.2}
$$

The parameter `Frac` depicts the fraction between the area of each Crystal Ball functions. The model parameters are obtained by fitting the MC and are summarised in Table 5.1 and Table 5.2. The results of the fits are shown in Figure 5.1, Figure 5.2 and Figure 5.3.

5.1.2 Combinatorial background

Combinatorial background contributes to every decay channel. It occurs due to random combinations of particles. We model this empirically using an exponential function, where the shape parameter is determined from the fits to the data. This component is the dominant background in the high mass region of the invariant mass distribution, where the contribution from the other backgrounds is rare.

5.1.3 Partially reconstructed background

Another common source of backgrounds is due to partially reconstructed decays in which a particle from a background decay process is not included in the reconstruction. The possible partially reconstructed backgrounds are listed below.

1. $\Xi_b^- \to \Sigma_c^+ h^- h'^-$ with $\Sigma_c^+ \to \Lambda_c^+ \pi^0$:

Table 5.1: Results of fits to simulated samples of $\Xi_b^-(\Omega_b^-) \to \Lambda_c^+ h^- h'^-$ decays. Units of MeV/c^2 for the peak and width parameters are implied.

	$\Xi_b^- \to \Lambda_c^+ K^- K^-$	$\Xi_b^- \to \Lambda_c^+ K^- \pi^-$	$\Xi_b^- \to \Lambda_c^+ \pi^- \pi^-$
		Run I	
a_1	1.08 ± 0.19	1.39 ± 0.13	0.63 ± 0.06
a_2	-2.05 ± 0.06	-1.89 ± 0.08	-2.02 ± 0.03
Frac	0.20 ± 0.05	0.44 ± 0.08	0.19 ± 0.02
Peak	5795.53 ± 0.06	5795.39 ± 0.06	5795.37 ± 0.05
n_1	2.32 ± 0.18	2.07 ± 0.08	2.82 ± 0.17
n_2	3.77 ± 0.26	3.10 ± 0.15	3.00 ± 0.11
Width	11.29 ± 0.05	12.09 ± 0.05	12.97 ± 0.05
		Run II	
a_1	1.33 ± 0.08	1.08 ± 0.07	0.90 ± 0.06
a_2	-2.04 ± 0.04	-2.00 ± 0.03	-1.99 ± 0.03
Frac	0.29 ± 0.03	0.27 ± 0.03	0.23 ± 0.02
Peak	5795.91 ± 0.03	5795.81 ± 0.03	5795.70 ± 0.03
n_1	2.17 ± 0.06	2.28 ± 0.07	2.39 ± 0.08
n_2	3.56 ± 0.14	3.59 ± 0.12	3.63 ± 0.11
Width	11.13 ± 0.03	11.90 ± 0.03	12.73 ± 0.03
	$\Omega_b^- \to \Lambda_c^+ K^- K^-$	$\Omega_b^- \to \Lambda_c^+ K^- \pi^-$	$\Omega_b^- \to \Lambda_c^+ \pi^- \pi^-$
		Run I	
a_1	1.02 ± 0.16	0.97 ± 0.12	0.78 ± 0.08
a_2	-2.03 ± 0.05	-2.11 ± 0.05	-1.99 ± 0.04
Frac	0.19 ± 0.04	0.24 ± 0.04	0.25 ± 0.03
Peak	6071.68 ± 0.07	6071.62 ± 0.06	6071.49 ± 0.06
n_1	2.21 ± 0.13	2.21 ± 0.11	2.43 ± 0.11
n_2	3.93 ± 0.29	2.86 ± 0.14	2.78 ± 0.11
Width	12.15 ± 0.06	12.97 ± 0.06	13.63 ± 0.06
		Run II	
a_1	1.32 ± 0.09	0.92 ± 0.09	0.74 ± 0.05
a_2	-2.05 ± 0.04	-2.02 ± 0.04	-2.06 ± 0.03
Frac	0.29 ± 0.04	0.21 ± 0.03	0.22 ± 0.02
Peak	6072.11 ± 0.04	6071.98 ± 0.04	6071.96 ± 0.04
n_1	2.07 ± 0.06	2.27 ± 0.09	2.47 ± 0.08
n_2	3.29 ± 0.14	3.66 ± 0.15	3.28 ± 0.11
Width	11.93 ± 0.04	12.65 ± 0.04	13.54 ± 0.04

Since the neutral pion of this decay is not included during the reconstruction, such decays can act as backgrounds to the Ξ_b^- modes. This shifts the invariant mass of the X_b candidate to lower values. The differences between the ${\Sigma_c}^+$ and Λ_c^+ baryon masses is $\approx 167\,\text{MeV}/c^2$ [93]. Hence the momentum carried away by the emitted pion is relatively low ($\approx 90\,\text{MeV}/c^2$). This explains that the shift in the X_b mass distribution will be slightly greater than the mass of the pion. The possibility of such backgrounds in all the three final

Table 5.2: Results of fits to simulated samples of control mode $B^- \to \Lambda_c^+ \bar{p} h^-$ decays. Units of MeV/c^2 for the peak and width parameters are implied.

	$\Lambda_c^+ \bar{p} K^-$	$\Lambda_c^+ \bar{p} \pi^-$
	Run I	
a_1	1.55 ± 0.09	1.17 ± 0.10
a_2	-1.94 ± 0.06	-1.88 ± 0.04
Frac	0.39 ± 0.06	0.29 ± 0.04
Peak	5279.66 ± 0.04	5279.58 ± 0.04
n_1	2.35 ± 0.08	2.34 ± 0.09
n_2	3.15 ± 0.16	3.38 ± 0.14
Width	8.68 ± 0.04	9.51 ± 0.04
	Run II	
a_1	1.51 ± 0.06	1.37 ± 0.06
a_2	-1.89 ± 0.03	-1.85 ± 0.03
Frac	0.37 ± 0.04	0.39 ± 0.03
Peak	5279.80 ± 0.02	5279.86 ± 0.03
n_1	2.29 ± 0.05	2.27 ± 0.05
n_2	2.97 ± 0.07	2.96 ± 0.07
Width	8.50 ± 0.02	9.49 ± 0.02

states of the Ξ_b^- channels is considered. Figure 5.4 shows fits to backgrounds which are produced from MC samples using `RapidSim` [92] and modelled with a `RooKeysPDF` function, which is a superposition of Gaussian kernels.

2. $\Xi_b^0 \to \Sigma_c^{++} h^- h'^-$ with $\Sigma_c^{++} \to \Lambda_c^+ \pi^+$: These backgrounds are similar to the previous ones except that the missing pion is charged instead of being neutral. The X_b mass distribution appears exactly the same as before. Hence, both backgrounds can be accommodated in the same shape for all three final states.

3. Λ_b^0 decays : Decays like $\Lambda_b^0 \to \Lambda_c^+ \pi^+ \pi^- \pi^-$ [99, 100] and $\Lambda_b^0 \to \Lambda_c^+ K^+ K^- \pi^-$ [101] could potentially act as possible backgrounds to our Ξ_b^- decays. But, given that the Λ_b^0 mass is significantly less than that of the Ξ_b^- baryon, we do not expect such decays to contribute in the chosen fit range for data as discussed in Section 5.2.

4. $\Xi_b \to \Lambda_c^+ h^- h'^- \pi$: Such decays not proceeding through the Σ_c resonance could be another possible background contribution when the pion is not reconstructed. The distribution of such background generated through `RapidSim`, is shown in Figure 5.5. It can be seen from the figure that the shape of the background that enters the fit range is the same as that populated by the $\Xi_b^- \to \Sigma_c^+ h^- h'^-$ with $\Sigma_c^+ \to \Lambda_c^+ \pi^0$ and $\Xi_b^0 \to \Sigma_c^{++} h^- h'^-$ with $\Sigma_c^{++} \to \Lambda_c^+ \pi^+$ decays. This tells that it is already accounted for through the modelling of the other decays.

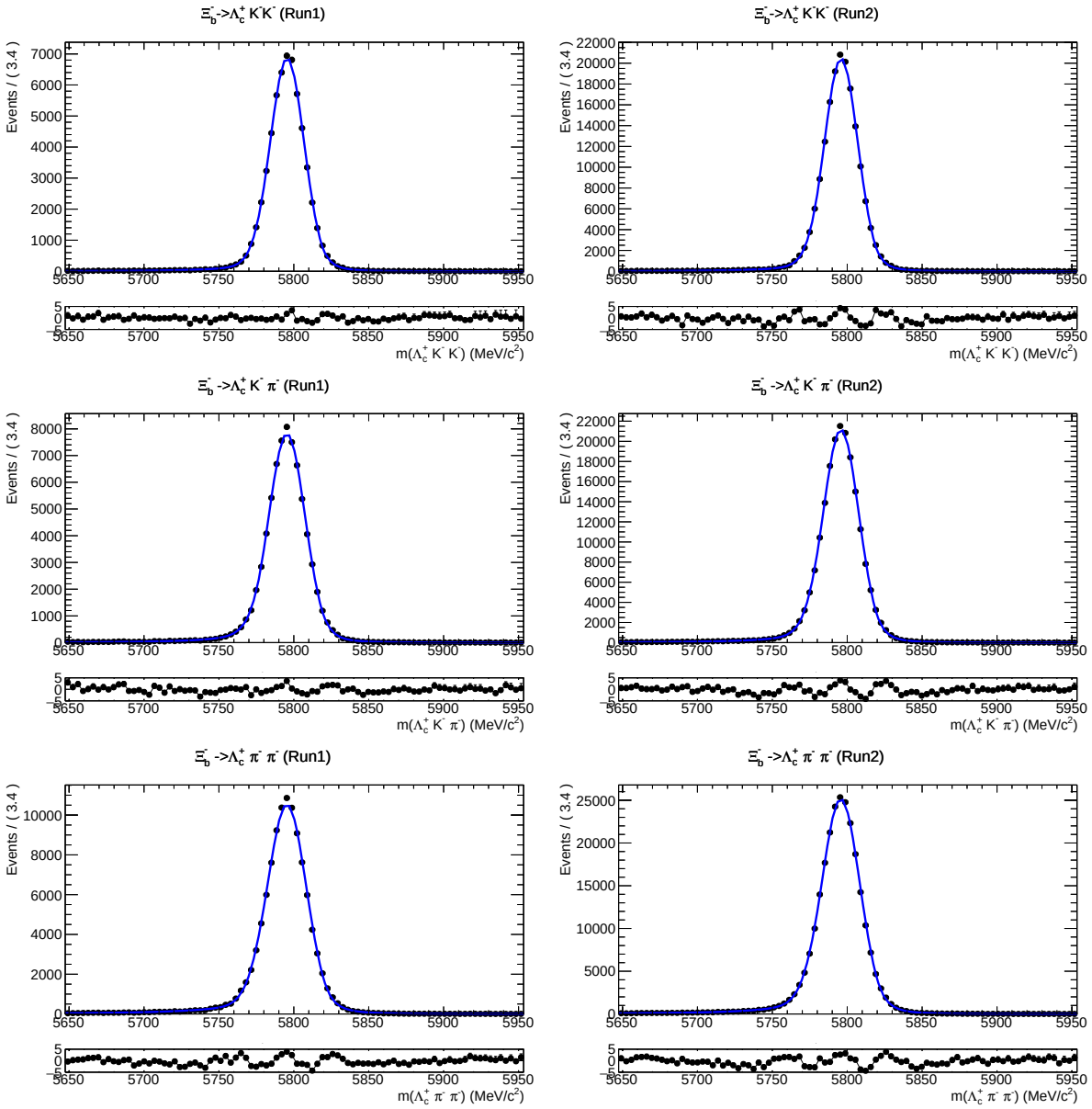

Figure 5.1: Fits to the X_b candidate invariant mass distribution in simulated samples, for (top) $\Xi_b^- \to \Lambda_c^+ K^- K^-$, (middle) $\Xi_b^- \to \Lambda_c^+ K^- \pi^-$, (bottom) $\Xi_b^- \to \Lambda_c^+ \pi^- \pi^-$ decays, for (left) Run I (left) and (right) Run II. The simulated data is shown in black and the fit result as the blue line.

5. $\Omega_b^- \to \Sigma_c^+ h^- h'^-$ with $\Sigma_c^+ \to \Lambda_c^+ \pi^0$: Such Ω_b^- decays with a missing pion could also be a possible source of background. However, we do not expect significant yields from Ω_b^- channels and no excess is seen in the data, in the mass region where this background would contribute. Thus such contributions are considered to be negligible.

Partially reconstructed backgrounds can also be present in the control channels, par-

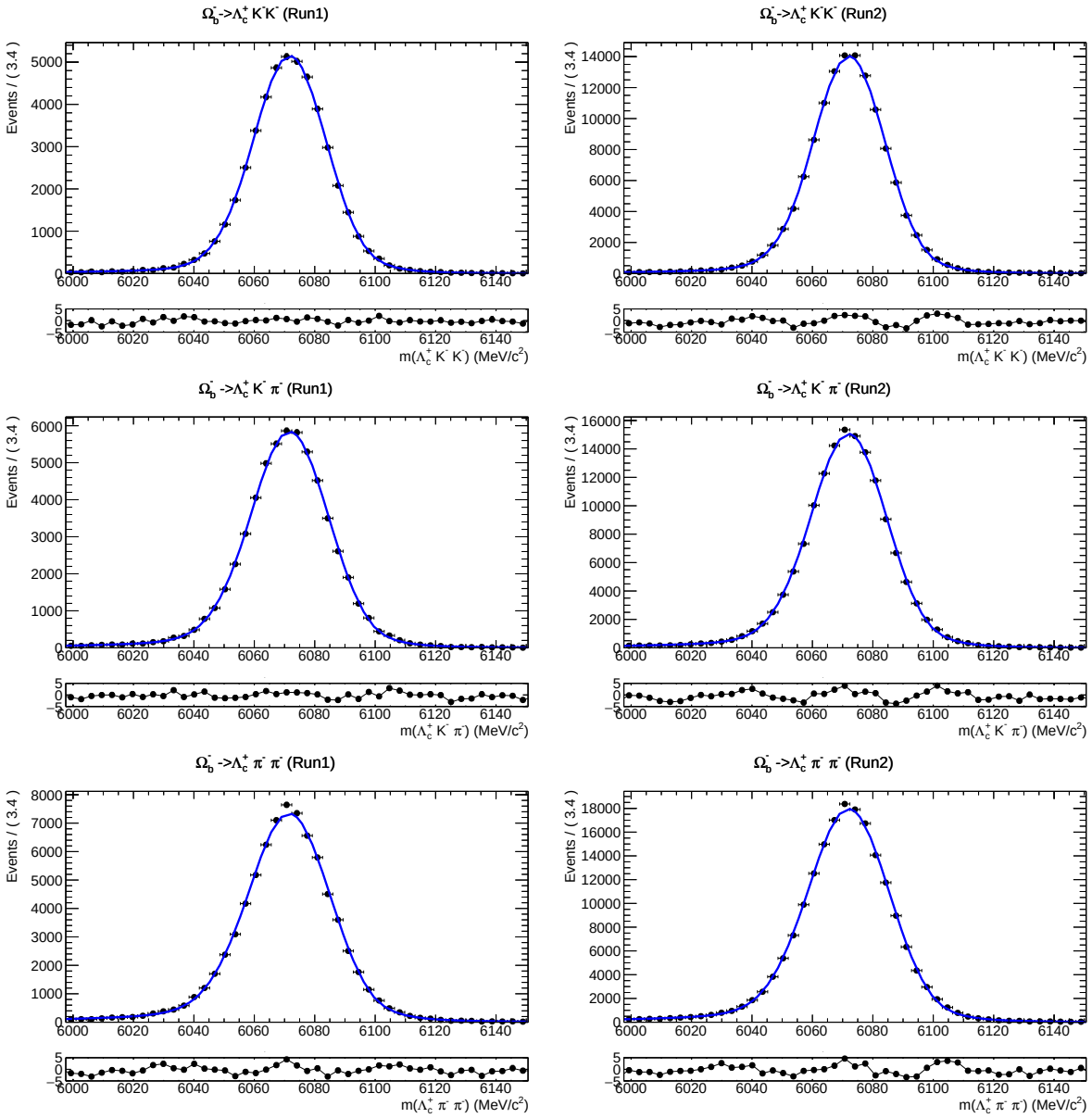

Figure 5.2: Fits to the X_b candidate invariant mass distribution in simulated samples, for (top) $\Omega_b^- \to \Lambda_c^+ K^- K^-$, (middle) $\Omega_b^- \to \Lambda_c^+ K^- \pi^-$, (bottom) $\Omega_b^- \to \Lambda_c^+ \pi^- \pi^-$ decays, for (left) Run I and (right) Run II. The simulated data are shown in black and the fit result as the blue line.

ticularly from $B^- \to \Sigma_c^+ \overline{p} h^-$ and $B^0 \to \Sigma_c^{++} \overline{p} h^-$ with $\Sigma_c^+ \to \Lambda_c^+ \pi^0$ and $\Sigma_c^{++} \to \Lambda_c^+ \pi^+$ and the pion not included in the reconstruction. However, since these components are shifted to lower mass, they can be excluded by appropriately choosing the mass fit range of the data as 5200–6800 MeV/c^2.

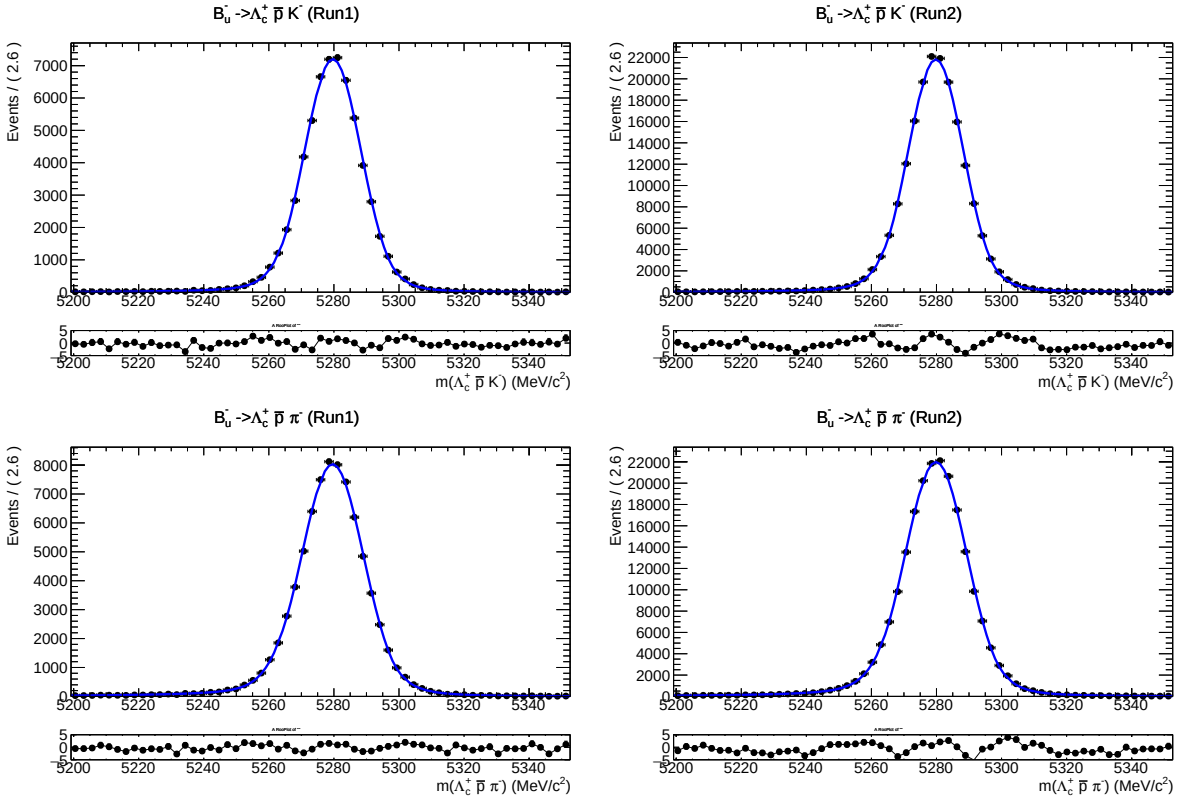

Figure 5.3: Fits to the X_b candidate invariant mass distribution in simulated samples, for the control channels (top) $B^- \to \Lambda_c^+ \overline{p} K^-$ and (bottom) $B^- \to \Lambda_c^+ \overline{p} \pi^-$, for (left) Run I and (right) Run II. The simulated data are shown in black and the fit result as the blue line.

5.1.4 Cross-feed background

In the decays under study, a kaon can be mis-identified as a pion and vice versa. This gives rise to the possibility of one signal channel acting as a background to another signal channel due to mis-identification of the final state particles. Such backgrounds are referred to as cross-feed backgrounds, and they are studied using simulation. The shapes of these backgrounds depend on the momentum of the particle that is being mis-identified. Hence, the Dalitz plot distribution of the decay which is being mis-identified affects the shape of the cross-feed backgrounds. Thus, before modelling such backgrounds the shapes of the cross-feed backgrounds are corrected by weighting to match the Dalitz plot distribution that is observed in data. This weighting is done only for the fits of the B meson modes as they are not blinded and therefore the information about the Dalitz plot distribution is available. We do not perform the weighting in the fits to the b baryons modes as the signals are blinded and therefore, we do not have any information about the Dalitz plot distributions. This weighting is then considered as a source of systematic uncertainty after we unblind the fits.

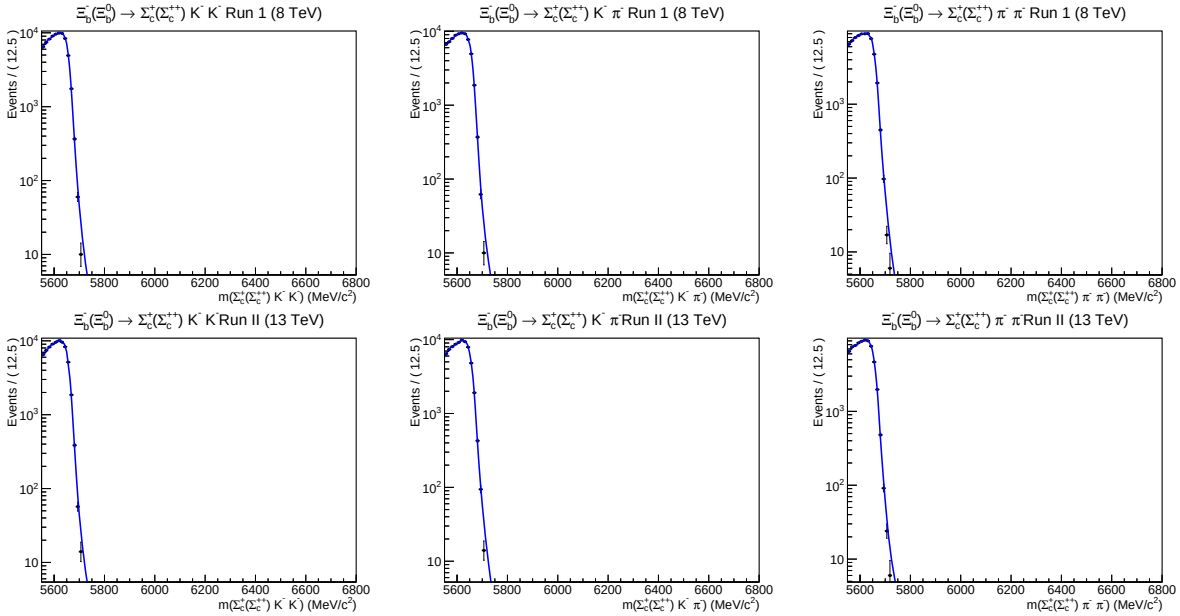

Figure 5.4: Fit to the partially reconstructed backgrounds to (left) $\Xi_b^- \to \Lambda_c^+ K^- K^-$, (middle) $\Xi_b^- \to \Lambda_c^+ K^- \pi^-$ and (right) $\Xi_b^- \to \Lambda_c^+ \pi^- \pi^-$ decays from the $\Xi_b^- \to \Sigma_c^+ K^- K^-$, $\Xi_b^- \to \Sigma_c^+ K^- \pi^-$ and $\Xi_b^- \to \Sigma_c^+ \pi^- \pi^-$ modes, respectively for Run I and Run II.

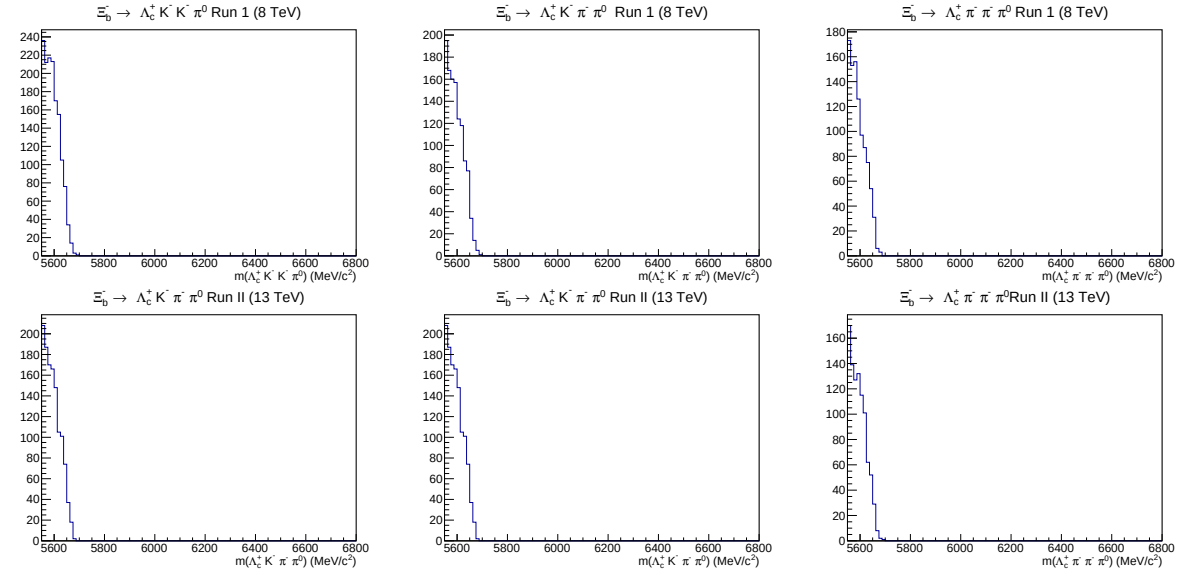

Figure 5.5: Partially reconstructed backgrounds to (left) $\Xi_b^- \to \Lambda_c^+ K^- K^-$, (middle) $\Xi_b^- \to \Lambda_c^+ K^- \pi^-$ and (right) $\Xi_b^- \to \Lambda_c^+ \pi^- \pi^-$ decays from the $\Xi_b^- \to \Lambda_c^+ K^- K^- \pi^0$, $\Xi_b^- \to \Lambda_c^+ K^- \pi^- \pi^0$ and $\Xi_b^- \to \Lambda_c^+ \pi^- \pi^- \pi^0$ modes, respectively for Run I and Run II.

For all possible cross-feed backgrounds, the shape is modelled with a double Crystal-Ball function using simulation. The results for misidentified Ξ_b^- (Ω_b^-) $\to \Lambda_c^+ K^- K^-$ decays are shown in Figure 5.6; for misidentified Ξ_b^- (Ω_b^-) $\to \Lambda_c^+ K^- \pi^-$ decays they are presented in Figure 5.7;

whereas for misidentified Ξ_b^- (Ω_b^-) $\to \Lambda_c^+\pi^-\pi^-$ decays they are shown in Figure 5.8. Similarly, the results for misidentified $B^- \to \Lambda_c^+\bar{p}K^-$ decays are shown in Figure 5.9; whereas those for misidentified $B^- \to \Lambda_c^+\bar{p}\pi^-$ decays are presented in Figure 5.10. There is also a possibility that both the final state particles originating from the b hadron are mis-identified simultaneously. The rate for such double mis-identification is very low, so these backgrounds are expected to be negligible and hence are not included in the baseline fit to the data. Since the kaon identification is sufficiently tight there is no mis-identified Ξ_b^- (Ω_b^-) $\to \Lambda_c^+\pi^-\pi^-$ background in the $\Lambda_c^+K^-K^-$ final state of the simulation.

The relative yields of the mis-identified channels with respect to the correctly identified channels can be estimated using the PID efficiencies and mis-identification rates. Thus the yields of the mis-identified background components can be constrained in the fit to the data depending upon the yields of the correctly identified mode of the same decay. The formulation for the mis-identified yields is given below for $B^- \to \Lambda_c^+\bar{p}\pi^-$ mis-ID backgrounds in $B^- \to \Lambda_c^+\bar{p}K^-$ for example,

$$\text{misID } B^- \to \Lambda_c^+\bar{p}\pi^- \text{ yield} = \text{correct reco. } B^- \to \Lambda_c^+\bar{p}\pi^- \text{ yield} \times R_B^{\Lambda_c^+\bar{p}\pi \to \Lambda_c^+\bar{p}K}, \quad (5.3)$$

$$\text{where } R_B^{\Lambda_c^+\bar{p}\pi \to \Lambda_c^+\bar{p}K} = \frac{\text{misID rate of } B^- \to \Lambda_c^+\bar{p}\pi^- \text{ as } B^- \to \Lambda_c^+\bar{p}K^-}{\text{PID efficiency for correct reco. } B^- \to \Lambda_c^+\bar{p}\pi^-}. \quad (5.4)$$

All the R_{X_b} factors for different mis-identified components are determined from the simulation and are quoted in Table 5.3. Gaussian constraints are applied to all such factors in the fit to data.

5.1.5 Charmless peaking backgrounds

There is also a possibility of charmless backgrounds occurring, where the Λ_c^+ candidate is not a real Λ_c^+ baryon. This is checked for by selecting events in the Λ_c^+ candidate mass sideband regions, defined as (lower) $m(pK\pi) \leq 2260\,\text{MeV}/c^2$ and (upper) $m(pK\pi) \geq 2310\,\text{MeV}/c^2$, for both signal and control modes. The presence of any peaking structure in the Ξ_b^- mass distribution obtained from the Λ_c^+ sidebands would be a clear indication of the existence of charmless backgrounds. The distributions are shown in Figure 5.11 and Figure 5.12 for the Ξ_b^-(Ω_b^-) candidates and the B^- meson candidates respectively. The sideband data distribution (red) is compared with the nominal data (black) where the signal regions around the Ξ_b^- and Ω_b^- mass peaks are blinded. The figures show no peaks in the sideband distributions and therefore such backgrounds are considered to be negligible.

Table 5.3: R_{Xb} factors that have been used as Gaussian constraints in the fit.

	Run I	Run II
Ξ_b signal modes ($\times 10^{-2}$)		
$R_{\Xi_b}^{\Lambda_c^+ KK \to \Lambda_c^+ K\pi}$	7.896 ± 0.085	3.637 ± 0.033
$R_{\Xi_b}^{\Lambda_c^+ KK \to \Lambda_c^+ \pi\pi}$	0.616 ± 0.033	0.250 ± 0.012
$R_{\Xi_b}^{\Lambda_c^+ K\pi \to \Lambda_c^+ KK}$	0.709 ± 0.031	0.143 ± 0.008
$R_{\Xi_b}^{\Lambda_c^+ K\pi \to \Lambda_c^+ \pi\pi}$	9.139 ± 0.109	4.453 ± 0.047
$R_{\Xi_b}^{\Lambda_c^+ \pi\pi \to \Lambda_c^+ KK}$	0	0
$R_{\Xi_b}^{\Lambda_c^+ \pi\pi \to \Lambda_c^+ K\pi}$	0.775 ± 0.019	0.168 ± 0.006
Ω_b^- signal modes ($\times 10^{-2}$)		
$R_{\Omega_b^-}^{\Lambda_c^+ KK \to \Lambda_c^+ K\pi}$	9.314 ± 0.102	4.370 ± 0.042
$R_{\Omega_b^-}^{\Lambda_c^+ KK \to \Lambda_c^+ \pi\pi}$	0.869 ± 0.042	0.327 ± 0.016
$R_{\Omega_b^-}^{\Lambda_c^+ K\pi \to \Lambda_c^+ KK}$	0.746 ± 0.035	0.191 ± 0.011
$R_{\Omega_b^-}^{\Lambda_c^+ K\pi \to \Lambda_c^+ \pi\pi}$	10.66 ± 0.131	5.262 ± 0.058
$R_{\Omega_b^-}^{\Lambda_c^+ \pi\pi \to \Lambda_c^+ KK}$	0	0
$R_{\Omega_b^-}^{\Lambda_c^+ \pi\pi \to \Lambda_c^+ K\pi}$	0.766 ± 0.022	0.200 ± 0.007
Control modes ($\times 10^{-2}$)		
$R_B^{\Lambda_c^+ \bar{p}K \to \Lambda_c^+ \bar{p}\pi}$	1.973 ± 0.040	1.124 ± 0.018
$R_B^{\Lambda_c^+ \bar{p}\pi \to \Lambda_c^+ \bar{p}K}$	0.326 ± 0.015	0.062 ± 0.004

5.2 Fits to the data sample

5.2.1 Fit results

As mentioned before, we perform blind fits and check the stability of the fit configuration prior to unblinding as discussed in Section 5.2.2. Once the fit configuration is finalised and shown to be stable, we then unblind the fits.

Unbinned extended maximum likelihood fits are performed with the fit components discussed in previous subsections. One simultaneous fit is performed to all the b baryon modes and a separate simultaneous fit is performed for the two meson modes. This is done in order to be able to constrain the misidentified background yields. The fits are performed independently for Run I and Run II as the two runs have independent MVAs used in the selection and also slightly different trigger conditions. The two meson modes were not blinded unlike the three baryon modes. The yields of the different fit components are considered to be free parameters of the fit, except for those of the cross-feed components which depends on the signal yield of the correctly identified decay as discussed previously. The shapes of the different components that

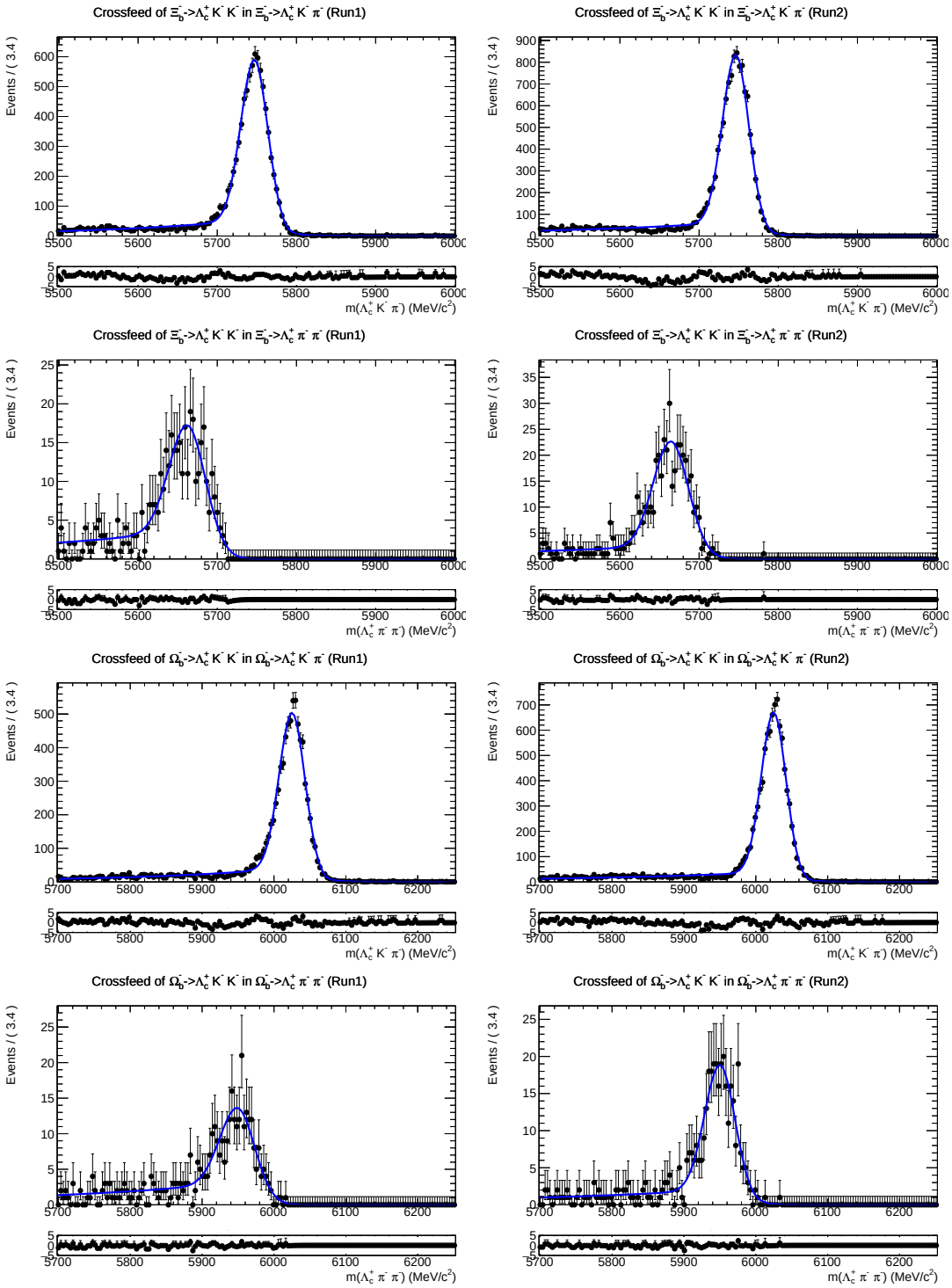

Figure 5.6: Fits to the misidentified background when $\Xi_b^- \to \Lambda_c^+ K^- K^-$ is reconstructed as (top) $\Lambda_c^+ K^- \pi^-$ and (second row) $\Lambda_c^+ \pi^- \pi^-$, for (left) Run I and (right) Run II. Third and bottom rows show similar for $\Omega_b^- \to \Lambda_c^+ K^- K^-$ decays. Simulated data are shown in black and the fit result as the blue line.

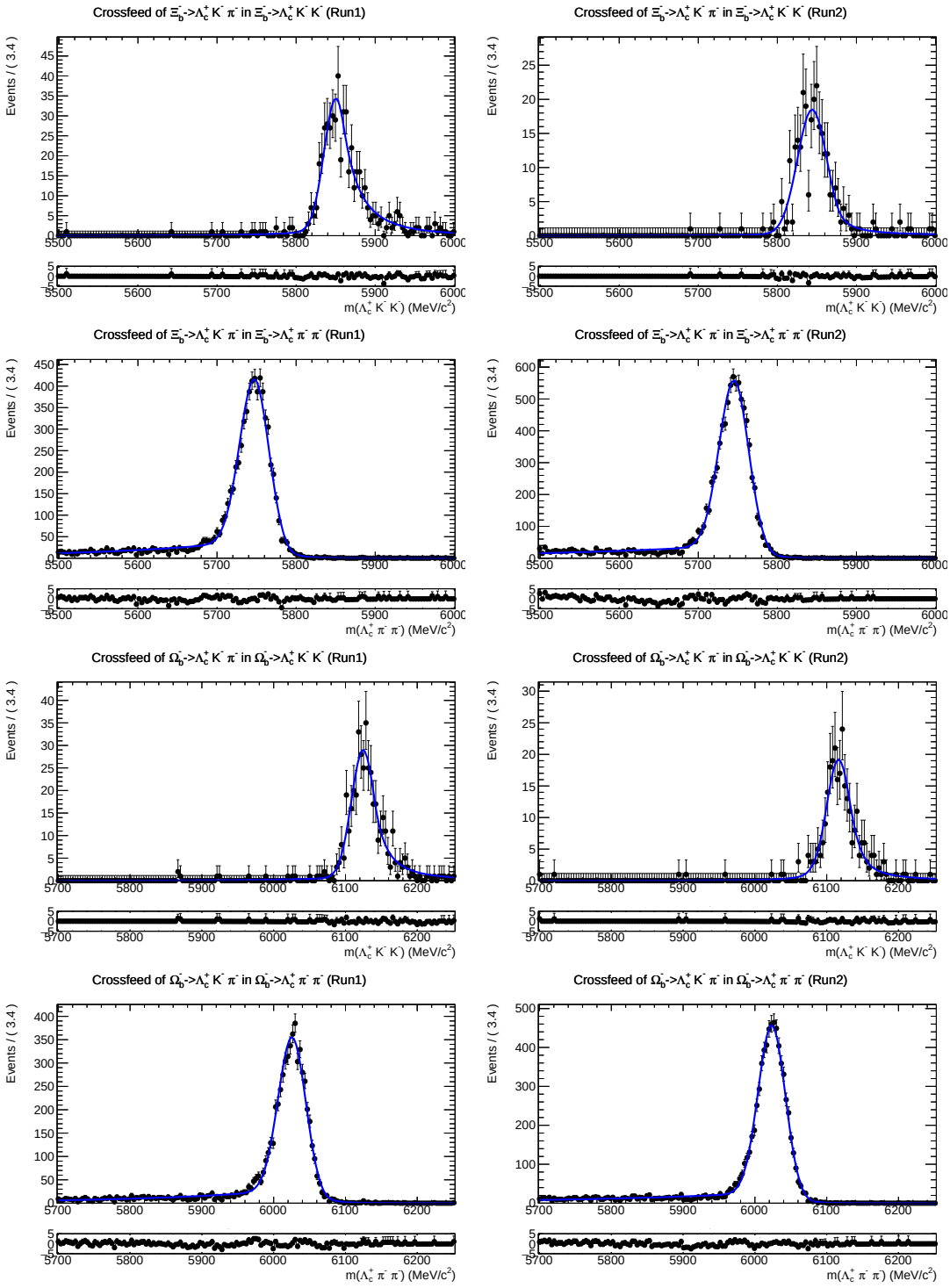

Figure 5.7: Fits to the misidentified background when $\Xi_b^- \to \Lambda_c^+ K^- \pi^-$ is reconstructed as (top) $\Lambda_c^+ K^- K^-$ and (second row) $\Lambda_c^+ \pi^- \pi^-$, for (left) Run I and (right) Run II. Third and bottom rows show similar for $\Omega_b^- \to \Lambda_c^+ K^- \pi^-$ decays. Simulated data are shown in black and the fit result as the blue line.

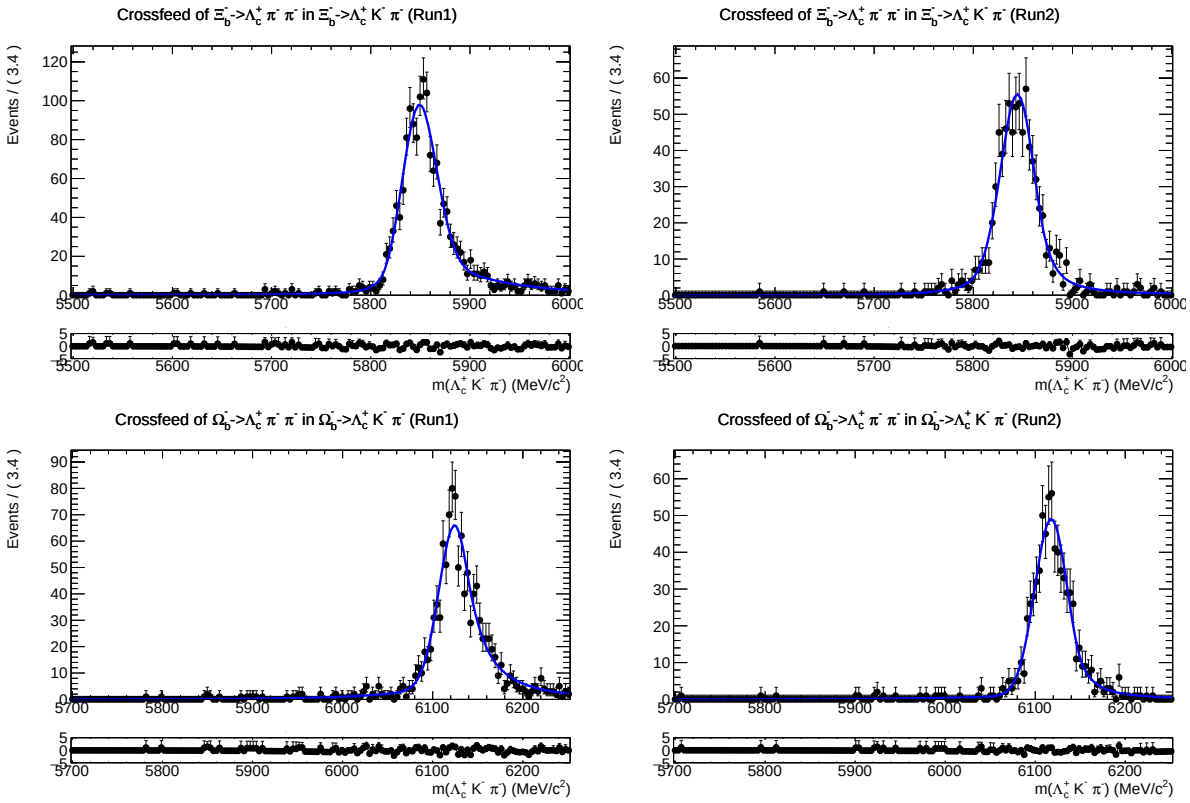

Figure 5.8: Fits to the misidentified background when (top) $\Xi_b^- \to \Lambda_c^+\pi^-\pi^-$ and (bottom) $\Omega_b^- \to \Lambda_c^+\pi^-\pi^-$ are reconstructed as $\Lambda_c^+K^-\pi^-$ for (left) Run I and (right) Run II. The rate for $\Xi_b^- \to \Lambda_c^+\pi^-\pi^-$ and $\Omega_b^- \to \Lambda_c^+\pi^-\pi^-$ to be misidentified as $\Lambda_c^+K^-K^-$ are negligible. Simulated data are shown in black and the fit result as the blue line.

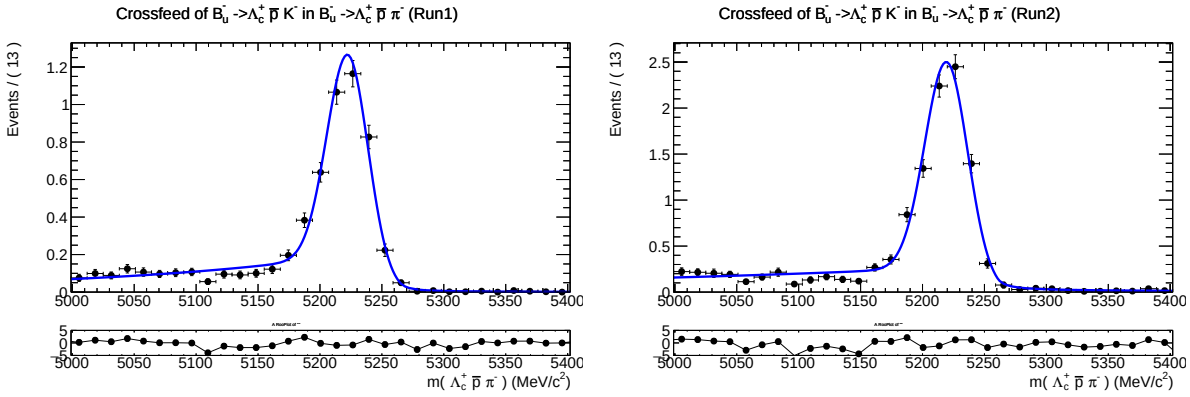

Figure 5.9: Fits to the misidentified background when $B^- \to \Lambda_c^+\bar{p}K^-$ is reconstructed as $B^- \to \Lambda_c^+\bar{p}\pi^-$ for (left) Run I and (right) Run II. Simulation, weighted to the Dalitz plot distribution observed in data, is shown in black and the fit result as the blue line.

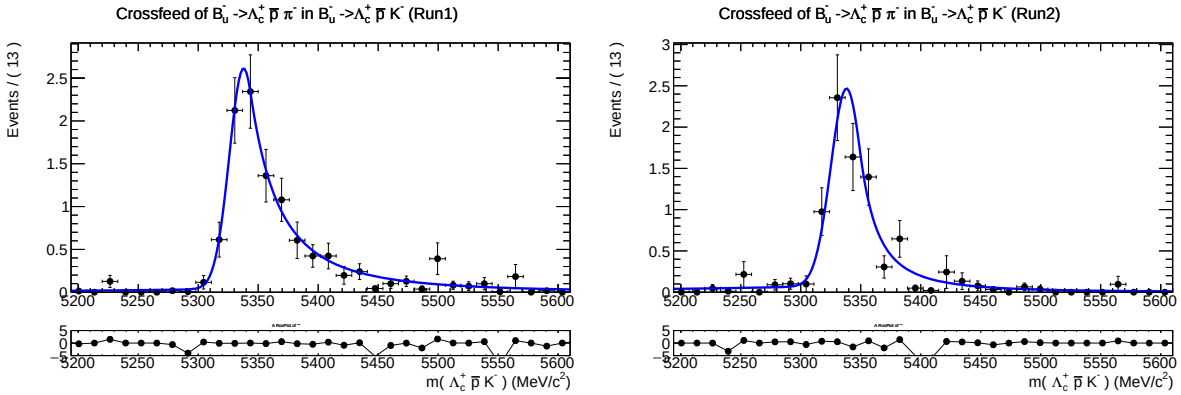

Figure 5.10: Fits to the misidentified background when $B^- \to \Lambda_c^+ \overline{p}\pi^-$ is reconstructed as $B^- \to \Lambda_c^+ \overline{p}K^-$ for (left) Run I and (right) Run II. Simulation, weighted to the Dalitz plot distribution observed in data, is shown in black and the fit result as the blue line.

have been modelled from MC, as discussed in previous subsections, are fixed in the data. This is however not the case with the combinatorial background components where the exponential factor is considered to be a free parameter of the fit which is independent in each final state. Furthermore, the simultaneous fit has additional parameters shared between different components in particular,

- peak offset of the double Crystal-Ball shape (`moffset`);
- width scale factor of the core Crystal-Ball function (`wscale`).

These parameters take into account the differences between the data and MC. This also includes the mis-identified backgrounds but not the partially reconstructed backgrounds from the `RapidSim`, as the data-MC corrections would have negligible impact on those components.

In summary, the different fit components for the b baryon candidates are summarised as :

- $\Lambda_c^+ K^- K^-$
  - Ξ_b^- and Ω_b^- signals
  - cross-feed from $\Xi_b^-(\Omega_b^-) \to \Lambda_c^+ K^- \pi^-$
  - ${\Xi_b}^{-(0)} \to \Sigma_c^{+(++)} K^- K^-$ partially reconstructed background
  - combinatorial background.
- $\Lambda_c^+ K^- \pi^-$
  - Ξ_b^- and Ω_b^- signals
  - cross-feed from $\Xi_b^-(\Omega_b^-) \to \Lambda_c^+ K^- K^-$

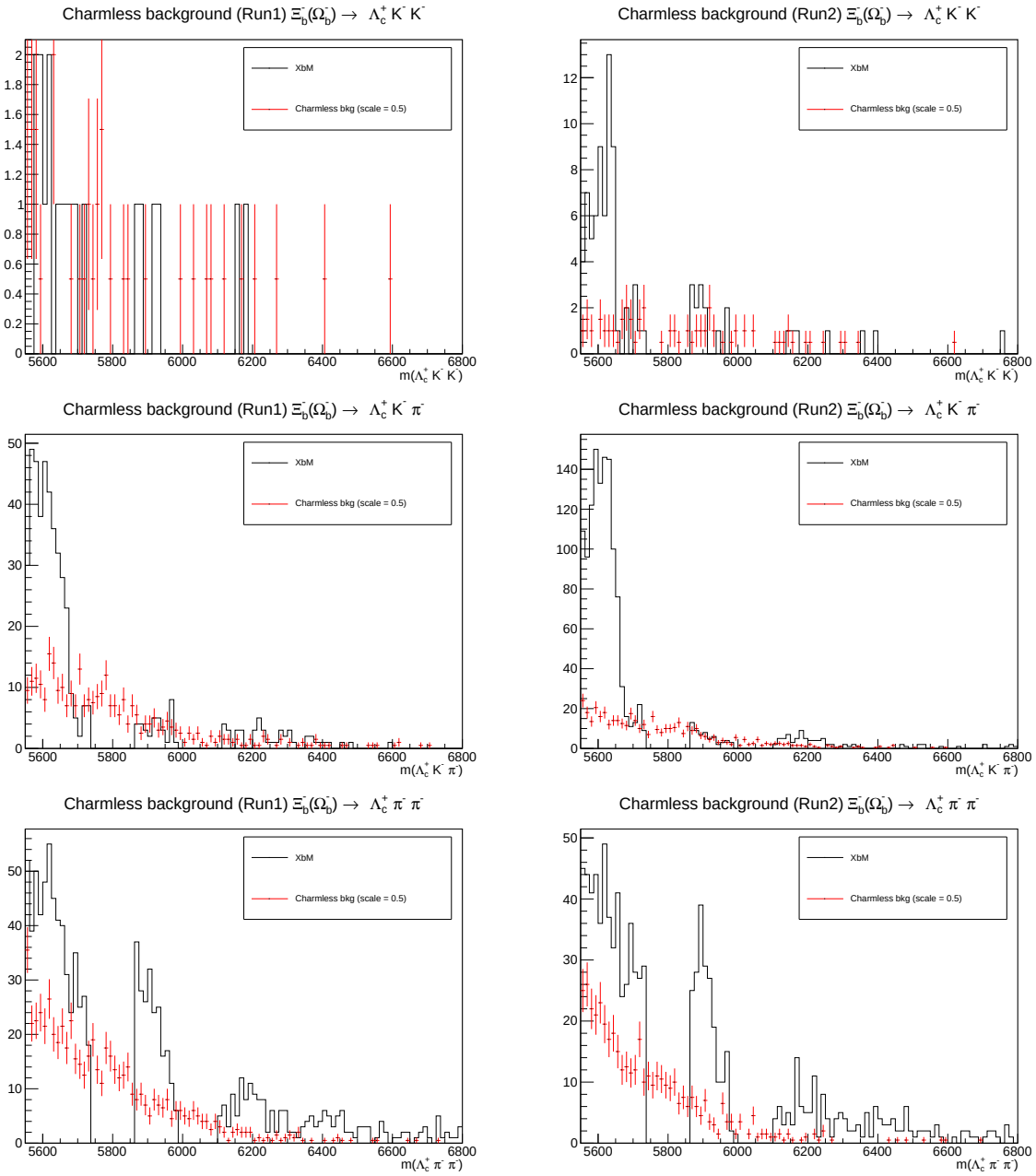

Figure 5.11: Expected pollution from charmless background underneath the charm hadron mass peak (red histogram), estimated from the sidebands of the Λ_c^+ mass distribution, for the (top) $\Xi_b^- \to \Lambda_c^+ K^- K^-$, (centre) $\Xi_b^- \to \Lambda_c^+ K^- \pi^-$ and (bottom) $\Xi_b^- \to \Lambda_c^+ \pi^- \pi^-$ samples, for (left) Run I and (right) Run II samples.

- cross-feed from $\Xi_b^-(\Omega_b^-) \to \Lambda_c^+ \pi^- \pi^-$
- ${\Xi_b}^{-(0)} \to \Sigma_c^{+(++)} K^- \pi^-$ partially reconstructed background
- combinatorial background

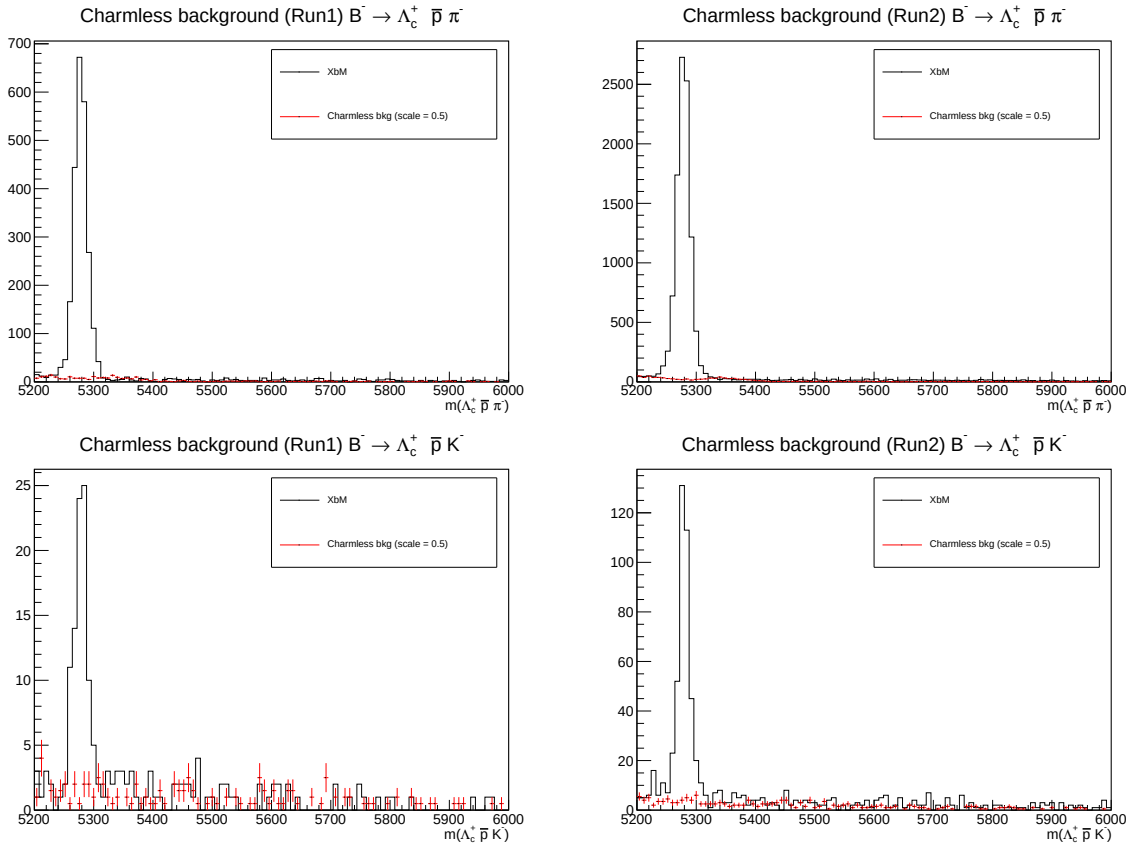

Figure 5.12: Expected pollution from charmless background underneath the charm hadron mass peak (red histogram), estimated from the sidebands of the Λ_c^+ mass distribution, for the control mode (upper) $B^- \to \Lambda_c^+ \bar{p}\pi^-$, and (lower) $B^- \to \Lambda_c^+ \bar{p}K^-$ samples, for (left) Run I and (right) Run II samples.

- $\Lambda_c^+\pi^-\pi^-$
  - Ξ_b^- and Ω_b^- signals
  - cross-feed from $\Xi_b^-(\Omega_b^-) \to \Lambda_c^+ K^-\pi^-$
  - cross-feed from $\Xi_b^-(\Omega_b^-) \to \Lambda_c^+ K^-K^-$
  - ${\Xi_b}^{-(0)} \to \Sigma_c^{+(++)}\pi^-\pi^-$ partially reconstructed background
  - combinatorial background

while the fit components for the B meson candidates are,

- $\Lambda_c^+\bar{p}\pi^-$
  - B^- signal
  - combinatorial background
  - cross-feed from $B^- \to \Lambda_c^+\bar{p}K^-$

- $\Lambda_c^+\overline{p}K^-$
  - B^- signal
  - combinatorial background
  - cross-feed from $B^- \to \Lambda_c^+\overline{p}\pi^-$

It can be concluded from this that there are in total 17 free parameters in the fit to the b baryon decay invariant mass distributions corresponding to 6 signal yields, 3 exponential shape parameters, 3 combinatorial yields, 3 partially reconstructed yields, 1 mean shift and 1 width scale. In addition, there are 10 constrained parameters governing the mis-identified background yields. For the fit to the B meson decay invariant mass distributions there are 8 free parameters corresponding to 2 signal yields, 2 combinatorial background yields, 2 exponential shape parameters, 1 mean shift and 1 width scale. There are also 2 constrained parameters governing the mis-identified background yields.

The results of the fit for the B meson modes can be seen in Figure 5.13 whereas the results of the fit for the b baryon modes can be seen from Figure 5.15, for both Run I and Run II. Figure 5.14 and Figure 5.16 are the log-scale versions of the fits. The residuals between the data points and the fit can be seen from the pulls plotted at the bottom of each fitted distribution. The fit results are given in Table 5.4 and Table 5.5 for the b baryon modes and the B meson modes respectively. The parameter N represents the yields of the given component in the mass fit.

Table 5.4: Results of the simultaneous mass fit to the control modes $B^- \to \Lambda_c^+\overline{p}h^-$. Units of MeV/$c^2$ for the wscale parameters are implied.

	Run I	Run II
$N(B^- \to \Lambda_c^+\overline{p}K^-)$	65.9 ± 8.81	288 ± 18.2
$N(B^- \to \Lambda_c^+\overline{p}\pi^-) \times 10^3$	2.02 ± 0.05	8.41 ± 0.09
$N_{\text{comb bkg}}(B^- \to \Lambda_c^+\overline{p}K^-)$	53.7 ± 8.68	218 ± 16.4
$N_{\text{comb bkg}}(B^- \to \Lambda_c^+\overline{p}\pi^-) \times 10^3$	0.28 ± 0.02	1.29 ± 0.04
$R_B^{\Lambda_c^+\bar{p}K \to \Lambda_c^+\bar{p}\pi} \times 10^{-2}$	1.97 ± 0.04	1.12 ± 0.02
$R_B^{\Lambda_c^+\bar{p}\pi \to \Lambda_c^+\bar{p}K} \times 10^{-3}$	3.28 ± 0.16	0.62 ± 0.04
comb slope $(B^- \to \Lambda_c^+\overline{p}K^-) \times 10^{-3}$	-2.26 ± 0.72	-1.86 ± 0.34
comb slope $(B^- \to \Lambda_c^+\overline{p}\pi^-) \times 10^{-3}$	-1.05 ± 0.33	-1.04 ± 0.15
`moffset`	-1.32 ± 0.26	-1.43 ± 0.13
`wscale`	1.11 ± 0.02	1.12 ± 0.01

5.2.2 Toy studies

Once the fit is finalised, toy studies are performed to check the stability of the fit and look for any biases in the fit parameters. This is done by generating 500 pseudoexperiments from the

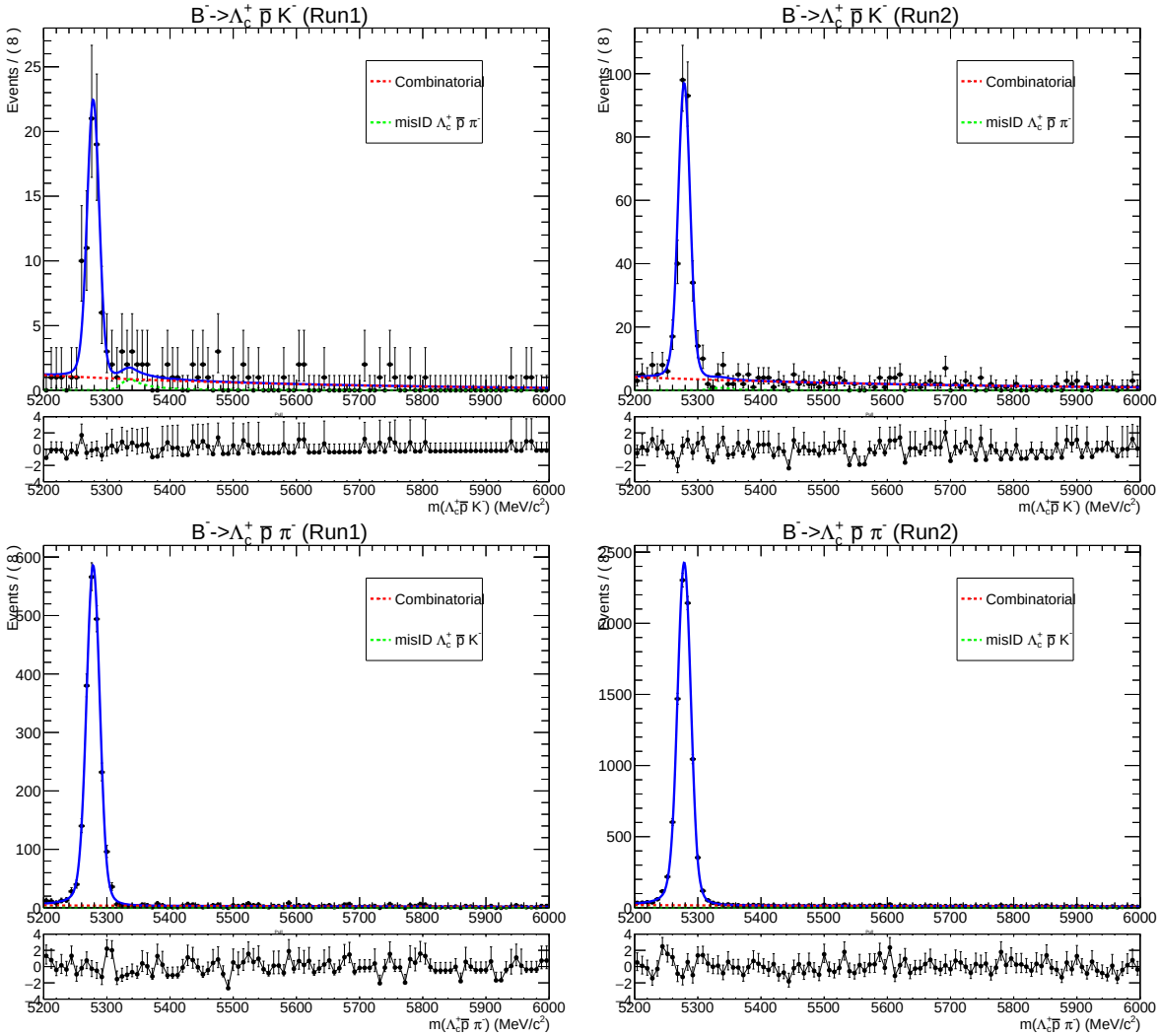

Figure 5.13: Mass fits to the B meson modes (top) $\Lambda_c^+\overline{p}K^-$ and (bottom) $\Lambda_c^+\overline{p}\pi^-$ for (left) Run I and (right) Run II.

result of the fit and then fitting each in the same way as the data. In each pseudoexperiment the yields of the components are sampled from a Poisson distribution. A pull distribution from the 500 pseudoexperiments for each of the signal yield parameters is plotted in Figure 5.17 and Figure 5.18 for the baryon and meson modes respectively. The pulls are defined to be the difference between the generated and the fitted value divided by the fitted uncertainty of the signal yield. Ideally, for a completely stable and unbiased fit we expect the pulls to be distributed normally with mean 0 and width 1. Hence, we fit Gaussian functions to these distributions. The results of the fits are shown in Table 5.6 and Table 5.7 for the baryon and meson modes respectively. The Gaussian fits appear to be reasonably compatible with the expected mean and width. Hence, it can be seen that there are no large biases to the fit parameters and the fit is

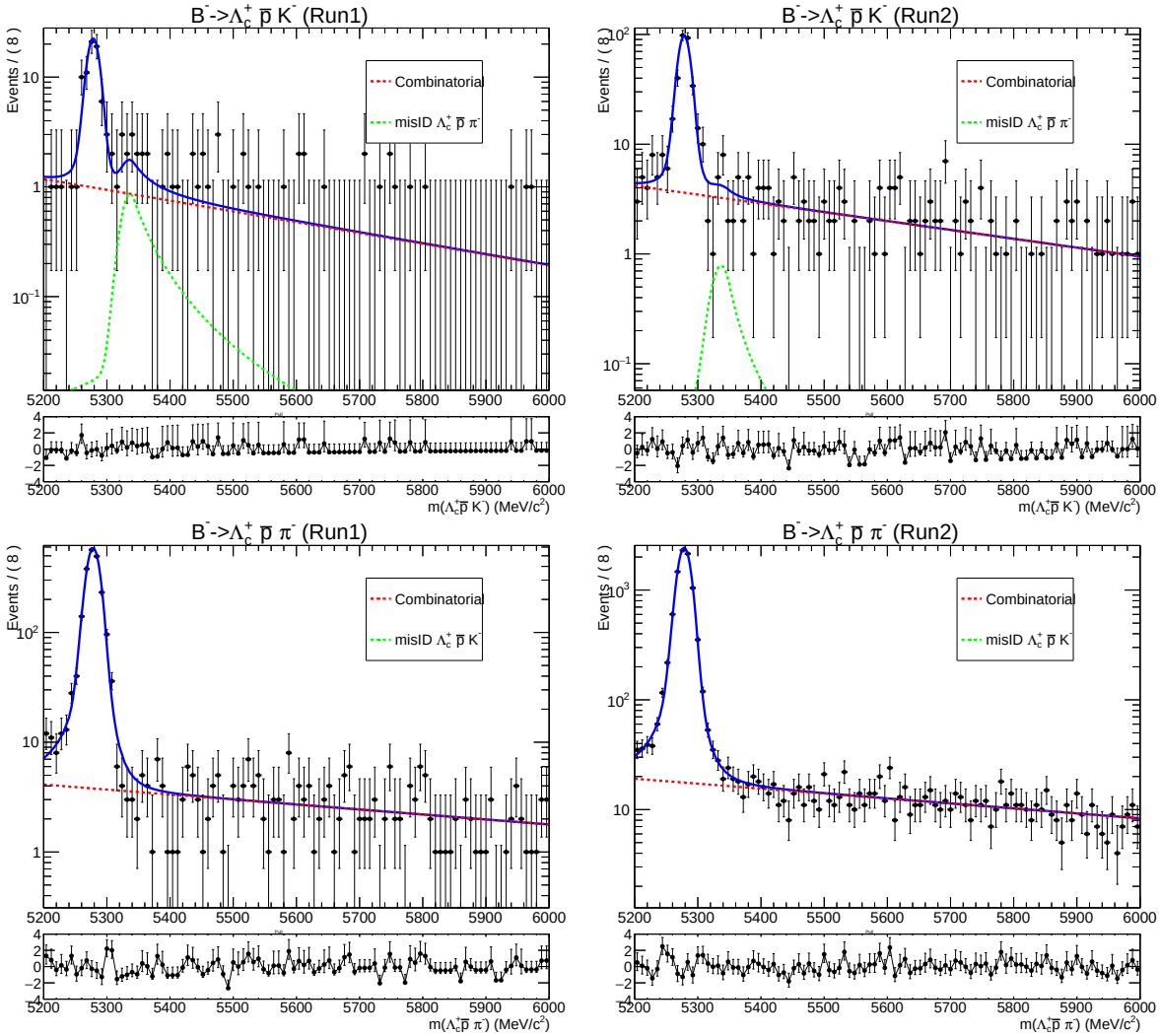

Figure 5.14: Mass fits to the control modes (top) $\Lambda_c^+\overline{p}K^-$ and (bottom) $\Lambda_c^+\overline{p}\pi^-$ for (left) Run I and (right) Run II (log scale).

stable. There are however, small biases seen through the mean deviating from zero. This is however taken into account as a source of systematic uncertainty, which will be discussed later.

5.2.3 Background subtraction

Once a stable fit is obtained, background subtraction can be performed to obtain the signal distributions in variables of interest. We determine a weight for every candidate using the *sPlot* technique [102]. This technique unfolds the data distributions for the signal and background components in such a way that requires that only the yields of the different components are free parameters of the fit, while the shape parameters must be fixed. Yield parameters of some components can be fixed, for example the mis-identified components in this case. Thus the fit is

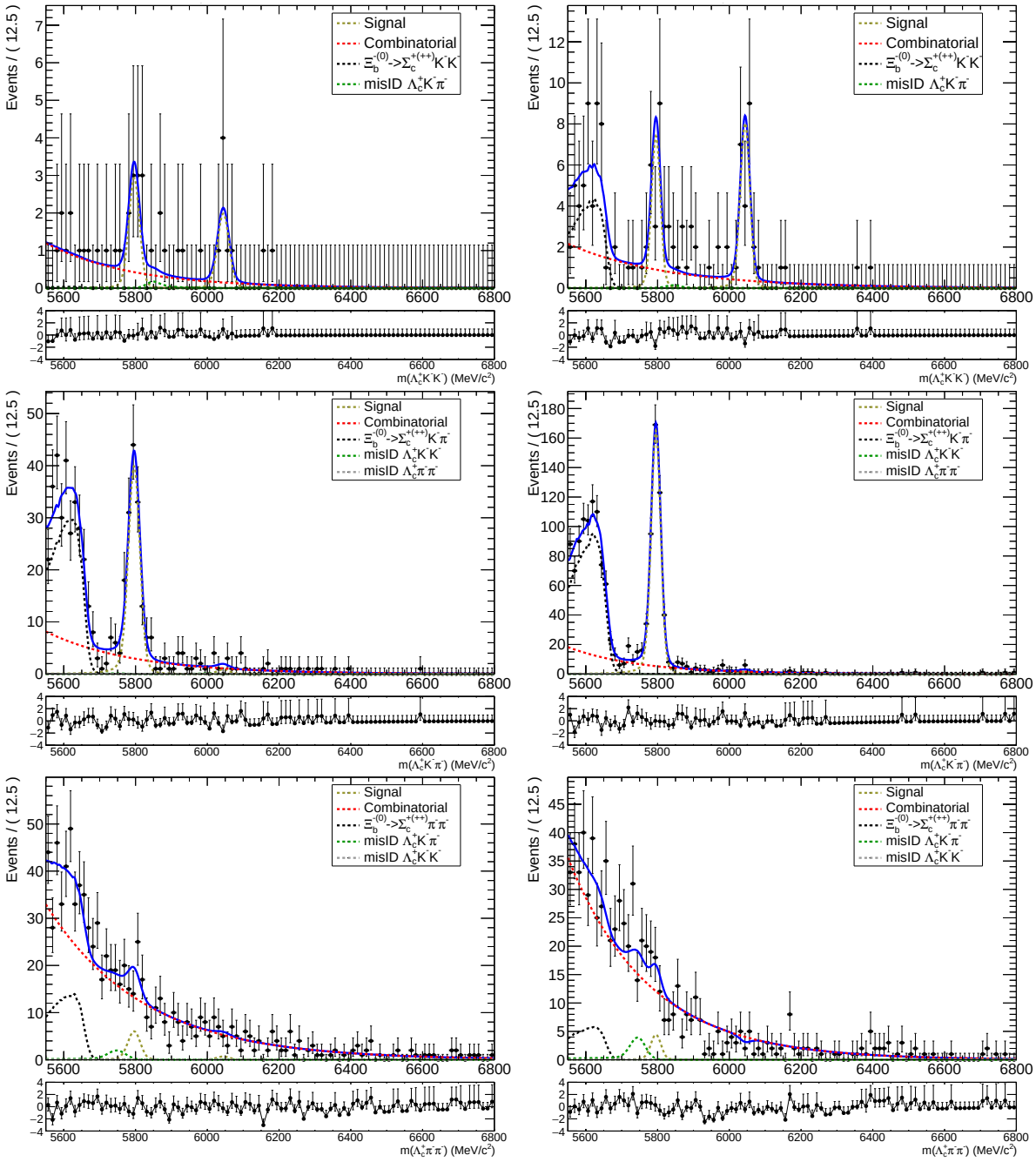

Figure 5.15: Unblinded mass fits to the b baryon channels (top) $\Lambda_c^+ K^- K^-$, (middle) $\Lambda_c^+ K^- \pi^-$ and (bottom) $\Lambda_c^+ \pi^- \pi^-$ for (left) Run I and (right) Run II.

performed separately for each channel after fixing all the shape parameters to the values obtained in the original fit to the data, as well as fixing the yields of the mis-identified backgrounds to the values obtained in the fit. The distributions of the *sWeights* with respect to the b-hadron candidate mass for the B meson modes are shown in Figure 5.19.

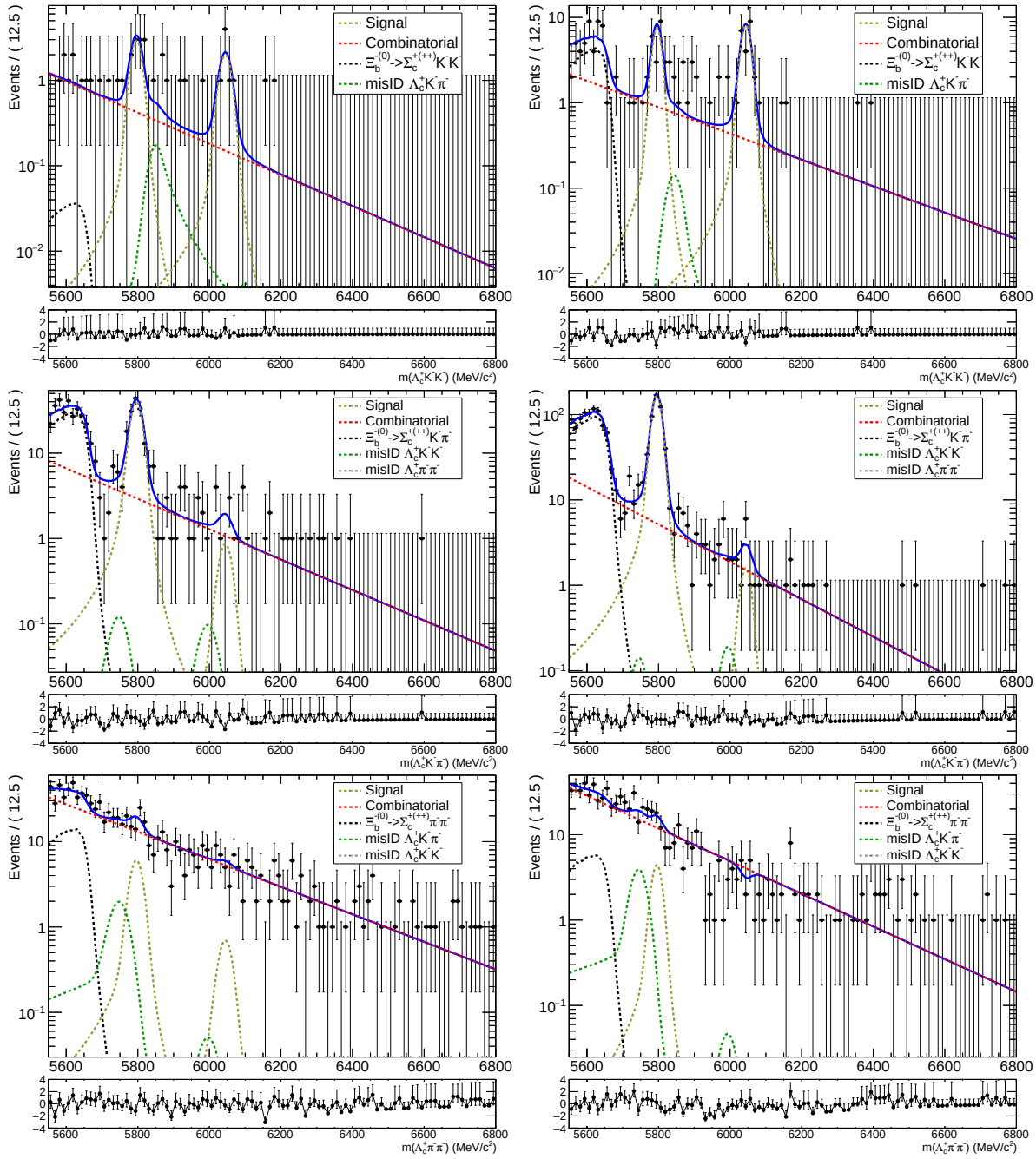

Figure 5.16: Unblinded mass fits to the b baryon channels (top) $\Lambda_c^+ K^- K^-$, (middle) $\Lambda_c^+ K^- \pi^-$ and (bottom) $\Lambda_c^+ \pi^- \pi^-$ for (left) Run I and (right) Run II (log scale).

The most use of this technique in this analysis is to obtain the previously unknown phase space distribution of the signal. This requires that the b-hadron candidate mass should be uncorrelated to the Dalitz plot variables. We make use of the Kendall Rank coefficient to quantify the correlation between the b-candidate invariant mass and the square Dalitz plot variables. This

Table 5.5: unblinded results of the simultaneous mass fits to the $\Lambda_c^+ h^- h'^-$ signal modes.

	Run I	Run II
$N(\Omega_b^- \to \Lambda_c^+ K^- K^-)$	6.71 ± 2.79	22.6 ± 5.15
$N(\Omega_b^- \to \Lambda_c^+ K^- \pi^-)$	3.18 ± 3.39	4.87 ± 3.46
$N(\Omega_b^- \to \Lambda_c^+ \pi^- \pi^-)$	2.77 ± 6.46	-2.99 ± 4.15
$N(\Xi_b^- \to \Lambda_c^+ K^- K^-)$	9.13 ± 3.58	19.4 ± 5.16
$N(\Xi_b^- \to \Lambda_c^+ K^- \pi^-)(\times 10^2)$	1.37 ± 0.14	4.71 ± 0.24
$N(\Xi_b^- \to \Lambda_c^+ \pi^- \pi^-)(\times 10)$	2.27 ± 1.12	1.36 ± 0.93
$N(\Xi_b^- \to \Sigma_c^+ K^- K^-)$	0.27 ± 4.60	32.07 ± 8.44
$N(\Xi_b^- \to \Sigma_c^+ K^- \pi^-)(\times 10^2)$	2.29 ± 0.22	7.11 ± 0.37
$N(\Xi_b^- \to \Sigma_c^+ \pi^- \pi^-)(\times 100)$	1.08 ± 0.29	0.44 ± 0.29
$N_{\text{comb bkg}}(\Xi_b^- \to \Lambda_c^+ K^- K^-)(\times 10)$	2.24 ± 0.75	4.78 ± 1.08
$N_{\text{comb bkg}}(\Xi_b^- \to \Lambda_c^+ K^- \pi^-)(\times 10^2)$	1.58 ± 0.25	2.89 ± 0.36
$N_{\text{comb bkg}}(\Xi_b^- \to \Lambda_c^+ \pi^- \pi^-)(\times 10^2)$	7.04 ± 0.43	6.41 ± 0.42
$R^{\Lambda_c^+ KK \to \Lambda_c^+ K\pi}_{\Omega_b^-}(\times 10^{-2})$	9.31 ± 0.10	4.37 ± 0.04
$R^{\Lambda_c^+ KK \to \Lambda_c^+ \pi\pi}_{\Omega_b^-}(\times 10^{-3})$	8.69 ± 0.42	3.27 ± 0.16
$R^{\Lambda_c^+ K\pi \to \Lambda_c^+ KK}_{\Omega_b^-}(\times 10^{-3})$	7.46 ± 0.35	1.91 ± 0.11
$R^{\Lambda_c^+ K\pi \to \Lambda_c^+ \pi\pi}_{\Omega_b^-}(\times 10^{-1})$	1.07 ± 0.01	0.53 ± 0.00
$R^{\Lambda_c^+ \pi\pi \to \Lambda_c^+ K\pi}_{\Omega_b^-}(\times 10^{-3})$	7.66 ± 0.22	2.00 ± 0.07
$R^{\Lambda_c^+ KK \to \Lambda_c^+ K\pi}_{\Xi_b^-}(\times 10^{-2})$	7.89 ± 0.08	3.64 ± 0.03
$R^{\Lambda_c^+ KK \to \Lambda_c^+ \pi\pi}_{\Xi_b^-}(\times 10^{-3})$	6.16 ± 0.33	2.50 ± 0.12
$R^{\Lambda_c^+ K\pi \to \Lambda_c^+ KK}_{\Xi_b^-}(\times 10^{-3})$	7.09 ± 0.30	1.43 ± 0.08
$R^{\Lambda_c^+ K\pi \to \Lambda_c^+ \pi\pi}_{\Xi_b^-}(\times 10^{-2})$	9.14 ± 0.11	4.45 ± 0.05
$R^{\Lambda_c^+ \pi\pi \to \Lambda_c^+ K\pi}_{\Xi_b^-}(\times 10^{-3})$	7.75 ± 0.19	1.68 ± 0.06
comb slope $(\Lambda_c^+ K^- K^-)$ $(\times 10^{-3})$	-4.21 ± 1.20	-3.55 ± 0.75
comb slope $(\Lambda_c^+ K^- \pi^-)$ $(\times 10^{-3})$	-4.10 ± 0.52	-5.05 ± 0.46
comb slope $(\Lambda_c^+ \pi^- \pi^-)$ $(\times 10^{-3})$	-3.71 ± 0.21	-4.40 ± 0.25
`moffset`	0.57 ± 1.67	-0.39 ± 0.71
`wscale`	1.33 ± 0.14	1.13 ± 0.05

is determined as

$$\text{KR coeff} = \frac{(\#\text{concordant pairs} - \#\text{discordant pairs})}{n(n-1)/2} \tag{5.5}$$

where concordant pairs are the pairs of candidates for which the differences in the invariant mass and a square Dalitz plot variable are of the same sign. For discordant pairs, the differences are of opposite signs. In Equation (5.5) n is the number of candidates in the sample, So $n(n-1)/2$ gives the number of pairs that can be formed. The coefficients are computed separately from MC samples for every component in the fits and with respect to each of the square Dalitz plot

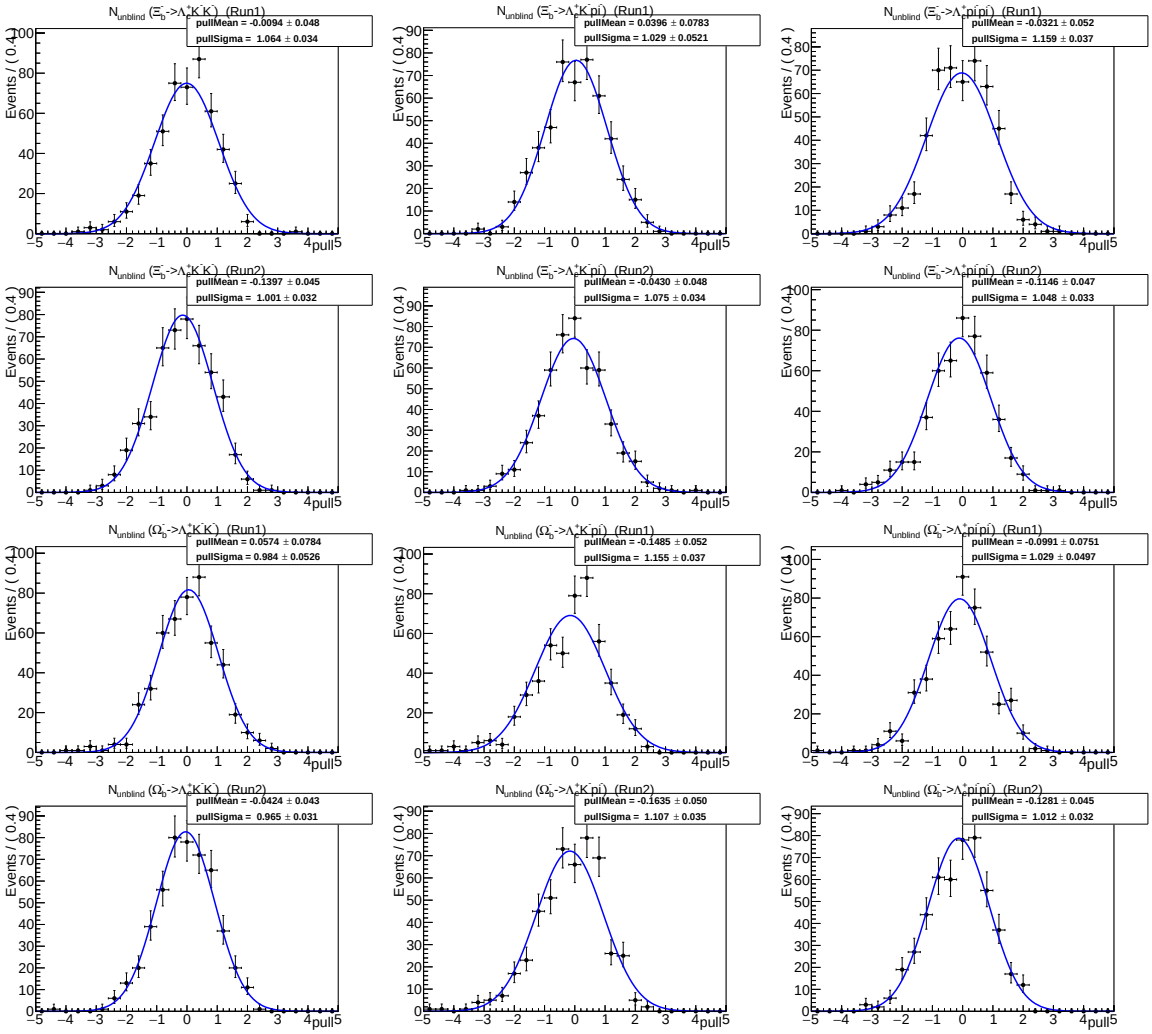

Figure 5.17: Pull distributions for the Ξ_b^- and Ω_b^- signal yields from the nominal set of pseudoexperiments for Run I and Run II

Table 5.6: Results for the signal yields obtained from the toy studies of the signal modes.

	Run I		Run II	
	Pull mean	Pull sigma	Pull mean	Pull sigma
$N(\Xi_b^- \to \Lambda_c^+ K^- K^-)$	-0.1637 ± 0.071	1.124 ± 0.050	-0.132 ± 0.050	1.116 ± 0.035
$N(\Xi_b^- \to \Lambda_c^+ K^- \pi^-)$	0.0879 ± 0.078	1.029 ± 0.052	-0.051 ± 0.045	0.998 ± 0.032
$N(\Xi_b^- \to \Lambda_c^+ \pi^- \pi^-)$	-0.032 ± 0.052	1.159 ± 0.037	-0.122 ± 0.046	1.031 ± 0.033
$N(\Omega_b^- \to \Lambda_c^+ K^- K^-)$	0.057 ± 0.078	0.984 ± 0.053	-0.101 ± 0.046	1.038 ± 0.033
$N(\Omega_b^- \to \Lambda_c^+ K^- \pi^-)$	-0.149 ± 0.052	1.155 ± 0.037	-0.130 ± 0.050	1.113 ± 0.035
$N(\Omega_b^- \to \Lambda_c^+ \pi^- \pi^-)$	-0.099 ± 0.075	1.029 ± 0.049	-0.119 ± 0.052	1.162 ± 0.037

variables m' and θ'. However, for the combinatorial background which is not modelled from MC,

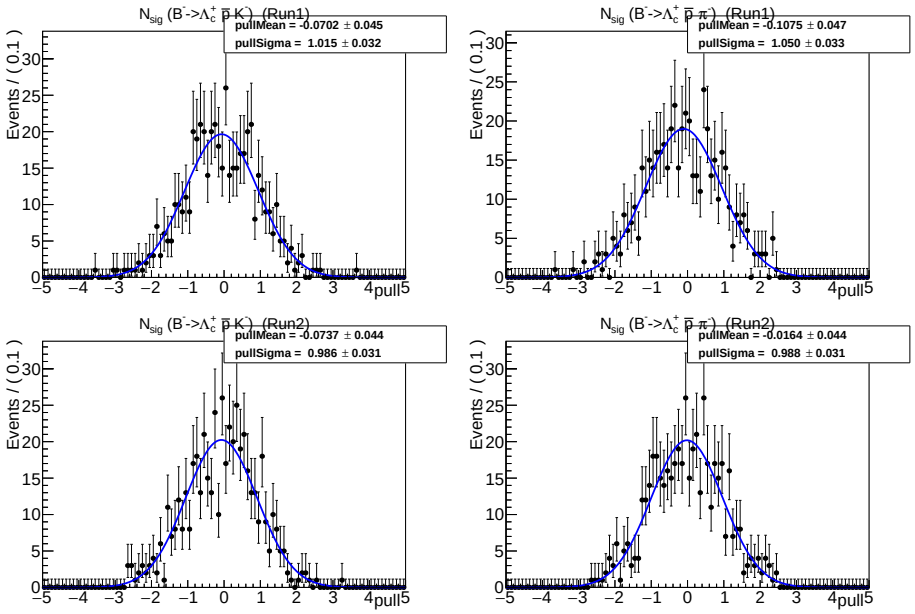

Figure 5.18: Pull distributions for signal yield parameters from the nominal set of pseudoexperiments for Run I and Run II $B^- \to \Lambda_c^+ \overline{p} h^-$ samples

Table 5.7: Results for the signal yields obtained from the toy studies of the signal modes.

	Run I		Run II	
	Pull mean	Pull sigma	Pull mean	Pull sigma
$N(B^- \to \Lambda_c^+ \overline{p} K^-)$	-0.0702 ± 0.045	1.015 ± 0.032	-0.0737 ± 0.044	0.986 ± 0.031
$N(B^- \to \Lambda_c^+ \overline{p} \pi^-)$	-0.1075 ± 0.047	1.050 ± 0.033	-0.0164 ± 0.044	0.988 ± 0.031

they are determined from the b-candidate mass sideband in data, defined as 5600–6000 MeV/c^2 for the B meson modes.

The coefficients are presented in Table 5.8. It can be seen that these correlations are very small and justify use of the `sPlot` technique. Figure 5.20, Figure 5.21 and Figure 5.22 show the scatter of the differences of the b-hadron candidate invariant mass and the differences of the square Dalitz plot variable for signal, cross-feed and combinatorial background, respectively. These support that there is very little correlation between the two variables. This is done for the B meson decays and the behaviour is expected to be similar for b baryon modes.

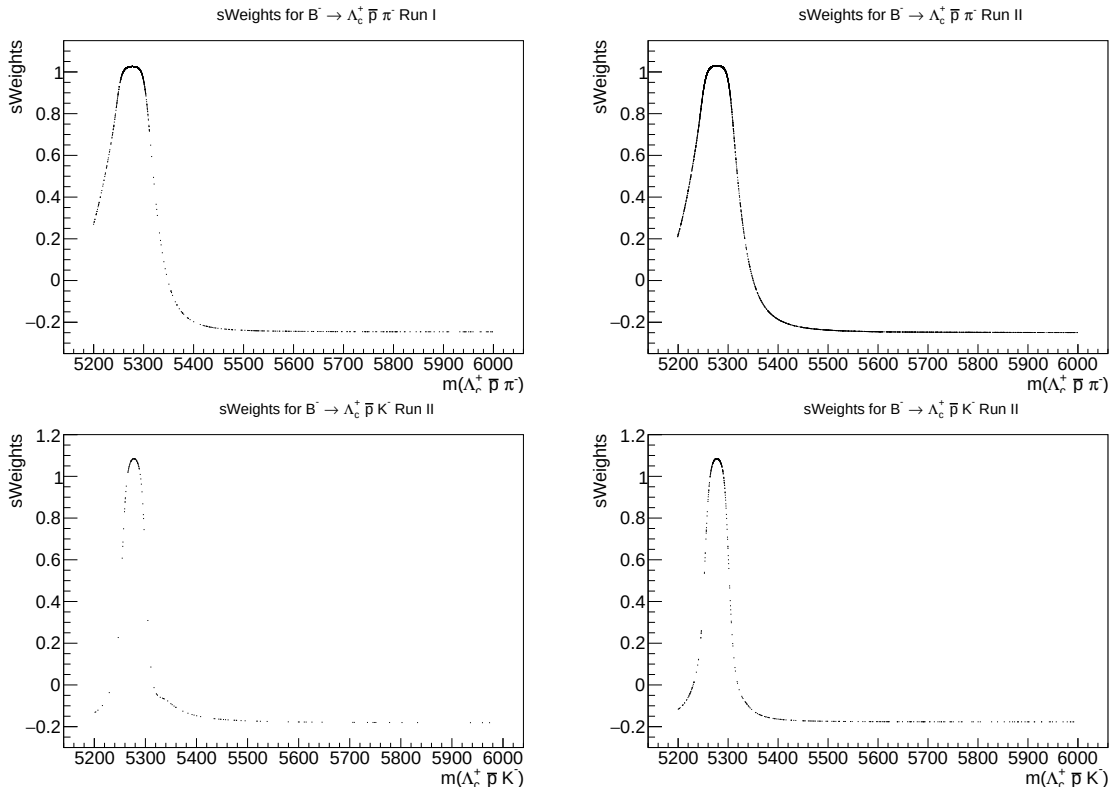

Figure 5.19: Obtained signal *sWeight* as a function of B-candidate mass for the control channels. (top)$B^- \to \Lambda_c^+ \overline{p}\pi^-$ and (bottom) $B^- \to \Lambda_c^+ \overline{p}K^-$, (left) Run I and (right) Run II.

Table 5.8: Kendall rank coefficient for control mode fit components.

	Run I		Run II	
Component	m'	θ'	m'	θ'
$B^- \to \Lambda_c^+ \overline{p}\pi^-$	0.003	0.021	−0.001	0.002
$B^- \to \Lambda_c^+ \overline{p}K^-$	−0.023	0.006	−0.019	0.009
$B^- \to \Lambda_c^+ \overline{p}\pi^-$ misID in $B^- \to \Lambda_c^+ \overline{p}K^-$	0.123	0.093	0.056	0.035
$B^- \to \Lambda_c^+ \overline{p}K^-$ misID in $B^- \to \Lambda_c^+ \overline{p}\pi^-$	−0.212	−0.281	−0.177	−0.246
$B^- \to \Lambda_c^+ \overline{p}\pi^-$ combinatorial background	−0.058	0.054	0.013	−0.005
$B^- \to \Lambda_c^+ \overline{p}K^-$ combinatorial background	0.258	−0.075	−0.029	0.086

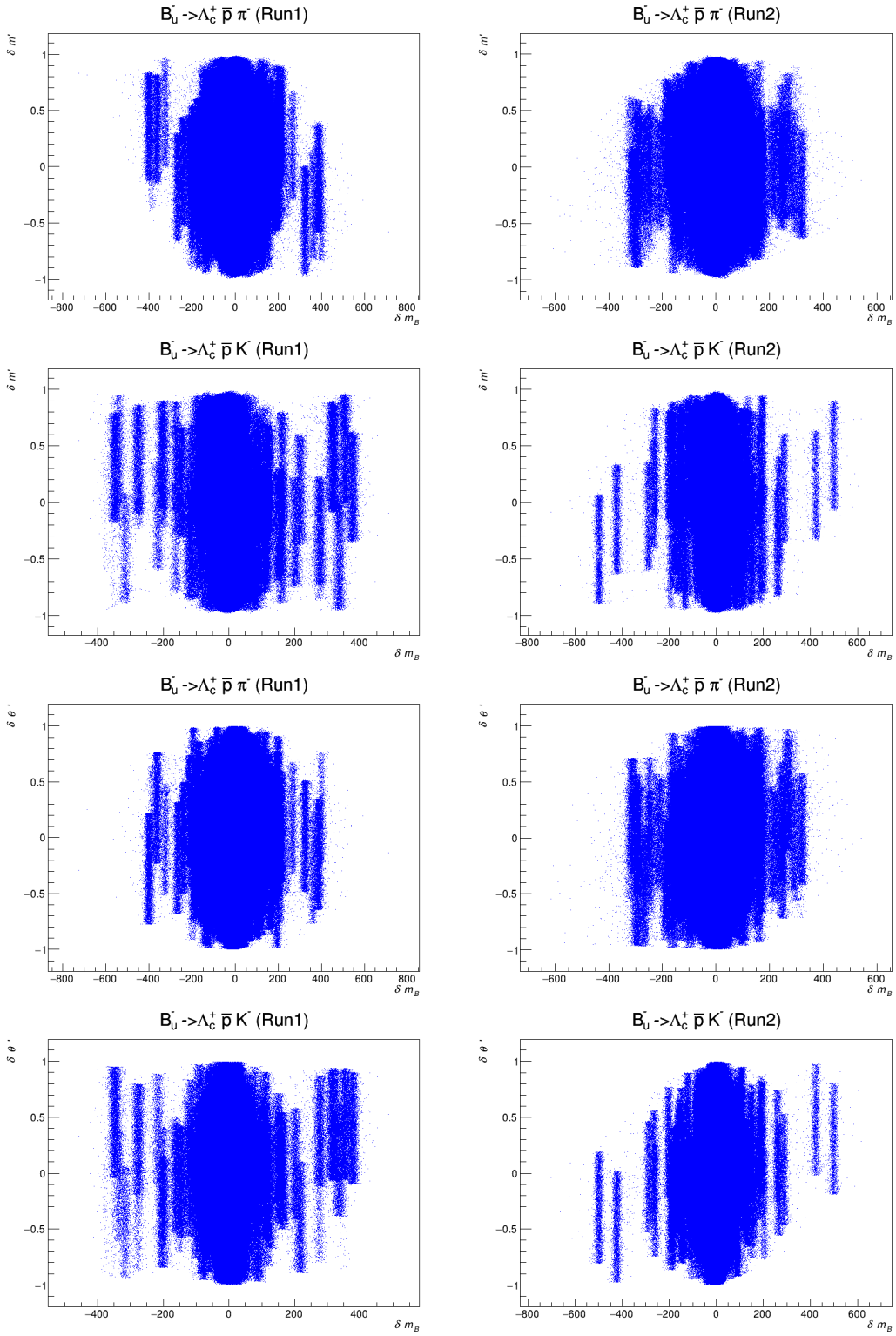

Figure 5.20: Differences in the square Dalitz plot variables (top four plots) m', (bottom four plots) θ' and the corresponding difference in invariant mass for the signal components of the control mode.

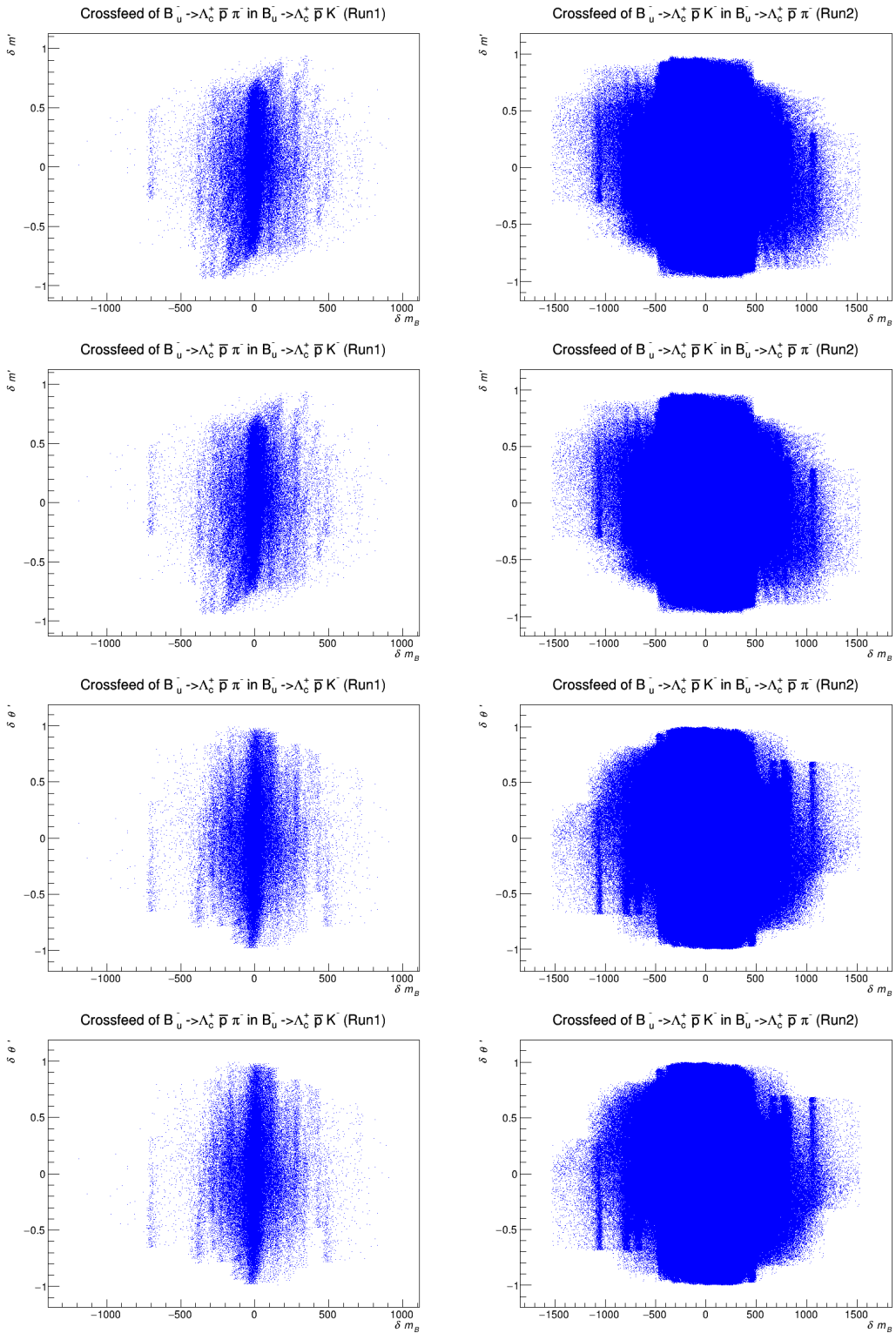

Figure 5.21: Differences in the square Dalitz plot variables (top four plots) m', (bottom four plots) θ' and the corresponding difference in invariant mass for the mis-identified background components of the control mode.

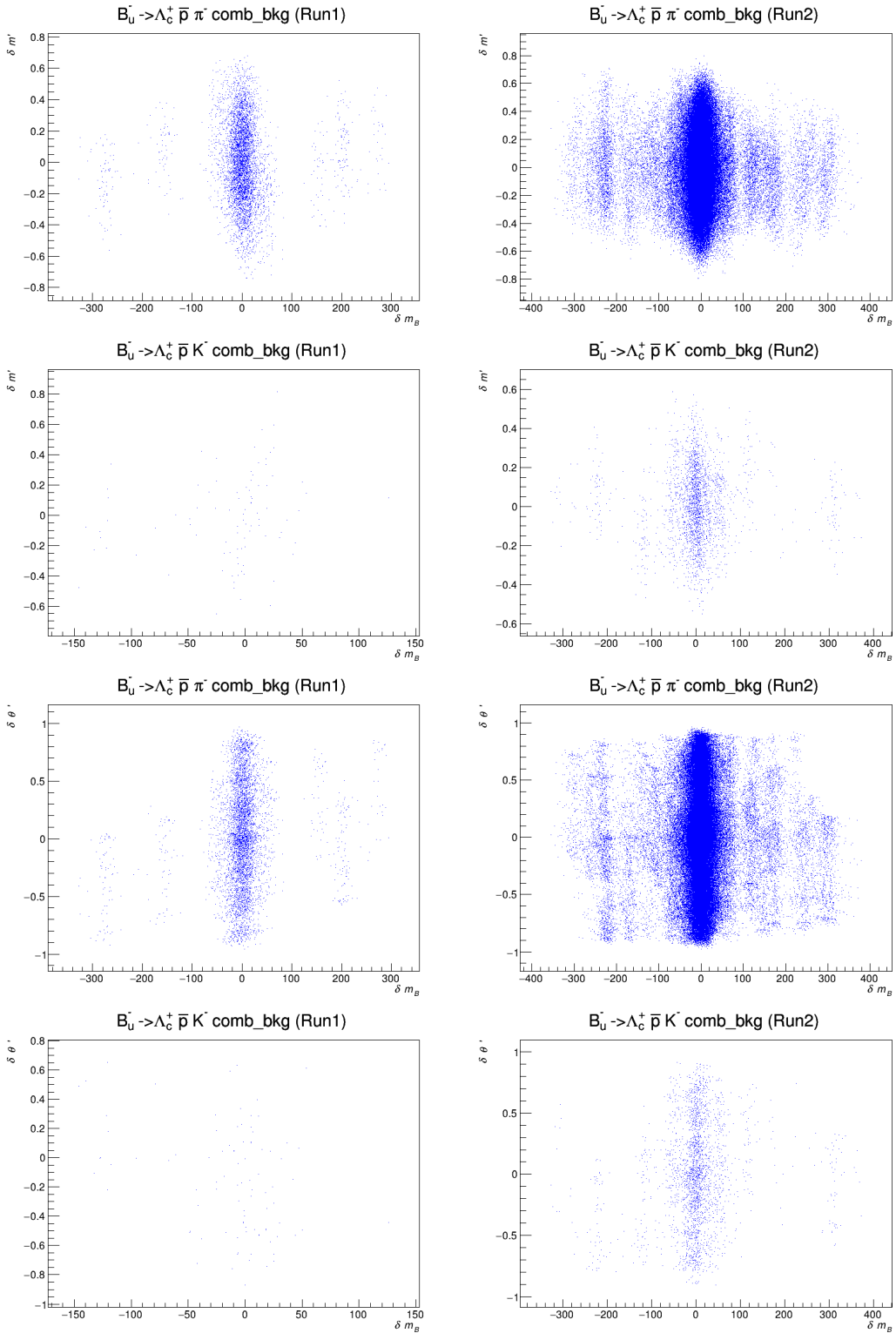

Figure 5.22: Differences in the square Dalitz plot variables (top four plots) m', (bottom four plots) θ' and the corresponding difference in invariant mass for the combinatorial background components of the control mode.

Chapter 6

Signal efficiency

The measurements that are being made in this thesis require the computation of the signal efficiency to correct the measured signal and control channel yields in order to be able to calculate the branching fraction ratios as seen in Equations (8.1) and (8.5). The efficiencies are computed from MC simulation as the number of selected events relative to the total number of generated events. In LHCb, knowledge of efficiencies requires input from various sources that include the geometrical acceptance of the LHCb detector, the reconstruction of the decay channels and effects due to trigger and stripping requirements. Since filtered MC samples are used in this analysis as discussed before in Chapter 4, these effects are studied together and cannot be disentangled. The efficiency corresponding to all of these sources is denoted as ϵ^{grts}. Furthermore, since we also have performed selection of the candidates along with the PID requirements, we need to compute the efficiencies of the candidates passing through the selection requirements. The efficiencies for PID requirements are determined separately from other selection requirements since the PID is corrected using the PIDcorr and is not computed directly from MC in order to have more information about the efficiency of the corrected PID variables. The efficiencies are denoted as ϵ^{sel} and ϵ^{PID} for the selection and PID requirements, respectively. The total efficiency of the measurement is then a combination of all of these efficiencies

$$\epsilon^{tot} = \epsilon^{grts} \times \epsilon^{sel} \times \epsilon^{PID} \tag{6.1}$$

Each contribution to the total efficiency is summarised in following sections.

6.1 Trigger, stripping, reconstruction and acceptance efficiencies

The efficiency for each sample due to the trigger, stripping, reconstruction and geometrical acceptance requirements is summarised in Table 6.1. These values are computed as the fraction of the total number of generated events that pass all the trigger, stripping and acceptance

requirements.

Table 6.1: Trigger, stripping, geometrical and reconstruction efficiencies, ϵ^{grts} for each year of data-taking and both magnet polarities.

	Polarity	2011(%)	2012(%)	2015(%)	2016(%)	2017(%)	2018(%)
$B^- \to \Lambda_c^+ \overline{p}\pi^-$	Up	0.395	0.325	0.209	0.237	0.252	0.221
$B^- \to \Lambda_c^+ \overline{p}\pi^-$	Down	0.395	0.345	0.209	0.239	0.260	0.225
$B^- \to \Lambda_c^+ \overline{p}K^-$	Up	0.166	0.153	0.210	0.237	0.258	0.216
$B^- \to \Lambda_c^+ \overline{p}K^-$	Down	0.165	0.148	0.210	0.237	0.258	0.221
$\Xi_b^- \to \Lambda_c^+ K^- K^-$	Up	0.208	0.188	0.269	0.296	0.319	0.273
$\Xi_b^- \to \Lambda_c^+ K^- K^-$	Down	0.215	0.185	0.276	0.302	0.317	0.274
$\Xi_b^- \to \Lambda_c^+ K^- \pi^-$	Up	0.216	0.192	0.271	0.290	0.311	0.264
$\Xi_b^- \to \Lambda_c^+ K^- \pi^-$	Down	0.214	0.188	0.268	0.294	0.318	0.265
$\Xi_b^- \to \Lambda_c^+ \pi^- \pi^-$	Up	0.211	0.193	0.271	0.295	0.316	0.276
$\Xi_b^- \to \Lambda_c^+ \pi^- \pi^-$	Down	0.209	0.195	0.268	0.286	0.317	0.274
$\Omega_b^- \to \Lambda_c^+ K^- K^-$	Up	0.191	0.167	0.234	0.259	0.271	0.236
$\Omega_b^- \to \Lambda_c^+ K^- K^-$	Down	0.189	0.168	0.236	0.252	0.277	0.239
$\Omega_b^- \to \Lambda_c^+ K^- \pi^-$	Up	0.193	0.161	0.229	0.250	0.266	0.232
$\Omega_b^- \to \Lambda_c^+ K^- \pi^-$	Down	0.189	0.164	0.231	0.257	0.274	0.228
$\Omega_b^- \to \Lambda_c^+ \pi^- \pi^-$	Up	0.189	0.166	0.233	0.246	0.271	0.233
$\Omega_b^- \to \Lambda_c^+ \pi^- \pi^-$	Down	0.187	0.163	0.236	0.257	0.275	0.236

6.2 Selection efficiency

The efficiencies corresponding to the selection cuts except the PID are given in Table 6.2. These include the effects due to requirements on the BDT outputs, X_b mass fit window, X_c candidate mass and the `isMuon` requirement, computed again from the MC. These correspond to the fraction of MC events that pass the selection requirements after having passed all the trigger, stripping, reconstruction and acceptance requirements. However, the $\Lambda_b^0 \to \Lambda_c^+ h^-$ vetoes are not included here while computing them as they remove a significant fraction of the phase space (*i.e.* the efficiency is zero in those regions). With no a priori knowledge of the distribution of the signal over phase space, the fraction of the signal that is removed by these vetoes cannot be estimated reliably. However, it is expected that the contributions to the Dalitz-plot are dominated by low-mass resonances, so the amount of signal that is lost should be small. Thus, the vetoes are not included in the efficiency computation, and instead the amount of signal lost is accounted for as a source of systematic uncertainty.

Table 6.2: Selection efficiencies ϵ^{sel} for each year of data-taking and both magnet polarities.

	Polarity	2011(%)	2012(%)	2015(%)	2016(%)	2017(%)	2018(%)
$B^- \to \Lambda_c^+ \overline{p}\pi^-$	Up	34.95	32.14	30.96	30.34	30.25	30.18
$B^- \to \Lambda_c^+ \overline{p}\pi^-$	Down	34.89	32.84	30.87	29.89	29.83	30.57
$B^- \to \Lambda_c^+ \overline{p}K^-$	Up	34.67	32.16	30.79	30.26	30.21	29.99
$B^- \to \Lambda_c^+ \overline{p}K^-$	Down	35.26	32.83	31.31	29.93	29.55	30.39
$\Xi_b^- \to \Lambda_c^+ K^- K^-$	Up	36.20	34.34	32.52	32.13	31.66	32.37
$\Xi_b^- \to \Lambda_c^+ K^- K^-$	Down	36.29	35.00	32.56	31.65	31.54	32.04
$\Xi_b^- \to \Lambda_c^+ K^- \pi^-$	Up	34.22	32.17	30.35	30.03	29.73	30.19
$\Xi_b^- \to \Lambda_c^+ K^- \pi^-$	Down	34.85	33.07	31.47	30.33	29.69	30.51
$\Xi_b^- \to \Lambda_c^+ \pi^- \pi^-$	Up	34.81	32.17	29.64	29.68	29.62	29.73
$\Xi_b^- \to \Lambda_c^+ \pi^- \pi^-$	Down	34.51	33.06	30.54	29.35	29.66	30.25
$\Omega_b^- \to \Lambda_c^+ K^- K^-$	Up	33.42	30.79	29.28	29.08	28.56	28.67
$\Omega_b^- \to \Lambda_c^+ K^- K^-$	Down	33.40	31.63	29.86	28.49	28.33	29.06
$\Omega_b^- \to \Lambda_c^+ K^- \pi^-$	Up	31.32	28.92	27.44	27.22	26.90	27.02
$\Omega_b^- \to \Lambda_c^+ K^- \pi^-$	Down	31.23	30.07	28.41	27.52	26.48	27.61
$\Omega_b^- \to \Lambda_c^+ \pi^- \pi^-$	Up	30.82	28.58	26.55	27.05	26.22	26.45
$\Omega_b^- \to \Lambda_c^+ \pi^- \pi^-$	Down	30.69	29.24	27.99	26.94	26.14	26.75

6.3 PID efficiency

The efficiencies corresponding to the PID cuts are given in Table 6.3. These correspond to the fraction of MC events that pass the PID requirements after having passed all the trigger, stripping, reconstruction, acceptance and selection requirements. Since the PID variables in MC are corrected using control samples, the efficiencies obtained in this way provide a reliable estimate.

6.4 Total efficiency

The total efficiency is then the product of the three terms described in previous section and is given in Table 6.4. These numbers are not what are used in the analysis and are only an estimate of the efficiencies for different categories. This is because the dynamics of these three-body decays are currently unknown and so the phase-space distribution in the simulation is unlikely to match that in data. Hence, the variation of the efficiency across the phase space of each decay is studied to perform candidate-by-candidate correction, using the square Dalitz-plot coordinates defined in Section 4.1.2. These maps are computed for every year of data-taking and both magnet polarities, and for every decay channel under study. They are obtained by taking the square Dalitz plot distribution of MC events that have passed all the criteria and dividing by the generated square Dalitz-plot distribution. We obtain the square Dalitz plot using generator only simulation through Laura^{++} [91] from the total number of generated events. This gives rise to

Table 6.3: PID efficiencies ϵ^{PID} for each year of data-taking and both magnet polarities.

	Polarity	2011(%)	2012(%)	2015(%)	2016(%)	2017(%)	2018(%)
$B^- \to \Lambda_c^+ \overline{p}\pi^-$	Up	69.23	68.31	92.37	93.70	92.29	91.68
$B^- \to \Lambda_c^+ \overline{p}\pi^-$	Down	68.83	71.49	93.38	93.20	92.19	91.19
$B^- \to \Lambda_c^+ \overline{p}K^-$	Up	53.53	52.90	73.99	75.89	79.25	78.72
$B^- \to \Lambda_c^+ \overline{p}K^-$	Down	55.32	54.39	75.62	75.08	79.77	79.41
$\Xi_b^- \to \Lambda_c^+ K^- K^-$	Up	46.09	44.43	52.90	54.33	60.97	59.22
$\Xi_b^- \to \Lambda_c^+ K^- K^-$	Down	47.28	45.52	54.51	54.66	60.81	60.39
$\Xi_b^- \to \Lambda_c^+ K^- \pi^-$	Up	59.79	58.23	67.47	68.21	70.54	69.14
$\Xi_b^- \to \Lambda_c^+ K^- \pi^-$	Down	59.26	59.84	67.76	67.63	69.94	69.06
$\Xi_b^- \to \Lambda_c^+ \pi^- \pi^-$	Up	78.22	78.72	88.92	89.61	84.62	83.41
$\Xi_b^- \to \Lambda_c^+ \pi^- \pi^-$	Down	77.08	80.84	88.57	88.69	83.77	82.09
$\Omega_b^- \to \Lambda_c^+ K^- K^-$	Up	45.00	43.63	52.59	52.82	59.39	57.76
$\Omega_b^- \to \Lambda_c^+ K^- K^-$	Down	46.99	44.48	52.90	53.63	59.03	58.25
$\Omega_b^- \to \Lambda_c^+ K^- \pi^-$	Up	57.63	56.51	66.42	66.61	68.58	67.84
$\Omega_b^- \to \Lambda_c^+ K^- \pi^-$	Down	58.33	57.93	65.63	65.69	67.84	67.43
$\Omega_b^- \to \Lambda_c^+ \pi^- \pi^-$	Up	76.82	77.68	87.61	87.68	84.08	81.75
$\Omega_b^- \to \Lambda_c^+ \pi^- \pi^-$	Down	75.58	79.26	87.25	86.68	82.54	81.43

an almost uniform distribution of the events in the square Dalitz plot. Some non-uniformity is visible at the corners of the SDP. This is due to a large Jacobian of the transformation from conventional Dalitz plot to square Dalitz-plot. However, since the data events after selection do not have kinematics near the corners of the phase space, this does not affect the efficiency of the events. As also mentioned in the Chapter 4, we use square Dalitz plot rather than conventional Dalitz plot to study the variation of efficiency. This is because the decays generally proceed via intermediate resonances. Thus they tend to populate the regions around the edges of the conventional Dalit plot, and the square Dalitz transform tends to enhance these regions with respect to the Dalitz plot centre. This ensures that there are more simulated events in the regions where there are more data events to make binned efficiency map.

The distribution for generated $B^- \to \Lambda_c^+ \overline{p}\pi^-$ samples can be seen in Figure 6.1.

Two important corrections have been applied while computing these maps, due to b-hadron production kinematics (for all samples) and due to the Ω_b^-- lifetime which will be discussed in the following sections. The corrected efficiency maps are shown in Figure 6.2 and Figure 6.3 for the channels $\Xi_b^- \to \Lambda_c^+ K^- \pi^-$ and $B^- \to \Lambda_c^+ \overline{p}\pi^-$ for the year 2012 and 2018 for both `MagUp` and `MagDown` polarities.

6.4.1 Kinematic correction

Since there is not a lot of knowledge about the production of Ξ_b^- and the Ω_b^- baryons in the high-energy pp collisions, the b-baryon kinematics in the MC simulation are not expected to

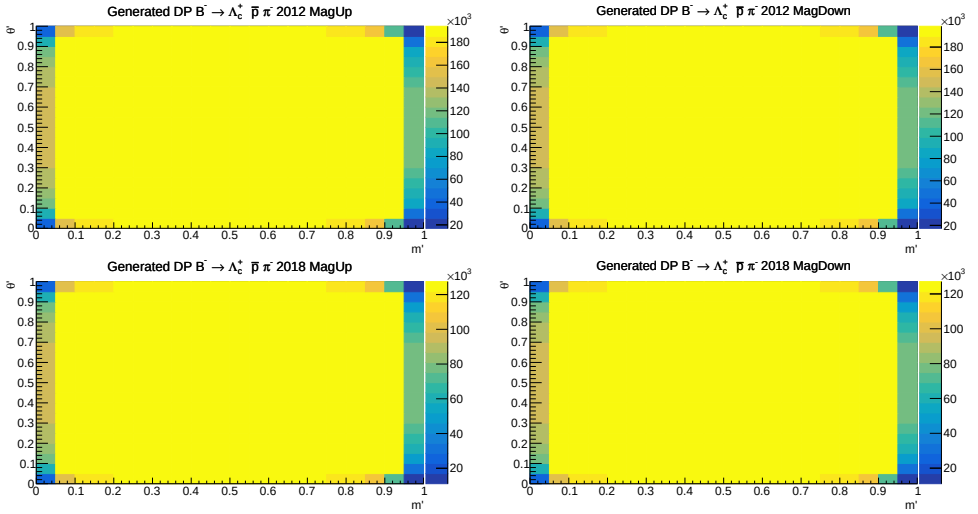

Figure 6.1: Generated `SQDALITZ` distribution for $B^- \to \Lambda_c^+ \overline{p}\pi^-$ decays for (top to bottom) 2011–2018 and (left and right) magnet Up and Down polarities.

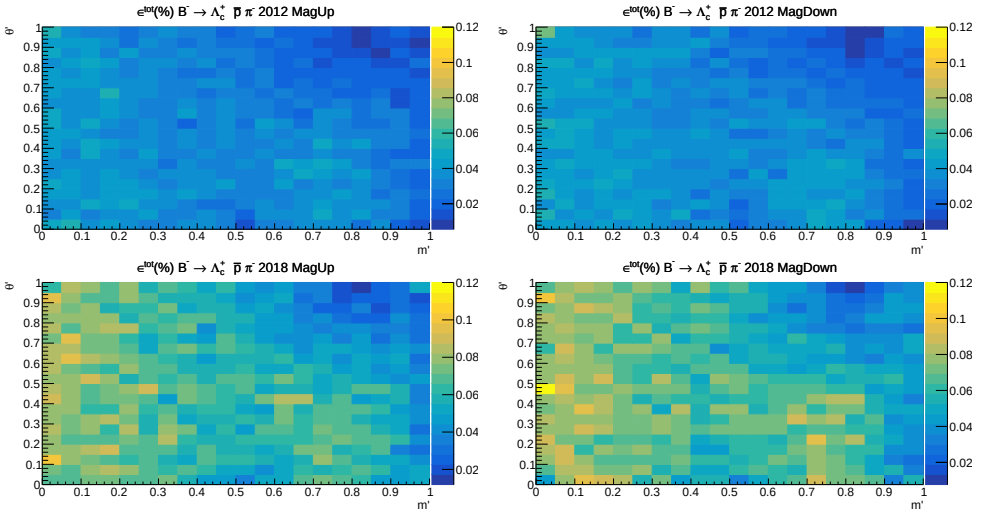

Figure 6.2: Total efficiencies as a function of position in the square Dalitz plot for $B^- \to \Lambda_c^+ \overline{p}\pi^-$ for (top,bottom) 2012,2018 and (left and right) magnet Up and Down polarities.

match the data. This can be seen from Figure 6.5 that shows the distribution of the background subtracted data in comparison to the MC simulation with respect to transverse momentum and pseudorapidity. The mismatch is corrected in the simulation using `GBReweighter` [103]. This assigns a weight to every event in the MC so that the corrected distribution matches the data in order to get reliable efficiencies. Since the B meson production in the simulation has been tuned, good agreement with data in the kinematic variables is seen in Figure 6.4. Nonetheless, these samples are corrected for consistency of all the measurements. The weighted simulation is then used to compute the efficiency maps.

Table 6.4: Total efficiencies ϵ^{tot} for each year of data-taking and both magnet polarities.

	Polarity	2011(%)	2012(%)	2015(%)	2016(%)	2017(%)	2018(%)
$B^- \to \Lambda_c^+ \overline{p}\pi^-$	Up	0.039	0.032	0.059	0.067	0.069	0.061
$B^- \to \Lambda_c^+ \overline{p}\pi^-$	Down	0.039	0.034	0.059	0.066	0.071	0.062
$B^- \to \Lambda_c^+ \overline{p}K^-$	Up	0.031	0.026	0.048	0.054	0.061	0.051
$B^- \to \Lambda_c^+ \overline{p}K^-$	Down	0.032	0.026	0.049	0.053	0.060	0.053
$\Xi_b^- \to \Lambda_c^+ K^- K^-$	Up	0.035	0.029	0.046	0.052	0.061	0.052
$\Xi_b^- \to \Lambda_c^+ K^- K^-$	Down	0.037	0.029	0.049	0.052	0.061	0.053
$\Xi_b^- \to \Lambda_c^+ K^- \pi^-$	Up	0.044	0.036	0.055	0.059	0.065	0.055
$\Xi_b^- \to \Lambda_c^+ K^- \pi^-$	Down	0.044	0.037	0.057	0.060	0.066	0.056
$\Xi_b^- \to \Lambda_c^+ \pi^- \pi^-$	Up	0.057	0.049	0.072	0.079	0.079	0.069
$\Xi_b^- \to \Lambda_c^+ \pi^- \pi^-$	Down	0.056	0.052	0.073	0.075	0.079	0.069

	Polarity	2011(%)	2012(%)	2015(%)	2016(%)	2017(%)	2018(%)
Uncorrected							
$\Omega_b^- \to \Lambda_c^+ K^- K^-$	Up	0.029	0.022	0.036	0.039	0.046	0.039
$\Omega_b^- \to \Lambda_c^+ K^- K^-$	Down	0.029	0.024	0.037	0.039	0.046	0.040
$\Omega_b^- \to \Lambda_c^+ K^- \pi^-$	Up	0.035	0.026	0.042	0.045	0.049	0.043
$\Omega_b^- \to \Lambda_c^+ K^- \pi^-$	Down	0.034	0.029	0.043	0.046	0.049	0.042
$\Omega_b^- \to \Lambda_c^+ \pi^- \pi^-$	Up	0.045	0.037	0.054	0.058	0.059	0.050
$\Omega_b^- \to \Lambda_c^+ \pi^- \pi^-$	Down	0.043	0.037	0.058	0.060	0.059	0.051
Lifetime corrected							
$\Omega_b^- \to \Lambda_c^+ K^- K^-$	Up	0.039	0.030	0.049	0.055	0.063	0.054
$\Omega_b^- \to \Lambda_c^+ K^- K^-$	Down	0.040	0.032	0.051	0.053	0.064	0.056
$\Omega_b^- \to \Lambda_c^+ K^- \pi^-$	Up	0.047	0.036	0.058	0.062	0.068	0.059
$\Omega_b^- \to \Lambda_c^+ K^- \pi^-$	Down	0.047	0.039	0.059	0.064	0.069	0.058
$\Omega_b^- \to \Lambda_c^+ \pi^- \pi^-$	Up	0.062	0.051	0.076	0.082	0.084	0.071
$\Omega_b^- \to \Lambda_c^+ \pi^- \pi^-$	Down	0.060	0.052	0.080	0.085	0.084	0.072

6.4.2 Lifetime correction

The world average value of the lifetime of the Ω_b^- particles was updated since the time the MC samples were generated as reported in Table 4.4. This presents a need to correct for the lifetime in the analysis. Since the selection relies on quantities that are related with vertex separation, this affects the efficiency calculations in particular the BDT cuts and the HLT trigger cuts. The increase in the lifetime causes the efficiencies to increase, bringing them more in line with the efficiencies of Ξ_b^- and B^- as can also be seen in Table 6.4. The simulation is weighted to correct for this effect. The weight is given as $w(t) = F(t;\tau_{\text{WA}})/F(t;\tau_{\text{gen}})$ where $F(t;\tau)$ is the decay time distribution for a lifetime τ given by $F(t;\tau) = \frac{1}{\tau}\exp(-t/\tau)$. Figure 6.6 shows the MC distribution before and after lifetime weighting of the decay time distribution in $\Omega_b^- \to \Lambda_c^+ K^- K^-$ simulation.

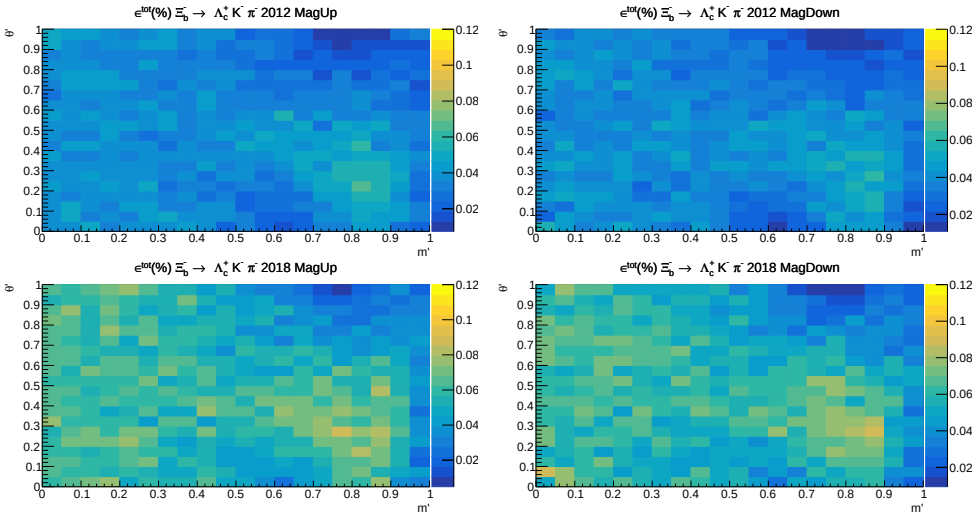

Figure 6.3: Total efficiencies as a function of square Dalitz plot for $\Xi_b^- \to \Lambda_c^+ K^- \pi^-$ for (top,bottom) 2012,2018 and (left and right) magnet Up and Down polarities.

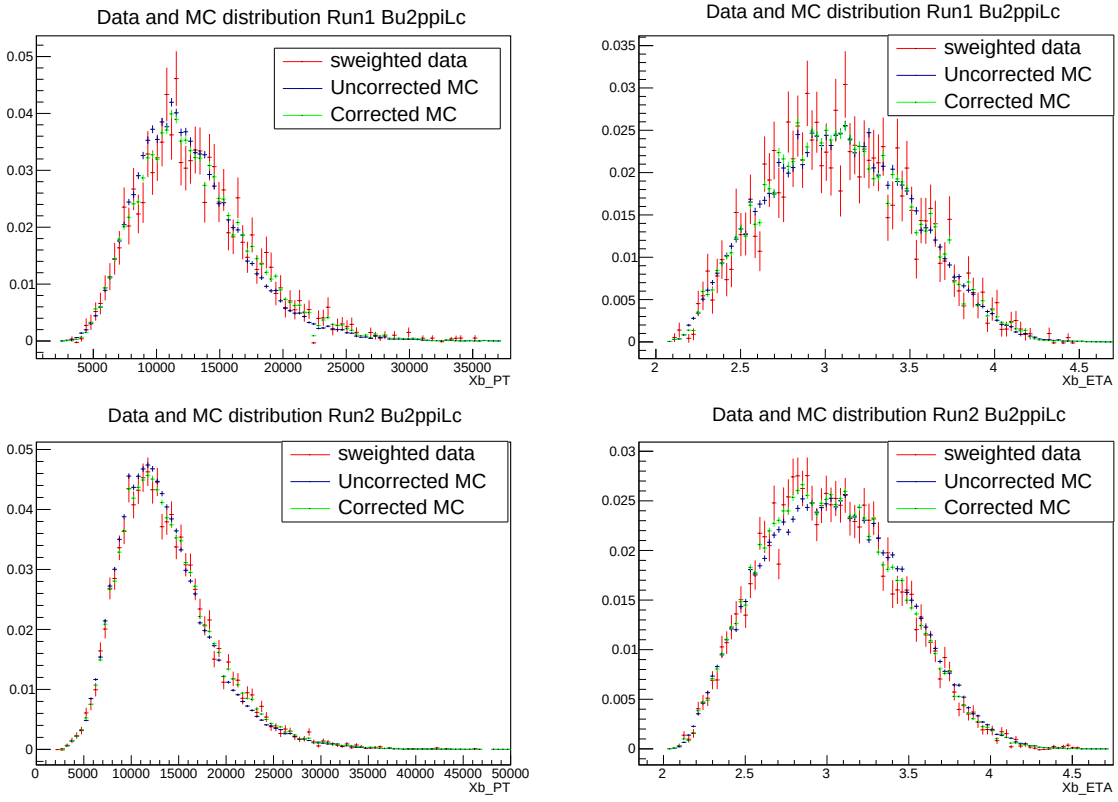

Figure 6.4: Distributions of (left) p_{T} and (right) η for $B^- \to \Lambda_c^+ \overline{p} \pi^-$ decays in (top) Run I and (bottom) Run II, obtained from the results of the invariant mass fits using *sWeights*.

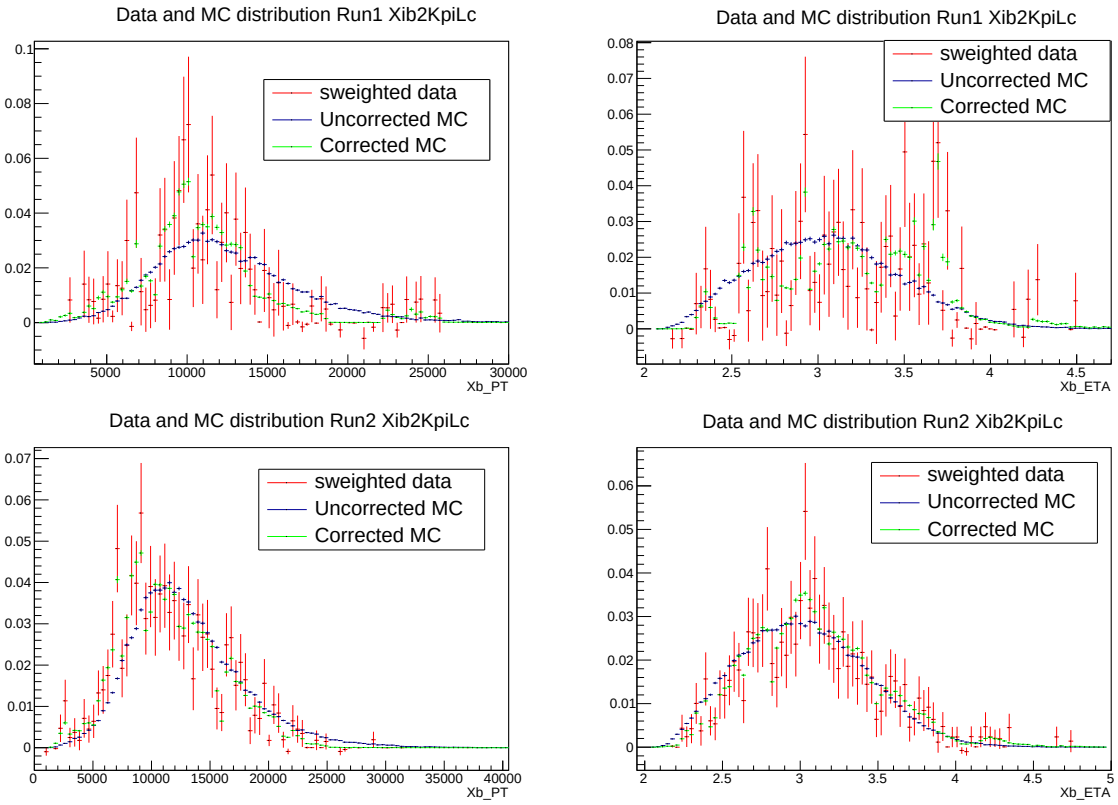

Figure 6.5: Distributions of (left) p_{T} and (right) η for $\Xi_b^- \to \Lambda_c^+ K^- \pi^-$ decays in (top) Run I and (bottom) Run II, obtained from the results of the invariant mass fits using *sWeights*.

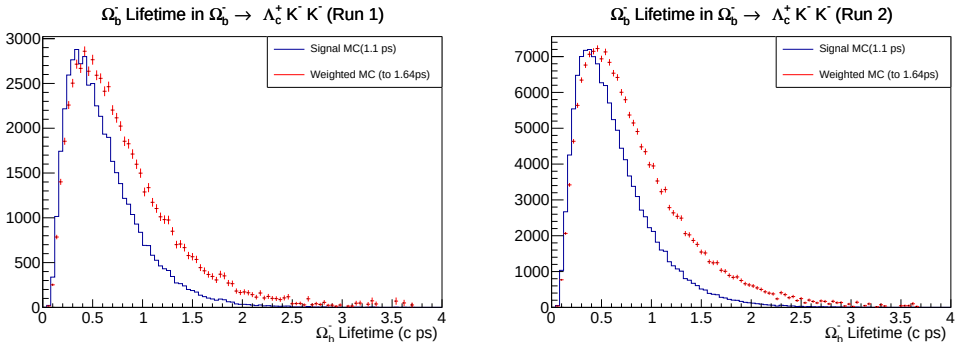

Figure 6.6: Lifetime plot for signal MC and weighted MC samples to the world average values of Ω_b^- lifetime for the Ω_b^- samples of Run I and Run II.

Chapter 7

Systematic uncertainties

All the measurements that are performed in this thesis require inputs from two components: the yields of the signals obtained from the fit and the efficiency computation. However, the fit configurations and the efficiency computation may not be perfect, potentially leading to biases. Systematic uncertainties are therefore assigned to account for potential imperfections in the analysis procedures and assumptions. The decay $B^- \to \Lambda_c^+ \overline{p}\pi^-$ is used as the control and normalisation mode for the measurements and in every channel Λ_c^+ decays to $pK^-\pi^-$, so that all channels studied have the same topology and similar kinematics, helping to reduce a lot of potential sources of systematic uncertainty. The systematics resulting from sources that are non-negligible are discussed below. The effects on the results for each source of systematic is considered as being either correlated or uncorrelated between Run I and Run II.

7.1 Systematic uncertainties related to the signal yields

The fit configuration can be imperfect due to various aspects that contribute to systematic uncertainties. For example, the choice of the fit model could lead to an inaccurate fit result. Furthermore, the choice of the veto window for the Λ_b^0 backgrounds and removal of any multiple candidates can also affect the fit results.

7.1.1 Fit model

The uncertainties due to the choice of fit model are computed by changing the fit models for the different components in the mass fit and performing the fit again. The changes in the results of the yields are propagated to compute the changes in the measurements of the branching fractions. The alternative models that are used are :

- Model I : The signal components in all the simultaneous fits for the B meson and baryon modes are modelled using a double Crystal Ball function in the baseline fit configuration.

However, for calculating the systematic uncertainties, this model is changed to a combination of Johnson [104] and Gaussian functions, while keeping the other components unchanged from same as the baseline fit.

- Model II : The combinatorial background component in all of the simultaneous fits is modelled with an exponential function. This function is changed to a second-order Chebyshev polynomial and the fits are performed again. However, in order to avoid introducing too many parameters in the fit, particularly for the b baryon modes where some channels have less statistics, the shape is constrained to be the same in all final states of the b baryon decays.

- Model III : All the mis-identified components in all the simultaneous fits have been modelled using a double Crystal Ball function in the baseline fit configuration. This is replaced with a `RooKeysPDF` [105], which is superposition of Gaussian kernels, to compute the systematic uncertainties.

- Model IV : The partially reconstructed background components in the fits of the b baryon modes are modelled using `RooKeysPDF` [105]. Since this consists of a superposition of Gaussian kernels, we modify the kernel density estimator, which smooths the fitted function, to estimate the systematic uncertainty.

All these modifications are made one at a time, while keeping the other components unchanged. The changes in the branching fraction due to the changes in the model are considered as the systematic uncertainties. The total uncertainty is then considered as the sum in quadrature of the uncertainties corresponding to all the individual modifications. Any differences in the changes in the model function shall be common for Run I and Run II, this implies that the associated uncertainties are correlated between the measurements with the two data samples.

7.1.2 Fixed parameters

The signal components and the cross-feed components in all of the simultaneous fits of B mesons and b baryons are modelled from MC. The shape parameters of these models that are obtained by fits to MC have uncertainties associated to them due to the finite size of the MC samples. The imperfection of the models due to uncertainties on the parameters is a source of systematic uncertainty.

An ensemble of 500 models is generated by varying the shape parameters within Gaussian uncertainties for each component independently. This ensemble of models is used to fit the data and compute the yields and the resulting branching fractions. The distributions of the branching fractions can be seen in Figures 7.1 and 7.2. The widths of these distribution are taken as the systematic uncertainties. Since this uncertainty arises due to MC sample size,

which is independent in Run I and Run II, the systematic uncertainty associated with the fixed parameters is completely uncorrelated between the results in the two data samples.

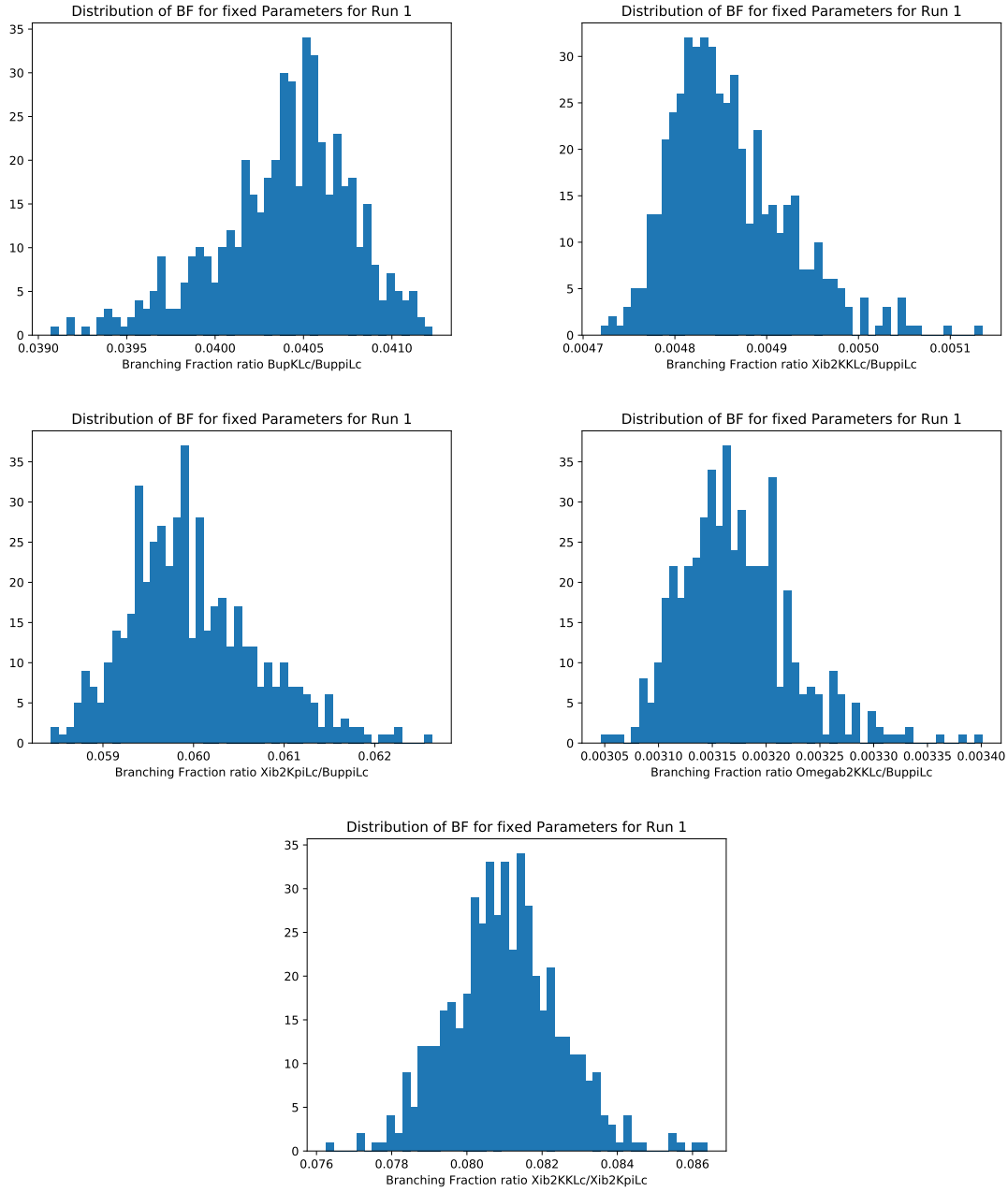

Figure 7.1: Distributions of the branching fraction ratios for the modes that are significant, for Run I obtained when varying fixed parameters.

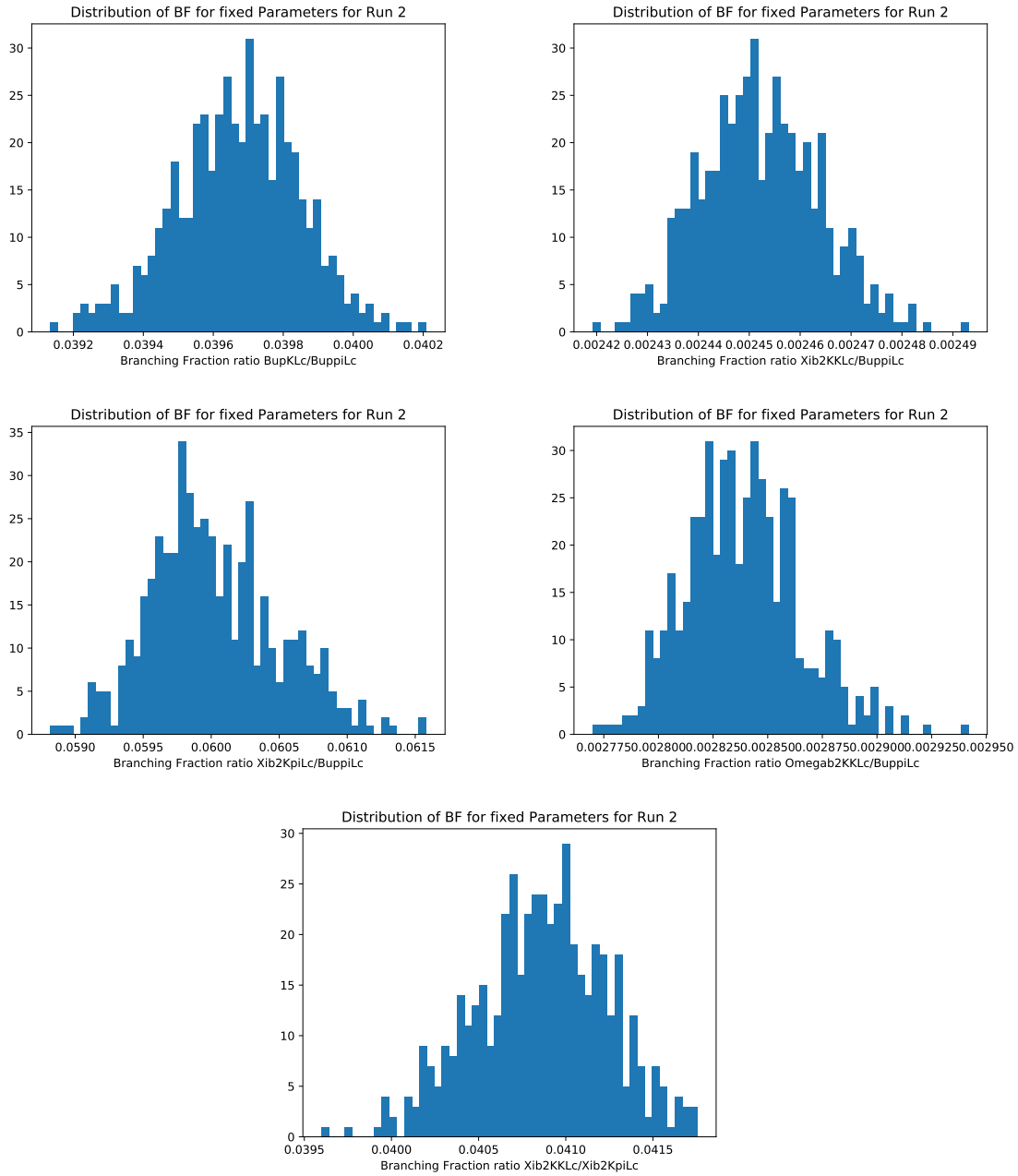

Figure 7.2: Distributions of the branching fraction ratios for the modes that are significant, for Run II obtained when varying fixed parameters.

7.1.3 Fit bias

As discussed in Section 5.2.2, toy studies were performed to check the stability of fit configuration and look for any biases in the signal yields. No large biases were seen in the fitted yields. However, the possibility of small biases is still a source of systematic uncertainty. The uncertainty on each

yield is estimated from the pulls obtained from the pseudoexperiments as quoted in Table 5.7 and Table 5.6. The mean value of the pull and its uncertainty are combined in quadrature and multiplied by the statistical uncertainty to get the uncertainty on the yield. The relative uncertainty on the branching fraction ratio is then estimated as the sum in quadrature of the relative uncertainty on the two yields.

7.1.4 Multiple candidates

An event may contain more than one candidate. Due to imperfect reconstruction, this becomes non-negligible. This could introduce correlations between the b-hadron mass for different candidates leading to biases in the fit. All such candidates need to be removed consistently to avoid the bias. The fractions of multiple candidate for different channels are summarised in Table 7.1. It can be seen from the table that the fraction is small enough to not cause significant biases. Thus it is considered as a source of systematic uncertainty. The effect is taken into account by randomly removing multiple candidates and retaining one candidate per event. The fit is performed again and the branching fraction is re-computed. The procedure is repeated 100 times. A distribution of the resultant branching fractions is obtained as can also be seen from Figures 7.3 and 7.4. The standard deviation of the distribution is taken to be the systematic uncertainty. It can also be seen that the distributions of branching fractions follows a multi-modal pattern. This is due to removal of specific candidates which have a large efficiency-corrected `sweight` in the baseline fit. Removal of such candidates can lead to a visible shift in the results. If there is a genuine bias due to the presence of multiple candidates, the effects on the results would be in the same direction for both Run I and Run II, therefore source of systematic is considered completely correlated between the two runs.

Table 7.1: Fraction of multiple candidates (%) in the mass fit window and in the signal region window of b-mass candidate

Decay	Fraction			
	Mass fit window		Signal region	
	Run I	Run II	Run I	Run II
$B^- \to \Lambda_c^+ \bar{p}\pi^-$	0.43	0.29	0.25	0.11
$B^- \to \Lambda_c^+ \bar{p}K^-$	0.78	0.98	1.33	0.62
$\Xi_b^-(\Omega_b^-) \to \Lambda_c^+ K^- K^-$	2.50	4.07	0.00	5.26
$\Xi_b^-(\Omega_b^-) \to \Lambda_c^+ K^- \pi^-$	0.95	0.34	1.09	0.19
$\Xi_b^-(\Omega_b^-) \to \Lambda_c^+ \pi^- \pi^-$	1.41	0.69	0.00	0.00

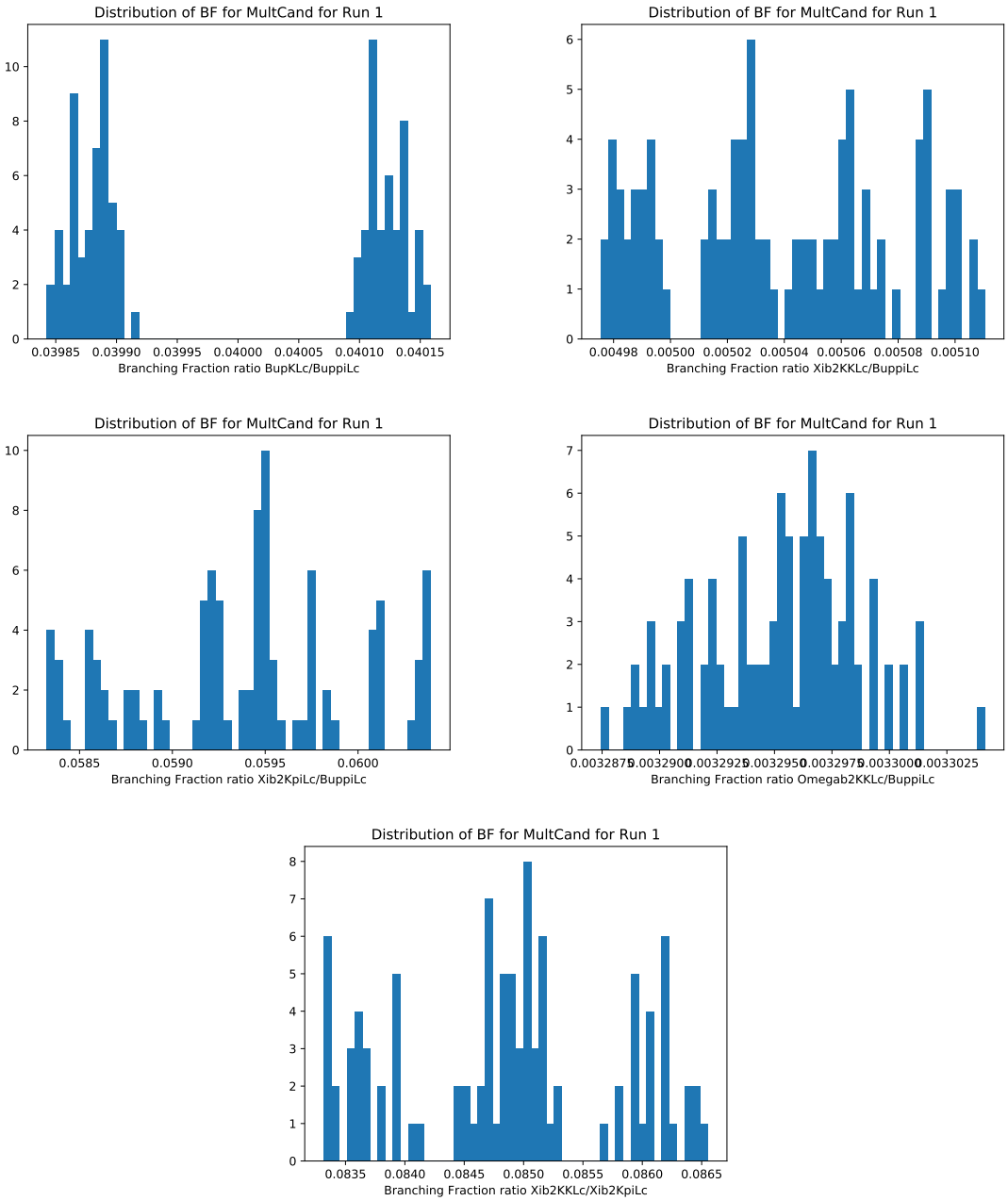

Figure 7.3: Distributions of the branching fraction ratios for significant modes for Run I obtained when randomly selecting multiple candidates.

7.1.5 Veto of partially combinatorial background

As described in the selection procedure in 4, a veto has been applied to partially combinatorial background coming from $\Lambda_b^0 \to \Lambda_c^+ h^-$ decays. However, since this contribution removes a part of the phase space of the signal decay, this results in some loss of the signal, which cannot be

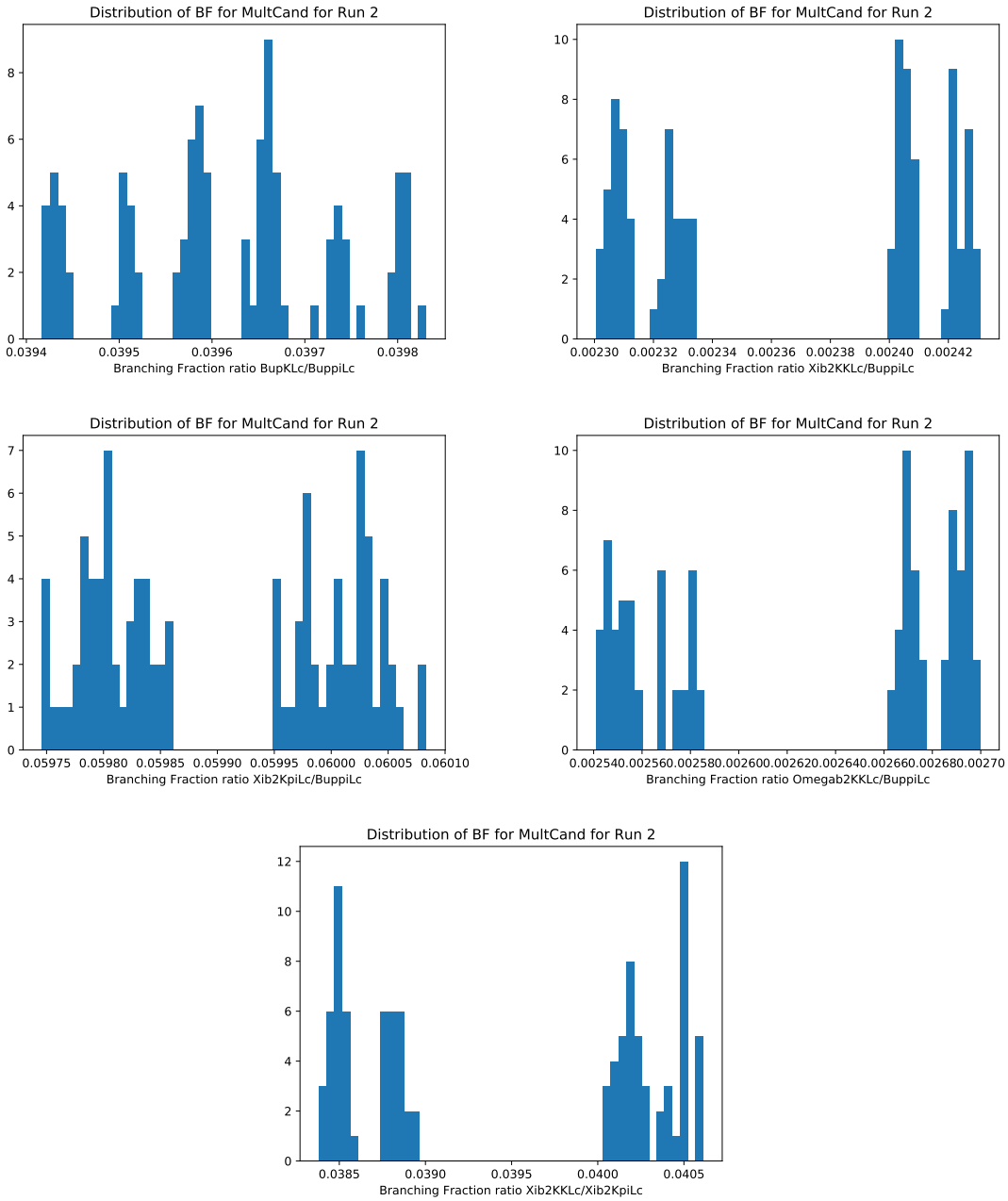

Figure 7.4: Distributions of the branching fraction ratios for significant modes for Run II obtained when randomly selecting multiple candidates.

corrected for through the candidate-by-candidate efficiency correction. The small loss of signal is considered as a source of systematic uncertainty. This is estimated by increasing the width of the window to $5450 < m(\Lambda_c^+ h^-) < 5800\,\mathrm{MeV}/c^2$. The change in the branching fraction with respect to the baseline result is taken to be the systematic uncertainty. Since the effects of the

change in window would be common between runs this is considered as a completely correlated source of uncertainty.

7.1.6 Model for misidentified $\Xi_b^- \to \Lambda_c^+ K^- \pi^-$ background

The cross-feed background components for the b baryons are modelled directly from MC for the baseline fits. The shapes of such components depend upon the momentum of the mis-identified particles. Thus the b-baryon candidate mass distribution of the cross-feed components depends upon their phase space distribution. The phase space distributions for the b baryons were unknown prior to blinding. Thus the shape of the components should be corrected in MC to match the data. This correction is considered as another source of uncertainty. The only non-negligible cross-feed components are due to the significant yields of $\Xi_b^- \to \Lambda_c^+ K^- \pi^-$. Thus the MC shapes for the cross-feed components of $\Xi_b^- \to \Lambda_c^+ K^- \pi^-$ being reconstructed as $\Xi_b^- \to \Lambda_c^+ K^- K^-$ and $\Xi_b^- \to \Lambda_c^+ \pi^- \pi^-$ are corrected by weighting the MC to match the Dalitz-plot distribution of the data. The fit to MC and then to data is performed again. The results are propagated and the shift in the branching fraction is assigned as the systematic uncertainty. The effects of the correction on the results would be in the same direction for Run I and Run II. Thus this is considered as a completely correlated source of uncertainty.

7.2 Systematic uncertainties related to efficiency computation

7.2.1 MC statistics

The efficiency maps are computed from the MC samples. However, since we have MC samples of finite size, this limits the precision of the efficiency calculation. This is thus considered to be a source of systematic uncertainty. To evaluate this uncertainty 100 efficiency maps are generated by varying the value of the efficiency in each bin of the square Dalitz plot of the baseline efficiency maps. The distributions of the branching fraction ratios are obtained corresponding to the propagation of the 100 efficiency maps and their candidate-by-candidate corrections and are shown in Figure 7.5 and Figure 7.6. The standard deviations of the distributions are taken as the systematic uncertainties. Since the generation of the efficiency maps is independent between different runs, this is considered to be a completely uncorrelated source of systematic uncertainty.

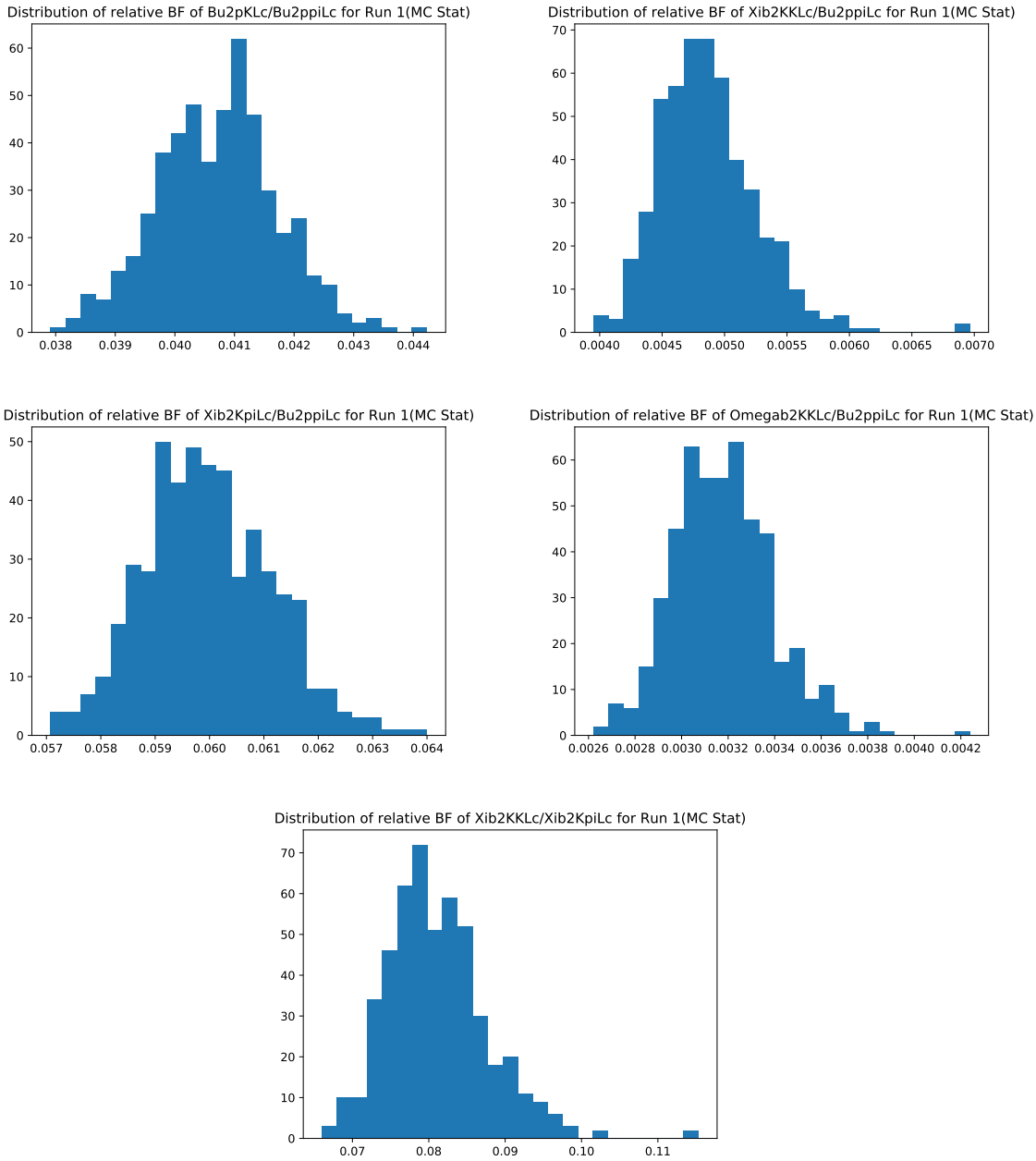

Figure 7.5: Distributions of the ratios of branching fractions and production rates obtained when varying the efficiency maps within the uncertainty due to limited MC statistics for Run I.

7.2.2 Unknown phase-space distribution of modes with insignificant signal yields

For the modes that do not have significant yields, the efficiencies are calculated directly from the MC, instead of performing candidate-by-candidate efficiency corrections with an efficiency map

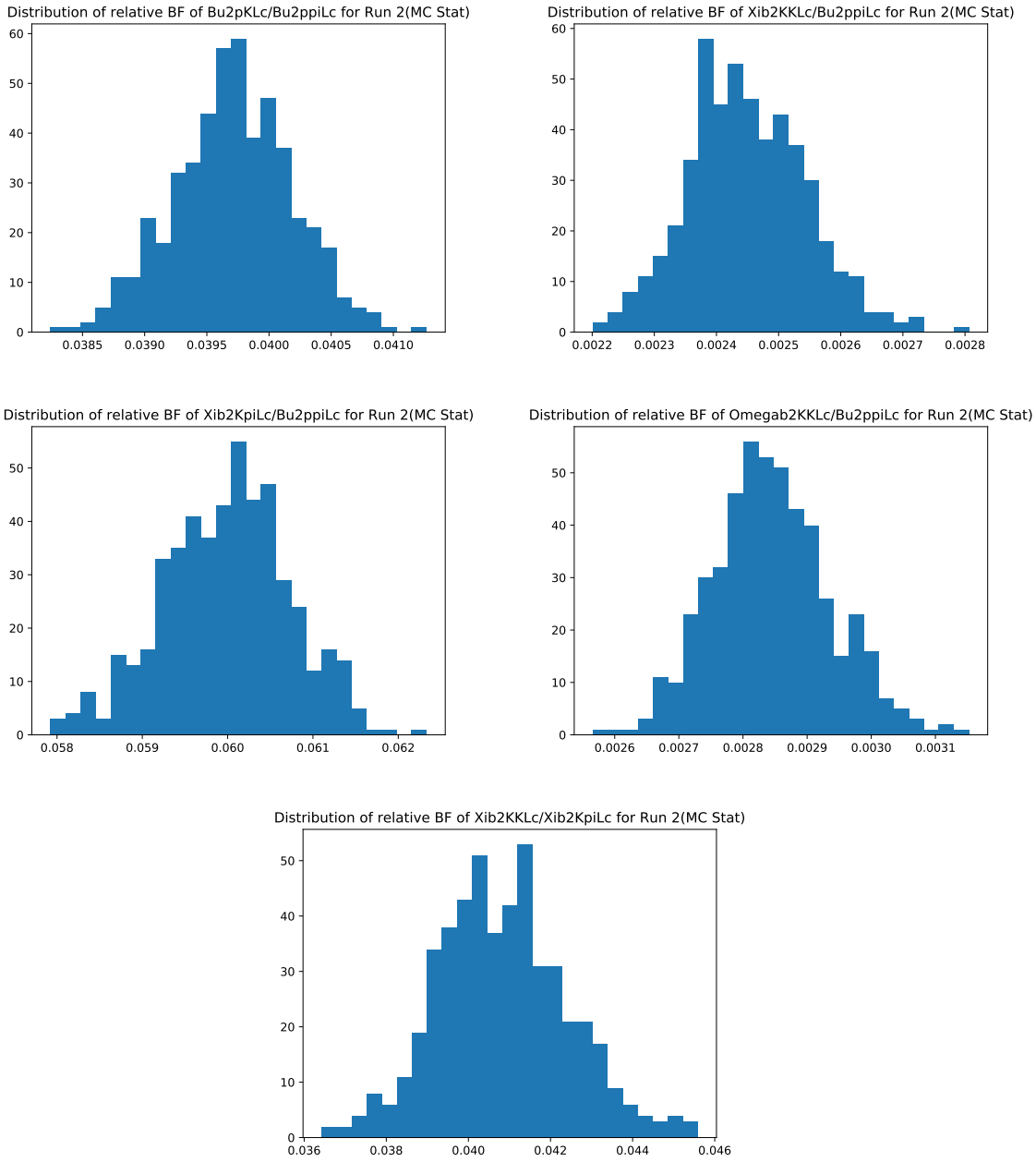

Figure 7.6: Distributions of the ratios of branching fractions and production rates obtained when varying the efficiency maps within the uncertainty due to limited MC statistics for Run II.

over the phase-space. However, the true phase-space distribution almost certainly differs from that of MC. Since the efficiencies vary across the phase-space, this is a source of uncertainty. The standard deviation of the per-bin efficiencies of the square Dalitz plot, relative to the mean value is considered as the relative systematic uncertainty on the branching fraction. Since the true

Dalitz plot distribution is the same between runs, this is considered to be a completely correlated source of systematic uncertainty.

7.2.3 Data-MC mismatch in MVA inputs

The input variables used in the MVA must show good agreement between the data and MC in order to be able to compute reliable efficiencies. Most of the input variables generally show good agreement between the background subtracted data and MC. However, the distribution of the variables `Lc_p_TRACK_CHI2NDOF`, `Lc_K_TRACK_CHI2NDOF`, `Lc_pi_TRACK_CHI2NDOF` which shows the χ^2 per degree of freedom for the 3 children particles of Λ_c^+ and `Lc_DIRA_OWNPV` which is the directional angle of the Λ_c^+ with respect to its primary vertex, show slight disagreement as seen from Figure 7.7–7.8. This is therefore a source of systematic uncertainty. The MC is weighted using a Gradient Boosted reweighter [106] for the variables so that they match the data. New efficiency maps are computed with the weighted MC and the changes are propagated to compute the branching fraction. The change of the branching fraction from the baseline value is taken to be the systematic uncertainty. The differences between the data and MC are common between runs. This is thus considered as a completely correlated source of uncertainty.

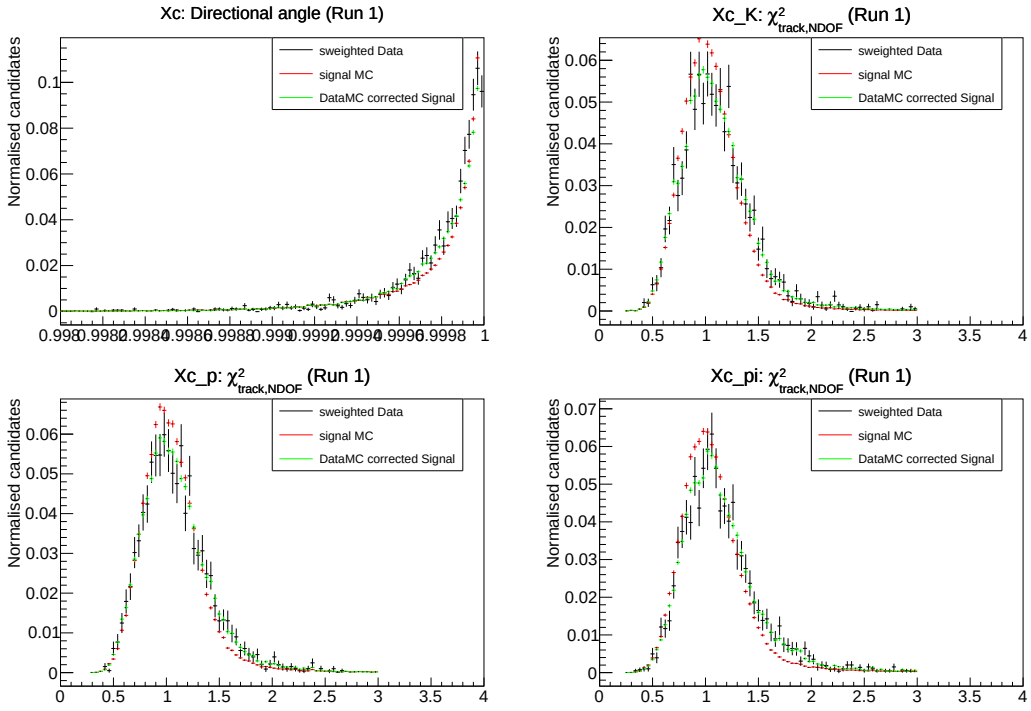

Figure 7.7: Comparison of *sWeight*ed data with MC distributions for the MVA input variables using $B^- \to \Lambda_c^+ \overline{p}\pi^-$ in Run I.

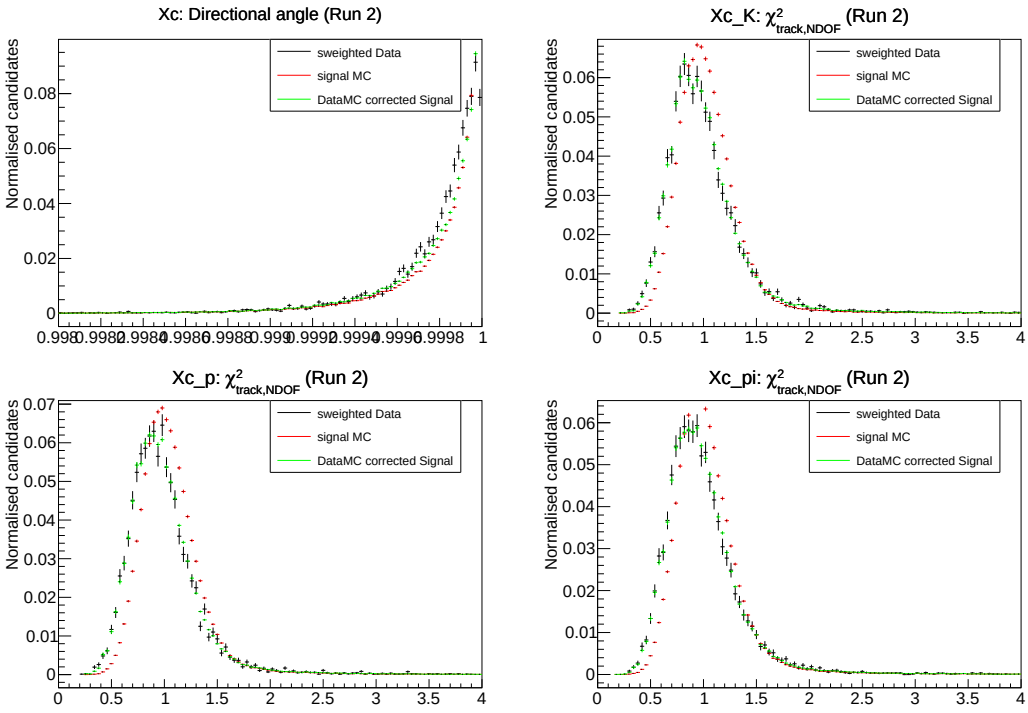

Figure 7.8: Comparison of *sWeight*ed data with MC distributions for the MVA input variables using $B^- \to \Lambda_c^+ \overline{p}\pi^-$ in Run II.

7.2.4 b baryon production kinematics

A further source of systematic uncertainty is due to the possibly imperfect correction of the baryon production kinematics as discussed in Chapter 6. This is accounted by correcting only the p_{T} distribution of the MC to match the data as opposed to both p_{T} and η distributions. The corrected MC is used to recalculate the efficiency maps and the shift in the branching fraction value with respect to the baseline value is considered as the systematic uncertainty.

7.2.5 Data-MC material mismatch

The final state particles of this analysis, namely pions, kaons and protons, have different probabilities of interaction with the detector material. This affects the efficiency of reconstruction. There is a possibility that the amount of material that is taken into account in the simulation differs to that of the true detector. This gives rise to another source of systematic uncertainty. The maximum potential data-MC mismatch in the material modelling of the detector is estimated to be 10%. On including the hadronic interaction probability, taken from Refs. [107, 108], there is 0.23%, 0.75% and 0.98% systematic uncertainties corresponding to per π/K, π/p and K/p difference in the final states of the branching fraction ratios respectively. The differences between the data and MC material mismatch are common between runs. This is thus considered as a

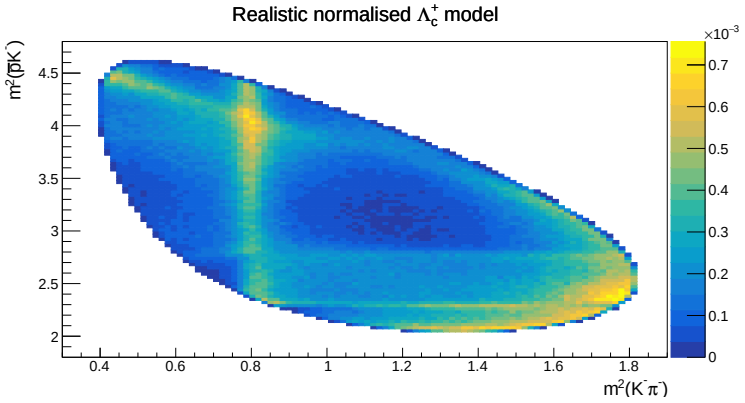

Figure 7.9: Distribution of normalised weights corresponding to the Dalitz plot model of $\Lambda_c^+ \to pK^-\pi^+$.

completely correlated source of uncertainty.

7.2.6 Λ_c^+ decay model and baryon polarisation effects

Λ_c^+-ecay model

The MC samples are generated by assuming a uniform distribution of the $\Lambda_c^+ \to pK^-\pi^+$ decay in phase space instead of a realistic model. This is therefore a source of systematic. Since both the numerator and the denominator of the branching fraction ratio results use $\Lambda_c^+ \to pK^-\pi^+$ as the secondary decay, the effect of this expected to be negligible. Nonetheless, it is checked as a source of systematic uncertainty. This is corrected by weighting the MC samples according to a realistic Dalitz plot model of $\Lambda_c^+ \to pK^-\pi^+$ decay as obtained in Ref. [109]. A normalised distribution of the weights is shown in Figure 7.9. The efficiency maps are re-computed from the corrected simulation and the changes are propagated to determine the branching fractions. The shift in the results from the baseline value is taken to be the systematic uncertainty.

Λ_c^+ polarisation

The Λ_c^+ can be polarised. This polarisation could differ in numerator and denominator modes of the branching fractions depending on the intermediate resonances in the decays. This would result in biases in the determination of the efficiency which would not cancel. Such effects would show up in one or more distributions of the angular variables defined in the Λ_c^+ rest frame. The frame of reference is defined as : the x-axis as the lab frame momentum direction of Λ_c^+, the z-axis as the cross product of the beam axis and x-axis which also corresponds to the polarisation axis of Λ_c^+ and the y-axis as the cross product of the z-axis and x-axis. The angular variables are then defined following Ref. [110] as : i) θ_p — the polar angle between the z-axis and the direction in which the proton is emitted from the Λ_c^+ decays; ii) ϕ_p — the azimuthal angle of

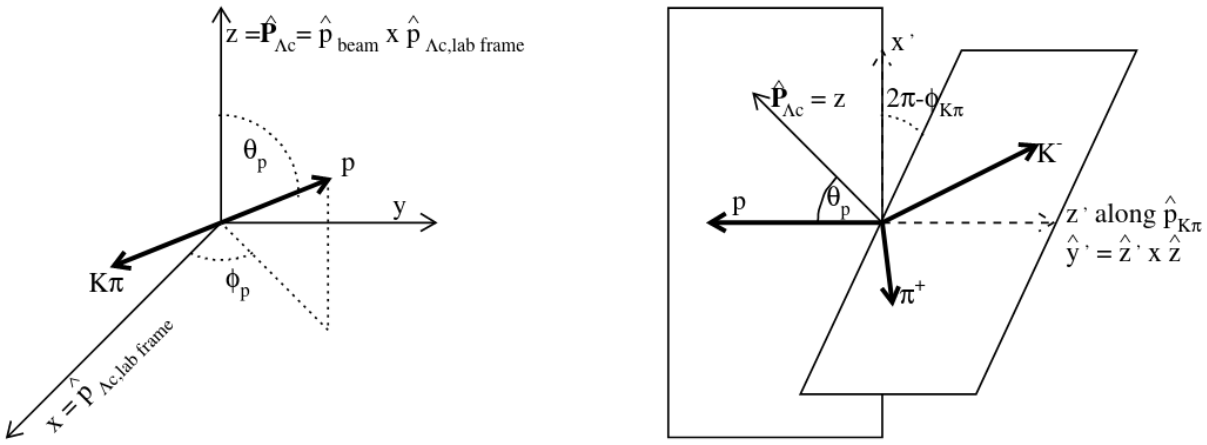

Figure 7.10: Pictorial representation of the angular variables sensitive to Λ_c^+ polarisation, taken from Ref. [110].

the direction of the Λ_c^+ proton, defined in the plane normal to the z-axis and relative to the Λ_c^+ direction in the lab frame; iii) $\phi_{K\pi}$ — the angle between the plane defined by the directions of the kaon and the pion emitted in the Λ_c^+ decay and the plane formed by the proton momentum and the z-axis. A representation of the angles can be seen in Figure 7.10

It can be seen from Figure 7.11, that the *sWeight*ed data and MC distribution for the three angles are in good agreement, hence we do not assign any systematic uncertainty due to this.

b baryon polarisation

There could also be systematics due to potential polarisation of the Ξ_b^- and Ω_b^- baryons. However, no studies so far have measured such effects for Ξ_b^- and Ω_b^-. Thus, we expect them to be small as observed for Λ_b^0 baryons [54, 111] and do not assign any associated systematic uncertainty.

7.2.7 Square Dalitz plot binning

The variation of the efficiency is studied with respect to the Dalitz plot map. This assumes that the efficiency within each bin of the map does not vary significantly. This is tested by changing the binning of the Dalitz plot map. The baseline efficiency maps are considered to be the finest possible binning of the Dalitz plot. The alternative binning is chosen coarser than the baseline as is summarised in Table 7.2. The branching fraction is re-evaluated using the alternative binning. The shift in the result is assigned as the systematic uncertainty. Any effect due to this would be common between runs. Thus, this is considered as a completely correlated source of systematic uncertainty.

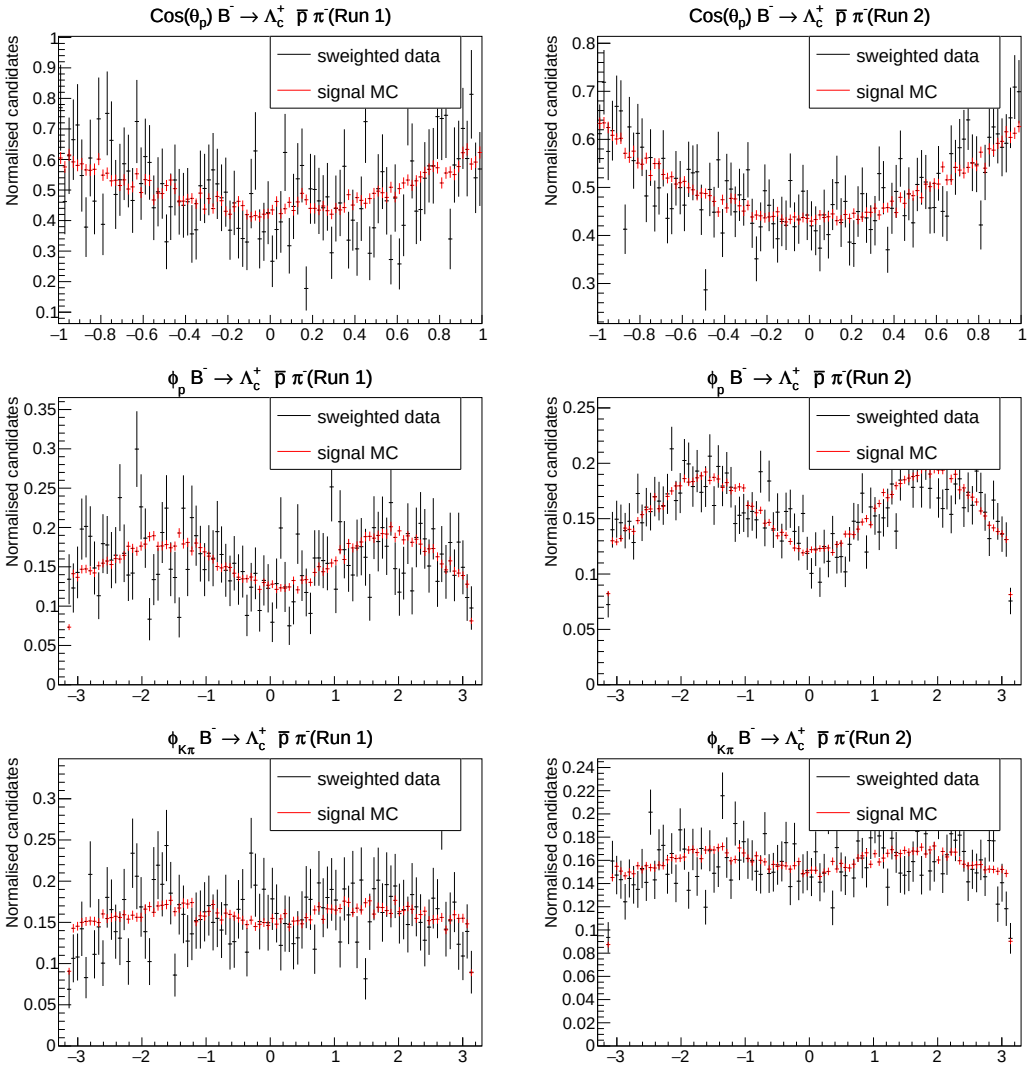

Figure 7.11: Distribution of the Λ_c^+ angular variables for *sWeighted* $B^- \to \Lambda_c^+ \overline{p}\pi^-$ data compared to the corresponding MC sample for (left) Run I and (right) Run II.

Table 7.2: Square Dalitz plot binning schemes for baseline and alternative efficiency maps. The quantities given correspond to the numbers of bins in both axes of the square Dalitz plots.

Year	Baseline # bins	Alternative # bins
2011	15	10
2012	20	10
2015	15	10
2016	20	10
2017	20	10
2018	20	10

7.2.8 PID

As mentioned in Section 4.1.2, the PID variables are corrected using `PIDcorr` package. These corrected variable are used to compute reliable efficiencies. Any assumptions in the technique would contribute to potential systematic uncertainty as described below.

- Source 1 - Finite statistics of calibration samples : The calibration samples used to correct the PID variables have finite statistics. The PIDcorr package provides an alternative template to correct the PID variables. The efficiency maps are computed again and the branching fractions are re-evaluated with the changes in the results assigned as the systematic uncertainties.
- Source 2 - Parameterisation procedure : The distribution of the PID variables in the control samples are parameterised using a kernel density estimation (KDE) procedure. The uncertainty due this procedure is accounted for by changing the width of the kernel compared to the standard procedure. An alternative template provides a different kernel width to parameterise the samples. Again the efficiency maps are computed again and the branching fraction is re-evaluated and the changes in the results are assigned as the systematic uncertainties.
- Source 3 - Disagreement between data and MC is seen in variables that characterise the detector occupancy, for example `nTracks`. The PID performance depends on the detector occupancy. This implies that the `PIDcorr` technique may not fully correct for data-MC differences, giving rise to systematic uncertainties. The impact is estimated by scaling the `nTracks` distribution by the ratio of the mean of `nTracks` from *sWeight*ed data and MC as also shown in Table 7.3. The `PIDcorr` procedure is performed again and the new efficiency maps are generated. The corresponding shifts in the branching fraction results with respect to the baseline values are assigned as the systematic uncertainties.

The combined systematic uncertainty due to the use of `PIDcorr` is determined as the sum in quadrature of the systematic uncertainties from the three sources. The largest systematic uncertainty among the three sources is due to the parametrisation of the control samples. Any effect due to this is expected to be common in both runs. Hence, this is considered as completely correlated source of systematic uncertainty.

7.2.9 Tracking efficiency correction

Another systematic arises due to the tracking procedure. The track reconstruction efficiency needs to be corrected in MC. This is done using official LHCb correction maps [112]. These corrections are provided in bins of kinematics, in particular p_T and η as shown in Figure 7.12.

Table 7.3: Mean of the distribution of `nTracks` in MC in Run I and Run II, with values from *sWeight*ed data also provided for channels with reasonably large and significant signal yields.

	Run I			Run II		
	Ratio	Data	MC	Ratio	Data	MC
$B^- \to \Lambda_c^+ \overline{p}\pi^-$	1.09	140.4	128.9	1.14	145.0	127.5
$B^- \to \Lambda_c^+ \overline{p}K^-$	1.04	132.0	127.5	1.10	140.4	127.4
$\Xi_b^- \to \Lambda_c^+ K^- K^-$			113.4			114.9
$\Xi_b^- \to \Lambda_c^+ K^- \pi^-$	1.18	135.7	114.8	1.28	147.0	115.1
$\Xi_b^- \to \Lambda_c^+ \pi^- \pi^-$			115.8			115.6
$\Omega_b^- \to \Lambda_c^+ K^- K^-$			111.1			112.8
$\Omega_b^- \to \Lambda_c^+ K^- \pi^-$			111.6			113.3
$\Omega_b^- \to \Lambda_c^+ \pi^- \pi^-$			111.5			113.4

The efficiency is recomputed using these corrections by combining them for all the final state particles. The corresponding shift in the branching fraction with respect to the baseline value is adopted as the systematic uncertainty. These corrections are independent between different runs. Thus this source of systematic uncertainty is considered to be completely correlated between Run I and Run II.

7.2.10 `L0Hadron` corrections

The efficiency of the `L0Hadron` trigger is difficult to estimate from the simulation as it depends on the ageing of the calorimeter and detector occupancy. Thus a correction to the efficiency is needed from data calibration samples. The standard efficiency tables [113] for data are determined from calibration samples for each type of final state particle and for each data-taking year and polarity. These tables are obtained as a function of the transverse energy E_{T}. The efficiency from the data is obtained as a function of the square Dalitz plot. Similar distributions are obtained from the MC samples by selecting the events satisfying `L0Global_TIS&&L0Hadron_TOS` and normalising to the events that satisfy `L0Global_TIS`. The data and MC histograms that are obtained are divided to get a data/MC correction histogram for each of the decay samples under consideration. The correction histograms for the $B^- \to \Lambda_c^+ \overline{p}\pi^-$ and $\Xi_b^- \to \Lambda_c^+ K^- \pi^-$ samples are shown in Figure 7.13 and Figure 7.14 respectively. These data/MC corrections are applied only to those events that satisfy the `L0Hadron_TOS` requirement. Thus the efficiency maps for the events satisfying `L0Hadron_TOS` and `L0Global_TIS&&!L0Hadron_TOS` are computed separately. Thus the total efficiency will be divided into the sum of the two histograms as $\epsilon^{\mathrm{tot}} = \epsilon^{\mathrm{tot}}_{\texttt{TOS}} + \epsilon^{\mathrm{tot}}_{\texttt{TIS\&\&!TOS}}$. The data/MC correction is applied to the $\epsilon^{\mathrm{tot}}_{\texttt{TOS}}$ term. The two terms are then combined by taking into account the amounts of `L0Hadron_TOS` and `L0Global_TIS&&!L0Hadron_TOS` in data, as

$$\epsilon_c^{\mathrm{tot}} orr = \frac{f^{\mathrm{data}}_{\texttt{TOS}}}{f^{\mathrm{MC}}_{\texttt{TOS}}} \epsilon^{\mathrm{tot}}_{\texttt{TOS}} + \frac{f^{\mathrm{data}}_{\texttt{TIS\&\&!TOS}}}{f^{\mathrm{MC}}_{\texttt{TIS\&\&!TOS}}} \epsilon^{\mathrm{tot}}_{\texttt{TIS\&\&!TOS}} \,, \tag{7.1}$$

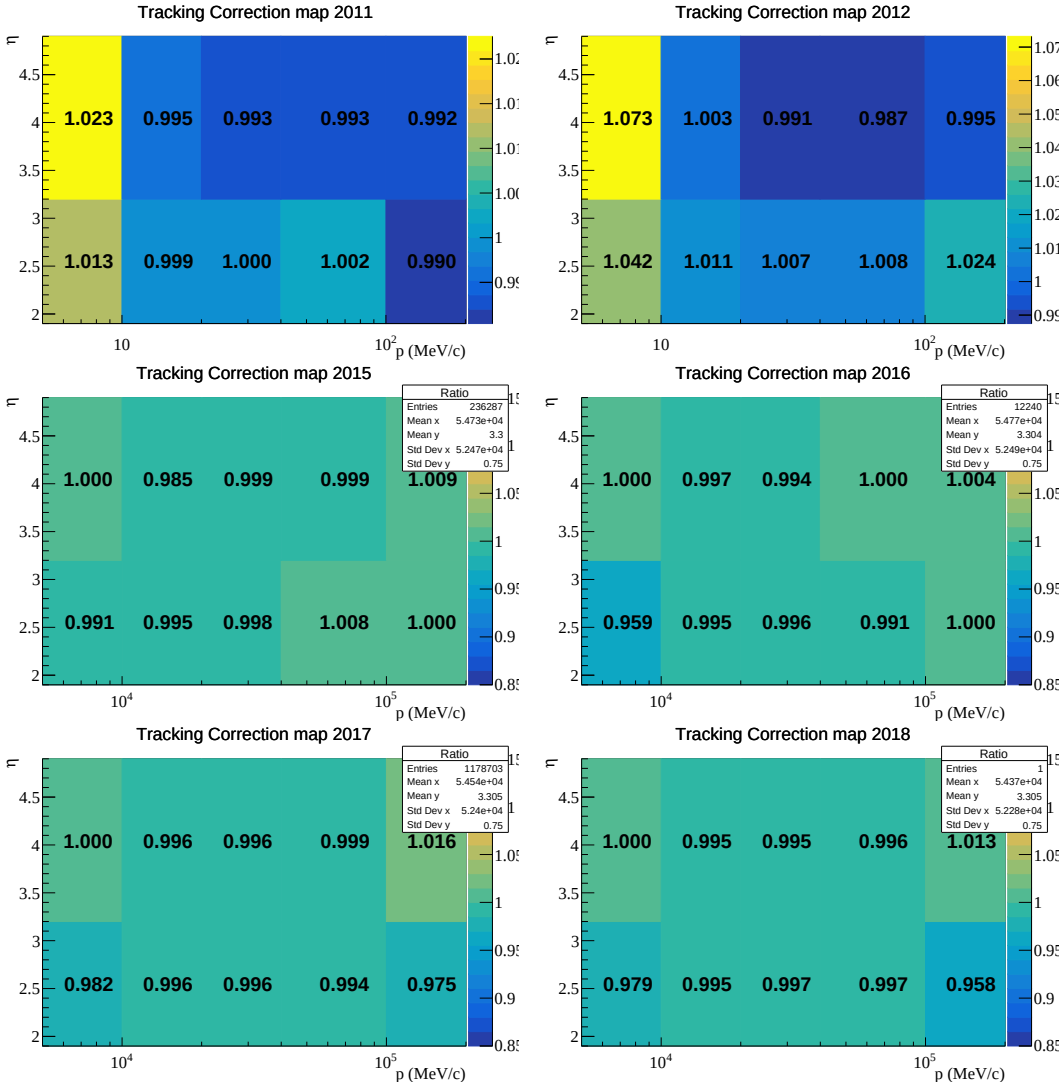

Figure 7.12: Tracking efficiency correction maps for different years.

where, f terms are the fractions of the given category in data and MC and are obtained from the $B^- \to \Lambda_c^+ \overline{p}\pi^-$ sample, since it has the largest yield.

The new efficiency maps are evaluated and the changes are propagated to get the new branching fraction. The shift in the result is taken as the associated systematic uncertainty.

7.3 Summary of systematic uncertainty

The summary of the absolute systematic uncertainty for the different measurements of branching fractions, production rates and production asymmetry that have been performed in this thesis is given in Tables 7.4 to 7.9. The statistical uncertainties are also provided in the tables for

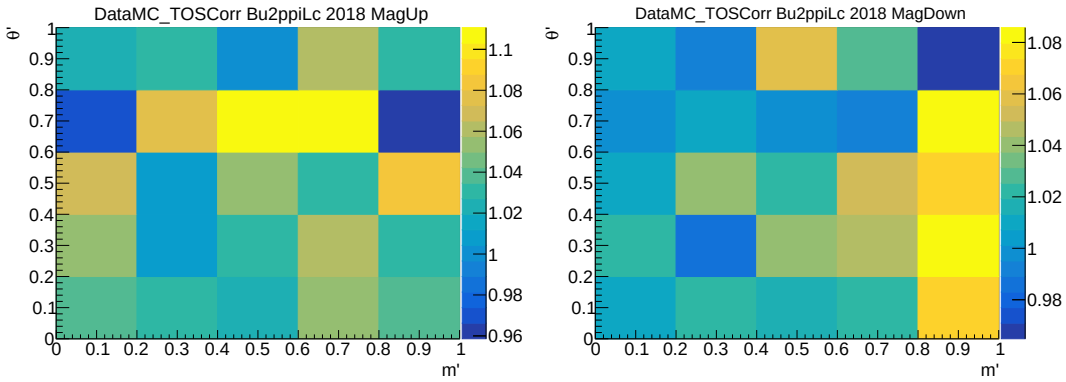

Figure 7.13: `L0Hadron` trigger efficiency data-MC correction maps for $B^- \to \Lambda_c^+ \overline{p}\pi^-$ decays.

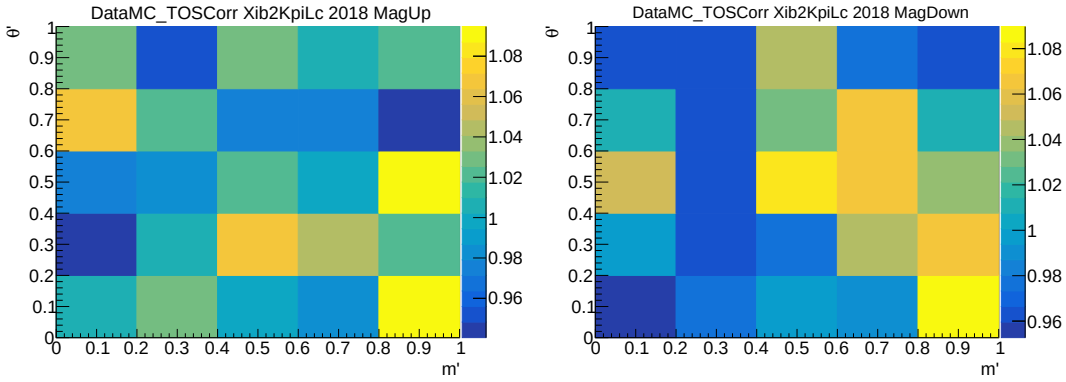

Figure 7.14: `L0Hadron` trigger efficiency data-MC correction maps for $\Xi_b^- \to \Lambda_c^+ K^- \pi^-$ decays.

comparison. The total systematic uncertainty is the sum in quadrature of the different sources of systematics. The correlated systematic uncertainties are : i) Fit model, ii) Multiple candidates, iii) Λ_b^0 veto, iv) $\Xi_b^- \to \Lambda_c^+ K^- \pi^-$ misID model, v) Unknown PHSP distributions, vi) Data-MC mismatch, vii) Production kinematics, viii) Data-MC material mismatch, ix) Λ_c^+ model, x) Square Dalitz plot binning, xi) PID resampling, xii) `L0Hadron`. Those that are completely uncorrelated are: i) Fixed parameters, ii) Fit bias, iii) Finite MC statistics, iv) Tracking correction.

Table 7.4: Absolute systematic uncertainties for the Run I ratios of branching fractions and production rates: [1] $\frac{\mathcal{B}(B^- \to \Lambda_c^+ \overline{p} K^-)}{\mathcal{B}(B^- \to \Lambda_c^+ \overline{p} \pi^-)}$, [2] $\frac{f_{\Xi_b^-}}{f_{B^-}} \cdot \frac{\mathcal{B}\left(\Xi_b^- \to \Lambda_c^+ K^- K^-\right)}{\mathcal{B}\left(B^- \to \Lambda_c^+ \overline{p} \pi^-\right)}$, [3] $\frac{f_{\Xi_b^-}}{f_{B^-}} \cdot \frac{\mathcal{B}\left(\Xi_b^- \to \Lambda_c^+ K^- \pi^-\right)}{\mathcal{B}\left(B^- \to \Lambda_c^+ \overline{p} \pi^-\right)}$, [4] $\frac{f_{\Omega_b^-}}{f_{B^-}} \cdot \frac{\mathcal{B}\left(\Omega_b^- \to \Lambda_c^+ K^- K^-\right)}{\mathcal{B}\left(B^- \to \Lambda_c^+ \overline{p} \pi^-\right)}$, [5] $\frac{\mathcal{B}\left(\Xi_b^- \to \Lambda_c^+ K^- K^-\right)}{\mathcal{B}\left(\Xi_b^- \to \Lambda_c^+ K^- \pi^-\right)}$.

	[1]	[2]	[3]	[4]	[5]
Fit model	0.0001	0.0002	0.0032	0.0003	0.0008
Fixed parameters	0.0004	0.0001	0.0014	0.0001	0.0014
Fit bias	0.0005	0.0005	0.0013	0.0005	0.0049
Multiple candidates	0.0001	0.0001	0.0011	0.0000	0.0009
Λ_b^0 veto	0.0000	0.0001	0.0003	0.0000	0.0003
$\Xi_b^- \to \Lambda_c^+ K^- \pi^-$ misID model	0.0000	0.0000	0.0001	0.0000	0.0000
Finite MC statistics	0.0010	0.0007	0.0022	0.0004	0.0061
Unknown PHSP distributions	0.0000	0.0000	0.0000	0.0000	0.0000
Data-MC mismatch	0.0002	0.0006	0.0018	0.0001	0.0066
Production kinematics	0.0000	0.0021	0.0280	0.0008	0.0004
Data-MC material mismatch	0.0001	0.0001	0.0011	0.0001	0.0002
Λ_c^+ model	0.0014	0.0002	0.0014	0.0005	0.0028
Square Dalitz plot binning	0.0003	0.0001	0.0005	0.0001	0.0016
PID resampling	0.0003	0.0002	0.0021	0.0001	0.0025
Tracking correction	0.0004	0.0001	0.0001	0.0000	0.0011
`L0Hadron`	0.0009	0.0000	0.0020	0.0000	0.0018
Subtotal (uncorrelated)	0.0019	0.0009	0.0032	0.0008	0.0085
Subtotal (correlated)	0.0011	0.0022	0.0284	0.0009	0.0076
Total (relative)	0.0527	0.4921	0.4776	0.3685	0.1408
Total systematic (absolute)	0.0021	0.0024	0.0286	0.0012	0.0114
Total statistical (absolute)	0.0055	0.0037	0.0116	0.0023	0.0337

Table 7.5: Absolute systematic uncertainties for the Run I ratios of branching fractions and production rates: [6] $\frac{f_{\Xi_b^-}}{f_{B^-}} \cdot \frac{\mathcal{B}\left(\Xi_b^- \to \Lambda_c^+ \pi^- \pi^-\right)}{\mathcal{B}\left(B^- \to \Lambda_c^+ \overline{p} \pi^-\right)}$, [7] $\frac{f_{\Omega_b^-}}{f_{B^-}} \cdot \frac{\mathcal{B}\left(\Omega_b^- \to \Lambda_c^+ K^- \pi^-\right)}{\mathcal{B}\left(B^- \to \Lambda_c^+ \overline{p} \pi^-\right)}$, [8] $\frac{f_{\Omega_b^-}}{f_{B^-}} \cdot \frac{\mathcal{B}\left(\Omega_b^- \to \Lambda_c^+ \pi^- \pi^-\right)}{\mathcal{B}\left(B^- \to \Lambda_c^+ \overline{p} \pi^-\right)}$, [9] $\frac{\mathcal{B}\left(\Xi_b^- \to \Lambda_c^+ \pi^- \pi^-\right)}{\mathcal{B}\left(\Xi_b^- \to \Lambda_c^+ K^- \pi^-\right)}$, [10] $\frac{\mathcal{B}\left(\Omega_b^- \to \Lambda_c^+ K^- \pi^-\right)}{\mathcal{B}\left(\Omega_b^- \to \Lambda_c^+ K^- K^-\right)}$, [11] $\frac{\mathcal{B}\left(\Omega_b^- \to \Lambda_c^+ \pi^- \pi^-\right)}{\mathcal{B}\left(\Omega_b^- \to \Lambda_c^+ K^- K^-\right)}$.

	[6]	[7]	[8]	[9]	[10]	[11]
Fit model	0.0016	0.0010	0.0027	0.0108	0.1827	0.5278
Fixed parameters	0.0001	0.0000	0.0000	0.0018	0.0095	0.0069
Fit bias	0.0002	0.0002	0.0002	0.0024	0.0502	0.0363
Multiple candidates	0.0005	0.0005	0.0000	0.0045	0.0926	0.0085
Λ_b^0 veto	0.0043	0.0000	0.0001	0.0386	0.0012	0.0126
$\Xi_b^- \to \Lambda_c^+ K^- \pi^-$ misID model	0.0001	0.0000	0.0000	0.0010	0.0013	0.0025
Finite MC statistics	0.0001	0.0000	0.0000	0.0017	0.0251	0.0159
Unknown PHSP distributions	0.0022	0.0005	0.0003	0.0196	0.1005	0.0528
Data-MC mismatch	0.0006	0.0001	0.0001	0.0033	0.0078	0.0048
Production kinematics	0.0022	0.0004	0.0002	0.0062	0.0250	0.0107
Data-MC material mismatch	0.0001	0.0000	0.0000	0.0002	0.0009	0.0011
Λ_c^+ model	0.0002	0.0000	0.0000	0.0030	0.0300	0.0178
Square Dalitz plot binning	0.0003	0.0001	0.0000	0.0021	0.0178	0.0104
PID resampling	0.0005	0.0001	0.0001	0.0024	0.0104	0.0093
Tracking correction	0.0000	0.0000	0.0000	0.0003	0.0008	0.0002
`L0Hadron`	0.0003	0.0000	0.0000	0.0010	0.0089	0.0052
Subtotal (uncorrelated)	0.0004	0.0002	0.0002	0.0046	0.0643	0.0440
Subtotal (correlated)	0.0056	0.0013	0.0027	0.0455	0.2308	0.5310
Total (relative)	0.8762	1.1606	3.6498	0.4241	0.6606	2.2621
Total systematic (absolute)	0.0057	0.0013	0.0027	0.0457	0.2396	0.5328
Total statistical (absolute)	0.0054	0.0021	0.0029	0.0491	0.4348	0.5670

Table 7.6: Absolute systematic uncertainties for the Run II ratios of branching fractions and production rates: [1] $\frac{\mathcal{B}(B^- \to \Lambda_c^+ \overline{p} K^-)}{\mathcal{B}(B^- \to \Lambda_c^+ \overline{p} \pi^-)}$, [2] $\frac{f_{\Xi_b^-}}{f_{B^-}} \cdot \frac{\mathcal{B}\left(\Xi_b^- \to \Lambda_c^+ K^- K^-\right)}{\mathcal{B}\left(B^- \to \Lambda_c^+ \overline{p} \pi^-\right)}$, [3] $\frac{f_{\Xi_b^-}}{f_{B^-}} \cdot \frac{\mathcal{B}\left(\Xi_b^- \to \Lambda_c^+ K^- \pi^-\right)}{\mathcal{B}\left(B^- \to \Lambda_c^+ \overline{p} \pi^-\right)}$, [4] $\frac{f_{\Omega_b^-}}{f_{B^-}} \cdot \frac{\mathcal{B}\left(\Omega_b^- \to \Lambda_c^+ K^- K^-\right)}{\mathcal{B}\left(B^- \to \Lambda_c^+ \overline{p} \pi^-\right)}$, [5] $\frac{\mathcal{B}\left(\Xi_b^- \to \Lambda_c^+ K^- K^-\right)}{\mathcal{B}\left(\Xi_b^- \to \Lambda_c^+ K^- \pi^-\right)}$.

	[1]	[2]	[3]	[4]	[5]
Fit model	0.0001	0.0000	0.0023	0.0001	0.0013
Fixed parameters	0.0002	0.0000	0.0006	0.0000	0.0004
Fit bias	0.0002	0.0001	0.0003	0.0001	0.0016
Multiple candidates	0.0001	0.0001	0.0001	0.0001	0.0009
Λ_b^0 veto	0.0000	0.0000	0.0001	0.0000	0.0002
$\Xi_b^- \to \Lambda_c^+ K^- \pi^-$ misID model	0.0000	0.0000	0.0000	0.0000	0.0001
Finite MC statistics	0.0005	0.0001	0.0009	0.0001	0.0016
Unknown PHSP distributions	0.0000	0.0000	0.0000	0.0000	0.0000
Data-MC mismatch	0.0005	0.0000	0.0029	0.0002	0.0019
Production kinematics	0.0002	0.0001	0.0043	0.0001	0.0009
Data-MC material mismatch	0.0001	0.0000	0.0007	0.0000	0.0001
Λ_c^+ model	0.0003	0.0001	0.0014	0.0002	0.0019
Square Dalitz plot binning	0.0001	0.0002	0.0002	0.0002	0.0024
PID resampling	0.0001	0.0001	0.0004	0.0001	0.0012
Tracking correction	0.0000	0.0000	0.0002	0.0000	0.0005
`L0Hadron`	0.0009	0.0000	0.0014	0.0000	0.0010
Subtotal (uncorrelated)	0.0006	0.0002	0.0018	0.0002	0.0030
Subtotal (correlated)	0.0011	0.0003	0.0059	0.0004	0.0038
Total (relative)	0.0318	0.1308	0.1027	0.1533	0.1195
Total systematic (absolute)	0.0013	0.0003	0.0062	0.0004	0.0049
Total statistical (absolute)	0.0025	0.0009	0.0041	0.0009	0.0116

Table 7.7: Absolute systematic uncertainties for the Run II ratios of branching fractions and production rates: [6] $\frac{f_{\Xi_b^-}}{f_{B^-}} \cdot \frac{\mathcal{B}\left(\Xi_b^- \to \Lambda_c^+ \pi^- \pi^-\right)}{\mathcal{B}\left(B^- \to \Lambda_c^+ \overline{p} \pi^-\right)}$, [7] $\frac{f_{\Omega_b^-}}{f_{B^-}} \cdot \frac{\mathcal{B}\left(\Omega_b^- \to \Lambda_c^+ K^- \pi^-\right)}{\mathcal{B}\left(B^- \to \Lambda_c^+ \overline{p} \pi^-\right)}$, [8] $\frac{f_{\Omega_b^-}}{f_{B^-}} \cdot \frac{\mathcal{B}\left(\Omega_b^- \to \Lambda_c^+ \pi^- \pi^-\right)}{\mathcal{B}\left(B^- \to \Lambda_c^+ \overline{p} \pi^-\right)}$, [9] $\frac{\mathcal{B}\left(\Xi_b^- \to \Lambda_c^+ \pi^- \pi^-\right)}{\mathcal{B}\left(\Xi_b^- \to \Lambda_c^+ K^- \pi^-\right)}$, [10] $\frac{\mathcal{B}\left(\Omega_b^- \to \Lambda_c^+ K^- \pi^-\right)}{\mathcal{B}\left(\Omega_b^- \to \Lambda_c^+ K^- K^-\right)}$, [11] $\frac{\mathcal{B}\left(\Omega_b^- \to \Lambda_c^+ \pi^- \pi^-\right)}{\mathcal{B}\left(\Omega_b^- \to \Lambda_c^+ K^- K^-\right)}$.

	[6]	[7]	[8]	[9]	[10]	[11]
Fit model	0.0008	0.0003	0.0005	0.0093	0.0657	0.1476
Fixed parameters	0.0000	0.0000	0.0000	0.0003	0.0029	0.0023
Fit bias	0.0001	0.0001	0.0001	0.0017	0.0173	0.0153
Multiple candidates	0.0001	0.0000	0.0000	0.0010	0.0046	0.0027
Λ_b^0 veto	0.0011	0.0002	0.0001	0.0138	0.0480	0.0142
$\Xi_b^- \to \Lambda_c^+ K^- \pi^-$ misID model	0.0001	0.0000	0.0000	0.0008	0.0000	0.0007
Finite MC statistics	0.0000	0.0000	0.0000	0.0002	0.0054	0.0027
Unknown PHSP distributions	0.0003	0.0001	0.0001	0.0040	0.0379	0.0168
Data-MC mismatch	0.0000	0.0000	0.0000	0.0005	0.0076	0.0030
Production kinematics	0.0001	0.0000	0.0000	0.0002	0.0051	0.0026
Data-MC material mismatch	0.0000	0.0000	0.0000	0.0000	0.0004	0.0004
Λ_c^+ model	0.0001	0.0000	0.0000	0.0006	0.0099	0.0106
Square Dalitz plot binning	0.0000	0.0000	0.0000	0.0000	0.0072	0.0065
PID resampling	0.0000	0.0000	0.0000	0.0003	0.0027	0.0014
Tracking correction	0.0000	0.0000	0.0000	0.0003	0.0006	0.0015
`L0Hadron`	0.0000	0.0000	0.0000	0.0002	0.0040	0.0018
Subtotal (uncorrelated)	0.0002	0.0001	0.0001	0.0019	0.0209	0.0190
Subtotal (correlated)	0.0014	0.0003	0.0005	0.0172	0.0908	0.1495
Total (relative)	1.1097	0.6899	2.0532	0.8459	0.5216	1.6217
Total systematic (absolute)	0.0014	0.0004	0.0005	0.0173	0.0932	0.1507
Total statistical (absolute)	0.0010	0.0005	0.0004	0.0135	0.1267	0.1182

Table 7.8: Absolute systematic uncertainties for the Run I production asymmetry of B^- meson as well as Ξ_b^- baryons for MagUp, MagDown and average over polarities: The total systematic uncertainty is the sum in quadrature of the contributions from different sources.

	B^- meson			Ξ_b^- baryon		
	MagUp	MagDown	MagAvg	MagUp	MagDown	MagAvg
Fit model	0.0329	0.0148	0.0085	0.0209	0.0043	0.0084
Fixed parameters	0.0011	0.0012	0.0001	0.0008	0.0034	0.0019
Multiple candidates	0.0007	0.0001	0.0003	0.0139	0.0008	0.0072
Λ_b^0 veto	0.0000	0.0000	0.0000	0.0079	0.0019	0.0028
$\Xi_b^- \to \Lambda_c^+ K^- \pi^-$ misID model	0.0000	0.0000	0.0000	0.0117	0.0012	0.0046
Finite MC statistics	0.0135	0.0114	0.0087	0.0255	0.0254	0.0183
Data-MC mismatch	0.0026	0.0036	0.0031	0.0023	0.0255	0.0127
Production kinematics	0.0012	0.0001	0.0006	0.0029	0.0108	0.0068
Data-MC material mismatch	0.0043	0.0043	0.0043	0.0043	0.0042	0.0042
Λ_c^+ model	0.0121	0.0169	0.0145	0.0004	0.0049	0.0009
Square Dalitz plot binning	0.0047	0.0094	0.0026	0.0051	0.0066	0.0055
PID resampling	0.0007	0.0024	0.0011	0.0109	0.0070	0.0069
Tracking correction	0.0010	0.0003	0.0003	0.0177	0.0041	0.0084
`L0Hadron`	0.0004	0.0008	0.0006	0.0047	0.0027	0.0038
Total systematic (absolute)	0.0382	0.0276	0.0199	0.0447	0.0401	0.0296
Total statistical (absolute)	0.0347	0.0328	0.0239	0.1333	0.1465	0.1007

Table 7.9: Absolute systematic uncertainties for the Run II production asymmetry of B^- meson as well as Ξ_b^- baryons for MagUp, MagDown and average over polarities: The total systematic uncertainty is the sum in quadrature of the contributions from different sources.

	B^- meson			Ξ_b^- baryon		
	MagUp	MagDown	MagAvg	MagUp	MagDown	MagAvg
Fit model	0.0019	0.0021	0.0001	0.0163	0.0076	0.0112
Fixed parameters	0.0002	0.0001	0.0001	0.0003	0.0010	0.0007
Multiple candidates	0.0002	0.0003	0.0002	0.0001	0.0027	0.0014
Λ_b^0 veto	0.0000	0.0000	0.0000	0.0069	0.0005	0.0035
$\Xi_b^- \to \Lambda_c^+ K^- \pi^-$ misID model	0.0000	0.0000	0.0000	0.0067	0.0008	0.0036
Finite MC statistics	0.0074	0.0081	0.0056	0.0145	0.0126	0.0098
Data-MC mismatch	0.0031	0.0018	0.0024	0.0019	0.0090	0.0056
Production kinematics	0.0003	0.0007	0.0002	0.0010	0.0058	0.0037
Data-MC material mismatch	0.0043	0.0043	0.0043	0.0042	0.0042	0.0042
Λ_c^+ model	0.0068	0.0020	0.0044	0.0150	0.0024	0.0061
Square Dalitz plot binning	0.0035	0.0004	0.0020	0.0128	0.0001	0.0062
PID resampling	0.0021	0.0015	0.0008	0.0020	0.0022	0.0017
Tracking correction	0.0002	0.0003	0.0002	0.0032	0.0003	0.0015
`L0Hadron`	0.0004	0.0007	0.0005	0.0052	0.0023	0.0038
Total systematic (absolute)	0.0122	0.0100	0.0089	0.0320	0.0194	0.0201
Total statistical (absolute)	0.0167	0.0167	0.0118	0.0733	0.0716	0.0516

Chapter 8

Results

8.1 Measurement strategy

8.1.1 Computing the yields

The true yield of a signal channel can be computed by dividing the measured yield from the fit (N_{fit}) by the efficiency. However, the dynamics of a three-body decay govern its phase space distribution. It can be seen from the efficiency maps obtained in Chapter 6 that the efficiency is not constant across the phase space. This variation needs to be taken into account in the calculation of the true yield. Thus, the efficiency maps are used to correct for this effect. This is done using signal weights for every event to subtract the contributions from the background. Thus the background-subtracted efficiency-corrected yield can be given as

$$N^{\text{corr}} = N^{\text{fit}}/\epsilon = \sum_{i=1}^{N} \frac{w_i}{\epsilon_i}, \tag{8.1}$$

where N is the total number of candidates for a given decay channel, and w_i and ϵ_i are the signal weight and efficiency of the event i and ϵ is the average efficiency obtained from the MC. The statistical uncertainty on this quantity is given by [102]

$$\sigma(N^{\text{corr}}) = \sqrt{\sum_{i=1}^{N} (\frac{w_i}{\epsilon_i})^2} \tag{8.2}$$

However, since the `sweights` are calculated from a separate fit where only the PDF yields are free parameters unlike baseline fit, it is necessary for the statistical uncertainty to be corrected by finding the difference between the nominal fit and the yields-only fit as

$$\sigma^{\text{shape}}(N) = \sqrt{\sigma^{\text{fit}}(N)^2 - \sigma^{\text{yields-only}}(N)^2} \tag{8.3}$$

where $\sigma^{\text{fit}}(N)$ and $\sigma^{\text{yields-only}}(N)$ are the uncertainties on the nominal fit and yields-only fit respectively. The corrected statistical uncertainty on Equation (8.2) is

$$\sigma^{\text{corr}}(N^{\text{corr}}) = \sqrt{\sigma(N^{\text{corr}})^2 + (\frac{N^{\text{corr}}}{N}\sigma^{\text{shape}}(N))^2} \tag{8.4}$$

For channels where significant signal is not observed, we cannot determine the phase space distribution in order to perform the candidate-by-candidate efficiency correction. In this case the corrected yield is obtained as the ratio of the fit yields and the average efficiency from the MC. The average efficiency is the mean of the square Dalitz plot map.

8.1.2 Determination of branching fractions

The relative production rate of two channels A and B can simply be obtained by taking the ratio of the background subtracted and efficiency corrected yields of the two channels as

$$\frac{f_A}{f_B}\frac{\mathcal{B}_A}{\mathcal{B}_B} = \frac{N_A^{\text{corr}}}{N_B^{\text{corr}}} \tag{8.5}$$

Where, f is the fragmentation fraction of the parent particle, $\mathcal{B}$ is the branching fraction and N is the yield, all with the relevant channel A and B indicated in the subscript. The statistical uncertainty on this quantity is given by

$$\sigma^2 = \frac{f_A}{f_B}\frac{\mathcal{B}_A}{\mathcal{B}_B}\left(\frac{\sigma_{N_A}^2}{N_A^2} + \frac{\sigma_{N_B}^2}{N_B^2} - 2\frac{\sigma_{N_A}}{N_A}\frac{\sigma_{N_B}}{N_B}\rho_{AB}\right), \tag{8.6}$$

where ρ_{AB} is the correlation between the two fitted yields. The last term is negligible in our calculation. Using these formulations the measurements can be obtained separately for Run I and Run II, since we compute the sWeights and efficiencies independently for both runs. Additionally, with proper consideration of correlations affecting systematic uncertainties, the results can be combined to provide a single measurement as discussed next.

8.1.3 Combining branching fractions for Run I and Run II

Since the production rate can vary with the centre-of-mass energy of the pp collision, we combine the relative branching fractions of the decays with same parent particle following Equation (8.5).

The combination can be done using the following equation that minimise the χ^2,

$$\mathcal{B}_{\text{comb}} = \frac{\frac{\mathcal{B}_{\text{Run I}}}{\delta\mathcal{B}^2_{\text{Run I}}} + \frac{\mathcal{B}_{\text{Run II}}}{\delta\mathcal{B}^2_{\text{Run II}}}}{\frac{1}{\delta\mathcal{B}^2_{\text{Run I}}} + \frac{1}{\delta\mathcal{B}^2_{\text{Run II}}}} \quad \text{with} \quad \delta\mathcal{B}_{\text{comb}} = \frac{1}{\sqrt{\frac{1}{\delta\mathcal{B}^2_{\text{Run I}}} + \frac{1}{\delta\mathcal{B}^2_{\text{Run II}}}}}. \tag{8.7}$$

where $\mathcal{B}_{\text{comb}}$ is the combined branching fraction and can be written as a linear combination of $\mathcal{B}_{\text{Run I}}$ and $\mathcal{B}_{\text{Run II}}$ as

$$\mathcal{B}_{\text{comb}} = F\,\mathcal{B}_{\text{Run I}} + (1-F)\,\mathcal{B}_{\text{Run II}}\,, \tag{8.8}$$

where F is a function of the uncertainties $\delta\mathcal{B}_{\text{Run I}}$ and $\delta\mathcal{B}_{\text{Run II}}$.

Correlations of the systematic uncertainties needs to be taken into account in this combination. We thus separate the systematic uncertainties into those that are completely uncorrelated (*i.e.* 0% correlation) and those that are completely correlated (*i.e.* 100% correlation), as done in Chapter 7. The central value of $\mathcal{B}_{\text{comb}}$ is computed including only the former sources. The total uncorrelated uncertainty of the branching fraction for each Run I and Run II can be given by, $(\delta\mathcal{B}_{\text{Run I,II}})_{\text{uncorr}} = \sqrt{\sigma^2_{\text{stat}} + \sigma^{\text{uncorr }2}_{\text{syst}}}$, where the values of σ_{stat} and $\sigma^{\text{uncorr}}_{\text{syst}}$ are mentioned in Table 7.4–7.7.

Thus, using Equation (8.7) and Equation (8.8), the value F can be determined. Furthermore, the statistical and uncorrelated systematic uncertainties on the combined value can then be obtained with simple error propagation, as

$$(\delta\mathcal{B}_{\text{comb}})_{\text{stat}} = \sqrt{F^2\,(\delta\mathcal{B}_{\text{Run I}})^2_{\text{stat}} + (1-F)^2\,(\delta\mathcal{B}_{\text{Run II}})^2_{\text{stat}}}\,. \tag{8.9}$$

$$(\delta\mathcal{B}_{\text{comb}})_{\text{uncorr}} = \sqrt{F^2\,(\delta\mathcal{B}_{\text{Run I}})^2_{\text{uncorr}} + (1-F)^2\,(\delta\mathcal{B}_{\text{Run II}})^2_{\text{uncorr}}}\,. \tag{8.10}$$

The correlated systematic uncertainties can also be obtained with simple error propagation, adding linearly rather than in quadrature,

$$(\delta\mathcal{B}_{\text{comb}})_{\text{corr}} = F\,(\delta\mathcal{B}_{\text{Run I}})_{\text{corr}} + (1-F)\,(\delta\mathcal{B}_{\text{Run II}})_{\text{corr}}\,, \tag{8.11}$$

where $(\delta\mathcal{B})_{\text{corr}} = \sigma^{\text{corr}}_{\text{syst}}$ same as the correlated systematic uncertainty.

8.1.4 Determination of production asymmetry

The production asymmetry of a particle is given in terms of the production cross-section of the particle as

$$\mathcal{A}_{\text{prod}}\,(pp \to X_b) = \frac{\sigma(pp \to X_b) - \sigma(pp \to \bar{X}_b)}{\sigma(pp \to X_b) + \sigma(pp \to \bar{X}_b)} \tag{8.12}$$

It is defined between the particle and its antiparticle ($B^- - B^+$, $\Xi_b^- - \overline{\Xi}_b^+$, $\Omega_b^- - \overline{\Omega}_b^+$). However, what we measure is the asymmetry of the true yields between the decay of the particle and its antiparticle which is given by

$$\mathcal{A}_{\text{meas}}\,(X_b \to Y) = \frac{N^{\text{corr}}(X_b \to Y) - N^{\text{corr}}(\bar{X}_b \to \bar{Y})}{N^{\text{corr}}(X_b \to Y) + N^{\text{corr}}(\bar{X}_b \to \bar{Y})} = \frac{\sum_{i=1}^{n_Y} \frac{w_i}{\epsilon_i} - \sum_{i=1}^{n_{\bar{Y}}} \frac{w_i}{\bar{\epsilon}_i}}{\sum_{i=1}^{n_Y} \frac{w_i}{\epsilon_i} + \sum_{i=1}^{n_{\bar{Y}}} \frac{w_i}{\bar{\epsilon}_i}}\,. \tag{8.13}$$

The production asymmetry can, in general, be related to the measured asymmetry as

$$\mathcal{A}_{\text{meas}}\left(X_b \to Y\right) = \mathcal{A}_{CP}\left(X_b \to Y\right) + \mathcal{A}_{\text{prod}}\left(X_b \to Y\right) + \mathcal{A}_{\text{det}}\left(X_b \to Y\right) . \tag{8.14}$$

where $\mathcal{A}_{\text{det}}$ is the detection asymmetry between the particle and antiparticle decays. However, in our case the detection asymmetry is taken into account while computing the true yield, if the efficiency maps used to calculate them are computed separately for charge conjugate decays and is taken into account while calculating the measured asymmetry from Equation (8.13). This explains that including the $\mathcal{A}_{\text{det}}$ in Equation (8.14) is not necessary, assuming that the MC-based estimates of efficiency accurately describes the detection asymmetry. The imperfection in the estimate would be a source of systematic. Furthermore, there is only one Feynman diagram contributing to the $\Xi_b^- \to \Lambda_c^+ K^- \pi^-$ and $B^- \to \Lambda_c^+ \overline{p} \pi^-$ decays, which are mediated exclusively by $b \to c$ quark-level transitions. Thus, no CP violation is expected from these decays, and therefore $\mathcal{A}_{\text{CP}} = 0$. Ultimately, with this approach the production asymmetry is the same as the measured asymmetry $\mathcal{A}_{\text{prod}} = \mathcal{A}_{\text{meas}}$.

8.2 Observation of new channels

To claim an evidence for or observation for a decay channel we need to compute the significance of the signal. This is done by obtaining likelihood scans, preferably with respect to the branching fractions or production rate ratios. This would facilitate combination of the likelihood scans for Run I and Run II in order to obtain a combined significance. The likelihood function from the fit, which includes statistical uncertainty only, is convoluted with a Gaussian of width equal to the total systematic uncertainty. Doing so leads to an underestimate of the combined significance as only the uncertainties related to fits should be included. Nonetheless, the effect is small and we only need to know if the significance is $> 3\sigma$ or $> 5\sigma$. To compute the significance with respect to branching fraction, we consider the $B^- \to \Lambda_c^+ \overline{p} \pi^-$ channel as the denominator mode which is fitted independently to the channel in question. This minimises the contribution from the denominator mode to the significance. The likelihood scans for Run I and Run II are shown in Figure 8.1. The combined scans are shown in Figure 8.2. These plots show the negative log-likelihood functions. From the mass fits, it can be seen that the channels $B^- \to \Lambda_c^+ \overline{p} K^-$ and $\Xi_b^- \to \Lambda_c^+ K^- \pi^-$ have signals with significance $> 15\sigma$. Thus, further quantification of the significance of these channels is considered to be unnecessary. The significances accounting for systematic uncertainties, for all the other channels showing peaks in the mass fits are given in Table 8.1. Thus the channels that are newly observed at LHCb are.

- $B^- \to \Lambda_c^+ \overline{p} K^- > 15\sigma$
- $\Xi_b^- \to \Lambda_c^+ K^- \pi^- > 15\sigma$

- $\Xi_b^- \to \Lambda_c^+ K^- K^- > 5\sigma$
- $\Omega_b^- \to \Lambda_c^+ K^- K^- > 5\sigma$

Table 8.1: Significances of different b-baryon decay modes obtained from the ratio of their fragmentation and branching fractions with respect to $B^- \to \Lambda_c^+ \overline{p}\pi^-$.

Decay	Run I	Run II	Combined
Statistical uncertainties only			
$\Xi_b^- \to \Lambda_c^+ K^- K^-$	3.6	5.5	6.3
$\Omega_b^- \to \Lambda_c^+ K^- K^-$	4.2	7.9	8.8
Including systematic uncertainties			
$\Xi_b^- \to \Lambda_c^+ K^- K^-$	3.5	5.2	5.9
$\Omega_b^- \to \Lambda_c^+ K^- K^-$	3.6	6.9	7.5

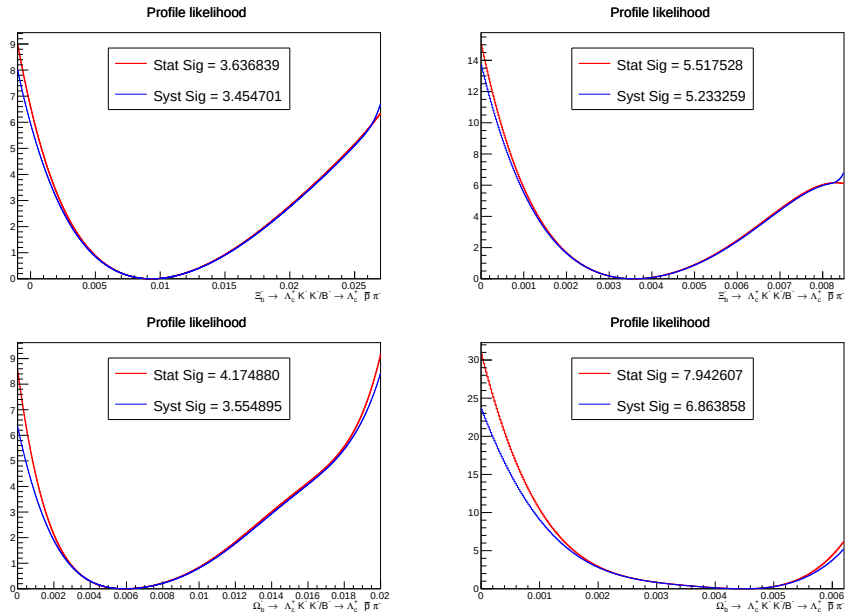

Figure 8.1: Negative log-likelihood curves as a function of the ratio of fragmentation and branching fractions of (top to bottom) $\Xi_b^- \to \Lambda_c^+ K^- K^-$, $\Omega_b^- \to \Lambda_c^+ K^- K^-$ with respect to the $B^- \to \Lambda_c^+ \overline{p}\pi^-$ control channel, for (left) Run I and (right) Run II. Curves are shown with (red) statistical only and (blue) including also systematic uncertainties.

8.3 Relative branching fractions and production rate

The background-subtracted and efficiency-corrected yields ($N^{\rm corr}$) of different channels are computed and are quoted in Table 8.2. The table also quotes the yields obtained from the simultaneous fits of the channels and the average efficiencies computed directly from the MC

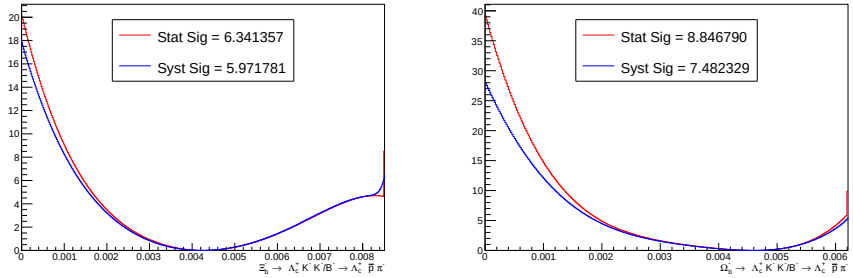

Figure 8.2: Negative log-likelihood curves as a function of the ratio of fragmentation and branching fractions of (left to right) $\Xi_b^- \to \Lambda_c^+ K^- K^-$, $\Omega_b^- \to \Lambda_c^+ K^- K^-$ with respect to the $B^- \to \Lambda_c^+ \overline{p}\pi^-$ control channel, for Run I and Run II combined, shown with (red) statistical only and (blue) including also systematic uncertainties.

for different runs. We also quote the yields from $N^{\rm fit}/\epsilon^{\rm SDP}$, the comparison of which with the ($N^{\rm corr}$) gives an idea of the impact of the candidate-by-candidate efficiency correction.

Table 8.2: Fitted yields, $N^{\rm fit}$ and corrected yields, $N^{\rm corr}$ as defined in Equation (8.1), for the signal and control channels. The efficiencies obtained directly from the MC samples generated with flat square Dalitz-plot models, $\epsilon^{\rm SDP}$ are also shown. Uncertainties are statistical only.

Decay	$N^{\rm fit}(10^3)$	$\epsilon^{\rm SDP}(10^{-4})$	$N^{\rm corr}(10^6)$	$N^{\rm fit}/\epsilon^{\rm SDP}(10^6)$
		Run I		
$B^- \to \Lambda_c^+ \overline{p} K^-$	0.066 ± 0.009	2.817 ± 0.002	0.266 ± 0.036	0.234 ± 0.031
$B^- \to \Lambda_c^+ \overline{p}\pi^-$	2.020 ± 0.046	3.609 ± 0.003	6.593 ± 0.159	5.597 ± 0.128
$\Xi_b^- \to \Lambda_c^+ K^- K^-$	0.009 ± 0.004	1.970 ± 0.002	0.052 ± 0.023	0.046 ± 0.018
$\Xi_b^- \to \Lambda_c^+ K^- \pi^-$	0.137 ± 0.014	2.229 ± 0.002	0.745 ± 0.074	0.615 ± 0.063
$\Xi_b^- \to \Lambda_c^+ \pi^- \pi^-$	0.023 ± 0.011	3.493 ± 0.002	0.081 ± 0.037	0.065 ± 0.032
$\Omega_b^- \to \Lambda_c^+ K^- K^-$	0.007 ± 0.003	2.119 ± 0.003	0.034 ± 0.015	0.032 ± 0.013
$\Omega_b^- \to \Lambda_c^+ K^- \pi^-$	0.003 ± 0.003	2.438 ± 0.003	0.028 ± 0.020	0.013 ± 0.014
$\Omega_b^- \to \Lambda_c^+ \pi^- \pi^-$	0.003 ± 0.006	3.740 ± 0.004	-0.000 ± 0.019	0.007 ± 0.017
		Run II		
$B^- \to \Lambda_c^+ \overline{p} K^-$	0.289 ± 0.018	5.585 ± 0.002	0.575 ± 0.036	0.517 ± 0.033
$B^- \to \Lambda_c^+ \overline{p}\pi^-$	8.406 ± 0.095	6.817 ± 0.003	14.54 ± 0.172	12.33 ± 0.139
$\Xi_b^- \to \Lambda_c^+ K^- K^-$	0.019 ± 0.005	4.459 ± 0.002	0.046 ± 0.013	0.043 ± 0.012
$\Xi_b^- \to \Lambda_c^+ K^- \pi^-$	0.471 ± 0.024	4.987 ± 0.003	1.109 ± 0.058	0.945 ± 0.048
$\Xi_b^- \to \Lambda_c^+ \pi^- \pi^-$	0.014 ± 0.009	6.215 ± 0.003	0.025 ± 0.018	0.022 ± 0.015
$\Omega_b^- \to \Lambda_c^+ K^- K^-$	0.023 ± 0.005	4.716 ± 0.003	0.054 ± 0.013	0.048 ± 0.011
$\Omega_b^- \to \Lambda_c^+ K^- \pi^-$	0.005 ± 0.003	5.284 ± 0.003	0.012 ± 0.008	0.009 ± 0.007
$\Omega_b^- \to \Lambda_c^+ \pi^- \pi^-$	-0.003 ± 0.004	6.545 ± 0.004	-0.012 ± 0.007	-0.005 ± 0.006

Using the background-subtracted and efficiency-corrected yields, we quote the results of the relative production rates, which are the ratios of the fragmentation fractions of the parent particles times the corresponding branching fractions as described in Section 8.1. The mode $B^- \to \Lambda_c^+ \overline{p}\pi^-$ is used as the normalisation mode. Therefore, we compute the production rates of all the other decay modes with respect to $B^- \to \Lambda_c^+ \overline{p}\pi^-$ mode. Further, since we also observed the decay $\Xi_b^- \to \Lambda_c^+ K^-\pi^-$ significantly, the production rates of all the Ξ_b^- decay modes are computed with respect with to $\Xi_b^- \to \Lambda_c^+ K^-\pi^-$. Similarly, observation of $\Omega_b^- \to \Lambda_c^+ K^- K^-$ above 5σ motivates the measurements of production rates of the Ω_b^- decay modes with respect to $\Omega_b^- \to \Lambda_c^+ K^- K^-$. In cases where the numerator and the denominator have the same parent particle, the relative production rate is equivalent to the branching fraction ratio, since the fragmentation fractions for both the numerator and denominator modes are the same. The results are computed separately for Run I and Run II and are quoted in Table 8.3 along with the statistical as well as systematic uncertainties.

The results for Run I and Run II are also combined following the procedure described in Section 8.1. Since the ratios of the fragmentation fractions and hence the production rates can vary between runs unlike the branching fractions, we combine the results of the branching fractions and obtain,

Table 8.3: Ratios of branching fractions and productions rates, with statistical and systematic uncertainties, separately for Run I and Run II.

	Run I	Run II
$\frac{\mathcal{B}(B^- \to \Lambda_c^+ \overline{p} K^-)}{\mathcal{B}(B^- \to \Lambda_c^+ \overline{p}\pi^-)}$	$0.0404 \pm 0.0056 \pm 0.0021$	$0.0395 \pm 0.0025 \pm 0.0013$
$\frac{f_{\Xi_b^-}}{f_{B^-}} \cdot \frac{\mathcal{B}\left(\Xi_b^- \to \Lambda_c^+ K^- K^-\right)}{\mathcal{B}\left(B^- \to \Lambda_c^+ \overline{p}\pi^-\right)}$	$0.0085 \pm 0.0037 \pm 0.0024$	$0.0032 \pm 0.0009 \pm 0.0003$
$\frac{f_{\Xi_b^-}}{f_{B^-}} \cdot \frac{\mathcal{B}\left(\Xi_b^- \to \Lambda_c^+ K^-\pi^-\right)}{\mathcal{B}\left(B^- \to \Lambda_c^+ \overline{p}\pi^-\right)}$	$0.1129 \pm 0.0121 \pm 0.0286$	$0.0763 \pm 0.0041 \pm 0.0062$
$\frac{f_{\Xi_b^-}}{f_{B^-}} \cdot \frac{\mathcal{B}\left(\Xi_b^- \to \Lambda_c^+ \pi^-\pi^-\right)}{\mathcal{B}\left(B^- \to \Lambda_c^+ \overline{p}\pi^-\right)}$	$0.0110 \pm 0.0054 \pm 0.0057$	$0.0015 \pm 0.0010 \pm 0.0014$
$\frac{f_{\Omega_b^-}}{f_{B^-}} \cdot \frac{\mathcal{B}\left(\Omega_b^- \to \Lambda_c^+ K^- K^-\right)}{\mathcal{B}\left(B^- \to \Lambda_c^+ \overline{p}\pi^-\right)}$	$0.0053 \pm 0.0023 \pm 0.0012$	$0.0037 \pm 0.0009 \pm 0.0004$
$\frac{f_{\Omega_b^-}}{f_{B^-}} \cdot \frac{\mathcal{B}\left(\Omega_b^- \to \Lambda_c^+ K^-\pi^-\right)}{\mathcal{B}\left(B^- \to \Lambda_c^+ \overline{p}\pi^-\right)}$	$0.0020 \pm 0.0021 \pm 0.00013$	$0.0006 \pm 0.0005 \pm 0.0004$
$\frac{f_{\Omega_b^-}}{f_{B^-}} \cdot \frac{\mathcal{B}\left(\Omega_b^- \to \Lambda_c^+ \pi^-\pi^-\right)}{\mathcal{B}\left(B^- \to \Lambda_c^+ \overline{p}\pi^-\right)}$	$0.0013 \pm 0.0029 \pm 0.0027$	$-0.0003 \pm 0.0004 \pm 0.0005$
$\frac{\mathcal{B}\left(\Xi_b^- \to \Lambda_c^+ K^- K^-\right)}{\mathcal{B}\left(\Xi_b^- \to \Lambda_c^+ K^-\pi^-\right)}$	$0.075 \pm 0.034 \pm 0.011$	$0.041 \pm 0.012 \pm 0.005$
$\frac{\mathcal{B}\left(\Xi_b^- \to \Lambda_c^+ \pi^-\pi^-\right)}{\mathcal{B}\left(\Xi_b^- \to \Lambda_c^+ K^-\pi^-\right)}$	$0.097 \pm 0.049 \pm 0.046$	$0.019 \pm 0.013 \pm 0.017$
$\frac{\mathcal{B}\left(\Omega_b^- \to \Lambda_c^+ K^-\pi^-\right)}{\mathcal{B}\left(\Omega_b^- \to \Lambda_c^+ K^- K^-\right)}$	$0.38 \pm 0.43 \pm 0.24$	$0.17 \pm 0.13 \pm 0.09$
$\frac{\mathcal{B}\left(\Omega_b^- \to \Lambda_c^+ \pi^-\pi^-\right)}{\mathcal{B}\left(\Omega_b^- \to \Lambda_c^+ K^- K^-\right)}$	$0.24 \pm 0.57 \pm 0.53$	$-0.08 \pm 0.12 \pm 0.15$

$$
\begin{aligned}
\frac{\mathcal{B}\left(B^- \to \Lambda_c^+ \overline{p} K^-\right)}{\mathcal{B}\left(B^- \to \Lambda_c^+ \overline{p} \pi^-\right)} &= 0.0397 \pm 0.0023\,(\text{stat}) \pm 0.0012\,(\text{syst})\,, \\
\frac{\mathcal{B}\left(\Xi_b^- \to \Lambda_c^+ K^- K^-\right)}{\mathcal{B}\left(\Xi_b^- \to \Lambda_c^+ K^- \pi^-\right)} &= 0.045 \pm 0.011\,(\text{stat}) \pm 0.005\,(\text{syst})\,, \\
\frac{\mathcal{B}\left(\Xi_b^- \to \Lambda_c^+ \pi^- \pi^-\right)}{\mathcal{B}\left(\Xi_b^- \to \Lambda_c^+ K^- \pi^-\right)} &= 0.025 \pm 0.013\,(\text{stat}) \pm 0.019\,(\text{syst})\,, \\
\frac{\mathcal{B}\left(\Omega_b^- \to \Lambda_c^+ K^- \pi^-\right)}{\mathcal{B}\left(\Omega_b^- \to \Lambda_c^+ K^- K^-\right)} &= 0.19 \pm 0.12\,(\text{stat}) \pm 0.10\,(\text{syst})\,, \\
\frac{\mathcal{B}\left(\Omega_b^- \to \Lambda_c^+ \pi^- \pi^-\right)}{\mathcal{B}\left(\Omega_b^- \to \Lambda_c^+ K^- K^-\right)} &= -0.07 \pm 0.12\,(\text{stat}) \pm 0.16\,(\text{syst})\,.
\end{aligned}
$$

For the modes where we did not observe significant yields, upper limits are placed on the branching fractions. This is done by obtaining combined likelihood scans for Run I and Run II with respect to branching fractions $\mathcal{L}(\mathcal{BF})$ and quoting the values at 90% and 95% confidence level. This is done by integrating the likelihood in the physical region of the non-negative branching fraction as

$$
\int_0^{\mathcal{BF}_{90(95)}} \mathcal{L}(\mathcal{BF})\, d\mathcal{BF} = 0.90(0.95) \int_0^{\inf} \mathcal{L}(\mathcal{BF})\, d\mathcal{BF}. \tag{8.15}
$$

The likelihoods are shown in Figure 8.3

The evaluated upper limits are

$$
\begin{aligned}
\frac{f_{\Xi_b^-}}{f_{B^-}} \cdot \frac{\mathcal{B}\left(\Xi_b^- \to \Lambda_c^+ \pi^- \pi^-\right)}{\mathcal{B}\left(B^- \to \Lambda_c^+ \overline{p} \pi^-\right)} &< 0.0049\ (0.0057) \text{ at } 90\%\ (95\%) \text{ confidence level}\,, \\
\frac{f_{\Omega_b^-}}{f_{B^-}} \cdot \frac{\mathcal{B}\left(\Omega_b^- \to \Lambda_c^+ K^- \pi^-\right)}{\mathcal{B}\left(B^- \to \Lambda_c^+ \overline{p} \pi^-\right)} &< 0.0019\ (0.0022) \text{ at } 90\%\ (95\%) \text{ confidence level}\,, \\
\frac{f_{\Omega_b^-}}{f_{B^-}} \cdot \frac{\mathcal{B}\left(\Omega_b^- \to \Lambda_c^+ \pi^- \pi^-\right)}{\mathcal{B}\left(B^- \to \Lambda_c^+ \overline{p} \pi^-\right)} &< 0.0012\ (0.0015) \text{ at } 90\%\ (95\%) \text{ confidence level}\,, \\
\frac{\mathcal{B}\left(\Xi_b^- \to \Lambda_c^+ \pi^- \pi^-\right)}{\mathcal{B}\left(\Xi_b^- \to \Lambda_c^+ K^- \pi^-\right)} &< 0.065\ (0.074) \text{ at } 90\%\ (95\%) \text{ confidence level}\,, \\
\frac{\mathcal{B}\left(\Omega_b^- \to \Lambda_c^+ K^- \pi^-\right)}{\mathcal{B}\left(\Omega_b^- \to \Lambda_c^+ K^- K^-\right)} &< 0.56\ (0.64) \text{ at } 90\%\ (95\%) \text{ confidence level}\,, \\
\frac{\mathcal{B}\left(\Omega_b^- \to \Lambda_c^+ \pi^- \pi^-\right)}{\mathcal{B}\left(\Omega_b^- \to \Lambda_c^+ K^- K^-\right)} &< 0.37\ (0.45) \text{ at } 90\%\ (95\%) \text{ confidence level}\,.
\end{aligned}
$$

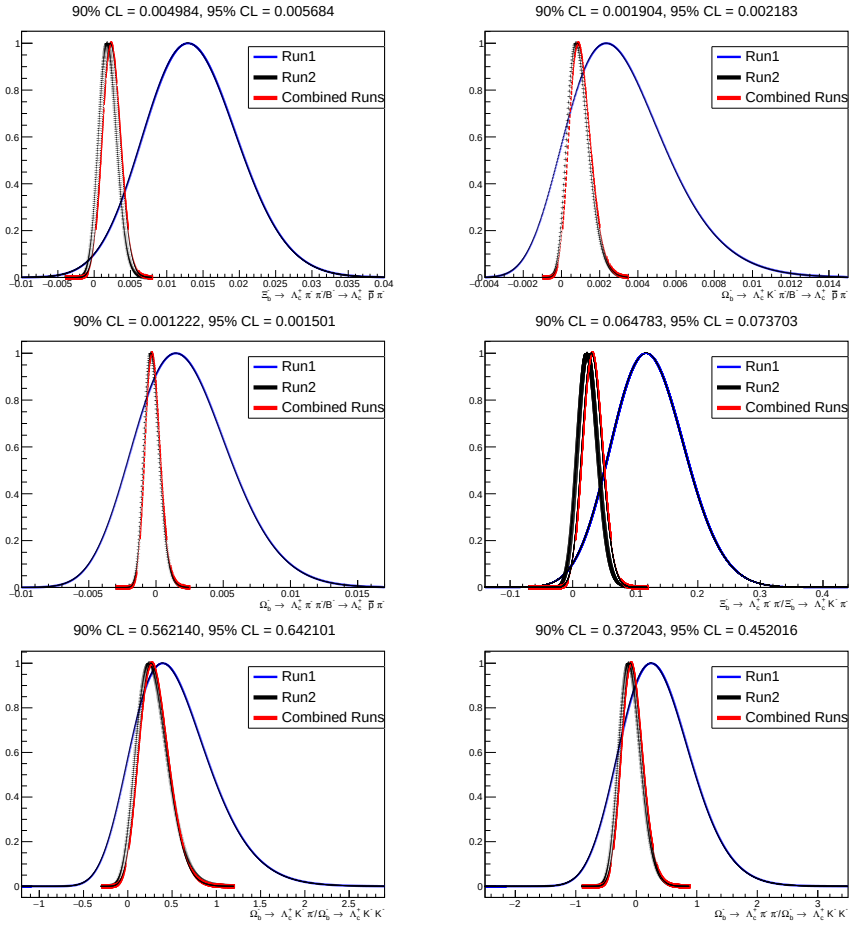

Figure 8.3: Combined likelihoods with respect to branching fraction.

which are effectively luminosity weighted averages over Run I and Run II.

8.4 Differential production rate

The kinematic dependence of the production rates is also studied, in particular with respect to the transverse momentum p_{T} and pseudorapidity η. We choose only three bins of η and p_T as also summarised in Table 8.4, since the yield of $\Xi_b^- \to \Lambda_c^+ K^- \pi^-$ is modest. Separate efficiency maps are computed in the different bins in order to calculate the corrected yields of the channels and obtain the production rate in each bin.

8.4.1 Validation of method using the B meson channels

To validate the method to obtain the kinematics dependence we make use of the relative production rates of the two meson modes $B^- \to \Lambda_c^+ \overline{p} K^-$ and $B^- \to \Lambda_c^+ \overline{p} \pi^-$. This is also

Table 8.4: Summary of the p_{T} and η binnings for kinematic studies.

Bin	p_{T} bins [GeV]	η bins
Bin 1	< 10	2–2.8
Bin 2	10–15	2.8–3.4
Bin 3	> 15	> 3.4

equivalent to the relative branching fraction of the two modes since the fragmentation fractions of the two meson modes are the same. This means there should be no kinematic dependence for the branching fraction of $\frac{B^- \to \Lambda_c^+ \overline{p} K^-}{B^- \to \Lambda_c^+ \overline{p} \pi^-}$, which is consistent with our measurement as shown in Figure 8.4. The uncertainties shown in these figures are statistical only.

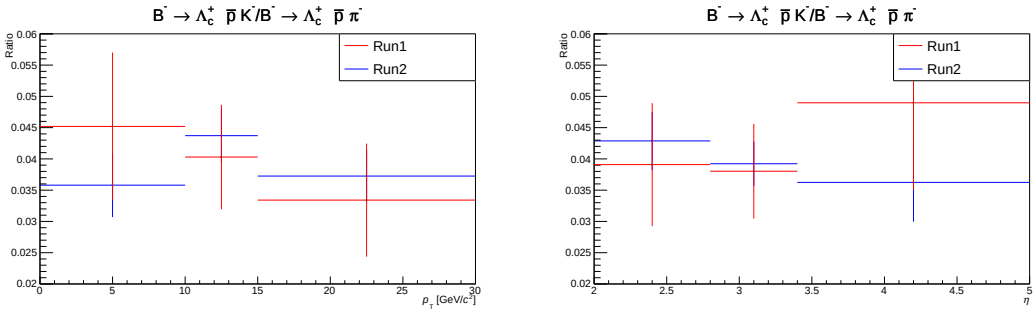

Figure 8.4: Variation of relative branching fraction of the B meson modes with B transverse momentum and pseudorapidity, separately for Run I and Run II, with statistical uncertainties only.

8.4.2 Differential production rate for b baryons

Since the only b baryon channel with a significant yield is the $\Xi_b^- \to \Lambda_c^+ K^- \pi^-$ mode, we obtain the kinematic dependence of its relative production rate with respect to $B^- \to \Lambda_c^+ \overline{p} \pi^-$ as shown in Figure 8.5. These yields are computed in different kinematic bins using efficiencies computed as a function of position in the square Dalitz plot for different bins. However, we use the same sWeights as obtained from the baseline fit, which can be done since the B candidate mass is uncorrelated with p_{T} and η. The uncertainties shown in the figures are statistical only. Since the branching fraction is a constant quantity, any kinematic dependence would be due to variation of the ratio of the fragmentation fractions of Ξ_b^- and B^-. No strong dependence is observed. A slight increase in the fragmentation ratios is seen for both p_{T} and η, but in both cases it is not statistically significant. For comparison, the ratio $f_{\Lambda_b^0}/f_{B^0}$ has been observed to decrease with p_{T}, while remaining constant with η [46, 114, 115]. More statistics would be needed to see if the same trends are present in the $f_{\Xi_b^-}/f_{B^-}$.

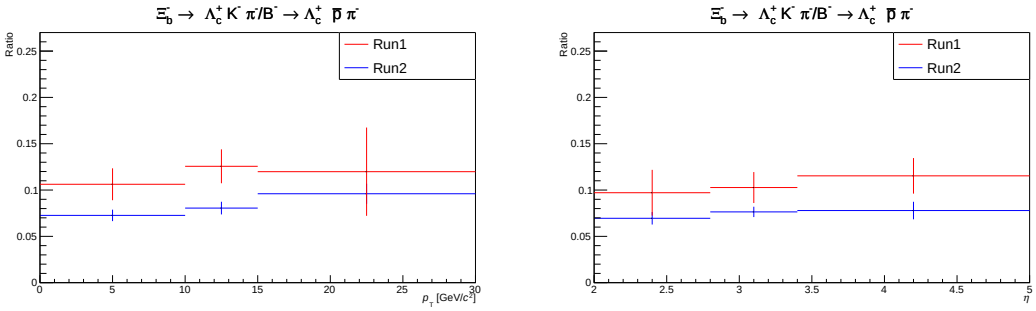

Figure 8.5: Variation of the ratio of fragmentation fractions times branching fractions of $\Xi_b^- \to \Lambda_c^+ K^- \pi^-$ and $B^- \to \Lambda_c^+ \overline{p} \pi^-$ decays with B transverse momentum and pseudorapidity, separately for Run I and Run II, with statistical uncertainties only.

8.5 Production asymmetry

Following the formalism in Section 8.1.4, the production asymmetries for the parent particles Ξ_b^- and B^- have been computed using the decays $\Xi_b^- \to \Lambda_c^+ K^- \pi^-$ and $B^- \to \Lambda_c^+ \overline{p} \pi^-$ for which significant signal was observed. The results are given in Table 8.5. The production asymmetry values for a particle appear to be consistent between the sub samples of different magnet polarities. They appear to be consistent with zero for the B^- meson as expected. They also appear to be consistent with zero for the Ξ_b^- baryon and with previous measurements of the Ξ_b^- production asymmetry [25]

Table 8.5: B^- and Ξ_b^- production asymmetries with statistical and systematic uncertainties determined with the $B^- \to \Lambda_c^+ \overline{p} \pi^-$ control mode and $\Xi_b^- \to \Lambda_c^+ K^- \pi^-$ respectively, separately for MagUp, MagDown and the average of both polarities.

Decay	Run I	Run II
	B^-	
$\mathcal{A}_{\text{prod}}$ (MagUp)	$0.007 \pm 0.035 \pm 0.038$	$-0.010 \pm 0.017 \pm 0.012$
$\mathcal{A}_{\text{prod}}$ (MagDown)	$0.035 \pm 0.033 \pm 0.028$	$-0.018 \pm 0.017 \pm 0.010$
$\mathcal{A}_{\text{prod}}$ (Average)	$0.021 \pm 0.024 \pm 0.020$	$-0.014 \pm 0.012 \pm 0.009$
	Ξ_b^-	
$\mathcal{A}_{\text{prod}}$ (MagUp)	$-0.179 \pm 0.133 \pm 0.045$	$-0.125 \pm 0.073 \pm 0.032$
$\mathcal{A}_{\text{prod}}$ (MagDown)	$-0.001 \pm 0.147 \pm 0.040$	$-0.075 \pm 0.072 \pm 0.019$
$\mathcal{A}_{\text{prod}}$ (Average)	$-0.098 \pm 0.101 \pm 0.030$	$-0.100 \pm 0.052 \pm 0.020$

8.6 Kinematic dependence of production asymmetry

We compute the production asymmetry as described in Section 8.1 using the corrected yields. In this computation, we use separate efficiency maps for the charge conjugate decays. This takes

into account the effects of detection asymmetry. The production asymmetry for both the B meson and the Ξ_b^- baryon are also computed in the bins of kinematics as shown in Figure 8.6 and Figure 8.7 respectively. The validation of the procedure is done by performing the studies for the B meson mode, where the production asymmetry has previously been measured. The results are found to be consistent with previous measurements [116, 117], as expected.

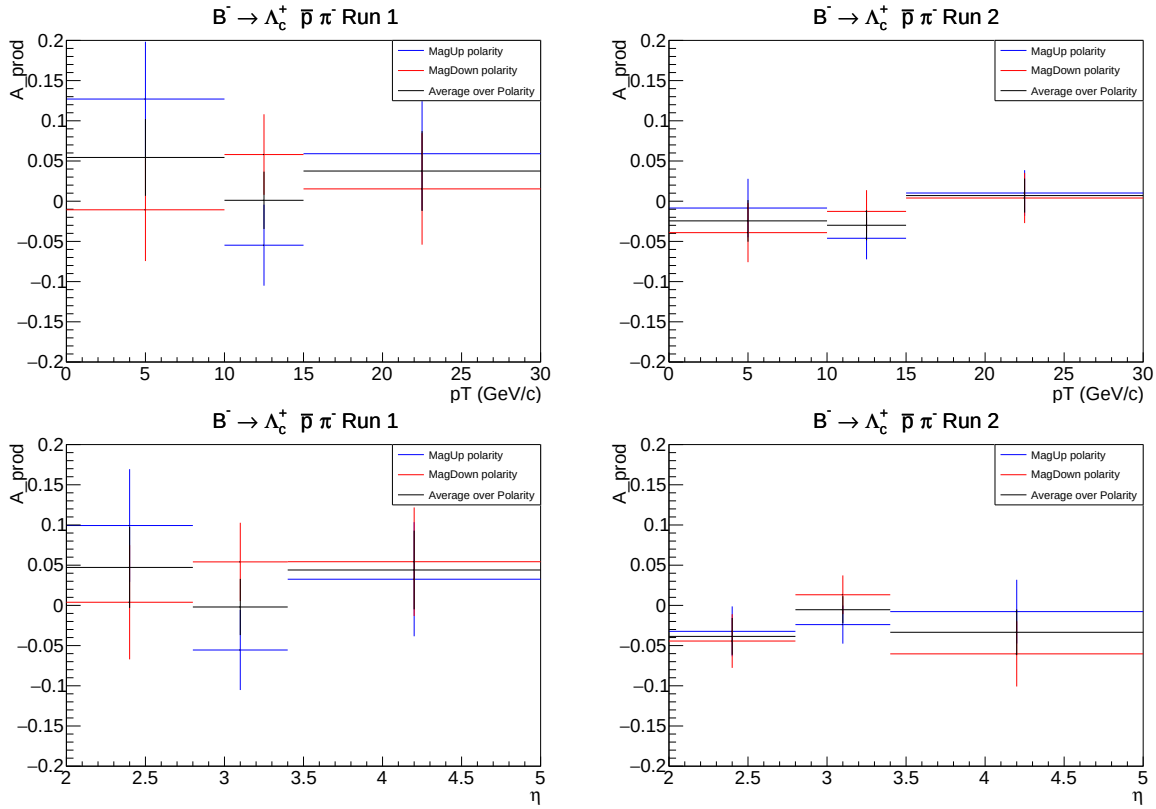

Figure 8.6: Variation of B^- production asymmetry with B transverse momentum (p_{T}) and pseudorapidity (η) determined with the $B^- \to \Lambda_c^+ \overline{p}\pi^-$ control mode.

8.7 Dalitz plot distributions

We study the distribution of the Dalitz plot from the background-subtracted and candidate-by-candidate efficiency-corrected yield for both the B meson modes and the $\Xi_b^- \to \Lambda_c^+ K^- \pi^-$ mode. This includes an inspection of the invariant mass distributions of the two-body combinations to check for any resonances. However, full amplitude analysis to quantify the contributions from different resonances is beyond scope of this analysis.

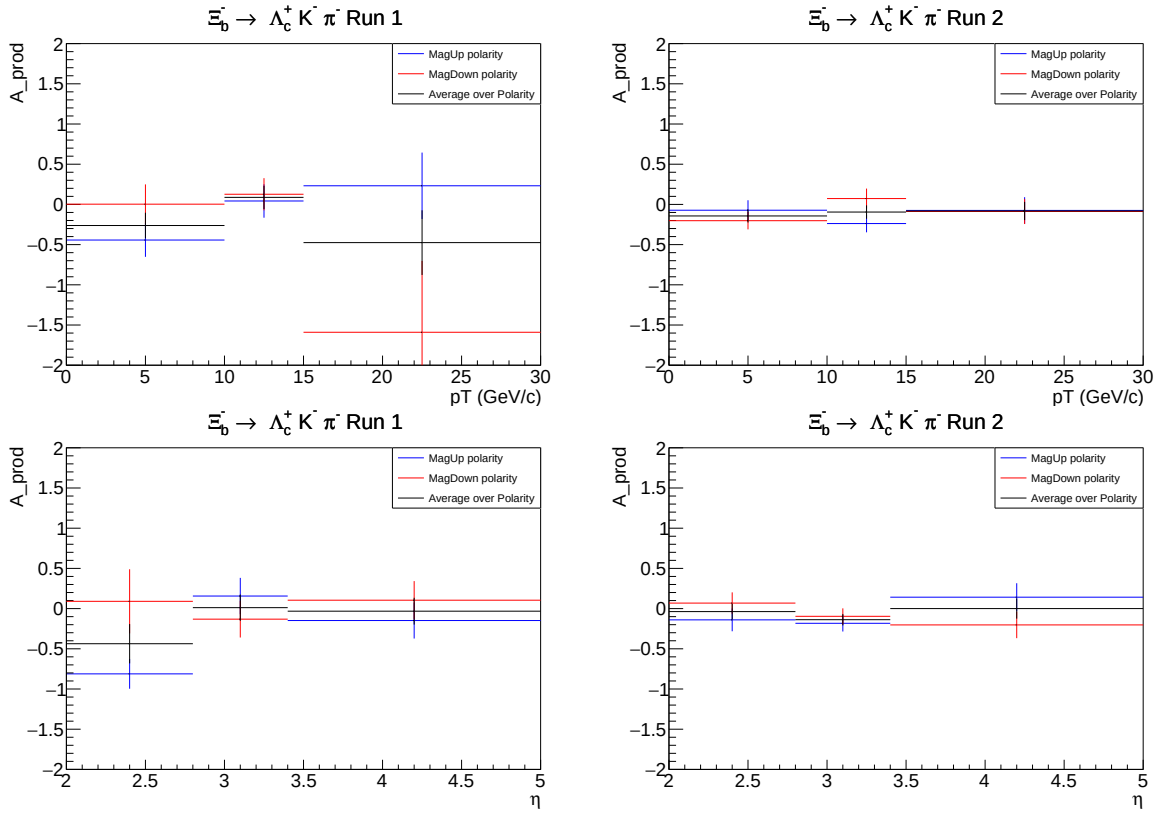

Figure 8.7: Variation of Ξ_b^- production asymmetry with Ξ_b^- transverse momentum (p_{T}) and pseudorapidity (η) determined with $\Xi_b^- \to \Lambda_c^+ K^- \pi^-$ decays.

8.7.1 B meson modes

Figure 8.8 shows the three possible Dalitz plot projections of the $B^- \to \Lambda_c^+ \overline{p} \pi^-$ and $B^- \to \Lambda_c^+ \overline{p} K^-$ modes. Resonances can be observed as bands in the Dalitz plot distribution. These can be seen clearly in the two-body combinations of the invariant mass for both $B^- \to \Lambda_c^+ \overline{p} \pi^-$ and $B^- \to \Lambda_c^+ \overline{p} K^-$ decays, as shown in Figure 8.9 and Figure 8.12 respectively. Thresholds observed in some distributions can cause reflections that obscure the resonances observed in another distribution. Thus to see the resonances more clearly in certain combinations, such thresholds effects and reflections are removed by applying vetoes on the the invariant mass distributions:

- $B^- \to \Lambda_c^+ \overline{p} \pi^-$ invariant masses

  For $m(\Lambda_c^+ \pi^-)$: None

  For $m(\Lambda_c^+ \overline{p})$: $m(\Lambda_c^+ \pi^-) > 2460\,\mathrm{MeV}/c^2$

  For $m(\pi^- \overline{p})$: $m(\Lambda_c^+ \pi^-) > 2460\,\mathrm{MeV}/c^2$ and $m(\Lambda_c^+ \overline{p}) > 3500\,\mathrm{MeV}/c^2$

- $B^- \to \Lambda_c^+ \overline{p} K^-$ invariant masses

For $m(K^-\overline{p})$: None

For $m(\Lambda_c^+\overline{p})$: None

For $m(\Lambda_c^+K^-)$: $m(\Lambda_c^+\overline{p}) > 3500\,\mathrm{MeV}/c^2$

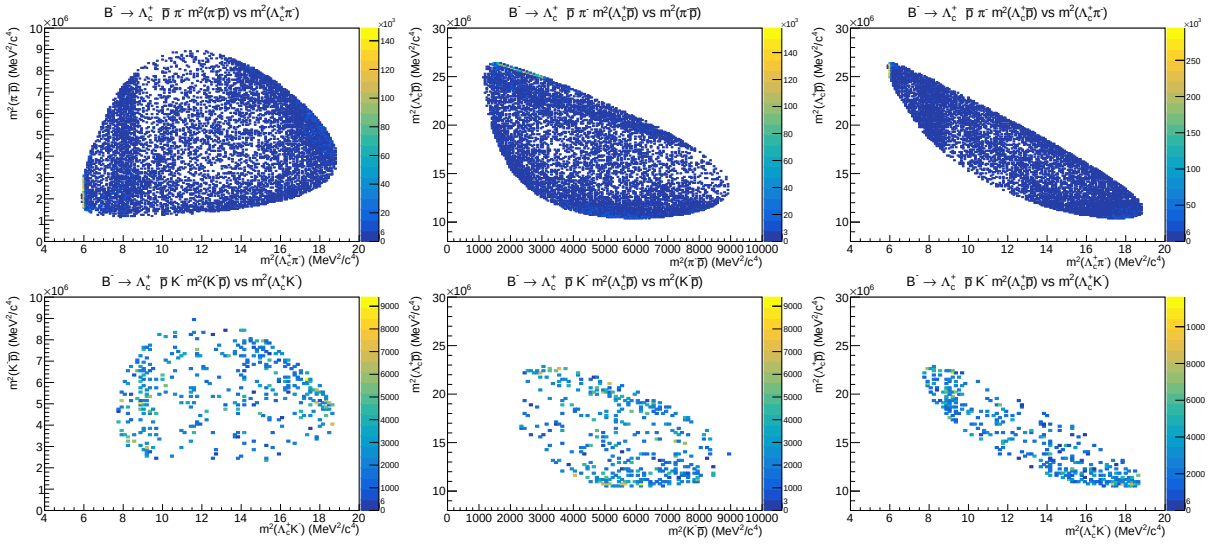

Figure 8.8: Background-subtracted and efficiency-corrected Dalitz plots of (top) $B^- \to \Lambda_c^+\overline{p}\pi^-$ and (bottom) $B^- \to \Lambda_c^+\overline{p}K^-$ decays.

$B^- \to \Lambda_c^+\overline{p}\pi^-$:

The invariant mass distribution of $\Lambda_c^+\pi^-$ obtained from $B^- \to \Lambda_c^+\overline{p}\pi^-$ shows structures corresponding to $\Sigma_c(2455)$, $\Sigma_c(2520)$, and $\Sigma_c(2840)$ as shown in Figure 8.9. A significant threshold enhancement is also observed in $\Lambda_c^+\overline{p}$ combination. These observations appear to be consistent with the studies of this channel done at Belle and BaBar collaborations [118, 119], shown for reference in Figure 8.10 and Figure 8.11 but with much more statistics from LHCb. Possible evidence for $\overline{\Delta}(1232)^{--}$ and $\overline{\Delta}(1600)^{--}$ or $\overline{\Delta}(1620)^{--}$ resonances is also seen in $\overline{p}\pi^-$ which has not been observed previously in this decay.

$B^- \to \Lambda_c^+\overline{p}K^-$:

The $\Lambda_c^+\overline{p}$ combination obtained from the $B^- \to \Lambda_c^+\overline{p}K^-$ mode also shows a threshold enhancement as shown in Figure 8.12. This seems consistent with that seen in the $B^- \to \Lambda_c^+\overline{p}\pi^-$ channel. The $\Lambda_c^+K^-$ combination from this decay also shows some broad structure around $3020\,\mathrm{MeV}/c^2$. This does not correspond to any known state so far. The closest ${\Xi_c}^{*0}$ state according to PDG [93] is the $\Xi_c(3055)$. However, this state has not previously been observed to decay to $\Lambda_c^+K^-$.

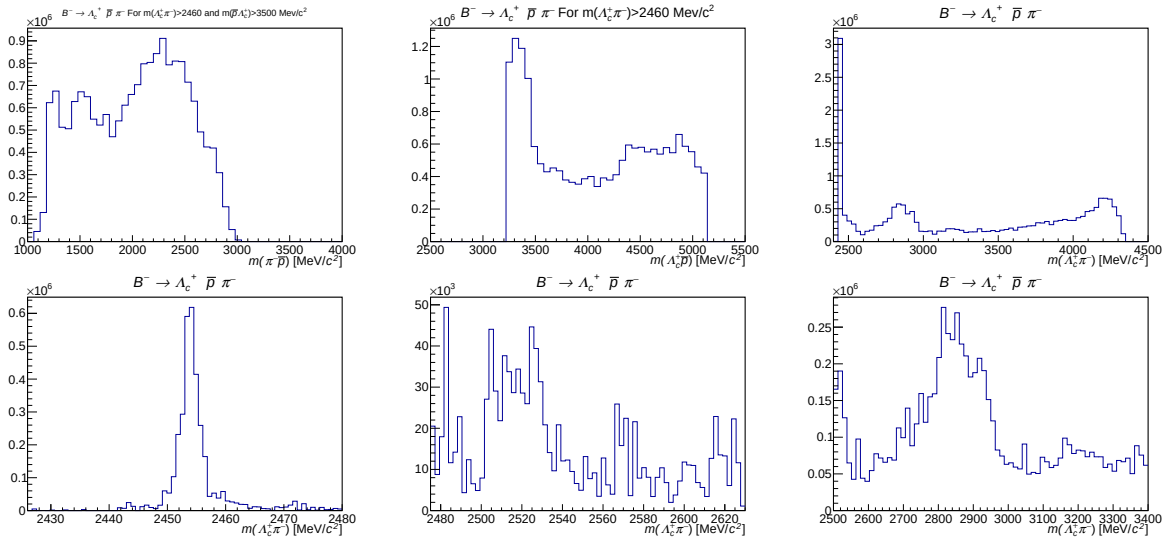

Figure 8.9: (Top) Background-subtracted and efficiency-corrected invariant mass projections of $B^- \to \Lambda_c^+ \overline{p}\pi^-$ decays, with reflections removed with requirements as specified in the text. The bottom plots show zooms around the most prominent $m(\Lambda_c^+\pi^-)$ structures at 2455, 2520 and 2840 MeV/c^2 .

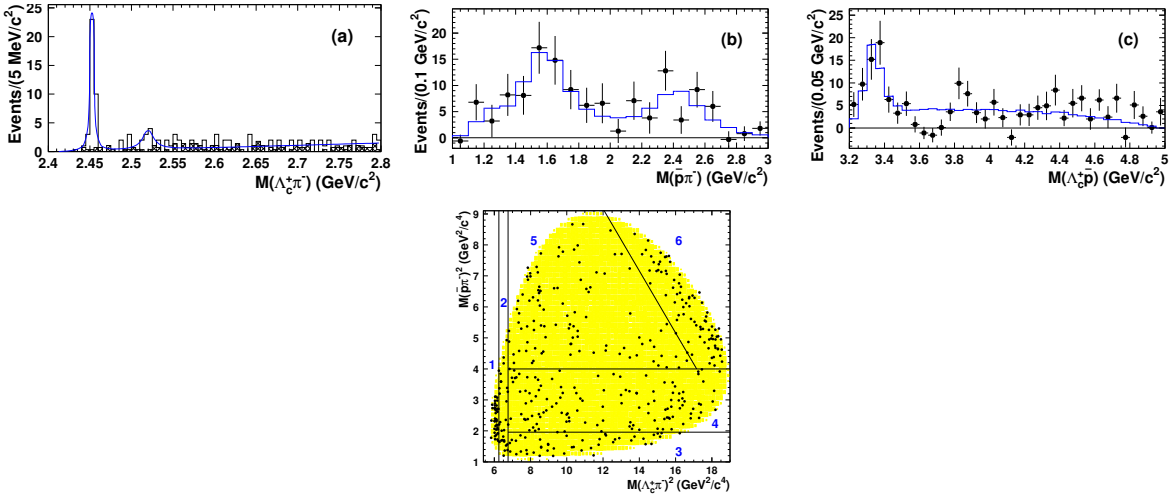

Figure 8.10: Dalitz plot distribution and invariant mass projections for $B^- \to \Lambda_c^+ \overline{p}\pi^-$ decays studied by the Belle collaboration [118].

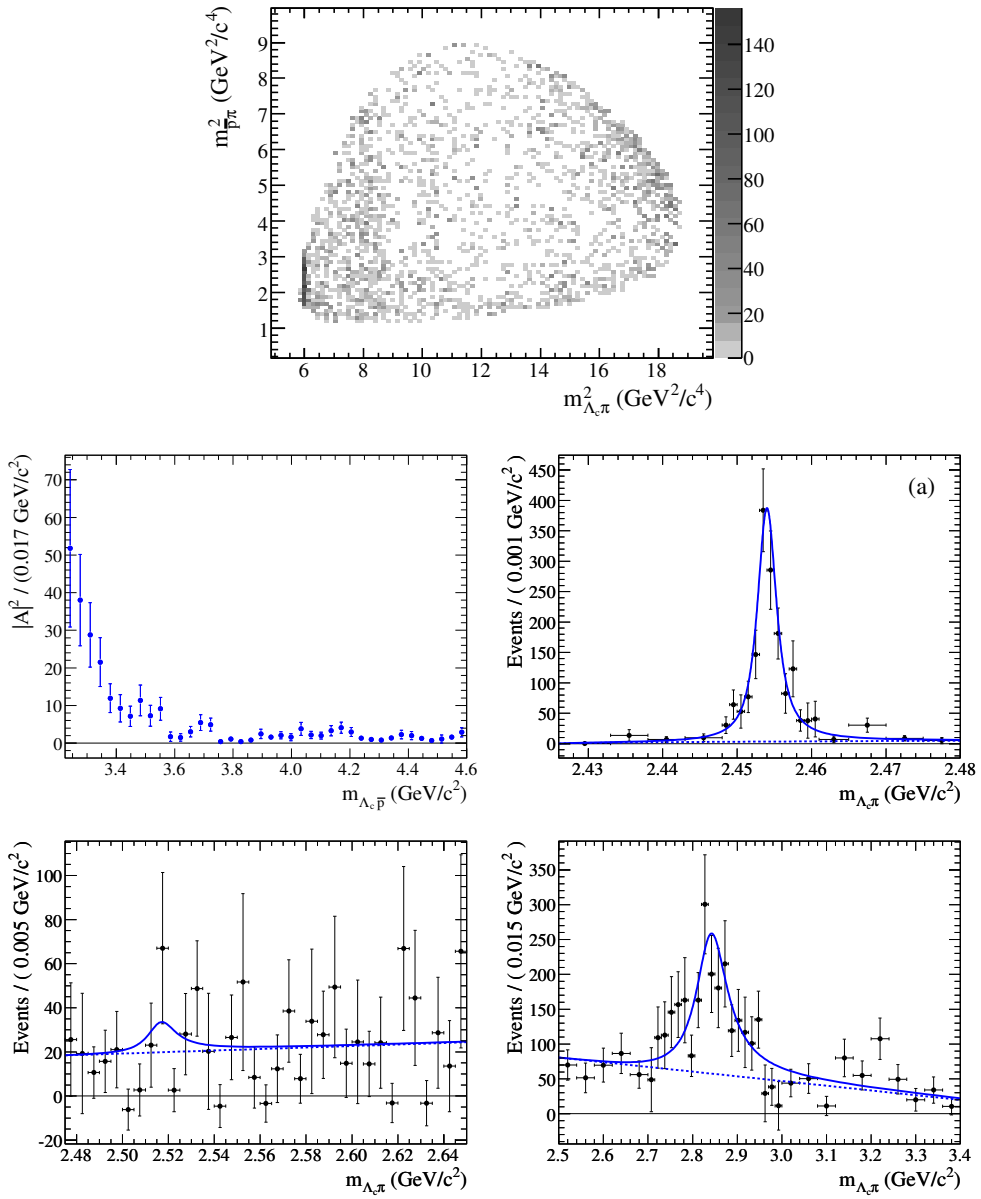

Figure 8.11: Dalitz plot distribution and invariant mass projections for $B^- \to \Lambda_c^+ \bar{p}\pi^-$ decays studied by the BaBar collaboration [119].

8.7.2 b baryon modes

The background-subtracted and efficiency-corrected Dalitz plot combinations for the channel $\Xi_b^- \to \Lambda_c^+ K^-\pi^-$ are shown in Figure 8.13. The two-body invariant mass projections are shown in Figure 8.14. The $m(\Lambda_c^+\pi^-)$ distribution shows clear structures at $\Sigma_c(2455)$. There also seem to be some structures around $\Sigma_c(2520)$ and $\Sigma_c(2840)$ which appear to be consistent with those observed for the $B^- \to \Lambda_c^+ \bar{p}\pi^-$ decay. Peaks are seen as well in the $m(\Lambda_c^+ K^-)$ distribution at

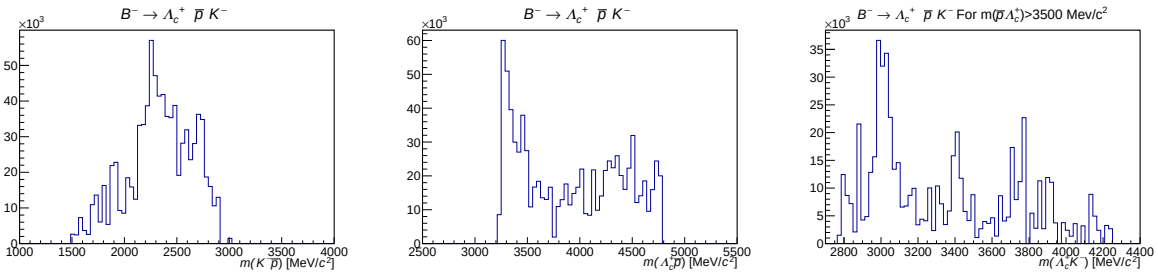

Figure 8.12: Background-subtracted and efficiency-corrected invariant mass projections of $B^- \to \Lambda_c^+ \bar{p} K^-$ decays, with reflections removed with requirements as specified in the text.

around $m(\Lambda_c^+ K^-) \sim 2940\,\mathrm{MeV}/c^2$ that seem to correspond with the $\Xi_c(2939)$ state.

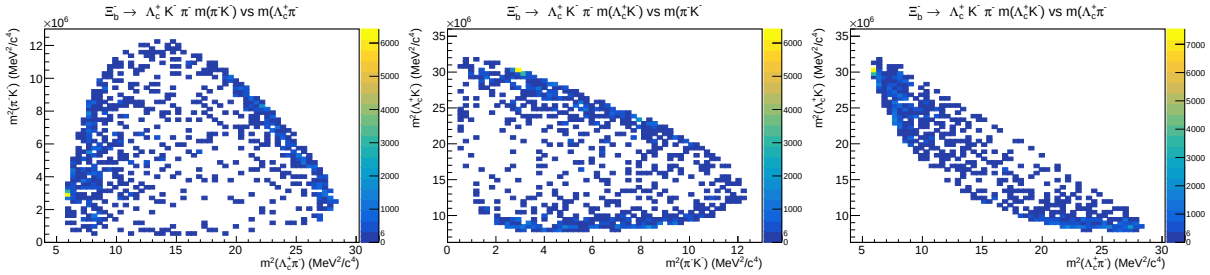

Figure 8.13: Background-subtracted and efficiency-corrected Dalitz plots of $\Xi_b^- \to \Lambda_c^+ K^- \pi^-$ decay.

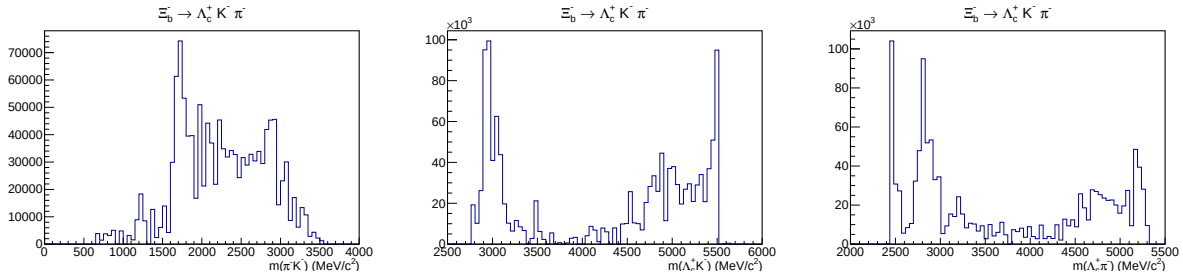

Figure 8.14: Background-subtracted and efficiency-corrected invariant mass projections of $\Xi_b^- \to \Lambda_c^+ K^- \pi^-$ decays. Left to right: $m(K^-\pi^-)$, $m(\Lambda_c^+ K^-)$, $m(\Lambda_c^+ \pi^-)$.

Chapter 9

Summary and Conclusions

- Searches are performed for the channels $\Xi_b^- \to \Lambda_c^+ h^- h'^-$ with $B^- \to \Lambda_c^+ \overline{p}\pi^-$ as the normalisation channel, using the data samples from the pp collisions at LHCb, recorded during Run I and Run II and corresponding to an integrated luminosity of $8.7\,\text{fb}^{-1}$. Three decay channels are observed: $\Xi_b^- \to \Lambda_c^+ K^-\pi^-$, $\Xi_b^- \to \Lambda_c^+ K^- K^-$ and $\Omega_b^- \to \Lambda_c^+ K^- K^-$, with significance $> 5\sigma$, which were never observed before. Additionally, the decay $B^- \to \Lambda_c^+ \overline{p} K^-$ is observed with large significance for the first time.

- The relative branching fraction of $B^- \to \Lambda_c^+ \overline{p} K^-$ is computed with respect to $B^- \to \Lambda_c^+ \overline{p}\pi^-$, which has been previously observed at B factories. The relative branching fractions of all the $\Xi_b^-(\Omega_b^-)$ modes are computed with respect to $\Xi_b^- \to \Lambda_c^+ K^-\pi^-(\Omega_b^- \to \Lambda_c^+ K^- K^-)$ and are found to be consistent between Run I and Run II within uncertainties, as expected.

- Relative production rates for all the Ξ_b^- and Ω_b^- modes are also computed with respect to $B^- \to \Lambda_c^+ \overline{p}\pi^-$. The kinematic dependence of the relative production rate of Ξ_b^- and B^- hadrons, using the $\Xi_b^- \to \Lambda_c^+ K^-\pi^-$ and $B^- \to \Lambda_c^+ \overline{p}\pi^-$ modes is also studied. With the current dataset, no strong variation in the production rate with respect to transverse momentum and pseudorapidity is observed. A larger sample would be needed to see any small variations with kinematics.

- The production asymmetry for the Ξ_b^- baryon is also measured and is consistent with zero. The variation of the Ξ_b^- production asymmetry is also studied with respect to the kinematics. This also does not show any strong dependence and the production asymmetry is found to be consistent with zero in different kinematic regions.

- These studies provide a significant amount of insight into the production and decay of the Ξ_b^- and Ω_b^-, and increases the existing knowledge about such decays. These decay modes can be used in future to control the systematic uncertainties for searches of other b

baryon decays and to improve knowledge about the production processes of b baryons in high energy pp collisions.

- This thesis also provides a first look at the Dalitz plot distributions for the observed modes, in particular for the $B^- \to \Lambda_c^+ \overline{p} K^-$, $B^- \to \Lambda_c^+ \overline{p} \pi^-$ and $\Xi_b^- \to \Lambda_c^+ K^- \pi^-$ channels. Peaks are observed in the $\Lambda_c^+ K^-$ and $\Lambda_c^+ \pi^-$ invariant mass distributions, which correspond to excited Ξ_c and Σ_c states, respectively. This motivates future studies of charm baryon spectroscopy and potentially exotic spectroscopy, which however is beyond the scope of this thesis.

Bibliography

[1] LHCb collaboration, *Study of Ξ_b^- and Ω_b^- decays to $\Lambda_c^+ h^- h'^-$ final states*, LHCb-CONF-2023-001. Cited on page xiii.

[2] A. D. Sakharov, *Violation of CP invariance, C asymmetry, and baryon asymmetry of the universe*, Soviet Physics Uspekhi **34** (1991) 392. Cited on page 1.

[3] N. Cabibbo, *Unitary symmetry and leptonic decays*, Phys. Rev. Lett. **10** (1963) 531. Cited on pages 1 and 9.

[4] M. Gell-Mann, *The Eightfold Way: A theory of strong interaction symmetry*, , https://inspirehep.net/literature/44998. Cited on page 1.

[5] B. J. Bjørken and S. L. Glashow, *Elementary particles and SU(4)*, Phys. Rev. Lett. **11** (1964), no. 3 255. Cited on page 1.

[6] S. L. Glashow, J. Iliopoulos, and L. Maiani, *Weak interactions with lepton-hadron symmetry*, Phys. Rev. D **2** (1970) 1285. Cited on page 1.

[7] J. H. Christenson, J. W. Cronin, V. L. Fitch, and R. Turlay, *Evidence for the 2π decay of the K_2^0 meson*, Phys. Rev. Lett. **13** (1964) 138. Cited on pages 1 and 13.

[8] M. Kobayashi and T. Maskawa, *CP violation in the renormalizable theory of weak interaction*, Progress of Theoretical Physics **49** (1973) 652, https://doi.org/10.1143/PTP.49.652. Cited on pages 1 and 9.

[9] E288 collaboration, J. Yoh, *The Discovery of the B quark at Fermilab in 1977: The experiment coordinator's story*, AIP Conf. Proc. **424** (1998), no. 1 29. Cited on page 1.

[10] CDF collaboration, F. Abe *et al.*, *Observation of top quark production in $\overline{p}p$ collisions with the collider detector at Fermilab*, Phys. Rev. Lett. **74** (1995) 2626. Cited on page 1.

[11] D0 collaboration, S. Abachi *et al.*, *Observation of the top quark*, Phys. Rev. Lett. **74** (1995) 2632. Cited on page 1.

[12] A. B. Carter and A. I. Sanda, CP *nonconservation in cascade decays of b mesons*, Phys. Rev. Lett. **45** (1980) 952. Cited on page 1.

[13] A. B. Carter and A. I. Sanda, *CP violation in B meson decays*, Phys. Rev. D **23** (1981) 1567, https://inspirehep.net/literature/9577. Cited on page 1.

[14] I. I. Y. Bigi and A. I. Sanda, *Notes on the observability of CP violations in B decays*, Nucl. Phys. B **193** (1981) 85, https://inspirehep.net/literature/165588. Cited on page 1.

[15] Belle collaboration, A. Abashian *et al.*, *The Belle detector*, Nucl. Instrum. Meth. A **479** (2002) 117, https://inspirehep.net/literature/541364. Cited on page 1.

[16] BaBar collaboration, B. Aubert *et al.*, *The BaBar detector*, Nucl. Instrum. Meth. A **479** (2002) 1, arXiv:hep-ex/0105044, https://inspirehep.net/literature/556767. Cited on page 1.

[17] LHCb collaboration, R. Aaij *et al.*, *Measurements of the mass and lifetime of the Ω_b^- baryon*, Phys. Rev. **D93** (2016) 092007 LHCb-PAPER-2016-008 CERN-EP-2016-081, arXiv:1604.01412. Cited on page 2.

[18] LHCb collaboration, R. Aaij *et al.*, *Observation of the decay $\Xi_b^- \to pK^-K^-$*, Phys. Rev. Lett. **118** (2017) 071801 LHCb-PAPER-2016-050 CERN-EP-2016-294, arXiv:1612.02244. Cited on page 2.

[19] LHCb collaboration, R. Aaij *et al.*, *Observation of the $\Xi_b^- \to J/\psi \Lambda K^-$ decay*, Phys. Lett. **B772** (2017) 265 LHCb-PAPER-2016-053 CERN-EP-2016-318, arXiv:1701.05274. Cited on page 2.

[20] LHCb collaboration, R. Aaij *et al.*, *Search for CP violation in $\Xi_b^- \to pK^-K^-$decays*, Phys. Rev. **D104** (2021) 052010 LHCb-PAPER-2020-017,CERN-EP-2021-036, arXiv:2104.15074. Cited on page 2.

[21] LHCb collaboration, R. Aaij *et al.*, *Observation of excited Ω_c^0 baryons in $\Omega_b^- \to \Xi_c^+ K^-\pi^+$ decays*, Phys. Rev. **D** (2021) L091102 LHCb-PAPER-2021-012, CERN-EP-2021-109, arXiv:2107.03419. Cited on page 2.

[22] LHCb collaboration, R. Aaij *et al.*, *Measurement of the mass difference and relative production rate of the Ω_b^- and Ξ_b^- baryons*, arXiv:2305.15329 LHCb-PAPER-2022-053,CERN-EP-2023-086, arXiv:2305.15329, submitted to Phys. Rev. D. Cited on page 2.

[23] LHCb collaboration, R. Aaij *et al.*, *Observation of new baryons in the $\Xi_b^-\pi^+\pi^-$ and $\Xi_b^0\pi^+\pi^-$ systems*, arXiv:2307.13399 LHCb-PAPER-2023-008, CERN-EP-2023-126, arXiv:2307.13399, submitted to Phys. Rev. Lett. Cited on page 2.

[24] LHCb collaboration, R. Aaij *et al.*, *Observation and branching fraction measurement of the decay* $\Xi_b^- \to \Lambda_b^0\pi^-$, arXiv:2307.09427 LHCb-PAPER-2023-015, arXiv:2307.09427, submitted to Phys. Rev. D. Cited on page 2.

[25] LHCb collaboration, R. Aaij *et al.*, *Measurement of the mass and production rate of* Ξ_b^- *baryons*, Phys. Rev. **D99** (2019) 052006 LHCb-PAPER-2018-047 CERN-EP-2018-348, arXiv:1901.07075. Cited on pages 2 and 122.

[26] M. E. Peskin, *An introduction to quantum field theory*, CRC press, 2018. https://doi.org/10.1201/9780429503559. Cited on page 4.

[27] D. Griffiths, *Introduction to elementary particles*, John Wiley & Sons, 2020. https://inspirehep.net/literature/806976. Cited on page 4.

[28] F. Halzen and A. D. Martin, *Quarks and leptones: An introductory course in modern particle physics*, Quarks and Leptones: An Introductory Course in Modern Particle Physics (1984) 416, https://inspirehep.net/literature/205394. Cited on page 4.

[29] Particle Data Group, R. L. Workman *et al.*, *Review of Particle Physics*, PTEP **2022** (2022) 083C01. Cited on pages 4 and 15.

[30] *Standard Model of elementary particles.svg*, 2023. Wikimedia Image. Cited on page 5.

[31] F. Englert and R. Brout, *Broken symmetry and the mass of gauge vector mesons*, Phys. Rev. Lett. **13** (1964) 321. Cited on page 7.

[32] G. S. Guralnik, C. R. Hagen, and T. W. B. Kibble, *Global conservation laws and massless particles*, Phys. Rev. Lett. **13** (1964) 585. Cited on page 7.

[33] P. W. Higgs, *Broken symmetries and the masses of gauge bosons*, Phys. Rev. Lett. **13** (1964) 508. Cited on page 7.

[34] J. Ellis, M. K. Gaillard, and D. V. Nanopoulos, *A Historical Profile of the Higgs Boson. An Updated Historical Profile of the Higgs Boson*, arXiv:1504.07217, https://cds.cern.ch/record/2012465. Cited on page 8.

[35] L. Wolfenstein, *Parametrization of the Kobayashi-Maskawa matrix*, Phys. Rev. Lett. **51** (1983) 1945. Cited on page 9.

[36] G. Isidori, *Flavor physics and CP violation*, arXiv:1302.0661, http://cds.cern.ch/record/1513468/. Cited on pages 10 and 12.

[37] C. Jarlskog, *Commutator of the quark mass matrices in the standard electroweak model and a measure of maximal* CP *nonconservation*, Phys. Rev. Lett. **55** (1985) 1039. Cited on page 10.

[38] J. Charles *et al.*, *CP violation and the CKM matrix: assessing the impact of the asymmetric B factories*, The European Physical Journal C **41** (2005) 1–131. Cited on page 11.

[39] Heavy Flavor Averaging Group collaboration, Y. Amhis *et al.*, *Averages of b-hadron, c-hadron, and τ-lepton properties as of 2021*, Phys. Rev. D **107** (2023) 052008. Cited on page 11.

[40] A. Mathad, *Search for CP violation in charmless three-body decays of strange-beauty baryons*, PhD thesis, Warwick U., 2018, CERN-THESIS-2018-237. Cited on page 13.

[41] Belle collaboration, K. Abe *et al.*, *Observation of large CP violation in the neutral B meson system*, Phys. Rev. Lett. **87** (2001) 091802. Cited on page 13.

[42] BABAR collaboration, B. Aubert *et al.*, *Observation of CP violation in the B^0 meson system*, Phys. Rev. Lett. **87** (2001) 091801. Cited on page 13.

[43] LHCb collaboration, R. Aaij *et al.*, *Observation of CP violation in charm decays*, Phys. Rev. Lett. **122** (2019) 211803. Cited on page 13.

[44] S. Frixione *et al.*, *Heavy flavor production and fragmentation*, J. Phys. G **27** (2001) 1111. Cited on pages 13 and 15.

[45] OPAL collaboration, G. Abbiendi *et al.*, *Measurement of the average polarization of b baryons in hadronic Z^0 decays*, Phys. Lett. B **444** (1998) 539, `arXiv:hep-ex/9808006`. Cited on pages 13, 14, and 15.

[46] LHCb collaboration, R. Aaij *et al.*, *Study of the productions of Λ_b^0 and $\overline{B}^0$ hadrons in pp collisions and first measurement of the $\Lambda_b^0 \to J/\psi p K^-$ branching fraction*, Chin. Phys. **C40** (2016) 011001 LHCb-PAPER-2015-032 CERN-PH-EP-2015-223, `arXiv:1509.00292`. Cited on pages 13 and 121.

[47] F. Ferrari, *Measurement of B^0, B_s^0, B^+ and Λ_b^0 production asymmetries in 7 and 8 TeV pp collisions at LHCb*, Nuovo Cimento C **41** (2018), no. 1-2 41. Cited on page 14.

[48] LHCb, R. Aaij *et al.*, *Observation of a $\Lambda_b^0 - \overline{\Lambda}_b^0$ production asymmetry in proton-proton collisions at $\sqrt{s} = 7$ and 8 TeV*, JHEP **10** (2021) 060, `arXiv:2107.09593`. Cited on page 14.

[49] LHCb collaboration, R. Aaij *et al.*, *Measurement of the mass and production rate of Ξ_b^- baryons*, Phys. Rev. D **99** (2019), no. 5 052006, `arXiv:1901.07075`. Cited on page 14.

[50] G. Gustafson and J. Häkkinen, *Γ-polarization in e^+e^--annihilation at the Z^0-pole*, Physics Letters B **303** (1993), no. 3 350. Cited on page 14.

[51] ALEPH collaboration, D. Buskulic *et al.*, *Measurement of the Λ_b polarization in Z decays*, Physics Letters B **365** (1996), no. 1 437. Cited on page 14.

[52] DELPHI collaboration, P. Abreu *et al.*, *Λ_b polarization in Z^0 decays at LEP*, Physics Letters B **474** (2000), no. 1 205. Cited on page 14.

[53] A. F. Falk and M. E. Peskin, *Production, decay, and polarization of excited heavy hadrons*, Physical Review D **49** (1994) 3320. Cited on page 15.

[54] LHCb collaboration, R. Aaij *et al.*, *Measurements of the $\Lambda_b^0 \to J/\psi\Lambda$ decay amplitudes and the Λ_b^0 polarisation in pp collisions at $\sqrt{s}$ =7TeV*, Phys. Lett. **B724** (2013) 27, arXiv:1302.5578. Cited on pages 15 and 101.

[55] G. Hiller, M. Knecht, F. Legger, and T. Schietinger, *Photon polarization from helicity suppression in radiative decays of polarized λ_b to spin-3/2 baryons*, Physics Letters B **649** (2007), no. 2 152. Cited on page 15.

[56] Z. J. Ajaltouni, E. Conte, and O. Leitner, *λ_b decays into λ-vector*, Physics Letters B **614** (2005), no. 3 165. Cited on page 15.

[57] *LHC Machine*, JINST **3** (2008) S08001. Cited on page 16.

[58] LHCb collaboration, A. A. Alves Jr. *et al.*, *The LHCb detector at the LHC*, JINST **3** (2008), no. LHCb-DP-2008-001 S08005. Cited on pages 16, 18, 20, 22, and 30.

[59] ATLAS collaboration, G. Aad *et al.*, *The ATLAS Experiment at the CERN Large Hadron Collider*, JINST **3** (2008) S08003. Cited on page 16.

[60] CMS collaboration, S. Chatrchyan *et al.*, *The CMS Experiment at the CERN LHC*, JINST **3** (2008) S08004. Cited on page 16.

[61] ALICE collaboration, K. Aamodt *et al.*, *The ALICE experiment at the CERN LHC*, JINST **3** (2008) S08002. Cited on page 16.

[62] E. Mobs, *The CERN accelerator complex - August 2018. Complexe des accélérateurs du CERN - Août 2018*, , https://cds.cern.ch/record/2636343. Cited on page 17.

[63] LHCb collaboration, R. Aaij *et al.*, *LHCb detector performance*, Int. J. Mod. Phys. **A30** (2015) 1530022 LHCB-DP-2014-002, CERN-PH-EP-2014-290, arXiv:1412.6352. Cited on pages 18, 26, 27, and 32.

[64] LHCb collaboration, *LHCb VELO (VErtex LOcator): Technical Design Report*, CERN-LHCC-2001-011. LHCb-TDR-005. Cited on pages 19 and 20.

[65] LHCb collaboration, *LHCb Tracker Upgrade Technical Design Report*, CERN-LHCC-2014-001. LHCb-TDR-015. Cited on page 22.

[66] LHCb collaboration, *LHCb inner tracker: Technical Design Report*, CERN-LHCC-2002-029. LHCb-TDR-008. Cited on page 21.

[67] LHCb collaboration, *LHCb outer tracker: Technical Design Report*, CERN-LHCC-2001-024. LHCb-TDR-006. Cited on pages 21 and 22.

[68] R. Arink *et al.*, *Performance of the LHCb Outer Tracker*, JINST **9** (2014) P01002 LHCB-DP-2013-003, `arXiv:1311.3893`. Cited on page 23.

[69] LHCb collaboration, *LHCb magnet: Technical Design Report*, CERN-LHCC-2000-007. LHCb-TDR-001. Cited on pages 23 and 24.

[70] LHCb collaboration, *LHCb reoptimized detector design and performance: Technical Design Report*, CERN-LHCC-2003-030. LHCb-TDR-009. Cited on page 25.

[71] LHCb collaboration, *LHCb RICH: Technical Design Report*, CERN-LHCC-2000-037. LHCb-TDR-003. Cited on page 24.

[72] R. Aaij *et al.*, *Performance of the LHCb RICH detectors during LHC Run 2*, LHCb-DP-2021-004, in preparation. Cited on pages 26, 32, 33, and 34.

[73] LHCb collaboration, *LHCb calorimeters: Technical Design Report*, CERN-LHCC-2000-036. LHCb-TDR-002. Cited on pages 27 and 28.

[74] Irina Machikhiliyan and LHCb calorimeter group, *The LHCb electromagnetic calorimeter*, Journal of Physics: Conference Series **160** (2009) 012047. Cited on page 28.

[75] *Performance of the LHCb muon system*, Journal of Instrumentation **8** (2013) P02022. Cited on page 29.

[76] LHCb collaboration, *LHCb muon system: Technical Design Report*, CERN-LHCC-2001-010. LHCb-TDR-004. Cited on page 29.

[77] R. Aaij *et al.*, *Selection and processing of calibration samples to measure the particle identification performance of the LHCb experiment in Run 2*, Eur. Phys. J. Tech. Instr. **6** (2019) 1 LHCb-DP-2018-001, `arXiv:1803.00824`. Cited on pages 31 and 40.

[78] R. Aaij *et al.*, *Performance of the LHCb Vertex Locator*, JINST **9** (2014) P09007, `arXiv:1405.7808`. Cited on page 31.

[79] P. d'Argent *et al.*, *Improved performance of the LHCb Outer Tracker in LHC Run 2*, JINST **12** (2017) P11016 LHCb-DP-2017-001, `arXiv:1708.00819`. Cited on page 32.

[80] LHCb collaboration, C. Marin Benito, *PID strategy and performance at LHCb in Run 2*, PoS **ICHEP2018** (2019) 687. Cited on page 32.

[81] LHCb collaboration, *LHCb trigger system: Technical Design Report*, CERN-LHCC-2003-031. LHCb-TDR-010. Cited on page 34.

[82] T. Head, *The LHCb trigger system*, JINST **9** (2014) C09015. Cited on page 34.

[83] LHCb collaboration, *Trigger Schemes*, LHCb Web. Cited on page 35.

[84] R. Aaij *et al.*, *Performance of the LHCb trigger and full real-time reconstruction in Run 2 of the LHC*, JINST **14** (2019), no. LHCb-DP-2019-001 P04013, `arXiv:1812.10790`. Cited on page 35.

[85] P. Billoir, M. De Cian, P. A. Günther, and S. Stemmle, *A parametrized Kalman filter for fast track fitting at LHCb*, Computer Physics Communications **265** (2021) 108026, https://doi.org/10.1016/j.cpc.2021.108026. Cited on page 36.

[86] T. Sjöstrand, S. Mrenna, and P. Skands, *A brief introduction to PYTHIA 8.1*, Computer Physics Communications **178** (2008) 852. Cited on page 38.

[87] I. Belyaev *et al.*, *Handling of the generation of primary events in Gauss, the LHCb simulation framework*, Journal of Physics: Conference Series **331** (2011) 032047. Cited on page 38.

[88] D. J. Lange, *The evtgen particle decay simulation package*, Nuclear Instruments and Methods in Physics Research Section A: Accelerators, Spectrometers, Detectors and Associated Equipment **462** (2001), no. 1 152, BEAUTY2000, Proceedings of the 7th Int. Conf. on B-Physics at Hadron Machines. Cited on page 38.

[89] S. Agostinelli *et al.*, *Geant4—a simulation toolkit*, Nuclear Instruments and Methods in Physics Research Section A: Accelerators, Spectrometers, Detectors and Associated Equipment **506** (2003), no. 3 250. Cited on page 38.

[90] J. Allison *et al.*, *Geant4 developments and applications*, IEEE Transactions on Nuclear Science **53** (2006), no. 1 270. Cited on page 38.

[91] J. Back *et al.*, *LAURA^{++}: A Dalitz plot fitter*, Comput. Phys. Commun. **231** (2018) 198, `arXiv:1711.09854`. Cited on pages 38 and 82.

[92] G. A. Cowan, D. C. Craik, and M. D. Needham, *Rapidsim: An application for the fast simulation of heavy-quark hadron decays*, Computer Physics Communications **214** (2017) 239. Cited on pages 39 and 55.

[93] Particle Data Group, R. L. Workman *et al.*, *Review of Particle Physics*, PTEP **2022** (2022) 083C01. Cited on pages 39, 54, and 125.

[94] T. Chen and C. Guestrin, *XGBoost: A scalable tree boosting system*, arXiv:1603.02754. Cited on page 41.

[95] G. Punzi, *Sensitivity of searches for new signals and its optimization*, 2003. Cited on page 44.

[96] C. Costa Sobral, *Measurement of the relative branching fractions of charmless three-body B^+ decays at LHCb*, PhD thesis, Warwick U., 2019, CERN-THESIS-2019-246. Cited on page 45.

[97] LHCb collaboration, R. Aaij *et al.*, *Study of beauty baryon decays to D^0ph^- and $\Lambda_c^+h^-$ final states*, Phys. Rev. **D89** (2014) 032001 CERN-PH-EP-2013-207 LHCb-PAPER-2013-056, arXiv:1311.4823. Cited on page 48.

[98] T. Skwarnicki, *A study of the radiative cascade transitions between the Upsilon-prime and Upsilon resonances*, PhD thesis, Institute of Nuclear Physics, Krakow, 1986, DESY-F31-86-02. Cited on page 52.

[99] LHCb collaboration, R. Aaij *et al.*, *Measurements of the branching fractions for $B^0_{(s)}\to D_{(s)}\pi\pi\pi$ and $\Lambda^0_b\to\Lambda^+_c\pi\pi\pi$*, Phys. Rev. **D84** (2011) 092001, Erratum ibid. **D85** (2012) 039904 LHCb-PAPER-2011-016 CERN-PH-EP-2011-151, arXiv:1109.6831. Cited on page 55.

[100] CDF collaboration, T. Aaltonen *et al.*, *Measurement of the branching fraction $\mathcal{B}(\Lambda_b^0\to\Lambda_c^+\pi^-\pi^+\pi^-)$ at CDF*, Phys. Rev. **D85** (2012) 032003, arXiv:1112.3334. Cited on page 55.

[101] LHCb collaboration, R. Aaij *et al.*, *Observation of the $\Lambda_b^0\to\Lambda_c^+K^+K^-\pi^-$ decay*, Phys. Lett. **B815** (2021) 136172 LHCb-PAPER-2020-028,CERN-EP-2020-209, arXiv:2011.13738. Cited on page 55.

[102] M. Pivk and F. R. Le Diberder, *SPlot: A statistical tool to unfold data distributions*, Nucl. Instrum. Meth. A **555** (2005) 356, arXiv:physics/0402083. Cited on pages 70 and 112.

[103] A. Rogozhnikov, *Reweighting with boosted decision trees*, Journal of Physics: Conference Series **762** (2016) 012036. Cited on page 84.

[104] N. L. JOHNSON, *SYSTEMS OF FREQUENCY CURVES GENERATED BY METHODS OF TRANSLATION*, Biometrika **36** (1949) 149, arXiv:https://academic.oup.com/biomet/article-pdf/36/1-2/149/513258/36-1-2-149.pdf. Cited on page 89.

[105] K. Cranmer, *Kernel estimation in high-energy physics*, Computer Physics Communications **136** (2001) 198. Cited on page 89.

[106] A. Rogozhnikov, *Reweighting with boosted decision trees*, Journal of Physics: Conference Series **762** (2016) 012036. Cited on page 98.

[107] LHCb collaboration, R. Aaij *et al.*, *Measurement of the track reconstruction efficiency at LHCb*, JINST **10** (2015) P02007 CERN-LHCB-DP-2013-002, arXiv:1408.1251. Cited on page 99.

[108] LHCb collaboration, R. Aaij *et al.*, *Observation of a* $\Lambda_b^0 - \overline{\Lambda}_b^0$ *production asymmetry in proton-proton collisions at* $\sqrt{s} = 7$ *and* 8 TeV, JHEP **10** (2021) 060 LHCb-PAPER-2021-016, CERN-EP-2021-121, arXiv:2107.09593. Cited on page 99.

[109] LHCb collaboration, R. Aaij *et al.*, *Amplitude analysis of the* $\Lambda_c^+ \to pK^-\pi^+$ *decay and* Λ_c^+ *baryon polarization measurement in semileptonic beauty hadron decays*, arXiv:2208.03262 LHCb-PAPER-2022-002, CERN-EP-2022-124, arXiv:2208.03262, to be published in Phys. Rev. D. Cited on page 100.

[110] E791 collaboration, E. M. Aitala *et al.*, *Multidimensional resonance analysis of* $\Lambda_c^+ \to pK^-\pi^+$, Phys. Lett. B **471** (2000) 449, arXiv:hep-ex/9912003. Cited on pages 100 and 101.

[111] LHCb collaboration, R. Aaij *et al.*, *Measurement of the* $\Lambda_b^0 \to J/\psi\,\Lambda$ *angular distribution and the* Λ *polarisation in pp collisions*, JHEP **06** (2020) 110 LHCb-PAPER-2020-005,CERN-EP-2020-051, arXiv:2004.10563. Cited on page 101.

[112] https://twiki.cern.ch/twiki/bin/view/LHCb/TrackCalib. The procedure to apply the tracking efficiency correction is given at https://twiki.cern.ch/twiki/bin/viewauth/LHCbInternal/TrackingEffRatio. Cited on page 103.

[113] A. Martín Sánchez, P. Robbe, and M.-H. Schune, *Performances of the LHCb L0 calorimeter trigger*, LHCb-PUB-2011-026. More details can be found here: https://twiki.cern.ch/twiki/bin/viewauth/LHCbPhysics/CalorimeterObjectsToolsGroupDOC#L0_Hadron_trigger_efficiencies. Cited on page 104.

[114] LHCb collaboration, R. Aaij *et al.*, *Measurement of b hadron production fractions in 7* TeV *pp collisions*, Phys. Rev. **D85** (2012) 032008 CERN-PH-EP-2011-172 LHCb-PAPER-2011-018, arXiv:1111.2357. Cited on page 121.

[115] LHCb collaboration, R. Aaij *et al.*, *Measurement of b-hadron fractions in 13* TeV *pp collisions*, Phys. Rev. **D100** (2019) 031102(R) LHCb-PAPER-2018-050 CERN-EP-2019-016, arXiv:1902.06794. Cited on page 121.

[116] LHCb collaboration, R. Aaij *et al.*, *Measurement of the $B^{\pm}$ production asymmetry and the CP asymmetry in $B^{\pm} \to J/\psi K^{\pm}$ decays*, Phys. Rev. **D95** (2017) 052005 LHCb-PAPER-2016-054 CERN-EP-2016-325, arXiv:1701.05501. Cited on page 123.

[117] LHCb collaboration, R. Aaij *et al.*, *Measurement of B^0, B_s^0, B^+ and Λ_b^0 production asymmetries in 7 and 8 TeV proton-proton collisions*, Phys. Lett. **B774** (2017) 139 LHCb-PAPER-2016-062 CERN-EP-2017-036, arXiv:1703.08464. Cited on page 123.

[118] Belle collaboration, N. Gabyshev *et al.*, *Study of decay mechanisms in $B^- \to \Lambda_c^+ \overline{p} \pi^-$ decays and observation of low-mass structure in the $\Lambda_c^+ \overline{p}$ system*, Phys. Rev. Lett. **97** (2006) 242001, arXiv:hep-ex/0409005. Cited on pages 125 and 126.

[119] BaBar collaboration, B. Aubert *et al.*, *Measurements of $\mathcal{B}(\overline{B}^0 \to \Lambda_c^+ \overline{p})$ and $\mathcal{B}(B^- \to \Lambda_c^+ \overline{p} \pi^-)$ and studies of $\Lambda_c^+ \pi^-$ resonances*, Phys. Rev. **D78** (2008) 112003, arXiv:0807.4974. Cited on pages 125 and 127.